



## Multiscale Modelling of Organic Solar Cell Materials – morphology evolution in solution processed bulk heterojunctions

**Gertsen, Anders Skovbo**

*Publication date:*  
2020

*Document Version*  
Publisher's PDF, also known as Version of record

[Link back to DTU Orbit](#)

*Citation (APA):*  
Gertsen, A. S. (2020). Multiscale Modelling of Organic Solar Cell Materials – morphology evolution in solution processed bulk heterojunctions. Technical University of Denmark.

---

### General rights

Copyright and moral rights for the publications made accessible in the public portal are retained by the authors and/or other copyright owners and it is a condition of accessing publications that users recognise and abide by the legal requirements associated with these rights.

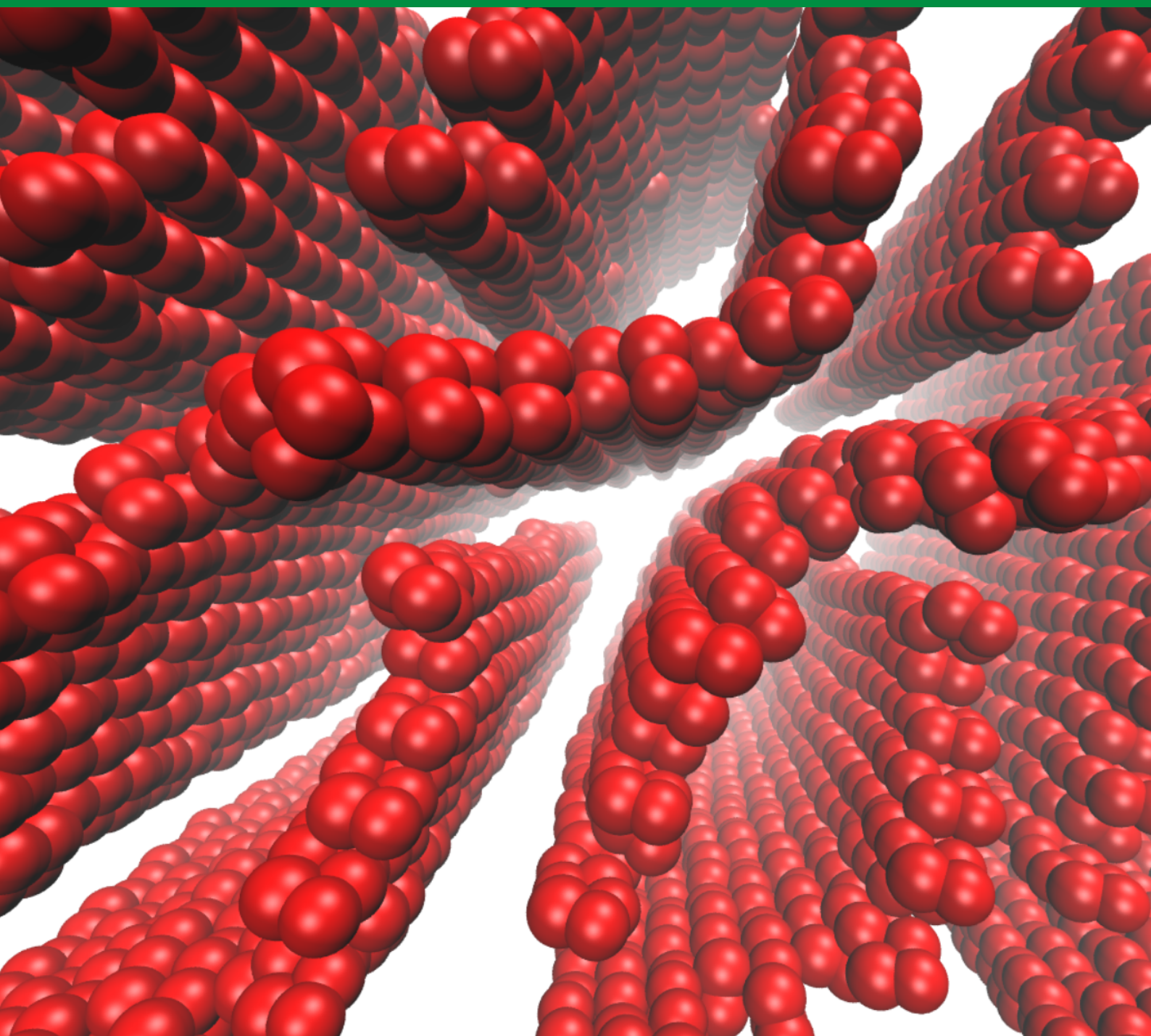
- Users may download and print one copy of any publication from the public portal for the purpose of private study or research.
- You may not further distribute the material or use it for any profit-making activity or commercial gain
- You may freely distribute the URL identifying the publication in the public portal

If you believe that this document breaches copyright please contact us providing details, and we will remove access to the work immediately and investigate your claim.

# Multiscale Modelling of Organic Solar Cell Materials

– morphology evolution in solution processed bulk heterojunctions

PhD Thesis by Anders S. Gertsen







## **Multiscale Modelling of Organic Solar Cell Materials**

– morphology evolution in solution processed bulk heterojunctions

PhD Thesis

December, 2020

By

Anders S. Gertsen

Copyright:      Reproduction of this publication in whole or in part must include the customary bibliographic citation, including author attribution, report title, etc.

Cover photo:    Anders S. Gertsen, 2020

Published by:    DTU, Department of Energy Conversion and Storage, Fysikvej, Building 310, 2800 Kgs. Lyngby Denmark  
[www.energy.dtu.dk](http://www.energy.dtu.dk)

ISSN:            [0000-0000] (electronic version)

ISBN:            [000-00-0000-000-0] (electronic version)

ISSN:            [0000-0000] (printed version)

ISBN:            [000-00-0000-000-0] (printed version)

## Preface

This thesis is a summary of the models, findings, and publications resulting from my past three years of PhD studies in the Department of Energy Conversion and Storage (DTU Energy), Technical University of Denmark (DTU) from January 1, 2018 to December 31, 2020. The majority of the work has been carried out at Risø DTU National Laboratory for Sustainable Energy under the supervision of Prof. Jens W. Andreasen, DTU Energy, DTU. The PhD project is two-thirds funded by the European Commission's Horizon 2020 framework programme through the SEEWHI (Solar Energy Enabled for the World by High-Resolution Imaging) consolidator grant ERC-2015-CoG-681881 and one-third funded by DTU Energy.

The first six months of my employment as a PhD student were spent on an external stay at Imperial College London under the inspiring supervision of Prof. Jenny Nelson, Department of Physics, Imperial College London (co-supervisor of the project). The external stay was facilitated by Prof. Natalie Stingelin (previously Department of Materials, Imperial College London, now School of Materials Science and Engineering, Georgia Institute of Technology; co-supervisor of the project) and in part funded by Otto Mønstedts Fond (grant no. 17-70-1617). I was lucky enough to visit again later in my studies on a short two-week stay in the fall of 2019.

In addition to this, I went to the University of Groningen on a fruitful one-month visit in the fall of 2019 to collaborate with Riccardo Alessandri and Prof. Siewert-Jan Marrink, Zernike Institute of Advanced Materials, University of Groningen. This visit was funded by the European Commission's Horizon 2020 framework programme through the HPC-Europa3 (Transnational Access Programme for a Pan-European Network of HPC Research Infrastructures and Laboratories for Scientific Computing) grant H2020-INFRAIA-2016-1-730897.

The outreach projects presented herein have been funded by the Danish National Research Foundation, the Carlsberg Foundation, and the William Demant Foundation under the Science Pavilion initiative as well as by DTU Energy.

This thesis is submitted in fulfilment of the PhD degree on the authority of the DTU Energy PhD school and the Chemistry, Biotechnology, and Chemical Engineering PhD Committee.

Anders S. Gertsen - s180292



.....  
*Signature*

31 December 2020

.....  
*Date*



## Abstract

Organic solar cells are presently used for niche applications due to their semi-transparency, flexibility, low weight, and possibilities of custom designs in terms of colours and shapes, but low efficiencies of large-scale fabricated modules have hampered grid implementations. However, with their low-cost solution processing and projected energy payback times of only fractions of those of silicon modules, the technology has a great potential to reach commercial viability within few years if the efficiency and lifetime can be improved. Important properties that directly affect the performance of organic solar cells such as charge carrier mobility and optical absorption are crucially dependent on the morphology of the active layer. These morphologies are in turn affected by a multitude of processing parameters and material properties, and advanced experimental techniques such as *in situ* X-ray scattering need to be applied to follow the blend microstructure formation during post-deposition drying. Computational modelling is often indispensable in the interpretation of these experiments, and it can furthermore provide a crucial link between structural studies and performance characteristics of devices.

This thesis aims to investigate these structure-property relationships in solution processed organic functional material systems through sequential multiscale simulations combining density functional theory, atomistic molecular dynamics simulations, and coarse-grained molecular dynamics simulations. The simulation and analysis frameworks presented represent a systematic approach to obtain morphologies and structural properties of organic functional materials at experimentally relevant conditions and to infer the electronic properties that govern their function directly from these. This has been applied to state-of-the-art materials for organic transistors and organic solar cells. OPLS-AA atomistic force fields and MARTINI 3.0 coarse-grained force fields have been developed for several donor polymers and small-molecule, non-fullerene acceptors as well as for the solvents from which they are processed. The atomistic models allow simulation of the dynamics and local interactions in materials where chemically specific interactions are decisive, and the coarse-grained models give access to the spatio-temporal resolution necessary to follow the morphology evolution in solvent evaporation simulations. Coupling these with quantum chemical calculations and kinetic Monte Carlo simulations can yield valuable insight into the structure-property relationships of these materials. Furthermore, the simulations provide molecular scale resolution, which fosters an intuitive insight into the nanostructure of the materials and enables easier interpretation of advanced experiments.

With the present work, a general simulation and analysis framework for solution deposition of organic materials has been established, and the outlined future extensions are believed to hold the potential to accelerate computational design of materials and processing parameters for organic solar cells.

## Dansk resumé

Organiske solceller bruges i øjeblikket til nicheapplikationer grundet deres halvgennem-sigtighed, fleksibilitet og lave vægt samt deres mulighed for at blive designet i forskellige former og farver, men lave effektiviteter af storskala-fabrikerede moduler har hæmmet implementeringen af dem i det generelle elnet. Muligheden for at printe organiske sol-celler direkte fra en type blæk i opløsning kombineret med deres lave energitilbagebetal-ingstider på kun brøkdele af siliciumsolcellers giver dog teknologien et stort potentiale til at opnå forretningsmæssig modenhed inden for få år, hvis deres effektivitet og levetid kan forbedres. Morfologien af det aktive lag i organiske solceller har afgørende betydning for vigtige egenskaber, der har direkte indflydelse på effektiviteten af organiske solceller, såsom mobiliteten af ladningsbærere og optisk absorption. Disse morfologier bliver påvir-ket af et væld af processeringsparametre og materialeegenskaber, når solcellerne printes, og avancerede eksperimentelle teknikker såsom *in situ* røntgenspredning skal bruges for at følge udviklingen af morfologien under tørringsprocessen af blækken efter printning. Computermodellering er ofte et uundværligt værktøj i fortolkningen af disse eksperi-menter, og det kan tilmed fungere som et afgørende link mellem studier af strukturen og af egenskaberne af organiske solceller.

Denne afhandling sigter mod at undersøge disse struktur-egenskabssammenhænge i printede, organiske, funktionelle materialer gennem sekventiel multiskalamodellering i en kombination af densitetsfunktionale teori, atomistiske molekyledynamiksimuleringer og grovkornede molekyledynamiksimuleringer. Simulerings- og analysemetoderne præsæn-teret her repræsenterer en systematisk tilgang til at opnå morfologier og strukturelle egenskaber af organiske, funktionelle materialer ved eksperimentelt relevante forhold og til at udlede elektroniske egenskaber fra disse. Metoderne er blevet anvendt på nogle af de nyeste og bedste materialer til organiske transistorer og organiske solceller. OPLS-AA atomistiske kraftfelter og MARTINI 3.0 grovkornede kraftfelter til molekyledy-namiksimuleringer er blevet udviklet for en samling donorpolymerer og småmolekylære acceptorer såvel som de solventer, de ofte bliver processeret fra. De atomistiske mod-eller muliggør simuleringer af dynamikkerne og de lokale interaktioner i materialer, hvor kemisk specifikke interaktioner er vigtige, og de grovkornede modeller giver adgang til de tids- og længdeskalaer, der er nødvendige for at følge udviklingen af morfologien i solventfordampningssimuleringer. Ved at kombinere disse solventfordampningssimu-leringer med kvantekemiske beregninger og kinetiske Monte Carlo-simuleringer kan der opnås værdifuld indsigt i struktur-egenskabssammenhængene af organiske, funktionelle materialer. Desuden giver simuleringerne adgang til visualiseringer med opløsninger på molekyleskala, hvilket kan give en intuitiv indsigt i nanostrukturen af materialerne og hjælpe fortolkningen af avancerede eksperimenter på vej.

Arbejdet præsenteret heri har etableret et generelt rammeværk for simulering og anal-yse af printede, organiske materialer, og de skitserede, fremtidige udvidelser forventes at have potentialet til at accelerere computerdesign af materialer og processeringsparametre for organiske solceller.

## Acknowledgements

Since I, on a cold January morning in 2018, started my PhD studies at DTU Energy, the field of organic solar cells has undergone a tremendous development. Back then, the world record efficiency was around 12 %, and now, at the time of writing in December 2020, reports of more than 18 % have been published. As inspiring as it has been to be part of a field advancing so rapidly, it is the disappointment of not having been able to contribute more to these advances that I am left with after these three years. However, I am also left with fond memories of philosophic lunch-break discussions, lost memories of Friday evenings, and last, but certainly not least, friendships. I owe what is left of my sanity to my fellow group members and colleagues, past and present: Tiago, Giovanni, Mariana, Raha, Marcial, Moises, Eva, Vanessa, Christian, Kristoffer, Mette, Sofie, and Elise. A special mention goes to my office-mates Michael and Azat with whom I have shared many laughs, a few cries, and the occasional PhD frustrations. I could not have wished for better company – you have been sincerely missed in the working-from-home-at-a-small-desk-in-the-bedroom times during the last year. If trying to do research without colleagues around for duck talking is an uphill struggle, writing the thesis has been my toughest climb in 2020. Passo del Mortirolo came in as a close second – Jeppe, thank you for leading the way!

My studies have, pre-COVID, brought me to many nice places for conferences, beam-times, and workshops, but my visits to London and Groningen stand out as the scientific highlights. Jenny, I am grateful to have had the chance to collaborate with you and your group. You are an inspiring scientist and supervisor, and I thoroughly enjoyed my time at Imperial. The gang at Wood Lane Studios also played a big role in making it a memorable six months in London – cheers!

Riccardo, working with you has been a true inspiration. I am indebted to you and Siewert-Jan for hosting me and for introducing me to MARTINI. Although I spent only a month in Groningen, the collaboration we initiated has helped me to stay motivated in a strange 2020.

Many deserve a thanks for keeping my work-life balance healthy, in particular Tune Bogklub and our lovely friends and girlfriends: I value your friendships more than you know. My most heartfelt acknowledgements are, however, reserved for my family and Vibe: your unconditional support and trust in me have carried me through the last couple of months, and words cannot express how grateful I am – af hele mit hjerte; tak.

Finally, no thesis is complete without a philosophical quote. My supervisor Jens has never failed to remind me that simulations are inferior to experimental evidence. Although it is not music to a theorist's ears, he is indeed correct. As the renowned statistician George Box rather elegantly phrased it:<sup>a</sup>

*"All models are wrong, but some are useful."*

I hope that my contribution to the field of materials modelling will be seen in this light – in particular, I hope that my mistakes and efforts can serve as stepping stones for future PhD students embarking on a journey into the world of molecular dynamics.

---

<sup>a</sup>A shout out to the GROMACS development team, who, with their inclusion of a quirky quote such as this in each `stdout`, has brought a smile to my face after countless simulations.



## List of publications

This thesis is partly based on the following publications and manuscripts:

- I Anders S. Gertsen<sup>†</sup>, Marcial Fernández Castro<sup>†</sup>, Roar R. Søndergaard, and Jens W. Andreasen\*, "Scalable fabrication of organic solar cells based on non-fullerene acceptors", *Flex. Print. Electron.*, vol. 5, 014004, **2020**.  
DOI: 10.1088/2058-8585/ab5f57
- II Anders S. Gertsen, Michael Korning Sørensen, and Jens W. Andreasen\*, "Nanostucture of organic semiconductor thin films: Molecular dynamics modeling with solvent evaporation", *Phys. Rev. Mater.*, vol. 4, 075405, **2020**.  
DOI: 10.1103/PhysRevMaterials.4.075405
- III Xingyuan Shi<sup>†</sup>, Anders S. Gertsen<sup>†</sup>, Jack Coker, Martin van der Schelling, Drew Pearce, Matt Bird, Garry Rumbles, Chad Snyder, Lee Richter, Weimin Zhang, Mariano Campoy Quiles, Jarvist M. Frost, Jens W. Andreasen, Iain McCulloch, and Jenny Nelson\* "Disentangling the impact of chain conformation and inter-chain packing on hole mobility in a stiff conjugated polymer", *in preparation*.<sup>‡</sup>
- IV Anders S. Gertsen, Riccardo Alessandri, Marcial Fernández Castro, Moises Espindola Rodriguez, Michael Korning Sørensen, Jack Coker, Jenny Nelson, Siewert-Jan Marrink\*, and Jens W. Andreasen\*, "The influence of processing parameters on structure-property relationships in organic solar cells: a coarse-grained molecular dynamics study", *in preparation*.<sup>‡</sup>

Other publications and manuscripts in which I have been involved but that are not in the scope of this thesis:

- V Khadijeh Khalili, Ludger Inhester, Caroline Arnold, Anders S. Gertsen, Jens W. Andreasen\*, and Robin Santra, "Simulation of time-resolved X-ray absorption spectroscopy of ultrafast dynamics in particle-hole-excited 4-(2-thienyl)-2,1,3-benzothiadiazole", *Struct. Dyn.*, vol. 7, 044101, **2020**.  
DOI: 10.1063/4.0000016
- VI Christian Rein, Jens Uhlig, David Carrasco-Busturia, Khadijeh Khalili, Anders S. Gertsen, Asbjørn Moltke, Xiaoyi Zhang, Tetsuo Katayama, Juan María García Lastra, Martin Meedom Nielsen, Shin-Ichi Adachi, Kristoffer Haldrup, and Jens W. Andreasen\*, "Element-specific investigations of ultrafast dynamics in photoexcited Cu<sub>2</sub>ZnSnS<sub>4</sub> nanoparticles in solution", *submitted*, **2020**.

---

<sup>†</sup>Equal contributions; \*corresponding authorship; <sup>‡</sup>titles and author lists of manuscripts III and IV are provisional.

# Contents

Preface . . . . .	ii
Abstract . . . . .	iii
Dansk resumé . . . . .	iv
Acknowledgements . . . . .	v
List of publications . . . . .	vi
<b>1 Introduction</b>	<b>1</b>
1.1 Scalability of organic solar cells . . . . .	2
1.2 Organic semiconductors and solar cells . . . . .	4
1.3 Multiscale modelling . . . . .	6
1.4 Scope and outline . . . . .	8
1.5 Notes on semantics and notation . . . . .	9
<b>2 Theoretical background and computational methods</b>	<b>11</b>
2.1 From classical to quantum and back . . . . .	11
2.1.1 Separation of space and time variables . . . . .	12
2.1.2 Separation of nuclear and electronic variables . . . . .	13
2.1.3 Separation of electronic variables . . . . .	15
2.2 Quantum chemical calculations . . . . .	19
2.2.1 Density functional theory . . . . .	19
2.2.2 Exchange-correlation functionals . . . . .	22
2.3 Molecular dynamics simulations . . . . .	25
2.3.1 Time propagation . . . . .	25
2.3.2 Non-bonded interactions . . . . .	27
2.3.3 Bonded interactions . . . . .	31
2.3.4 Atomistic models . . . . .	33
2.3.5 Coarse-grained models . . . . .	34
2.4 Bridging the scales . . . . .	35
<b>3 Electronic coupling in neat, solution processed thin-films</b>	<b>39</b>
3.1 Introduction . . . . .	40
3.2 Methods . . . . .	41
3.2.1 Torsions . . . . .	42
3.2.2 Solvent evaporation simulations . . . . .	43
3.2.3 Persistence length . . . . .	45
3.2.4 Structural analysis . . . . .	47
3.2.5 Electronic coupling . . . . .	47

3.3	Results . . . . .	48
3.3.1	Persistence lengths of IDTBT polymers . . . . .	48
3.3.2	Substrate effects . . . . .	49
3.3.3	Thin-film morphologies . . . . .	50
3.3.4	Electronic properties . . . . .	53
3.4	Discussion . . . . .	54
3.5	Conclusions . . . . .	56
3.6	Appendix . . . . .	56
3.6.1	Detailed parametrisation procedure . . . . .	56
3.6.2	Error analysis of persistence length simulations . . . . .	59
<b>4</b>	<b>Morphology evolution in solution processed organic solar cell blends</b>	<b>61</b>
4.1	Introduction . . . . .	62
4.2	Force field development . . . . .	63
4.2.1	Mapping . . . . .	65
4.2.2	Free energies of transfer . . . . .	67
4.2.3	Torsions . . . . .	68
4.3	Solvent evaporation simulations . . . . .	69
4.3.1	Methodological considerations . . . . .	70
4.4	Analysis methods . . . . .	71
4.4.1	Close contacts . . . . .	71
4.4.2	Spatial discretisation . . . . .	72
4.4.3	Domain sizes and purity . . . . .	73
4.4.4	Percolating pathways and mobility simulations . . . . .	74
4.4.5	Specific interface areas . . . . .	75
4.4.6	Crystallinity and crystallite sizes . . . . .	76
4.5	Results . . . . .	77
4.5.1	Close contacts . . . . .	77
4.5.2	Domain sizes and purity . . . . .	82
4.5.3	Percolating pathways and mobility simulations . . . . .	86
4.5.4	Specific interface areas . . . . .	89
4.5.5	Crystallite sizes . . . . .	89
4.6	Discussion . . . . .	91
4.6.1	Comparison to device measurements . . . . .	91
4.6.2	Impact of evaporation rate and statistics . . . . .	92
4.6.3	Impact of simulation box size . . . . .	94
4.7	Conclusions . . . . .	94
4.8	Appendix . . . . .	96
4.8.1	Structural figure of merit . . . . .	96
<b>5</b>	<b>Outreach projects</b>	<b>97</b>
5.1	Motivation . . . . .	98
5.2	Science Pavilion at Roskilde Festival . . . . .	98
5.3	Grand Opening of Amager Bakke/CopenHill . . . . .	100
5.4	Appendix A: Solar Tree catalogue . . . . .	101
5.5	Appendix B: Explanatory posters and quiz . . . . .	107
<b>6</b>	<b>Outlook</b>	<b>113</b>



<b>Bibliography</b>	<b>115</b>
<b>Publications</b>	<b>131</b>
Paper I . . . . .	131
Paper II . . . . .	155



# 1 Introduction

Sustainability has through the last two decades been cemented as a key issue in global politics. This materialised in 2015 as the Paris Agreement<sup>1</sup> and United Nation's 17 sustainable development goals,<sup>2</sup> which today are an integral part of the strategies in most large companies and universities around the globe. The mitigation of climate change is intimately connected to several of these goals, and an economically viable and environmentally friendly transition from fossil fuels to sustainable energy sources thus represents the most pressing challenge of our generation.

Arguably, ensuring affordable, clean energy for all relies on either economical incentive or political willingness, but ultimately, it relies on technological maturity and scalability. The global energy production from renewable energy sources such as wind and solar is increasing at unprecedented rates, and their cumulative installed capacities are expected to continue the rapid growth in the coming decade.<sup>3</sup> Although this to some degree can be ascribed to the political landscape and governmental subsidies in a few pioneering countries, large scale production has been a central driver in propelling wind turbines and silicon solar cells to cost competitiveness with fossil fuels.<sup>4</sup> Scaling these technologies is, however, not unproblematic. Measures like toxicity and material availability have a substantial impact on the scalability of energy technologies,<sup>5</sup> but also the energy use and CO<sub>2</sub> emission associated with the production of a turbine or cell constitute an important consideration. Whereas modern wind turbine magnets rely on difficult-to-mine rare earth elements,<sup>6</sup> wind turbines only need to be in operation for around 6-12 months before having generated as much energy as went into producing them.<sup>7</sup> Conversely, silicon solar cells do not depend on scarce materials, but their production is quite energy intensive, meaning that they have to be in operation for around 18-30 months to reach zero net consumption.<sup>8</sup> This figure of merit is referred to as the *energy payback time*.

Emerging sustainable energy technologies must stand out from or even outperform existing technologies to increase their chances of reaching maturity and commercialisation. Efficiency and lifetime can be mentioned as universally important parameters for grid implementation in addition to the above toxicity, material availability, and energy payback time. However, also module weight as well as freedom of design in terms of shapes, colours, flexibility, and transparency are important parameters for building integration and niche applications, and sacrificing efficiency in order to obtain added functionality can therefore be justifiable. Whereas commercial crystalline silicon solar cell modules are both efficient ( $\sim 20\%$  power conversion efficiency, PCE) and long-term stable ( $> 25$  years), the freedom of design is limited. Organic photovoltaics (OPV) represent a new generation of solar cells that can be fabricated to be lightweight, flexible, and transparent. Their active layers consist of organic, semiconducting molecules, allowing them to undergo a low-energy solution processing in the form of an ink. Printing organic solar



cells continuously on roll-to-roll machinery is hence possible,<sup>9,10</sup> leading to remarkably low energy payback times.<sup>11</sup> Organic solar cells are, however, still inferior to silicon solar cells in terms of stability and efficiency,<sup>12–14</sup> and although the record efficiency for an OPV research cell is now above 18 %, <sup>15,16</sup> it has proven difficult to maintain the high efficiencies when upscaling the cells.

In this chapter, the concepts of scalability, organic semiconductors, and multiscale modelling will be introduced. They will, respectively, specify why this project came to be, what types of materials we consider, and how we are simulating them. This will be followed by an outline of the thesis and a few notes on semantics and notation.

## 1.1 Scalability of organic solar cells

As alluded to above, the great potential for the OPV technology to enable low-cost solar cells with a minimal energy payback time can be realised if the high research cell efficiencies can be somewhat maintained in large-scale modules fabricated using roll-to-roll processes.<sup>11,17–19</sup> This can be coined as the lab-to-fab challenge. The SEEWHL project (Solar Energy Enabled for the World by High-resolution Imaging), which this work is part of, aims to take on the lab-to-fab challenge and *"derive new and fundamental insight in the relation between nanoscale structure and the performance of third-generation solar cells, and determine how to apply this in large-scale processing."*<sup>a</sup> This ambition has motivated a close interplay between large-scale device manufacturing, advanced X-ray measurements, and modelling of nanoscale structure formation, the latter of which the present work addresses. Before diving into the details of the modelling efforts, it is thus beneficial to put them in context of the project as a whole.

Back in 2016 when the SEEWHL project was initiated, the field of OPV had been stagnant for several years, and the best research cell efficiencies seemed to have reached a plateau just above 10 %. <sup>14</sup> Despite concentrated effort being put into upscaling the small-scale cells to roll-to-roll fabrication,<sup>20–27</sup> the efficiencies rarely got close to even half of that of the research cells. The structure formation in the active layer inks during roll-coating was therefore studied with *in situ* X-ray techniques in the hope of being able to suggest guidelines for optimal large-scale processing parameters in order to close this gap.<sup>28–31</sup> The interpretation of such experiments is, however, not straightforward, and simulations of structure formation could hence prove useful.

With the advent of a new class of acceptor materials in late 2017 (cf. Section 1.2),<sup>32</sup> the OPV field was revitalised, and the record efficiencies have since gone up from around 12 % to more than 18 %. <sup>15,16</sup> Although the fundamental function of the acceptors have not changed with the new class, they behave differently during solution processing and in the thin-films. The OPV literature has naturally been focused on optimising efficiency, but the understanding of the influence of processing parameters, especially when seeking to upscale the active layer deposition, is trailing behind the huge effort put into the synthesis of these new acceptor materials.

High-efficiency research cells are most often fabricated with spin-coated active layers and areas of only a few square millimetres, and stability tests are rarely reported. A collective effort towards reporting stabilities of square centimetre cells fabricated with roll-to-roll compatible deposition methods such as slot-die coating could thus help identifying important focus points for the effort of bridging the efficiency gap between lab-scale cells

---

<sup>a</sup>Information about SEEWHL can be found at <https://cordis.europa.eu/project/id/681881>.

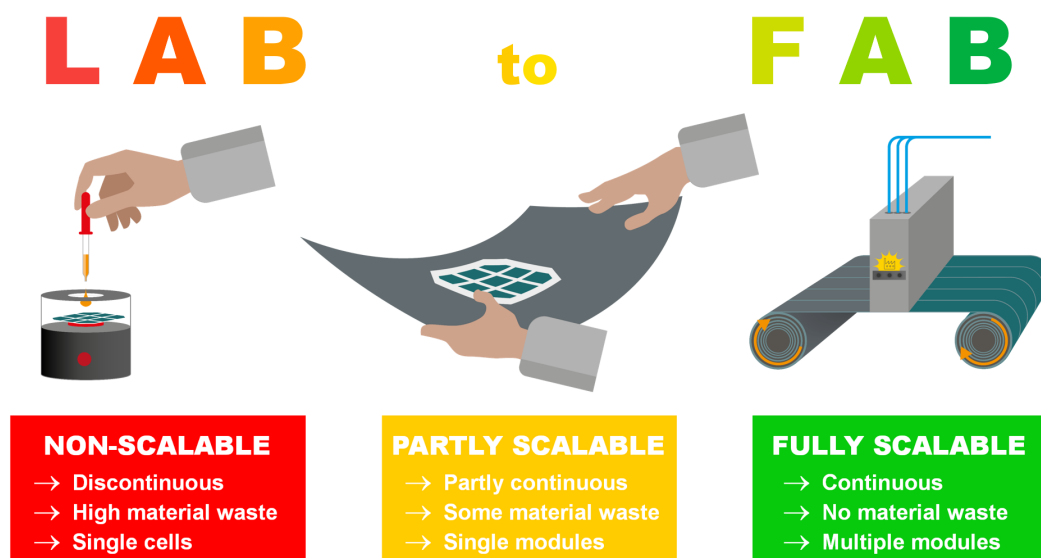


Figure 1.1: The lab-to-fab challenge and categorisation of organic solar cell fabrication methods. Spin-coating represents a strictly non-scalable deposition method, whereas only roll-to-roll methods can be said to be fully scalable; research should focus on partly or fully scalable methods to bridge the efficiency gap between lab-scale cells and large-scale modules. Adapted from Paper I.

and scalably fabricated modules. In Paper I (enclosed as an appendix to this thesis), we have outlined this challenge and discussed the concept of scalability with respect to deposition methods (see Fig. 1.1). Additionally, we have reviewed the recent literature to identify the degree to which scalable techniques are used in the fabrication of fullerene-free organic solar cells and to suggest strategies for overcoming the lab-to-fab challenge. Only few reports utilised fully scalable deposition methods for both the active layers and electrodes, and the resulting cells were in general of low efficiency. A couple of noteworthy examples of flexible cells with slot-die coated active layers – but vacuum processed top electrodes – were reported, reaching efficiencies of more than 7 %, <sup>33,34</sup> but the conclusion remained that the literature on scalably fabricated organic solar cells was sparse.

Very recently, in November 2020, an encouraging report of large-scale, flexible organic solar cell modules with high efficiencies was published.<sup>35</sup> It was shown that 1 cm<sup>2</sup> slot-die coated cells retained almost the full 12.4 % efficiency of small-scale, spin-coated cells. Most notably, a 25 cm<sup>2</sup> roll-coated module exhibited a PCE of more than 10 %, representing the current record for flexible OPV. Less than two months before, in September 2020, the current record efficiency of any OPV module of 12.6 % for a 26 cm<sup>2</sup> rigid device with a blade-coated active layer was published along with an impressive efficiency of 11.7 % for a corresponding 204 cm<sup>2</sup> module.<sup>36</sup> Although the top electrodes were thermally evaporated for all modules in both reports, they represent the first two times that the 10 % efficiency mark has been reached for large-scale OPV modules. More importantly, they have shown that the solution processing of active layers can be upscaled without significantly compromising the efficiency by carefully controlling the processing conditions. Combined with recent reports of organic solar cells with exceptionally long  $T_{80}$  lifetimes of 10-20 years (extrapolated from accelerated stability tests),<sup>37,38</sup> the OPV

technology now seems to be coming within reach of commercialisation.<sup>39</sup>

## 1.2 Organic semiconductors and solar cells

An organic compound can generally be defined as a molecule consisting mainly of carbon and hydrogen atoms, but also nitrogen, oxygen, sulfur, fluorine, and chlorine are common components in these. The definition thus spans a wide range of materials, including proteins, polymers, sugars, and most biological matter. Organic semiconductors constitute a subclass of organic molecules and polymers that form solid materials which become semiconducting when photoexcited or when charges are injected into the material from electrodes. These solid materials can exhibit different degrees of order, from single molecular crystals to amorphous thin-films. Common for all organic semiconductors is that they have conjugated electronic systems, most often in the form of alternating single- and double bonds between carbons. Whereas a single bond is the sharing of two electrons localised as a  $\sigma$ -type bond between two atoms, a double bond is the sharing of four electrons; two in the form of a strong, localised  $\sigma$ -bond and two in a more weak  $\pi$ -bond. In conjugated systems, the electrons constituting  $\pi$ -bonds are mobile, which leads to delocalised electron probability distributions; this delocalisation is the main facilitator of their conductive properties. The effect is particularly strong in aromatic ring-systems, and these are thus often seen in well-performing organic semiconductors. The  $\pi$ -electrons are also responsible for most intermolecular connectivities between individual molecules or polymers in the solid materials, as their probability distributions overlap when they come in close contact. This is referred to as  $\pi$ -stacking, which creates a pathway for charges to "jump" between molecules or polymers.

In this thesis, organic solar cells are the main topic. The focus will hence be on organic semiconductors with optical gaps (partly) matching the spectrum of the sun. The optical gap of a material is defined as the energetic threshold for photon absorption, and it is thus essentially a function of the (electronic) ground state energy of a molecule and its (vertically) excited state energy. For molecular systems, the molecular orbital picture is commonly used as a representation of these energy levels. In the electronic ground state, a molecule will have two electrons in its highest occupied molecular orbital (HOMO). When excited by a photon with the correct energy, an electron will be promoted from the HOMO to the lowest unoccupied molecular orbital (LUMO). In organic semiconductors, the excited electron will have an attractive electrostatic interaction with the positively charged hole left behind in the HOMO, and they can therefore not immediately dissociate into free charges. Such a Coulombically bound electron-hole pair is referred to as an exciton. For inorganic solar cell materials such as crystalline silicon, a high dielectric constant effectively screens the two charges to a degree where the exciton binding energy can be overcome by thermal fluctuations. Organic semiconductors, however, have quite low dielectric constants, and the exciton binding energies are thus often an order of magnitude larger than the thermal energy at room temperature. Efficiently splitting excitons into free charges and transporting these to the electrodes thus constitute the central challenge of OPV design.

In 1986, Ching W. Tang<sup>b</sup> published the first report of a two-component organic solar cell.<sup>40</sup> By subsequently depositing two different organic small molecule materials

---

<sup>b</sup>C. W. Tang was also one of the inventors of organic light emitting diodes (OLED) and received the 2011 Wolf Prize in chemistry for his accomplishments in the field of organic functional materials.

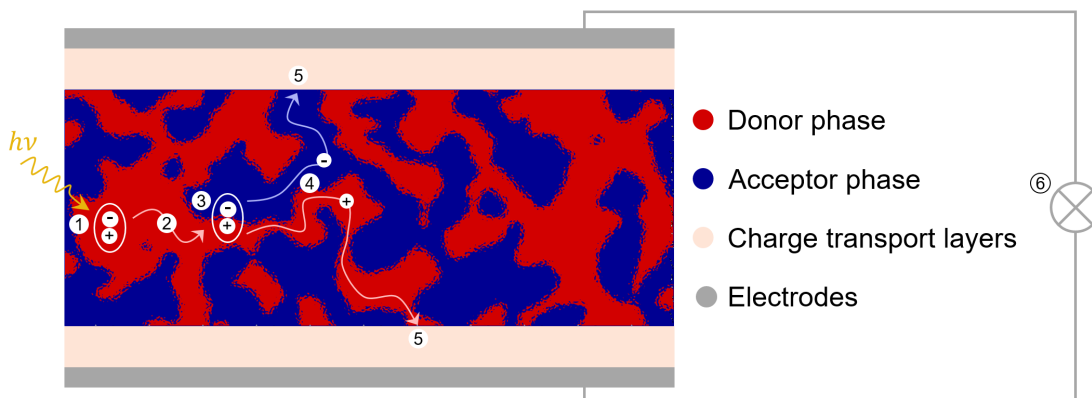


Figure 1.2: Schematic of a bulk heterojunction organic solar cell. Its operation can, in a simplified picture, be explained as follows: a photon is absorbed, creating an exciton (1). The exciton diffuses to an interface between donors and acceptors (2). Having reached an interface, the exciton separates into free charges (3), and these charges are transported in the respective phases (4) via the charge selective transport layers to the electrodes, where they are collected (5). The current generated can then drive an external circuit (6).

by thermal evaporation to create a bilayer, he found that photogenerated excitons would dissociate into free charges at the interface between the two layers. The free electrons would then be transported to the cathode in the acceptor (or *n*-type) material, and the holes to the anode in the donor (or *p*-type) material. As groundbreaking as this concept was, the efficiency was limited to around 1 %. Almost a decade later, in 1995, the concept of bulk heterojunction organic solar cells was introduced.<sup>41–43</sup> It was noted that the characteristic length over which an exciton could diffuse before recombining was an order of magnitude lower than the optical absorption depth of the commonly used materials, meaning an implicit compromise between exciton generation and exciton dissociation was present. To overcome this limitation, the donor and acceptor materials were blended in solution before deposition, meaning that an interpenetrating network of donor and acceptor domains would form via phase-separation; a bulk heterojunction. This allowed thicker active layers with better absorption, but it also means that the solution processing parameters had to be carefully tuned to maintain the delicate balance between forming domains of a sufficient size and purity to form percolating pathways for charge transport to the electrodes and keeping them small enough for excitons to reach an interface before recombining. A schematic of a bulk heterojunction active layer sandwiched between charge transport layers and electrodes can be seen in Fig. 1.2 along with a simplified explanation of the operational principles of organic solar cells.

Given the apparent strong influence of the nano- and mesoscale structure of the donor:acceptor blends on the efficiencies of organic solar cells, being able to follow and visualise the domain formation during solution deposition would be desirable for predicting optimal processing parameters. Multiscale modelling represents a possible way of gaining insight in the intermolecular interactions governing the structure formation and its connection to the device properties. This will be introduced below.

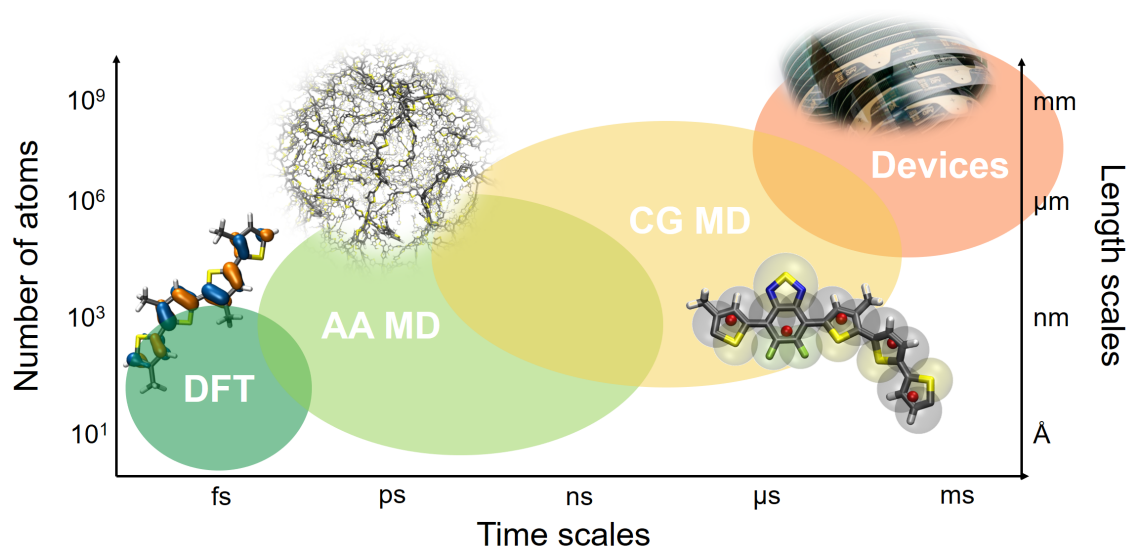


Figure 1.3: The scales of the simulation methods used in this thesis: density functional theory (DFT), all-atom/atomistic molecular dynamics (AA MD), and coarse-grained molecular dynamics (CG MD).

### 1.3 Multiscale modelling

The physical chemistry of organic functional materials inherently spans several orders of magnitude in both time and space: from the ultrafast, femtosecond response of electrons to external stimuli to the slow self-assembly processes of macromolecules on the order of seconds; from nanoscale local molecular packing through domain sizes of tens of nanometres to micrometre-thick thin-films (see Fig. 1.3). No single computational method which is able to span all these scales simultaneously currently exists, and we must therefore either focus on a limited subset of scales using simulation techniques designed specifically for those or combine existing methods to span more scales. The latter is generally what is referred to as multiscale modelling, but it has been suggested that the idea of what a multiscale problem truly is and how it should be defined should rather be rooted in the physics of the problem itself and the separability of its scales.<sup>44</sup> Three major categories were identified in this Ref. 44:

1. if the scales of interest are separated, sequential multiscale modelling can be applied. Here, simulation data from one model of a given resolution are used to inform another model of a different resolution, which can then run without any reference to the first;
2. if the scales are only separable, meaning that one needs to continuously switch between scales to refine the simulations, the strategy of back-mapping can be applied. Back-mapping can generally be defined as restoring the resolution of one model based on the simulation data of another,<sup>45,46</sup> and it is in general useful for reliable switching between scales;
3. if the scales are highly interconnected and cannot meaningfully be separated, concurrent multiscale simulations must be applied. Example methods include quantum mechanical/molecular mechanics (QM/MM) simulations<sup>47,48</sup> and adaptive

resolution schemes (AdResS).<sup>49–51</sup> Although they represent powerful simulation methods, they will not be used herein.

The former two will constitute the framework for bridging the scales of simulations herein, primarily sequential multiscale modelling. As the main objective is to simulate the structural properties of organic functional materials, the specific simulation techniques employed will all be particle based with some degree of molecular resolution to ensure an intuitive translation between scales and methods. The techniques applied to the different scales will be introduced below.

A full treatment of interactions in and between molecules would require a relativistic, quantum chemical description of all electron- and nuclear dynamics in the system. This is, however, not feasible for any but the smallest of molecules. In order to simulate larger systems, we apply a series of approximations that allows us to focus on the properties that are most important for the given scale of interest. First of all, we neglect relativistic effects and adopt the time-dependent Schrödinger equation as our starting point. By separating space and time variables, we can focus on a time-independent problem and thus the probability distributions of the electrons and nuclei at a given instant. Realising that the electrons are much lighter than the nuclei, however, means that we can also separate the electronic motion from the nuclear motion. This is the Born-Oppenheimer approximation, which constitutes the basis for the first group of simulation methods addressed herein, namely quantum chemical calculations. Quantum chemical calculations allow us to investigate the electronic properties of molecules "frozen" in a specific nuclear configuration and to energetically optimise their conformations by varying the nuclear configurations. This is only feasible for molecular systems of up to  $\mathcal{O}(10^3)$  atoms depending on the specific method applied, but it can yield high accuracy information about relative energetics of molecular conformers and interactions. Quantum chemical methods can furthermore yield information about the interaction of molecules with time-dependent fields such as light, but still only for single nuclear configurations. Including the nuclear motion to simulate the dynamics of molecules is hence the next step.

Nuclei are, in most cases, sufficiently massive to be treated classically, and we can thus utilise Newton's laws to propagate them in time. However, as nuclei move on potential energy surfaces defined by the electrons, we need a way of approximating these surfaces, as we are otherwise still limited by the time it takes to quantum chemically derive them at each time step. By approximating intramolecular bonds, angles, and dihedrals as harmonic oscillators or other simple functional forms with parameters derived from quantum chemical calculations, it is possible to propagate the nuclear positions in time in a computationally feasible framework. Including a description of *intermolecular* forces through a simple potential parametrised to reproduce van der Waals interactions, collections of molecules can also be simulated. Sets of parameters for such intra- and intermolecular potential energy surfaces are called force fields and are the key ingredients in molecular dynamics simulations. Molecular dynamics simulations with full atomistic resolution can span several orders of magnitude in both time and space, but they are, however, limited by the fact that the discrete time steps used for the propagation of nuclear positions should be significantly shorter than the fastest dynamics probed. This implies that the interatomic vibrational frequencies limit the time steps to one or two femtoseconds, but practically, systems of hundreds of thousands of atoms can be simulated for hundreds of nanoseconds. Although studies of mesoscale structures or self-assembly

processes are therefore not feasible, atomistic molecular dynamics simulations are indispensable for simulating dynamics of local order and atom-specific interactions.

In order to reach longer simulation times for even larger systems, one can define force fields for coarse-grained representations of molecules in which several atoms are described as single particles. These particles are obviously heavier than atoms, and the time steps can thus be increased. Furthermore, fewer calculations have to be performed at each time step due to the lower relative number of particles, yielding a significant computational advantage over atomistic models; systems corresponding to millions of atoms can be simulated for several microseconds. Coarse-grained models often rely on being fitted to atomistic models, and they can thus conceptually be seen as averaging over atom-specific details that are not crucial for simulating nano- and mesoscale structure formation.

In summary, sequential multiscale modelling can, in the context of this thesis, be described as using quantum chemical simulations to inform atomistic molecular dynamics simulations, which in turn can be used to inform coarse-grained molecular dynamics simulations, allowing studies of mesoscale properties. This process can also be reversed, allowing studies of electronic properties of molecules or molecular complexes extracted from simulated morphologies. Multiscale modelling hence represents a practical tool for investigating the structure-property relationships of organic functional materials.

## 1.4 Scope and outline

This thesis aims to explore how multiscale simulations can be used to simulate the structural evolution of solution processed organic solar cell materials during post-deposition drying. Emphasis will be placed on a) aiding the interpretation of experiments, b) making sense of and predicting macroscopic properties from a detailed understanding of atomic scale behaviour, and c) visualising blend, mesoscale structures to improve our understanding of domain formation. The chapters are organised as follows:

- **Chapter 2** gives an account of the theoretical background of molecular simulations and the details of the computational methods used. First, the series of approximations made to feasibly simulate structural properties at different time and length scales will be outlined. Secondly, density functional theory will be presented along with a description of exchange-correlation functionals and considerations regarding their applicability to organic functional materials. Thirdly, the physical concepts behind intermolecular interactions are introduced and put in the context of molecular dynamics simulations and the atomistic and coarse-grained force fields used in these simulations. Finally, a brief account of how the scales between the different simulations have been bridged will be given.
- **Chapter 3** addresses the intermolecular electronic coupling in thin-films of organic semiconductors. By combining new molecular dynamics models for high mobility polymers and small-molecule acceptors with quantum chemical calculations, some light can be shed on the structure-property relationships of these systems.
- **Chapter 4** investigates the effects of various solution processing parameters on the morphology evolution in bulk heterojunctions using coarse-grained solvent evaporation simulations. New models for widely used donor polymers and a small-molecule, non-fullerene acceptor will be presented alongside an extensive analysis framework of general use for simulated blends of organic molecules.

- **Chapter 5** briefly showcases two outreach projects and their success in engaging young people in solar energy and in particular the OPV technology.
- **Chapter 6** will conclude the work by outlining the perspectives for further simulations and the OPV technology as a whole.

Finally, the two published manuscripts, Paper I and Paper II, resulting from the work presented herein will be enclosed as appendices.

## 1.5 Notes on semantics and notation

- Throughout, vectors will be denoted in bold, non-italic fonts and scalars in non-bold, italic fonts, e.g.:

$$\mathbf{r}_i = \begin{pmatrix} x_i \\ y_i \\ z_i \end{pmatrix} \quad (1.1)$$

$$r_{ij} = |\mathbf{r}_i - \mathbf{r}_j| \quad (1.2)$$

- Unless otherwise stated, all integrals are implicitly assumed definite with boundaries from  $-\infty$  to  $\infty$ .
- When writing sums over pairs of particles in a system of  $N$  particles, the following notation is used:

$$\sum_{i < j}^N x_{ij} = \sum_{i=1}^{N-1} \sum_{j=i+1}^N x_{ij} \quad (1.3)$$

where  $x_{ij}$  is a variable dependent on the properties of particles  $\{i, j\}$ . This can be interpreted as the upper triangular block of a square 2D-matrix of dimension  $N$  *without* the diagonal, i.e. only counting unique pairs and not counting any self-interactions. Equivalently:

$$\sum_{i < j < k}^N x_{ijk} = \sum_{i=1}^{N-2} \sum_{j=i+1}^{N-1} \sum_{k=j+1}^N x_{ijk} \quad (1.4)$$

- In connection with the sections on quantum chemical theory, the Dirac (or bra-ket) notation will occasionally be used:

$$|\psi\rangle \equiv \psi(\mathbf{x}), \quad \langle\psi| \equiv \psi(\mathbf{x})^* \quad (1.5)$$

$$|\psi\rangle^\dagger = \langle\psi|, \quad \langle\psi|^\dagger = |\psi\rangle \quad (1.6)$$

$$\langle\psi| \hat{O} |\psi\rangle = \int \psi(\mathbf{x})^* \hat{O} \psi(\mathbf{x}) d\mathbf{x} \quad (1.7)$$

where  $\mathbf{x}$  is a collection of spatial and spin coordinates,  $*$  denotes a complex conjugate, and  $\dagger$  denotes a Hermitian conjugate. Eq. 1.7 is essentially an expectation value of an operator  $\hat{O}$  and represents an observable  $O$ .

- Regarding the term "particle": a particle is here defined as any spherically symmetrical entity comprising a basic building block in a molecular model of a given resolution - i.e. the term "particle" covers the terms "electron", "atom", "ion", and "bead", the latter of which is the common denotation of basic building blocks in coarse-grained molecular models (cf. Section 2.3.5).





## 2 Theoretical background and computational methods

A fundamental understanding of the physical chemistry governing the properties of organic materials is a prerequisite to determining the relative importance of molecular interactions at different time and length scales. In this chapter, a brief introduction to the most important concepts and limitations of the methods used in this thesis will thus be given. An emphasis will be placed on providing an intuitive explanation of the mathematical expressions describing the forces that govern inter- and intramolecular interactions as well as their interaction with light. The seminal works of great scientists such as Newton, Coulomb, Pauli, Schrödinger, Einstein, London, and Debye form the basis for the physical concepts presented, whereas modern implementations of these in efficient, highly-parallelised programs have enabled simulations of technologically relevant functional materials.

Countless lecture notes<sup>52–54</sup> and original literature have contributed to my understanding of the various concepts discussed below, but few things beat books and well-written software documentation. This chapter is hence in part based on Frank Jensen's *Introduction to Computational Chemistry*,<sup>55</sup> Jan H. Jensen's *Molecular Modeling Basics*,<sup>56</sup> and, to a lesser degree, other works.<sup>57,58</sup> In addition, the GROMACS 2018 reference manual has provided valuable insight into their specific implementations of the equations presented here.<sup>59</sup> I am indebted to my old supervisor Kurt V. Mikkelsen as well as Sten Rettrup for, during my Bachelor's and Master's studies, teaching me most of what I know about quantum chemistry; their brilliant lectures form the basis for Section 2.2.

### 2.1 From classical to quantum and back

The dawn of quantum mechanics in the early 20<sup>th</sup> century marked the beginning of a new paradigm in theoretical physics and chemistry. For the past 200 years, classical mechanics based on Newton's laws had defined the theory of dynamics, but experimental observations of e.g. light-matter interactions that could not be reconciled with classical mechanics made it increasingly clear that new, unifying theories were needed. The theory of quantum mechanics was formulated to address this, and today, concepts like the wave-particle duality, photons, and quantisation are commonly known.

The field of organic functional materials is closely tied to quantum mechanics. The functionalities of these are often related to interaction with light, and theoretically resolving their properties demand an understanding of their molecular building blocks. This calls for a quantum chemical approach. It features an explicit treatment of electrons, nuclei, and their interaction, and the dynamical evolution of any given molecular system

containing  $N$  nuclei and  $n$  electrons with a wave-function  $\Psi = \Psi(\mathbf{R}, \mathbf{r}, t)$  depending on time  $t$ , nuclear coordinates  $\mathbf{R} = \{\mathbf{R}_1, \mathbf{R}_2, \dots, \mathbf{R}_N\}$ , and electron coordinates  $\mathbf{r} = \{\mathbf{r}_1, \mathbf{r}_2, \dots, \mathbf{r}_n\}$  can formally be written as

$$i\hbar \frac{\partial}{\partial t} \Psi(\mathbf{R}, \mathbf{r}, t) = \hat{H}(\mathbf{R}, \mathbf{r}, t) \Psi(\mathbf{R}, \mathbf{r}, t). \quad (2.1)$$

Here,  $\hbar$  is Planck's constant divided by  $2\pi$  and  $\hat{H}$  is the Hamiltonian of the system. For a relativistic Hamiltonian, Eq. 2.1 takes the identity of the Dirac equation, whereas for a non-relativistic Hamiltonian, Eq. 2.1 represents the time-dependent Schrödinger equation.<sup>60–62</sup> Neither of these have analytical solutions for many-body systems (i.e. for  $N + n > 2$ ), and we must thus apply a series of approximations in order to feasibly simulate the dynamics of molecules:

1. separate space and time variables (essentially by assuming a time-independent interaction potential);
2. separate nuclear and electronic variables (i.e. apply the Born-Oppenheimer approximation);
3. separate electronic variables (i.e. transform the intractable many-body problem into a conceptually and computationally more simple independent particle model using the self-consistent field method);
4. determine how to describe the nuclear part depending on which scale and properties that are of interest;
5. determine how to describe the electronic part depending on which scale and properties that are of interest.

Below, an illustration of this process will be given without the attempt to be comprehensive. Atomic units will be used throughout this section ( $\hbar = e = a_0 = m_e = 1$ ).

### 2.1.1 Separation of space and time variables

Considering only the non-relativistic case (which is justifiable for most organic molecules)<sup>55</sup>, the Hamiltonian can be expressed as the sum of the operator  $\hat{T}$  describing the kinetic energy of the system and the operator  $\hat{V}$  describing the potential energy of the system as

$$\hat{H}(\mathbf{R}, \mathbf{r}, t) = \hat{T}(\mathbf{R}, \mathbf{r}) + \hat{V}(\mathbf{R}, \mathbf{r}, t). \quad (2.2)$$

We can convince ourselves that the kinetic energy operator does not depend on time by remembering that the kinetic energy of a single particle with mass  $m$  and coordinates  $\mathbf{r}$  is essentially described by a momentum operator  $-\frac{\hbar}{2m} \frac{\partial^2}{\partial \mathbf{r}^2}$ . We thus see that the left-hand side of Eq. 2.1 has a partial time derivative working on the wave-function, whereas the right-hand side has a (collection of) spatial second order partial derivatives working on the wave-function. A common way of solving problems like this is by separation of variables. Looking for solutions to where  $\Psi$  can be written as a product of a time-independent part and a time-dependent part

$$\Psi(\mathbf{R}, \mathbf{r}, t) = \Psi(\mathbf{R}, \mathbf{r}) f(t), \quad (2.3)$$

we find the following when inserting this into Eq. 2.1, using Eq. 2.2, and rearranging:

$$i\hbar \frac{df(t)}{dt} \frac{1}{f(t)} = \hat{T}(\mathbf{R}, \mathbf{r}) \Psi(\mathbf{R}, \mathbf{r}) \frac{1}{\Psi(\mathbf{R}, \mathbf{r})} + \hat{V}(\mathbf{R}, \mathbf{r}, t). \quad (2.4)$$

We now see that the left-hand side has only functions of time, whereas the right-hand side has only functions of positions and momenta – except for the potential  $\hat{V}(\mathbf{R}, \mathbf{r}, t)$ . This leads us to consider cases only for which the potential is time-independent, i.e.  $\hat{V}(\mathbf{R}, \mathbf{r}, t) \rightarrow \hat{V}(\mathbf{R}, \mathbf{r})$ . This is valid for the larger part of the cases discussed herein, but we will have to explicitly treat the time-dependence when considering molecules interacting with time-dependent fields such as light.

With the assumption of a time-independent potential, it is now clear that the time variable is separated and independent from the spatial variables in Eq. 2.4, which in turn means that each of the left-hand side and right-hand side must be equal to the same constant; this constant is postulated to be the energy  $E$  of the system, yielding

$$i\hbar \frac{df(t)}{dt} \frac{1}{f(t)} = E \quad \text{and} \quad (2.5)$$

$$E = \hat{T}(\mathbf{R}, \mathbf{r}) \Psi(\mathbf{R}, \mathbf{r}) \frac{1}{\Psi(\mathbf{R}, \mathbf{r})} + \hat{V}(\mathbf{R}, \mathbf{r}). \quad (2.6)$$

From Eq. 2.5, we can now solve the differential equation and obtain the time-dependent part (also called the *phase factor*) of the wave-function in Eq. 2.3 as<sup>55</sup>

$$\Psi(\mathbf{R}, \mathbf{r}, t) = \Psi(\mathbf{R}, \mathbf{r}) f(t) = \Psi(\mathbf{R}, \mathbf{r}) e^{-\frac{iEt}{\hbar}}. \quad (2.7)$$

From Eq. 2.6, we then get the familiar eigenvalue problem of the time-independent Schrödinger equation:<sup>60–62</sup>

$$\hat{H}(\mathbf{R}, \mathbf{r}) \Psi(\mathbf{R}, \mathbf{r}) = E \Psi(\mathbf{R}, \mathbf{r}). \quad (2.8)$$

Here,  $\Psi(\mathbf{R}, \mathbf{r})$  represents the eigenstate of the system with the corresponding eigenvalue  $E$  representing the energy of the system. As long as we are only interested in properties described by time-independent operators, the above treatment will hence suffice, yielding what is referred to as stationary states as eigenfunctions. The time evolution of these stationary states is then considered "separately" by including the phase factor when time-dependent properties are of interest. Nevertheless, this Eq. 2.8 represents the first step towards simplifying molecular interactions. The next step will be to de-couple the electronic and nuclear degrees of freedom.

### 2.1.2 Separation of nuclear and electronic variables

In 1927, Max Born and J. Robert Oppenheimer presented an approximation that allowed the separation of nuclear and electronic variables.<sup>63</sup> To introduce the implications of this Born-Oppenheimer approximation, we start by writing out the individual components of the Hamiltonian for a molecular system with subscripts  $n$  referring to nuclei and  $e$  to electrons:

$$\hat{H}(\mathbf{R}, \mathbf{r}) = \hat{T}_n(\mathbf{R}) + \hat{V}_{nn}(\mathbf{R}) + \underbrace{\hat{T}_e(\mathbf{r}) + \hat{V}_{ne}(\mathbf{R}, \mathbf{r}) + \hat{V}_{ee}(\mathbf{r})}_{\hat{H}_e(\mathbf{R}, \mathbf{r})}. \quad (2.9)$$

Here, we see that the nuclear-electron interaction potential  $\hat{V}_{\text{ne}}(\mathbf{R}, \mathbf{r})$  prevents us from cleanly separating electronic and nuclear coordinates in Eq. 2.9. Strictly speaking, a mass-polarisation term will also arise as part of the Hamiltonian for systems in centre of mass coordinates with more than two particles. This happens because it is not possible to directly separate the centre of mass motion from the internal motion for such systems. The Born-Oppenheimer approximation relies on the assumption that the mass-polarisation can be disregarded and that this separation of the potential can be performed anyway, essentially building on the premise that the difference in masses of electrons and nuclei make them move on different time scales. To hand-wavily illustrate this with a classical analogue, one can consider a system with a negatively charged particle moving relative to a positively charged particle. If the interaction between the two opposite charges is purely electromagnetic of nature, the resulting forces acting on the two are of similar magnitude. From Newton's second law, we know that similar forces,  $\mathbf{F}$ , correspond to similar changes in momentum,  $\mathbf{p}$ , as

$$\frac{d\mathbf{p}}{dt} = m \frac{d\mathbf{v}}{dt} = \mathbf{F}, \quad (2.10)$$

meaning that if the masses,  $m$ , of the two particles are substantially different (as is the case for electrons and nuclei), this will result in substantially different velocities,  $\mathbf{v}$ . The heavy nucleus will thus move significantly slower than the light electron by a factor of  $\frac{m_{\text{n}}}{m_{\text{e}}} \sim 10^4$ . Back in the quantum picture, this generally means that electrons adjust very rapidly to changes in the nuclear conformation, and we thus "guess" that the eigenfunction of a molecular system can be written as

$$\Psi(\mathbf{R}, \mathbf{r}) \approx \psi(\mathbf{r}; \mathbf{R})\chi(\mathbf{R}), \quad (2.11)$$

where  $\psi(\mathbf{r}; \mathbf{R})$  is an electronic wave-function and the semicolon indicates a parametric dependence of the electrons on only the nuclear coordinates (and not their momenta), and where  $\chi(\mathbf{R})$  is a function describing the nuclei. If we now consider a set of *fixed* nuclear positions and assume that the electronic wave-function is an eigenfunction to a time-independent electronic (or clamped-nuclei) Schrödinger equation (where  $\hat{H}_{\text{e}}(\mathbf{r}; \mathbf{R})$  is the electronic Hamiltonian, cf. Eq. 2.9, and  $E_{\text{e}}(\mathbf{R})$  is the electronic energy of the system)

$$\hat{H}_{\text{e}}(\mathbf{r}; \mathbf{R})\psi(\mathbf{r}; \mathbf{R}) = E_{\text{e}}(\mathbf{R})\psi(\mathbf{r}; \mathbf{R}), \quad (2.12)$$

we can insert our trial wave-function, our *ansatz*, from Eq. 2.11 in the full time-independent Schrödinger equation (Eq. 2.8) and evaluate the outcome. A mathematically rigorous derivation of the electronic and nuclear Schrödinger equations in the Born-Oppenheimer picture is not too involved,<sup>a</sup> but for the sake of brevity, only the conceptual form and a brief discussion of its implications will be presented here. By combining these Eqs. 2.8 and 2.11 and carefully evaluating all terms and derivatives arising from the molecular Hamiltonian (Eq. 2.9), two correction terms, namely the non-adiabatic coupling elements, will arise. These are important for systems involving more than one electronic surface, but are neglected in the Born-Oppenheimer approximation.<sup>55</sup> This leads to a nuclear Schrödinger equation of the form

$$(\hat{T}_{\text{n}}(\mathbf{R}) + E_{\text{e}}(\mathbf{R}))\chi(\mathbf{R}) = E\chi(\mathbf{R}). \quad (2.13)$$

<sup>a</sup>The full derivation of the nuclear Schrödinger equation in the Born-Oppenheimer picture can be found in Ref. 55, pp. 82-86.

Here, the electronic energy takes the role of a potential energy, which implies that, in the Born-Oppenheimer picture, the nuclei move on a potential energy surface defined by the solutions to the electronic Schrödinger equation (Eq. 2.12). One can thus map out the energetic landscape of a molecule by varying the nuclear positions and solving the electronic Schrödinger equation at each point. Owing to the "large" mass of the nuclei, a classical treatment of the nuclear dynamics will usually suffice when the potential energy surface is known;<sup>56</sup> this will be described in detail in Section 2.3. We can therefore concentrate on solving the electronic Schrödinger equation in the next Section 2.1.3.

The Born-Oppenheimer approximation is a cornerstone in computational chemistry. Most, if not all, electronic structure methods are based on this – even those that treat situations for which it breaks down, where it is instead used as a starting point for more refined treatments. These breakdowns generally happen when two potential energy surfaces come in close proximity energetically and the assumption of separable nuclear and electronic motion is no longer valid; examples include photochemical reactions and conical intersections.<sup>64</sup> In most other cases, it is an excellent approximation.

### 2.1.3 Separation of electronic variables

Solving the many-body time-independent Schrödinger equation analytically is, as mentioned, not possible for molecular systems larger than the hydrogen atom. Even though the Born-Oppenheimer approximation reduced the problem to finding solutions to the electronic Schrödinger equation (Eq. 2.8), the many-body nature of the exact electronic wave-function was still prohibitive for this. In 1928,<sup>65</sup> Douglas Hartree first suggested a self-consistent field method and a set of equations that could provide an approximate, numerical solution to this problem. Later refined by John C. Slater in 1928<sup>66</sup> and 1930<sup>67</sup> and independently by Vladimir Fock in 1930,<sup>68</sup> the self-consistent field method and the formalism behind it laid the foundation for modern quantum chemical calculations.

In his seminal 1928 paper,<sup>65</sup> Hartree envisioned that the complex many-body wave-function could be written as a product of independent one-body functions representing spatial orbitals:

$$\psi(\mathbf{r}) \approx \phi_1(\mathbf{r}_1)\phi_2(\mathbf{r}_2) \cdots \phi_n(\mathbf{r}_n) = \prod_{i=1}^n \phi_i(\mathbf{r}_i). \quad (2.14)$$

Each of these would then satisfy an eigenvalue equation of the same form as the electronic Schrödinger equation for a one-electron operator  $\hat{f}$ :

$$\hat{f}(\mathbf{r}_i)\phi_i(\mathbf{r}_i) = \varepsilon_i\phi_i(\mathbf{r}_i) \quad (2.15)$$

with associated eigenvalues  $\varepsilon_i$  (from Eq. 2.14 forward, only the notation of a dependence on nuclear coordinates, not the dependence itself, has been dropped, i.e.  $\psi(\mathbf{r}) \equiv \psi(\mathbf{r}; \mathbf{R})$ ). The operator  $\hat{f}$  was derived from a mean-field approximation in which the electron  $i$  was assumed to see only an average field of all other electrons, yielding a one-electron operator

$$\hat{f}(\mathbf{r}_i) = -\frac{1}{2} \frac{\partial^2}{\partial \mathbf{r}_i^2} - \sum_{a=1}^N \frac{Z_a}{r_{ai}} + \int \frac{\rho(\mathbf{r}')}{|\mathbf{r}_i - \mathbf{r}'|} d\mathbf{r}'. \quad (2.16)$$

Here, the first term is the kinetic energy of electron  $i$ , the second term is the potential energy arising from the Coulombic interaction with nuclei  $a = 1, 2, \dots, N$  of charge  $Z_a$ ,

and the third term is the mean-field electron-electron repulsion with

$$\rho(\mathbf{r}') = \sum_{j \neq i}^n |\phi_j(\mathbf{r}_j)|^2 \quad (2.17)$$

being the charge density of all electrons, except electron  $i$  itself, evaluated at a position  $\mathbf{r}'$  from the expectation value of the orbitals. This meant that the electron-electron repulsion  $\hat{V}_{ee}$  (cf. Eq. 2.9) could now be evaluated one electron at a time. The intriguing aspect of this formalism was that, by applying an ansatz of the wave-function, i.e. a trial set of orbitals, one could solve Eq. 2.15 and generate a new set of orbitals. This set could then be input as a new ansatz, and iterating this until self-consistency, i.e. until the ansatz and the new set of orbitals were the same within a given threshold, would provide an approximate solution to the electronic Schrödinger equation. The approach was mainly supported by qualitative arguments and good correspondence with some experiments,<sup>69</sup> but later the same year, Slater provided a theoretically founded argument for the validity of Hartree's equations by showing that the self-consistent field method obeyed the variational principle.<sup>66</sup> This can generally be written as

$$E_e \leq E_\lambda = \langle \psi_\lambda | \hat{H}_e | \psi_\lambda \rangle, \quad (2.18)$$

where  $\psi_\lambda(\mathbf{r})$  is a normalised ansatz.

In 1930, Slater noted<sup>67</sup> that Hartree's ansatz (Eq. 2.14) could be improved upon by considering the symmetry of the wave-function with respect to electron spin. To illustrate this with a simple example (with no direct link to Hartree's work), we can consider the helium atom. Using Eq. 2.14 as an ansatz and applying the variational principle, we find that the minimum energy solution would place two electrons in the same spatial orbital, i.e. double occupancy.<sup>56</sup> Doing the same for the lithium atom would yield a triple occupancy.<sup>56</sup> Triple occupancy is a violation of Pauli's exclusion principle,<sup>70</sup> which states that no two electrons can have all quantum numbers equal, meaning that only two electrons can share the same spatial orbital: one with spin  $+\frac{1}{2}$  and one with spin  $-\frac{1}{2}$ . Spin is a relativistic effect, thus calling for the application of the relativistic Dirac equation, but introducing spin as an *ad hoc* quantum effect by enforcing anti-symmetry of the wave-function proved sufficient in the non-relativistic framework of the Schrödinger equation. Anti-symmetry is the requirement that the wave-function must change sign upon exchanging any two electrons coordinates in a system. For a wave-function in Hartree's orbital approximation, this can be done by assigning a spin to each electron and linearly combining all possible permutations of spatial orbitals. Such a linear combination can be compactly written as what has come to be known as a Slater determinant

$$\Phi(\mathbf{r}) = \frac{1}{\sqrt{n!}} \begin{vmatrix} \phi_1(\mathbf{r}_1) & \phi_2(\mathbf{r}_1) & \cdots & \phi_n(\mathbf{r}_1) \\ \phi_1(\mathbf{r}_2) & \phi_2(\mathbf{r}_2) & \cdots & \phi_n(\mathbf{r}_2) \\ \vdots & \vdots & \ddots & \vdots \\ \phi_1(\mathbf{r}_n) & \phi_2(\mathbf{r}_n) & \cdots & \phi_n(\mathbf{r}_n) \end{vmatrix}, \quad (2.19)$$

where each orbital  $\phi_i(\mathbf{r})$  now implicitly denotes a spin-orbital, and where the pre-factor takes care of normalisation. Conceptually, this means that electrons are indistinguishable and that each electron is thus associated with every orbital.

Simultaneously and independently in 1930, Fock published an extension to Hartree's work which utilised the properties of such determinants.<sup>68</sup> He showed that an anti-

symmetric wave-function like Eq. 2.19 could be constructed from Eq. 2.14 as

$$\Phi(\mathbf{r}) = \hat{A}\psi(\mathbf{r}) \quad (2.20)$$

using an anti-symmetrising operator<sup>55</sup>

$$\hat{A} = \frac{1}{\sqrt{n!}} \sum_{p=0}^{n-1} (-1)^p \hat{P} = \frac{1}{\sqrt{n!}} \left[ \hat{I} - \sum_{ij} \hat{P}_{ij} + \sum_{ijk} \hat{P}_{ijk} - \dots \right]. \quad (2.21)$$

Here,  $\hat{I}$  is the identity operator,  $\hat{P}_{ij}$  generates a permutation between two electron coordinates  $i$  and  $j$ ,  $\hat{P}_{ijk}$  generates a permutation between three electron coordinates  $i$ ,  $j$ , and  $k$ , and so on with the sums running over all possible combinations of electron coordinates. The electronic energy of the system can then be determined as the expectation value<sup>55</sup>

$$E_e = \langle \Phi | \hat{H}_e | \Phi \rangle = \sum_{p=0}^{n-1} (-1)^p \langle \psi | \hat{H}_e | \hat{P}\psi \rangle, \quad (2.22)$$

of the electronic Hamiltonian

$$\hat{H}_e(\mathbf{r}) = \hat{T}_e(\mathbf{r}) + \hat{V}_{ne}(\mathbf{r}) + \hat{V}_{ee}(\mathbf{r}) \quad (2.23a)$$

$$= - \sum_{i=1}^n \frac{1}{2} \frac{\partial^2}{\partial \mathbf{r}_i^2} - \sum_{i=1}^n \sum_{a=1}^N \frac{Z_a}{r_{ai}} + \sum_{i < j}^n \frac{1}{r_{ij}}. \quad (2.23b)$$

From this, it is clear that only the electron-electron repulsion operator depends on more than one electron coordinate and that the kinetic energy operator and the nuclear-electron attraction operator will thus give rise to the same terms as for Eqs. 2.15 and 2.16. The electron-electron repulsion operator, however, will, due to the permutation operator  $\hat{P}_{ij}$ , give rise to an extra term in addition to the classical Coulomb repulsion when working on the anti-symmetric wave-function. The one-electron integral yields

$$\underbrace{\langle \psi | -\frac{1}{2} \frac{\partial^2}{\partial \mathbf{r}_i^2} - \sum_{a=1}^N \frac{Z_a}{r_{ai}} | \psi \rangle}_{\hat{h}_i} = \langle \phi_i(\mathbf{r}_i) | \hat{h}_i | \phi_i(\mathbf{r}_i) \rangle \equiv h_i \quad (2.24)$$

as a consequence of only the identity operator of Eq. 2.21 yielding non-zero results when a one-electron operator works on the anti-symmetrised wave-function. For a two-electron operator, both the identity operator and the two-electron permutation operator will yield non-zero results. These are, respectively, the classical Coulomb term

$$\langle \psi | \frac{1}{r_{ij}} | \psi \rangle = \langle \phi_i(\mathbf{r}_i) \phi_j(\mathbf{r}_j) | \frac{1}{r_{ij}} | \phi_i(\mathbf{r}_i) \phi_j(\mathbf{r}_j) \rangle \equiv J_{ij} \quad (2.25)$$

and the so-called exchange term

$$\langle \psi | \frac{1}{r_{ij}} | \hat{P}_{ij} \psi \rangle = \langle \phi_i(\mathbf{r}_i) \phi_j(\mathbf{r}_j) | \frac{1}{r_{ij}} | \phi_i(\mathbf{r}_j) \phi_j(\mathbf{r}_i) \rangle \equiv K_{ij}, \quad (2.26)$$

from which it is seen that the electron indices in the ket have been exchanged relative to the classical Coulomb term. It should be noted that each of these Eqs. 2.24, 2.25,



and 2.26 rely on the orbitals being orthonormal, i.e.  $\langle \phi_i | \phi_j \rangle = \delta_{ij}$ . The total energy can thus, using Eq. 2.22, be written as

$$E_e = \sum_{i=1}^n h_i + \sum_{i < j}^n (J_{ij} - K_{ij}). \quad (2.27)$$

Based on the variational principle (Eq. 2.18),<sup>b</sup> Fock showed that the stationary points in this energy with respect to an orbital variation were related to an effective one-electron operator

$$\hat{F}(\mathbf{r}_i) = \hat{h}_i + \sum_j^n (\hat{J}_j - \hat{K}_j), \quad \text{where} \quad (2.28)$$

$$\hat{J}_j |\phi_i(\mathbf{r}_i)\rangle = \langle \phi_j(\mathbf{r}_j) | \frac{1}{r_{ij}} | \phi_j(\mathbf{r}_j) \rangle |\phi_i(\mathbf{r}_i)\rangle \quad \text{and} \quad (2.29)$$

$$\hat{K}_j |\phi_i(\mathbf{r}_i)\rangle = \langle \phi_j(\mathbf{r}_j) | \frac{1}{r_{ij}} | \phi_j(\mathbf{r}_i) \rangle |\phi_i(\mathbf{r}_j)\rangle, \quad (2.30)$$

which could enter a one-electron Schrödinger equation

$$\hat{F}(\mathbf{r}_i) \phi_i(\mathbf{r}_i) = \varepsilon_i \phi_i(\mathbf{r}_i) \quad (2.31)$$

similar to that of Eq. 2.15 from Hartree's work. This can be solved iteratively and self-consistently to yield a stationary, minimal energy for an anti-symmetric wave-function in the independent particle picture. The orbital energies can then be obtained as the expectation values of the Fock operator when all (occupied) orbitals are known as

$$\varepsilon_i = \langle \phi_i | \hat{F}_i | \phi_i \rangle = h_i + \sum_j^n (J_{ij} - K_{ij}). \quad (2.32)$$

We thus see that the total energy of the system (Eq. 2.27) is not simply a sum of the orbital energies (Eq. 2.32), as the latter would double-count the electron-electron repulsion terms, but it is straightforward to correct for this. The Hartree-Fock method, as this framework was dubbed, explicitly includes the important quantum mechanical exchange contribution, and it hence represents the starting point for most modern quantum chemical methods.

Although Hartree-Fock theory in general accounts for on the order of 99 % of the total energy of multi-electron systems, correctly describing the last 1 % is decisive in chemistry.<sup>55</sup> The difference between the exact energy of a system and the corresponding Hartree-Fock result (in the complete basis-set limit) is coined the correlation energy. This difference arises from the mean-field approximation and the fact that the pair density of two electrons is not strictly separable, i.e.

$$\rho(\mathbf{r}_1, \mathbf{r}_2) \neq \rho(\mathbf{r}_1) \rho(\mathbf{r}_2). \quad (2.33)$$

<sup>b</sup>In practice, a constrained optimisation with Lagrange multipliers are used, cf. Section 2.2.1 for an analogous problem. The exact derivation is out of the scope of this thesis, but it can be found in Ref. 55, pp. 86-92.

In general, electron correlation can hence be described as the influence of the movement of all other electrons on the movement of the electron in question. Strictly speaking, Hartree-Fock theory partly includes correlation through the exchange terms, which describe the correlation between electrons of parallel spin, often referred to as Fermi correlation. The Coulomb correlation arising from the instantaneous, repulsive interaction between electrons is, however, not accounted for in the independent particle picture of the mean-field approximation. Several post-Hartree-Fock wave-function methods such as Møller-Plesset perturbation theory and Coupled-Cluster theory aim to include this correlation energy, whereas also electron density-based methods build on Hartree-Fock theory in the quest for chemical accuracy.

With this in mind, we are now ready to dive deeper into the different formalisms for describing molecular interactions at different time and length scales (i.e. points 4. and 5. from the introductory paragraph of Section 2.1). The next Section 2.2 will describe how density functional theory is used to describe ground- and excited state electronic properties of molecular systems. After this, a description of how classical mechanics are used to propagate positions of particles in time on (semi-)empirical potential energy surfaces will be given in Section 2.3 followed by an account of how quantum chemical calculations are used to inform these classical simulations. Finally, Section 2.4 will briefly introduce the methods used to bridge the scales between simulations.

## 2.2 Quantum chemical calculations

As described in Section 2.1.3, the self-consistent field method and Hartree-Fock theory laid the foundation for quantum chemical calculations of molecular systems in the late 1920's and early 1930's. Numerous improvements over Hartree-Fock theory have been developed since, but these are often accompanied by large increases in computational cost. The formal scaling<sup>c</sup> of wave-function methods to the number  $n$  of electrons range from  $\mathcal{O}(n^4)$  for Hartree-Fock, through  $\mathcal{O}(n^5)$  for second-order Møller-Plesset perturbation theory (MP2), to  $\mathcal{O}(n^7)$  for the "gold standard" in quantum chemistry, namely Coupled-Cluster singles and doubles with perturbative triples, CCSD(T). Treating large molecular systems of organic functional materials with post-Hartree-Fock wavefunction methods thus quickly becomes infeasible. Density functional theory (DFT), however, represents a computational method with a scaling similar to that of Hartree-Fock theory and a – potentially – comparable precision to that of post-Hartree-Fock methods. For many applications in materials science, using DFT is thus rarely a difficult choice, and it represents a versatile and practical tool if used with care. In this section, the theoretical foundation of DFT will be presented along with methodological considerations relevant for the choices of functionals and basis-sets. Atomic units will be used throughout this section ( $\hbar = e = a_0 = m_e = 1$ ).

### 2.2.1 Density functional theory

The foundation for density-based quantum chemistry methods was laid in 1964 by Hohenberg and Kohn.<sup>72</sup> Considering a many-electron system moving in an external potential  $v_{\text{ext}}(\mathbf{r})$ , they proved in their first theorem that the external potential as well as the electronic energy of the system are uniquely determined by the electron density  $\rho(\mathbf{r})$ . They furthermore proved in their second theorem that the exact, non-degenerate ground state

<sup>c</sup>The practical scaling can in many cases be better due to clever implementations with e.g. integral screenings; see for example Ref. 71.

energy could be obtained using the variational principle. Putting this in the context of molecules, the  $n$  electrons in a molecular system will, in the standard Born-Oppenheimer interpretation, be moving in an external potential defined by the  $N$  nuclei. As outlined in Section 2.1.2, the electronic Hamiltonian is then given by

$$\hat{H}_e(\mathbf{r}; \mathbf{R}) = \hat{T}(\mathbf{r}) + \hat{V}_{ne}(\mathbf{r}; \mathbf{R}) + \hat{V}_{ee}(\mathbf{r}) \quad (2.34a)$$

$$= - \sum_i^n \frac{1}{2} \hat{\nabla}_i^2 + \sum_i^n \hat{V}_{\text{ext}}(\mathbf{r}_i) + \sum_{i < j}^n \frac{1}{r_{ij}}, \quad (2.34b)$$

where the external potential operator depends on the charge  $Z_a$  of the  $a$ 'th nuclei and the electron-nucleus distance  $r_{ai}$  as

$$\hat{V}_{\text{ext}}(\mathbf{r}_i) = - \sum_a^N \frac{Z_a}{r_{ai}}. \quad (2.35)$$

Assuming that two external potentials  $v_1(\mathbf{r})$  and  $v_2(\mathbf{r})$  (which differ by more than a constant) exist and give rise to the same ground state density  $\rho(\mathbf{r})$ , the resulting two Hamiltonians  $\hat{H}_1$  and  $\hat{H}_2$  would, due to having the same ground state density, have different wave-functions  $\psi_1$  and  $\psi_2$  according to the Schrödinger eigenvalue problem (Eq. 2.8). However, by applying the variational principle (Eq. 2.18) we find that

$$\begin{aligned} \langle \psi_1 | \hat{H}_1 | \psi_1 \rangle &= E_1^0 < \langle \psi_2 | \hat{H}_1 | \psi_2 \rangle = \langle \psi_2 | \hat{H}_2 + \hat{V}_1(\mathbf{r}) - \hat{V}_2(\mathbf{r}) | \psi_2 \rangle \\ &= E_2^0 + \int \rho(\mathbf{r}) [v_1(\mathbf{r}) - v_2(\mathbf{r})] d\mathbf{r}. \end{aligned} \quad (2.36)$$

Exchanging indices 1 and 2 leads to a second, equivalent inequality

$$E_2^0 < E_1^0 + \int \rho(\mathbf{r}) [v_2(\mathbf{r}) - v_1(\mathbf{r})] d\mathbf{r} \quad (2.37)$$

and thus

$$E_1^0 + E_2^0 < E_1^0 + E_2^0, \quad (2.38)$$

which is contradictory. A given  $\rho(\mathbf{r})$  hence uniquely defines the external potential *and* the Hamiltonian of the system given the trivial relationship

$$\int \rho(\mathbf{r}) d\mathbf{r} = n, \quad (2.39)$$

and in turn the wave-function and the ground state energy of the system. This leads to the basic principle of density functional theory, namely that the energy is a unique functional of the density:

$$E[\rho(\mathbf{r})] = T[\rho(\mathbf{r})] + V_{ne}[\rho(\mathbf{r})] + V_{ee}[\rho(\mathbf{r})] \quad (2.40a)$$

$$= T[\rho(\mathbf{r})] + \int \rho(\mathbf{r}) v_{\text{ext}}(\mathbf{r}) d\mathbf{r} + V_{ee}[\rho(\mathbf{r})]. \quad (2.40b)$$

The second Hohenberg-Kohn theorem states that this energy can then be variationally minimised with respect to small density variations under the restriction of Eq. 2.39. This can be written as a constrained optimisation in the form of an Euler-Lagrange equation<sup>73</sup>

$$\frac{\partial}{\partial \rho(\mathbf{r})} \left( E[\rho(\mathbf{r})] - \lambda \left[ \int \rho(\mathbf{r}) d\mathbf{r} - n \right] \right) = 0, \quad (2.41)$$

where the Lagrange multiplier  $\lambda$  can be identified as

$$\lambda = v_{\text{ext}}(\mathbf{r}) + \frac{\partial T[\rho(\mathbf{r})]}{\partial \rho(\mathbf{r})} + \frac{\partial V_{ee}[\rho(\mathbf{r})]}{\partial \rho(\mathbf{r})} \quad (2.42)$$

using Eq. 2.40a. This can, in principle, be solved for the exact  $\rho(\mathbf{r})$ . Hohenberg and Kohn did, however, not offer a practical framework for calculating the ground state energy of molecular systems. Although their theorems are exact for many-body systems, it is only under the condition that the exact functional is known. As described in Section 2.1.3, we need to approximate the kinetic energy operator  $\hat{T}(\mathbf{r})$  and the electron-electron repulsion operator  $\hat{V}_{ee}(\mathbf{r})$  in practice, and especially the former is very difficult to determine from the density. The kinetic energy is on the order of the total energy, and even small errors in its description can thus lead to serious deviations from the exact result.<sup>55,73</sup> The following year, in 1965, Kohn and Sham presented a solution to this problem.<sup>74</sup> By introducing the concept of molecular orbitals known from wave-function methods (cf. Section 2.1.3) into the density functional framework of Hohenberg and Kohn, Kohn and Sham showed that a set of self-consistent equations similar to those of Hartree-Fock theory could be solved in a density basis, now also including correlation effects. They correspondingly approximated the wave-function as a single Slater determinant, i.e. in the independent particle picture, allowing the kinetic energy to be estimated as

$$T_S[\rho(\mathbf{r})] = - \sum_i^n \langle \phi_i(\mathbf{r}_i) | \frac{1}{2} \hat{\nabla}_i^2 | \phi_i(\mathbf{r}_i) \rangle, \quad (2.43)$$

which yielded a significant improvement over earlier density-based descriptions of this. The classical Coulomb electron-electron repulsion was determined as

$$J[\rho(\mathbf{r})] = \frac{1}{2} \iint \frac{\rho(\mathbf{r}_1)\rho(\mathbf{r}_2)}{r_{12}} d\mathbf{r}_1 d\mathbf{r}_2, \quad (2.44)$$

and the exchange and correlation effects not captured by these approximations compared to a real, interacting system were simply included in an exchange-correlation functional

$$E_{xc}[\rho(\mathbf{r})] = T[\rho(\mathbf{r})] - T_S[\rho(\mathbf{r})] + V_{ee}[\rho(\mathbf{r})] - J[\rho(\mathbf{r})]. \quad (2.45)$$

This meant that the total energy can be written as

$$E[\rho(\mathbf{r})] = \int \rho(\mathbf{r})v_{\text{ext}}d\mathbf{r} + T_S[\rho(\mathbf{r})] + J[\rho(\mathbf{r})] + E_{xc}[\rho(\mathbf{r})]. \quad (2.46)$$

The variational principle from the second Hohenberg-Kohn theory applies to this, and a constrained variational optimisation of Eq. 2.46 using the same procedure as above then yields

$$\lambda = v_{\text{ext}}(\mathbf{r}) + \frac{\partial T_S[\rho(\mathbf{r})]}{\partial \rho(\mathbf{r})} + \frac{\partial J[\rho(\mathbf{r})]}{\partial \rho(\mathbf{r})} + \frac{\partial E_{xc}[\rho(\mathbf{r})]}{\partial \rho(\mathbf{r})} \quad (2.47a)$$

$$= v_{\text{KS}}(\mathbf{r}) + \frac{\partial T_S[\rho(\mathbf{r})]}{\partial \rho(\mathbf{r})}, \quad (2.47b)$$

where the definition of the Kohn-Sham potential  $v_{\text{KS}}(\mathbf{r})$  is introduced. It takes the role as an effective external potential in which the electrons move and thus bear great resemblance to the mean-field approximation of Hatree-Fock theory. The distinct difference is,

however, that if one considers a fictitious system of non-interacting electrons moving in the Kohn-Sham potential, the result will be the same as for the above exact derivation – Kohn-Sham density functional theory is thus formally exact, and as the Kohn-Sham potential is multiplicative (as opposed to the exchange-term of Hartree-Fock theory), the Hamiltonian is separable as

$$\hat{H}_{\text{KS}} = \sum_i^N \left( -\frac{1}{2} \hat{\nabla}_i^2 + \hat{v}_{\text{KS}}(\mathbf{r}_i) \right) = \sum_i^N \hat{f}_{\text{KS}}(\mathbf{r}_i), \quad (2.48)$$

meaning that the exact density can simply be obtained as

$$\rho(\mathbf{r}) = \sum_i^n |\phi_i(\mathbf{r}_i)|^2 \quad (2.49)$$

from orbitals  $\phi_i(\mathbf{r}_i)$  that are solutions to the one-particle Schrödinger equation

$$\hat{f}_{\text{KS}}(\mathbf{r}_i) \phi_i(\mathbf{r}_i) = \varepsilon_i \phi_i(\mathbf{r}_i). \quad (2.50)$$

These equations represent a feasible framework for the simulation of molecular systems with the inclusion of correlation effects. As the Kohn-Sham operator  $\hat{f}_{\text{KS}}(\mathbf{r}_i)$  is dependent on the electron density, which, in turn, is determined from the molecular orbitals, the Kohn-Sham equations must thus be solved in an iterative, self-consistent manner – algorithms for which were already developed to handle the Hartree-Fock equations. The attention could now be focused on determining the elusive exchange-correlation functional. Despite this seminal work of Kohn and Sham being published in 1965, it was, however, not until the emergence of hybrid functionals in the early 1990's that the quality of exchange-correlation functionals became sufficient for the description of molecular systems. The evolution of DFT functionals will be briefly described in the next Section 2.2.2.

## 2.2.2 Exchange-correlation functionals

The Kohn-Sham density functional theory described above is formally an exact theory in the sense that if the exact potential is used, the fictitious Kohn-Sham system of non-interacting electrons will yield the same density as a corresponding real, interacting system. The exchange-correlation functional describing this potential, however, remains unknown, and it must thus be approximated. Different approaches to approximating this exist, with the most common being a) parametrisation with respect to large, experimental data sets, b) parametrisation with respect to higher-order *ab initio* wave-function methods, c) trying to meet physical constraints that must apply to the exact functional, e.g. that it must be self-interaction free and must be inversely proportional to  $-r_{12}$  and thus asymptotically go to zero for  $r_{12} \rightarrow \infty$ ,<sup>75</sup> or d) a mix of two or more of these. The design of the exchange-correlation functional is hence what distinguishes DFT methods from one another, and each of these has its strengths and weaknesses. Especially the empirical functionals can prove insufficient for describing types of molecules for which they are not parametrised, and choosing an appropriate method for the problem at hand is therefore crucial.

As opposed to true *ab initio* methods, a systematic convergence of the results towards the correct value cannot necessarily be expected for DFT. In 2001, however, John Perdew

introduced an analogue of the biblical "Jacob's Ladder" to categorise reductionist (as opposed to semi-empirical) DFT methods in order of their complexity as the rungs of the ladder.<sup>76</sup> It was hypothesised that the further up the ladder one climbs, the closer one will get to the heaven of chemical accuracy.

The first rung represents the original local spin density (LSD) approximation by Kohn and Sham.<sup>74</sup> The exchange-correlation functional depends only locally on the electron density  $\rho(\mathbf{r})$  at a position  $\mathbf{r}$  in this approximation. It is principally exact for materials with slowly varying electron densities, inheriting the properties of a uniform electron gas. The LSD approximation hence accurately describes solids and solid surfaces, but molecular systems are not well described.

The second rung represents the generalised gradient approximation (GGA), which, building on LSD, also considers the non-uniformity of the electron densities by including their gradients  $\nabla\rho(\mathbf{r})$ . It thus requires a knowledge of the density in an infinitesimal neighbourhood around an electron's position  $\mathbf{r}$  and can be seen as semi-local. This significantly improved the description of molecular systems, and e.g. the PBE exchange-correlation functional by Perdew, Berke, and Ernzerhof<sup>77</sup> was a noteworthy contribution to the development of *ab initio* DFT methods. An alternative approach of dividing the exchange-correlation ( $xc$ ) functional into separate contributions ( $x$  and  $c$ ) as

$$E_{xc}[\rho(\mathbf{r})] = E_x[\rho(\mathbf{r})] + E_c[\rho(\mathbf{r})] = \int \rho(\mathbf{r})\varepsilon_x[\rho(\mathbf{r})]d\mathbf{r} + \int \rho(\mathbf{r})\varepsilon_c[\rho(\mathbf{r})]d\mathbf{r} \quad (2.51)$$

also became common, allowing one to express the exchange and correlation energies in terms of their respective energy densities,  $\varepsilon_x$  and  $\varepsilon_c$ .<sup>55</sup> Several semi-empirical GGA functionals that utilised this construction emerged in the late 1980's, and e.g. the combination of Becke's B88 exchange gradient correction<sup>78</sup> and the LYP correlation functional by Lee, Yang, and Parr<sup>79</sup> lead to the BLYP exchange-correlation functional, which found widespread use for molecular systems in the 1990's.

The third rung represents the meta-GGA functionals, which further include the kinetic energy densities  $\tau(\mathbf{r})$ . These kinetic energy densities are semi-local functionals of the Kohn-Sham orbitals (cf. Eq. 2.50) but non-local functionals of the electron densities (cf. Eq. 2.49),<sup>76</sup> the former meaning that the computationally demanding calculation of two-electron integrals can be avoided but still with the advantages of the latter. However, the meta-GGA functionals were overshadowed due to the simultaneous, rapid development of the hybrid functionals.

The fourth rung represents the hybrid functionals, which explicitly include Hartree-Fock exact exchange contributions. The hybrids are thus fully non-local functionals of the Kohn-Sham orbitals and rely on the computation of two-electron integrals (cf. Eq. 2.26), making them computationally more demanding than the previous rungs. This is, however, often accompanied by a much improved description of organic molecular systems.<sup>80</sup> The hybrid exchange-correlation functionals can in their simplest form be constructed by substituting a fraction  $\zeta$  of GGA exchange energy with Hartree-Fock exact exchange, i.e.

$$E_{xc}^{\text{hybrid}} = E_{xc}^{\text{GGA}} + \zeta(E_x^{\text{HF}} - E_x^{\text{GGA}}). \quad (2.52)$$

An example of this is the non-empirical, parameter-free PBE0 functional,<sup>77,81</sup> for which an optimal fraction of exact exchange of  $\zeta = \frac{1}{4}$  was determined. Due to the added exact exchange, which is inherently a functional of the orbitals, the working equation of "pure" Kohn-Sham DFT (Eq. 2.50) cannot be directly minimised with respect to

the electron density, as this requires a multiplicative Kohn-Sham potential  $v_{\text{KS}}(\mathbf{r})$ . The working equation implemented in most modern quantum chemistry packages thus takes the following form:<sup>73</sup>

$$\left( -\frac{1}{2}\hat{\nabla}_1^2 + \hat{v}(\mathbf{r}_1) + \frac{\partial J[\rho]}{\partial \rho(\mathbf{r}_1)} + \frac{\partial(E_{xc}^{\text{GGA}} - \zeta E_x^{\text{GGA}})}{\partial \rho(\mathbf{r}_1)} \right) \phi_i(\mathbf{r}_1) - \frac{\zeta}{2} \int \frac{\rho_1(\mathbf{r}_1, \mathbf{r}_2)}{r_{12}} \phi_i(\mathbf{r}_2) d\mathbf{r}_2 = \varepsilon_i \phi_i(\mathbf{r}_1), \quad (2.53)$$

which is minimised with respect to the orbitals  $\phi_i(\mathbf{r})$  due to its explicit dependence on these - a procedure which is similar to Hartree-Fock theory.

Higher rungs on "Jacob's Ladder" also exist, but they often depend on virtual orbitals and thus come with a significantly increased computational cost. The hybrid functionals of the fourth rung provides a good compromise between accuracy and cost (assuming a careful choice of method), and only these will therefore be used in this thesis.

Whereas truly *ab initio* DFT methods like PBE0 have the advantage of not being biased by empirically determined parameters, semi-empirical hybrid exchange-correlation functionals have dominated the field. The B3LYP functional<sup>78–80,82</sup> was for a long time almost synonymous with DFT, and it has undoubtedly had an enormous impact on the field of organic functional materials and on chemistry in general. Composed of LSDA with a B88 gradient correction and a fraction of Hartree-Fock exact exchange as well as the LYP and VWN (Vosko, Wilk, and Nusair)<sup>83</sup> correlation functionals as

$$E_{xc}^{\text{B3LYP}} = (1 - a_0)E_x^{\text{LSDA}} + a_0E_x^{\text{HF}} + a_x\Delta E_x^{\text{B88}} + a_cE_c^{\text{LYP}} + (1 - a_c)E_c^{\text{VWN}}, \quad (2.54)$$

the three empirical parameters  $a_0 = 0.20$ ,  $a_x = 0.72$ , and  $a_c = 0.81$  were fitted against experimental heats of formation, ionisation potentials, and proton affinities to yield what has probably been *the* most popular functional since its introduction in 1994. However, it is well known that although the partial inclusion of exact exchange improves the description of short-range electron-electron interactions, deviations from the correct  $-r_{12}^{-1}$  asymptotic behaviour at long-range (cf. Eq. 2.72 and Fig. 2.1b) can lead to poor descriptions of non-local properties such as charge transfer excitations. Naively, a full inclusion of exact exchange could thus be thought to remedy this, but it was found to notably worsen the description of short-range properties. Inspired by the work of Peter Gill's group on algorithms for efficient computations of Coulomb interactions in many-body systems,<sup>84,85</sup> Yanai and co-workers introduced several long-range corrections of GGA functionals by partitioning the electron-electron repulsion operator into a short- and a long-range component with some success.<sup>86,87</sup> It was, however, not until defining a three-parameter Coulomb-attenuating method (CAM) and applying it to the B3LYP hybrid that a good description of both short- and long-range properties were achieved with one and the same functional.<sup>88</sup> The resulting CAM-B3LYP exchange-correlation functional utilises the partitioning

$$\frac{1}{r_{12}} = \frac{(\alpha + \beta \text{erf}(\mu r_{12}))}{r_{12}} + \frac{1 - (\alpha + \beta \text{erf}(\mu r_{12}))}{r_{12}}, \quad (2.55)$$

where the rate of attenuation between the short- and long-range terms is controlled by the parameter  $\mu = 0.33$ , smoothly turning up the fraction of exact Hartree-Fock exchange from  $\alpha = 0.19$  at short range to  $\alpha + \beta = 0.65$  at long range. CAM-B3LYP has been

shown to perform well for e.g. charge transfer excitations and polarisabilities of long, conjugated chains without compromising the description of short-range properties,<sup>88–90</sup> and long-range corrected functionals thus in many cases represent an improvement over standard hybrids.

Whereas long-range corrections of the repulsive electron-electron interactions are important for *intramolecular* or -atomic properties, long-range dispersion corrections are important for *intermolecular* or -atomic interactions. As will be discussed in Section 2.3.2, an  $-r_{12}^{-6}$  dependence of the potential energy on the interatomic distance is expected at long range (cf. Eq. 2.70; see also Fig. 2.1a). This effect is particularly important for molecular complexes, but standard DFT methods do not include it. Dispersion corrections to density functionals, the most popular of which are Grimme's DFT-D series of empirical correction terms, have thus proved crucial for correct descriptions of intermolecular van der Waals interactions.<sup>91</sup> An example of a range-separated hybrid exchange-correlation functional with empirical atom-atom dispersion is  $\omega$ B97X-D,<sup>92–94</sup> which includes 100 % exact exchange at long range and is optimised against different experimental data through 10 fitting parameters. It has in an extensive benchmark study been shown to perform very well across a wide range of difficult test-sets,<sup>95</sup> and it thus represents an appropriate choice of method for calculating e.g. the thermodynamical properties of organic molecules.

## 2.3 Molecular dynamics simulations

As described in Section 1.3, classical mechanics constitute the mathematical framework used herein to describe the spatio-temporal evolution of the material systems in question. The molecular dynamics simulation method relies on a knowledge of the force acting on a particle  $i$  to predict its future position  $\mathbf{r}_i$  and velocity  $\mathbf{v}_i$  through numerical integration of Newton's second law of motion. Considering a system of  $N$  interacting particles, the equation of motion for the  $i$ 'th particle with a constant mass  $m_i$  is given as

$$m_i \frac{d^2 \mathbf{r}_i}{dt^2} = m_i \mathbf{a}_i = \mathbf{F}_i, \quad \text{where } i = 1, 2, \dots, N. \quad (2.56)$$

The force  $\mathbf{F}_i$  acting on particle  $i$  can be determined as the negative derivative with respect to the position of the  $i$ 'th particle of a function  $V(\mathbf{r}_1, \mathbf{r}_2, \dots, \mathbf{r}_N)$  describing the potential energy surface of the full system of interacting particles, i.e.

$$-\frac{\partial V}{\partial \mathbf{r}_i} = \mathbf{F}_i. \quad (2.57)$$

Combining Eqs. 2.56 and 2.57 tells us that the spatial evolution of a particle as a function of time is accessible through integration if the potential energy surface on which the particle moves is known (and, as will be shown below in Section 2.3.1, an initial position and velocity) as

$$-\frac{\partial V}{\partial \mathbf{r}_i} = m_i \frac{d^2 \mathbf{r}_i}{dt^2}. \quad (2.58)$$

### 2.3.1 Time propagation

To show how the MD machinery works, we will consider the simple case of constant acceleration; remembering that  $\mathbf{a}_i = \frac{d\mathbf{v}_i}{dt} = \frac{d^2 \mathbf{r}_i}{dt^2}$ , we can get an expression for the



spatio-temporal evolution of a particle by integrating these expressions with respect to time. The velocity at time  $t$  is given by

$$\mathbf{v}_i(t) = \int \mathbf{a}_i dt = \mathbf{v}_{i,0} + \mathbf{a}_i t, \quad (2.59)$$

and the corresponding position at time  $t$  is given by

$$\mathbf{r}_i(t) = \int \mathbf{v}_i(t) dt = \int (\mathbf{v}_{i,0} + \mathbf{a}_i t) dt \quad (2.60a)$$

$$= \mathbf{r}_{i,0} + \mathbf{v}_{i,0} t + \frac{1}{2} \mathbf{a}_i t^2 \quad (2.60b)$$

when substituting Eq. 2.59 into Eq. 2.60a. Using Eqs. 2.56 and 2.58 with this Eq. 2.60b then yields

$$\mathbf{r}_i(t) = \mathbf{r}_{i,0} + \mathbf{v}_{i,0} t - \frac{t^2}{2m_i} \frac{\partial V}{\partial \mathbf{r}_i}, \quad (2.61)$$

which makes it clear that, in addition to the potential  $V$ , a knowledge of the initial conditions  $\{\mathbf{r}_{i,0}, \mathbf{v}_{i,0}\}$  is necessary to obtain a trajectory, i.e. the position of the particle as a function of time. Eq. 2.58 thus represents a second order initial value problem which can be solved through numerical integration by discretisation of the time  $t$  in small steps  $\Delta t$ .

The two standard numerical integration algorithms for MD simulations in GROMACS are the velocity Verlet and the leap-frog integrator. The position and velocity evaluations of the former can be written as<sup>59</sup>

$$\mathbf{r}_i(t + \Delta t) = \mathbf{r}_i(t) + \mathbf{v}_i(t) \Delta t + \frac{\Delta t^2}{2m_i} \mathbf{F}_i(t) \quad \text{and} \quad (2.62)$$

$$\mathbf{v}_i(t + \Delta t) = \mathbf{v}_i(t) + \frac{\Delta t}{2m_i} (\mathbf{F}_i(t) + \mathbf{F}_i(t + \Delta t)). \quad (2.63)$$

As seen, it relies on a memory of the velocities and forces at a time  $t$  computed in the previous step at time  $t'$  as  $\mathbf{F}_i(t' + \Delta t)$  (where  $t' = t - \Delta t$ ) in order to compute the velocities at time  $t + \Delta t$  using the force at time  $t + \Delta t$  (i.e.  $-\partial V / \partial \mathbf{r}_i(t + \Delta t)$ ). This means that both the positions and velocities can be made available for the time  $t + \Delta t$  at the cost of a small memory overhead and that the algorithm still only requires a single force evaluation per time step. This is key for the performance of a simulation, as force evaluations are the most resource-demanding steps.

The leap-frog integrator evaluates the positions and velocities at separate times, shifted by a half-step  $\frac{1}{2} \Delta t$ :<sup>59</sup>

$$\mathbf{v}_i(t + \frac{1}{2} \Delta t) = \mathbf{v}_i(t - \frac{1}{2} \Delta t) + \frac{\Delta t}{m_i} \mathbf{F}_i(t) \quad \text{and} \quad (2.64)$$

$$\mathbf{r}_i(t + \Delta t) = \mathbf{r}_i(t) + \mathbf{v}_i(t + \frac{1}{2} \Delta t) \Delta t. \quad (2.65)$$

Here, the velocity at a half-step  $(t + \frac{1}{2} \Delta t)$  is evaluated from the force at time  $t$  and the memory of the velocity at the previous half-step  $(t - \frac{1}{2} \Delta t)$ , which in turn is used for the evaluation of the position at a full step  $t + \Delta t$ . This can be thought of as two

frogs taking turn leaping over each other, hence its name. It is for this integrator more obvious that it only requires one force evaluation per time step.

As mentioned, the initial conditions of the particles  $\{\mathbf{r}_{i,0}, \mathbf{v}_{i,0}\}$  have to be defined prior to running the dynamics using these integrators. Depending on the goal of a simulation, the user can input initial positions based on e.g. an experimental crystal structures or a set of randomly distributed molecules in a solvent. In order to ensure that these are sufficiently close to the potential energy surface given by  $V$  for the numerical integration to be stable, an energy minimisation (using for example the steepest descent or the conjugated gradient method) has to be performed. The initial velocities are usually automatically generated by the program from a Maxwell-Boltzmann distribution at a given temperature  $T$  with a scaling applied to ensure a net momentum of zero, unless one is continuing previous trajectories, in which case the velocities are taken from the last step of this. For new trajectories initiated at time  $t = 0$ , the leap-frog integrator will interpret initial velocities as corresponding to  $t = -\frac{1}{2}\Delta t$ , whereas the velocity Verlet integrator will interpret them as corresponding to  $t = 0$ .<sup>59</sup> Although the two integrators would in principle produce identical trajectories for *corresponding* initialisations, this small difference makes them diverge in practice.

Now that we know how to initialise and propagate the positions and velocities of a system of particles in time given a knowledge of the force acting on these particles, the next step is to determine an expression for the potential energy surface on which the particles are moving, in turn giving us access to these forces through Eq. 2.57.

### 2.3.2 Non-bonded interactions

As stated above, the potential energy surface of a system of  $N$  particles,  $V$ , depends on the positions of all  $N$  particles, and Eq. 2.58 thus represents a many-body problem. Without losing generality, the potential can be expanded in a many-body expansion as

$$V(\mathbf{r}_1, \mathbf{r}_2, \dots, \mathbf{r}_N) = \sum_{i=1}^N V_i^{(1)}(\mathbf{r}_i) + \sum_{i<j}^N \Delta V_{ij}^{(2)}(\mathbf{r}_i, \mathbf{r}_j) + \sum_{i<j<k}^N \Delta V_{ijk}^{(3)}(\mathbf{r}_i, \mathbf{r}_j, \mathbf{r}_k) + \dots \quad (2.66)$$

Here, the first order  $V_i^{(1)}$  represents one-body terms arising from e.g. an external field. The second order correction

$$\Delta V_{ij}^{(2)} = V_{ij}^{(2)} - (V_i^{(1)} + V_j^{(1)}) \quad (2.67)$$

represents two-body terms, i.e. pair potentials describing the interaction of pairs of particles, and the third order correction

$$\Delta V_{ijk}^{(3)} = V_{ijk}^{(3)} - (V_{ij}^{(2)} + V_{jk}^{(2)} + V_{ik}^{(2)}) - (V_i^{(1)} + V_j^{(1)} + V_k^{(1)}) \quad (2.68)$$

represents three-body terms, i.e. the potential arising from the interaction of a third particle with a particle pair, etc. Note that each order subtracts contributions from lower orders to avoid over-counting, meaning that the expansion is formally exact if carried through to  $n = N$ . This is obviously not feasible for large systems, and truncating this expansion for orders higher than  $V^{(2)}$  yields what is commonly referred to as pair-potentials, namely

$$V(\mathbf{r}_1, \mathbf{r}_2, \dots, \mathbf{r}_N) \approx \sum_{i<j}^N V_{ij}^{(2)}(\mathbf{r}_i, \mathbf{r}_j), \quad (2.69)$$

whereas including terms on the order of  $V^{(3)}$  or even higher is referred to as many-body potentials. In this thesis, only pair-potentials of the form in Eq. 2.69 will be used and discussed for treating non-bonded interactions.

For simple uncharged atomic systems (atomic as opposed to molecular), as for example a noble gas, the potential describing the interatomic interactions arises from quantum chemical effects in the form of attractive London dispersion forces and repulsive forces of overlapping electron clouds at short interatomic distances. The former are named after German physicist Fritz London<sup>96</sup> and are essentially due to Heisenberg's uncertainty principle and the resulting zero-point motion of electrons: the negatively charged electron(s) moving around a positively charged nucleus in an atom give rise to a quickly varying dipole moment, i.e. a fluctuating electric field, which *"acts upon the polarisability of the other atom and produces there induced dipoles, which are in phase and in interaction with the instantaneous dipoles producing them."*<sup>97</sup> This attractive force was shown to be isotropic and pairwise additive<sup>96,97</sup> and its associated potential energy to inversely depend on the sixth power of the interatomic distance  $r_{ij}$  between atoms  $i$  and  $j$  as<sup>96,97</sup>

$$V_{\text{London}} = -\frac{3}{2(4\pi\epsilon_0\epsilon_r)^2} \sum_{i<j}^N \frac{\alpha_i\alpha_j}{r_{ij}^6} \frac{h^2\nu_i\nu_j}{h(\nu_i + \nu_j)}. \quad (2.70)$$

Here,  $h$  is Planck's constant,  $\epsilon_0$  is the vacuum permittivity,  $\epsilon_r$  is the relative permittivity (loosely termed the relative dielectric constant; defaults to 1 for all standard simulations with explicit consideration of the medium), and  $\alpha_i$  is the polarisability and  $\nu_i$  the orbiting frequency of the electron cloud of the  $i$ 'th atom. An approximate form of this is frequently seen with  $h\nu_i \approx I_i$ , where  $I_i$  is the ionisation energy (IE) of the  $i$ 'th atom. The latter forces mentioned, namely the repulsive forces of overlapping electron clouds, arise from Pauli's exclusion principle.<sup>70</sup> The resulting potential rises steeply with decreasing interatomic distance, thus preventing atoms from collapsing ( $V \rightarrow \infty$  for  $r \rightarrow 0$ ). The combination of these two effects into a computationally efficient pair-potential is realised as

$$V_{\text{LJ}} = \sum_{i<j}^N 4\epsilon_{ij} \left( \left( \frac{\sigma_{ij}}{r_{ij}} \right)^{12} - \left( \frac{\sigma_{ij}}{r_{ij}} \right)^6 \right), \quad (2.71)$$

which is named after British mathematician Sir John Lennard-Jones based on his works on cohesion.<sup>98</sup> Here, the term describing Pauli's exclusion principle has been chosen to decay as  $r_{ij}^{-12}$ , but a more physical functional form of this would be closer to exponential due to electron wave-functions, and thus their overlap, decaying exponentially with interparticle distance. The reason for choosing  $r_{ij}^{-12}$  is mainly related to computational efficiency, as it can be implemented as the square of the dispersion term, but of course also that it has proved to be a decent approximation.

The Lennard-Jones potential  $V_{\text{LJ}}$  is plotted in Fig. 2.1a alongside its contributions from the attractive  $-r_{ij}^{-6}$  term and the repulsive  $r_{ij}^{-12}$  term for a set of particle pair parameters  $\epsilon_{ij}$  and  $\sigma_{ij}$ ; as seen,  $\epsilon_{ij}$  can be interpreted as the well-depth and thus the equilibrium interaction energy, whereas  $\sigma_{ij}$  can be interpreted as the interparticle distance below which a severe energy penalty has to be paid. From the functional form of  $V_{\text{LJ}}$ , the equilibrium interparticle distance can be shown to be  $r_{eq} = 2^{1/6}\sigma_{ij}$ . The interactions described by the Lennard-Jones potential only persist at short range and are of relatively low magnitude compared to covalent and ionic bonding, but dispersion effects are fundamental to the description of important intermolecular effects such as

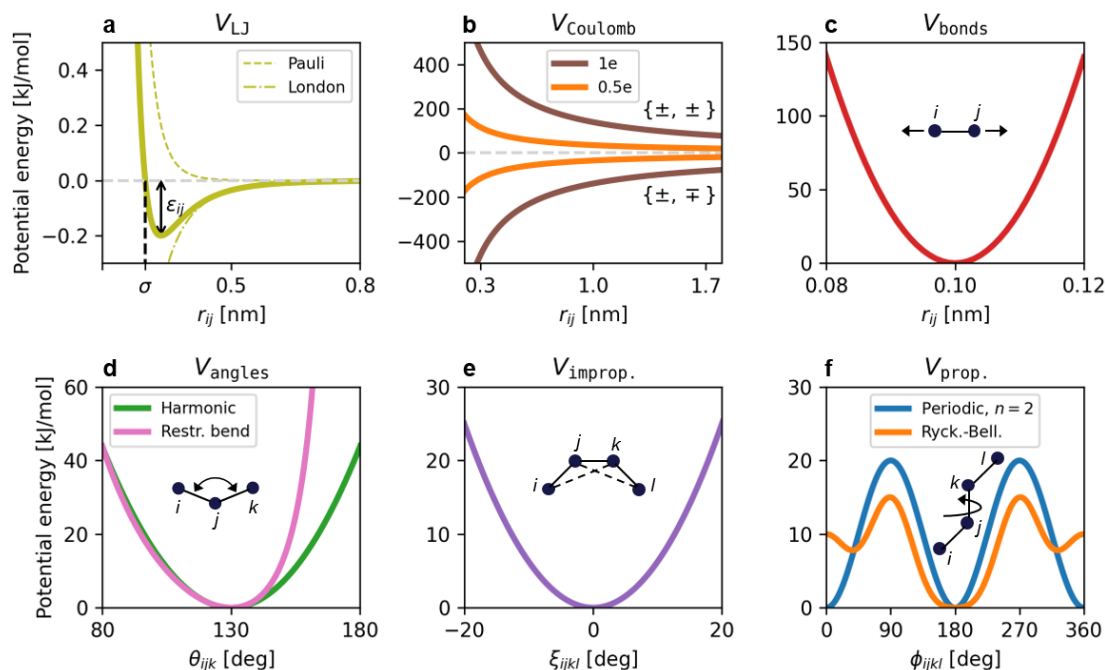


Figure 2.1: Examples of different types of non-bonded and bonded potentials included in molecular dynamics force fields. Although the parameters are arbitrarily chosen, the energies are representative for typical atom-atom pairs, triplets, and quadruplets in organic molecules and can be used for ball-park estimates of relative magnitudes.

$\pi$ -stacking. It is hence paramount to validate the interaction parameters  $\epsilon_{ij}$  and  $\sigma_{ij}$  against quantum chemical calculations and/or experimental data (also for reasons that will be explained below).

For charged atomic systems, e.g. ions, their electrostatic interaction also needs to be accounted for. This is generally done by considering atoms as point charges and calculating their electrostatic interaction via Coulomb's law

$$V_{\text{Coulomb}} = \frac{1}{4\pi\epsilon_0\epsilon_r} \sum_{i < j}^N \frac{q_i q_j}{r_{ij}}, \quad (2.72)$$

where  $q_i$  is the (partial) charge on the  $i$ 'th particle. Coulomb's law simply states that opposite charges attract and like charges repel with a magnitude inversely proportional to the distance between them. As can be seen in Fig. 2.1b, this effect is of a substantial magnitude and furthermore persists at long range.

When the non-bonded interactions are sought extended to *intermolecular* interactions (as opposed to *interatomic* interactions), the concept of charge distribution becomes important. For a molecule with a net charge of zero, its (lack of) symmetry can result in an anisotropic charge distribution, giving rise to a permanent dipole moment – these molecules are termed polar molecules and include e.g. water. Even molecules with no permanent dipole moment can, if their symmetry allows, carry a permanent quadrupole moment, e.g.  $\text{CO}_2$  and benzene. These multipoles are electrostatic of nature, and it hence becomes clear that two noteworthy effects arise: molecules carrying a permanent multipole interact with other permanent multipoles (the Keesom effect) and give rise

to induced multipoles in nearby molecules (the induction effect or the Debye force). The force related to the former is attractive (repulsive) for opposite (like) poles and will result in a preferential orientation of two multipoles in close proximity. The latter is always attractive and depends on the polarisability of a molecule, i.e. the degree to which its electron cloud can be distorted by a nearby electric field – an effect which is not accounted for in standard MD force fields with fixed point charges (see below).

Collectively, the weak intermolecular forces arising from the Keesom effect, induction, and dispersion are termed van der Waals interactions. The former two are inherently anisotropic, i.e. dependent on the orientation of the molecules, and as macroscopic properties are often averages of microscopic fluctuations, it is informative in the context of MD to consider these. For the Keesom effect, which can be either attractive or repulsive depending on the signs of the poles, it is tempting to assume that an angular average over all orientations will go to zero in a thermalised ensemble in which the multipoles can move freely – this is, however, not the case. From the angular- and Boltzmann averaged contribution for permanent dipole-permanent dipole interactions (higher order multipoles neglected here), it can be seen that the net contribution of the Keesom effect is attractive and depends inversely on temperature and inversely on the sixth power of the intermolecular distance as<sup>d</sup>

$$V_{\text{Keesom}} = -\frac{1}{(4\pi\epsilon_o\epsilon_r)^2} \frac{2}{3k_B T} \sum_{\alpha < \beta}^N \frac{\mu_\alpha^2 \mu_\beta^2}{r_{\alpha\beta}^6}, \quad \text{for } \frac{\mu_\alpha \mu_\beta}{r_{\alpha\beta}^3} \ll k_B T. \quad (2.73)$$

Here,  $k_B$  is Boltzmann's constant,  $T$  is temperature, and  $\mu_\alpha$  is the permanent dipole moment of the molecule  $\alpha$  (note that we distinguish between molecules [Greek indices] and particles [Latin indices]). We should also note that this Eq. 2.73 is only valid when the magnitude of the strongest interaction (which happens for aligned dipoles:  $V_{\text{Keesom}}(r_{\alpha\beta}) \propto \frac{\mu_\alpha \mu_\beta}{r_{\alpha\beta}^3}$ ) is significantly lower than the thermal energy  $k_B T$ , thus fulfilling the assumption of freely moving molecules. The induction effect does not depend on temperature, but an angular average also yields an attractive  $-r_{\alpha\beta}^{-6}$  dependence on the intermolecular distance as<sup>a</sup>

$$V_{\text{Debye}} = -\frac{1}{(4\pi\epsilon_o\epsilon_r)^2} \sum_{\alpha < \beta}^N \frac{\mu_\alpha^2 \alpha_\beta + \mu_\beta^2 \alpha_\alpha}{r_{\alpha\beta}^6}, \quad (2.74)$$

where  $\alpha_\beta$  is the polarisability of molecule  $\beta$ . From this, it can be seen that a polar molecule  $\alpha$  ( $\mu_\alpha > 0$ ) can induce a dipole in a non-polar molecule  $\beta$  (i.e.  $\mu_\beta = 0$ ).

Having now established the three most important contributions to molecular cohesion (Eqs. 2.70, 2.73, and 2.74), it becomes clear that they are all attractive and all depend inversely on the sixth power of the interparticle/-molecular distance. This, to some degree, explains the success and widespread use of the LJ potential (Eq. 2.71) in classical dynamics: suitably chosen  $\epsilon_{ij}$  and  $\sigma_{ij}$  that are (semi-)empirically parametrised in order for a system to reproduce macroscopic properties of interest represent a computationally cheap way of simulating the dynamics of large systems. Albeit, empirical parametrisation often compromises transferability, and one must be careful before using MD force fields for simulating systems or properties for which they are not directly parametrised. Furthermore, standard molecular dynamics force fields have an inherent deficiency in

<sup>d</sup>Original publications could not be obtained; see Ref. 97 and references therein.

their physical description of intermolecular interactions in the sense that they are not able to simulate induction effects, i.e. the responses of charge distributions to electrical fields, it being an external electrical field, a monopole (e.g. ion), a permanent dipole, or any higher order multipole. To explain this, the concept of partial charges becomes important: within the approximation of fixed point charges applied in standard MD, each atom  $i$  in a molecule  $\alpha$  in a given conformation can be assigned a partial charge corresponding to the relative electron density close to that atom (cf. Section 2.3.4). As both the LJ potential and the Coulomb potential are pairwise summations, it renders the description of non-bonded interactions isotropic around each particle; this can, to a certain degree, account for the Keesom effect, but well-known molecular properties such as hydrogen bonding to lone pairs, intermolecular stacking via  $\pi$ -cloud interactions, and halogen bonding through  $\sigma$ -hole interactions arise from anisotropy in atomic charge distributions and thus rely on a proper description of induction effects. These are sought included in the framework of classical MD simulations using different strategies as e.g. fluctuating charges, Drude oscillators, or multipole electrostatics; methods that are collectively referred to as polarisable force fields.<sup>99</sup> Recently, polarisable force fields such as  $\Delta\text{MOEBA}$  (Atomic Multipole Optimized Energetics for Biomolecular Applications)<sup>100,101</sup> have gained increasing interest, and these are likely to define the next era of molecular dynamics simulations.<sup>102</sup>

Despite the above described shortcomings of standard, non-polarisable MD force fields, they can indeed still be applied to numerous systems with success. For large, low-polarity molecules (as the ones that will be the main focus of this thesis), dispersion effects will usually be energetically dominant over the Keesom and induction effects, and the non-bonded interactions of many organic molecular systems are thus well described by the sum of the LJ (Eq. 2.71) and Coulomb (Eq. 2.72) pair-potentials when carefully parametrised:

$$V_{\text{non-bonded}} = V_{\text{LJ}} + V_{\text{Coulomb}} \quad (2.75)$$

This is by far the most widespread treatment of non-bonded interactions in MD simulations, and it is also the one that has been used in this thesis. The parametrisation strategies of the LJ parameters differs between force fields; those relevant for this thesis will be described below in Sections 2.3.4 and 2.3.5.

### 2.3.3 Bonded interactions

Molecular systems and their properties are defined by how their constituent atoms are bound together. The concept of chemical bonding is deeply rooted in quantum chemistry, and a proper physical treatment is thus not readily implementable in a classical force field. However, as the light, organic elements tend to form strong covalent bonds through their  $s$ - and  $p$ -orbitals that do not deviate far from their equilibrium bond lengths and angles ( $r_{\text{eq}}$  and  $\theta_{\text{eq}}$ , respectively), bonded potentials can be fairly well approximated by simple analytical expressions derived from ball-and-spring models. This comes at the cost of sacrificing the description of bond-breakage and -formation (i.e. reactivity) but allows for a straightforward inclusion of bond-, angle-, and dihedral contributions into the potential as

$$V = \underbrace{V_{\text{bonds}} + V_{\text{angles}} + V_{\text{dihedrals}}}_{V_{\text{bonded}}} + \underbrace{V_{\text{LJ}} + V_{\text{Coulomb}}}_{V_{\text{non-bonded}}} \quad (2.76)$$

For these cases of strongly bound particles, the resulting bond- and angle potentials can be approximated by harmonic oscillators (essentially Hooke's law, see Figs. 2.1c and

2.1d), i.e.

$$V_{\text{bonds}} = \frac{1}{2} \sum_{\text{bonds}} k_{ij}^r (r_{ij} - r_{\text{eq}})^2 \quad \text{and} \quad (2.77)$$

$$V_{\text{angles}} = \frac{1}{2} \sum_{\text{angles}} k_{ijk}^\theta (\theta_{ijk} - \theta_{\text{eq}})^2, \quad (2.78)$$

where the summations run over all bonds and angles, respectively. Here,  $k_{ij}^r$  and  $k_{ijk}^\theta$  are force constants for the bond stretching and angle bending, respectively, which depend on the chemical identity of the particles  $\{i, j\}$  and  $\{i, j, k\}$ . As an example, the frequency of vibrational motion in a bond is given by

$$\nu = \frac{1}{2\pi} \sqrt{\frac{k_{ij}^r}{\mu}}, \quad \text{where} \quad \mu = \frac{m_i m_j}{m_i + m_j}. \quad (2.79)$$

Here,  $\mu$  is the reduced mass, which essentially reduces the two-body problem to a one-body problem and ensures that the centre of mass of the molecule is not affected by the vibration.

In addition to the two- and three-body terms of bonds and angles, respectively, part of the dihedral four-body terms, namely improper dihedrals, are usually also approximated by a harmonic potential (see Fig. 2.1e), whereas the simplest functional form of the proper dihedrals is periodic around the equilibrium dihedral angle(s)  $\phi_{ijkl}$  (number of minima determined by the multiplicity  $n$ , see Fig. 2.1f):

$$V_{\text{dihedrals}} = \underbrace{\frac{1}{2} \sum_{\text{improp.}} k_{ijkl}^\xi (\xi_{ijkl} - \xi_{\text{eq}})^2}_{V_{\text{improper}}} + \underbrace{\sum_{\text{prop.}} k_{ijkl}^\phi (1 + \cos(n\phi_{ijkl} - \phi_{\text{eq}}))}_{V_{\text{proper}}}. \quad (2.80)$$

Similarly to the bond and angle potentials, the steepness of an harmonic improper dihedral potential is determined by the force constant  $k_{ijkl}^\xi$ . These improper dihedrals serve the purpose of keeping planar groups (e.g. aromatic rings) planar by restricting the angle between planes  $\{i, j, k\}$  and  $\{j, k, l\}$  to a harmonic centred around  $\xi_{\text{eq}}$  (cf. Fig. 2.1e). The proper dihedrals are related to torsional motion, and the periodic proper dihedral force constant  $k_{ijkl}^\phi$  thus holds information about the torsional barrier height. However, for many groups of organic molecules, as for example branched alkanes and polymers, the periodic dihedrals do not suffice in describing the often asymmetrical potential energy landscapes of their torsions. In these cases, a Ryckaert-Bellemans (RB) functional form can be applied to a proper dihedral as

$$V_{\text{RB}}(\phi_{ijkl}) = \sum_{n=0}^5 C_n \cos^n(\psi), \quad \text{where} \quad \psi = \phi_{ijkl} - 180^\circ. \quad (2.81)$$

The six coefficients  $C_n$  allow for the fitting of almost any torsional profile - an example can be seen in Fig. 2.1f. This is particularly important for simulations of polymers, whose structural properties depend strongly on the intermonomer torsional potentials.

The specific parametrisations of the potential energy function in Eq. 2.76, i.e. choices of interaction parameters and force constants of the individual components, is what separates different force fields from one another (see the below Sections 2.3.4 and 2.3.5).

### 2.3.4 Atomistic models

Atomistic, or all-atom (AA), models employ, as the name implies, full atomistic resolution. Each atom in a given molecule is represented as exactly that, having an atomic mass  $m_i$  and being assigned a (partial) charge dependent on the "type" of molecular configuration that it is in. Each atom is furthermore assigned a set of atom specific non-bonded interaction parameters (e.g.  $\epsilon_{ii}$  and  $\sigma_{ii}$  for LJ-based pair-potential force fields), again dependent on the "type" of molecular configuration it is in. An important concept for force fields is that of combination rules: how are the atom-specific  $\epsilon_{ii}$  and  $\sigma_{ii}$  parameters combined to form the pairwise LJ parameters  $\epsilon_{ij}$  and  $\sigma_{ij}$ ? Some, such as OPLS-AA (see below), use a geometric average for both parameters, e.g.  $\epsilon_{ij} = \sqrt{\epsilon_{ii}\epsilon_{jj}}$ , whereas other force fields use an arithmetic average, e.g.  $\epsilon_{ij} = \frac{1}{2}(\epsilon_{ii} + \epsilon_{jj})$ .<sup>59</sup> A distinction is made between atoms of the same atom number in different functional groups, e.g. a carbon atom in an acid group and a carbon atom in an aromatic ring, and these will, in most force fields, be assigned different charges and different non-bonded parameters. These parameters, as well as the bonded parameters such as force constants for bond stretching and angle bending, can be determined from quantum chemical calculations, experimental data, or a mix of both. Most often, partial charges, force constants, and lengths and angles for bonded interactions are determined from *ab initio* wave-function methods or density functional theory (see Section 2.2), whereas non-bonded parameters are refined for specific systems to reproduce experimental data such as heats of vaporisation, diffusion constants, and densities.

Popular groups of atomistic force fields (and related simulation packages) include AMBER,<sup>103,104</sup> CHARMM,<sup>105,106</sup> GROMOS,<sup>107,108</sup> and OPLS.<sup>109</sup> In the context of this thesis, the atomistic force field of choice is the latter, namely *Optimized Potentials for Liquid Simulations*, in particular the all-atom version OPLS-AA. It is developed by the William L. Jorgensen group (originally Purdue University, later Yale University) and is mainly geared towards peptide simulations,<sup>110</sup> but provides an extensive library of most organic functional groups,<sup>109,111</sup> heterocycles,<sup>112</sup> and a wide range of aromatic solvents.<sup>113,114</sup> OPLS-AA is parametrised towards describing these organic molecules in solution by fitting to densities, heats of vaporisation, and free energies of hydration,<sup>109</sup> whereas the torsional parameters are determined from gas-phase quantum chemical dihedral scans and implemented using an RB functional form (Eq. 2.81) or a corresponding Fourier cosine series.<sup>109,115</sup> Bonds, angles, and improper dihedrals are all described with the harmonic expressions in Eqs. 2.77, 2.78, and the first term of 2.80, respectively, whereas non-bonded interactions are described using the LJ and Coulomb potential forms in Eqs. 2.71 and 2.72, respectively. It, however, only considers *intra*-molecular, non-bonded interactions for atoms that are three or more bonds apart, whereas it utilises a so-called "fudge factor" of  $f_{ij} = 0.5$  to scale non-bonded interactions of atoms that are exactly three bonds apart (1,4 pairs).

As mentioned above, atoms of the same atom number can be assigned different sets of parameters dependent on their chemical environment. This distinction leads to what is commonly referred to as atom types. OPLS-AA includes more than 700 atom types, and after assigning an atom type to a specific atom and its given connectivities in a topology, the force-field will use the type of this atom (and the types of the ones that it is connected to) to look up bond, angle, and dihedral parameters of these specific combinations in a large parameter file and non-bonded parameters in another parameter file. Hence, one must take care to select the correct types when building a "new"



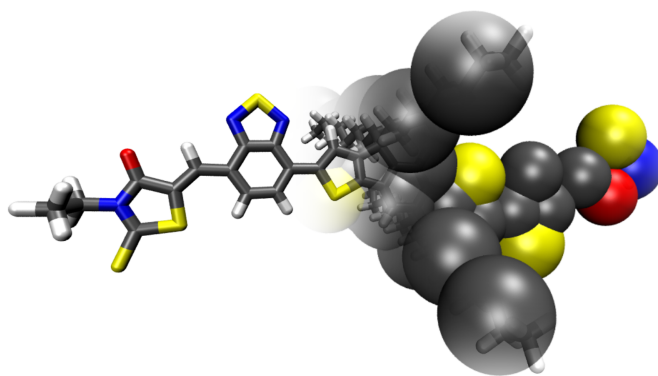


Figure 2.2: Illustration of the bead concept employed in the MARTINI model.

molecule, and if the need to define a new atom type arises, compatibility with the force field must be checked. The specific parametrisation procedures of the OPLS-AA-inspired force fields built in the context of this thesis will be described in detail in Chapter .

Atomistic models are in general feasible to employ when simulating dynamics of pre-assembled systems. Although hundreds of nanoseconds are within reach for systems of up to a million atoms ( $< \mathcal{O}(10^4)$  nm<sup>3</sup> simulation box sizes) if vast supercomputer resources are available, one is most often practically limited to shorter times and/or smaller systems. The majority of self-assembly processes are thus out of reach, and atomistic models are more regularly applied to problems where atom-resolved dynamics or interactions are important. United-atom models (where hydrogen atoms are omitted and their effects implicitly included in the parameters of the atoms to which they are bonded) can yield a small speed-up, but when the microscale is of interest, only coarse-grained models are practically applicable. These will be introduced in the below Section 2.3.5.

### 2.3.5 Coarse-grained models

Coarse-grained (CG) models employ a reduced representation in which several atoms are grouped into effective interaction sites represented by larger particles; the so-called *beads* (see Fig. 2.2). This reduction of chemical resolution implies a potential loss of atom-specific interactions, but it enables computational speed-ups on the order of  $> 10^3$  compared to atomistic models – this is due partly to the lower number of particles and thus degrees of freedom, partly to the smoothened potential energy surface of the system, and partly to the possibility of taking longer time steps. The main justification of CG models is that by averaging over non-essential details, one can reach the time and/or length scales relevant for the properties of interest. Self-assembly processes such as domain formation are thus readily within reach, and one can routinely simulate systems corresponding to tens of millions of atoms or more ( $< \mathcal{O}(10^6)$  nm<sup>3</sup> simulation box sizes) for hundreds of microseconds – of course depending on the resolution of the CG model.

In general, two paradigms can be said to exist in the field of CG MD, each defined by either the "top-down" or the "bottom-up" philosophy. Loosely speaking, the former relies on parametrising a CG model to reproduce experimentally measured structural or thermodynamic properties, whereas the latter relies on parametrising a CG model to reproduce the properties of a finer resolution model, usually atomistic. However, CG force field developers are increasingly integrating aspects of both philosophies in their

models.

Many different CG force fields have been developed based on varying philosophies and with varying resolutions,<sup>116–120</sup> but one of the most reasonable compromises between chemical specificity, transferability, and computational efficiency is the MARTINI force field.<sup>121,122</sup> It originates in the group of Siewert-Jan Marrink (University of Groningen), and has undergone tremendous progress since its introduction in 2007.<sup>123,124</sup> Originally developed for lipid bilayers,<sup>121,122</sup> the MARTINI force field is now, after extensions to proteins,<sup>125,126</sup> carbohydrates,<sup>127</sup> DNA and RNA,<sup>128,129</sup> implicit water models,<sup>130</sup> and a few polymer systems,<sup>131–133</sup> one of, if not *the*, most popular CG force field in literature. Originally, it relied mainly on a four-to-one mapping, i.e. the grouping of four non-hydrogen atoms into one regular (R) bead, but also small (S) bead were available for three-to-one mappings. Later, the tiny (T) beads were introduced,<sup>128</sup> allowing two-to-one mappings of atoms in planar residues, which has paved the way for improved models of conjugated ring-systems due to better descriptions of their planar structure and the related  $\pi$ -stacking effects. These tiny beads have, however, not been fully implemented and parametrised in until very recently in the newly developed MARTINI 3.0.<sup>e</sup> The previous version (MARTINI 2.2) has with some success been used to model organic functional materials based on fullerene acceptors in a few cases,<sup>133–135</sup> but the new version represents an even more promising framework for modelling mesoscale properties of organic functional material systems. The MARTINI force field will thus form the basis for the CG simulations herein.

In addition to the different bead sizes (R, S, and T), MARTINI 3.0 employs six main types of particles: polar (P), non-polar (N), apolar (C), charged (Q), halogen (X), and water (W) as well as a degree of polarity from 1 (low polarity) to 6 (high polarity) assigned to each bead (except water beads). The former five can furthermore be assigned a *sub-type* related to their electronic properties or hydrogen bonding capabilities, e.g. hydrogen bond donating (d) or accepting (a), which in total amounts to more than 800 bead types – a few examples are SN3a (small bead, non-polar, medium polarity, hydrogen bond acceptor; could describe e.g. an ether group) and TC5 (tiny bead, apolar, high polarity). With respect to parametrisation, MARTINI utilises a combination of the "top-down" and "bottom-up" approaches: the bonded parameters are determined from atomistic models, whereas the non-bonded parameters (essentially the bead types described above) are chosen to reproduce the free energies of transfer between polar and non-polar solvents and the densities of liquids. Expression similar to the ones used for atomistic force fields describe the bonded and non-bonded parameters, but in general, MARTINI beads carry no partial charge and are not assigned bead-specific LJ parameters, so the Coulomb term can be disregarded in most cases, whereas the LJ parameters are explicitly defined in a tabulated form for each pair-interaction.

## 2.4 Bridging the scales

Multiscale modelling is more than just applying different computational techniques to the time and length scales for which they are designed.<sup>44</sup> The different scales need to be bridged, and a range of different techniques will be used for this in the present work. As described above, the mapping and bonded parameters of the coarse-grained

---

<sup>e</sup>A beta version of MARTINI 3.0 (v3.0.b.3.2) is available at <http://cgmartini.nl/index.php/martini3beta>; in this thesis, the final to-be-published version has been used (v3.0.b.4.27).

MARTINI models are inferred from atomistic models. As opposed to more coarse-grained models, the building block approach used in the MARTINI force fields ensures that a high degree of chemical specificity is maintained. Not only does this high chemical specificity allow for reliable simulations of self-assembly processes that depend on functional group interactions, but also for reliable back-mappings to atomistic resolution.<sup>45</sup> This allows for the utilisation of large-scale morphologies, or parts hereof, as input to quantum chemical calculations. Back-mapping thus provides a link between the scales relevant for domain formation and the scales relevant for electronic properties, which holds promise of an improved insight into the structure-property relationships of organic solar cell blends.

Having back-mapped the coarse-grained morphologies to atomistic resolution, we still rely on atomistic force fields to equilibrate the structures. Atomistic force fields with QM/DFT refined bonded parameters (bond lengths, angles, dihedrals) allow for better compatibility with direct single point QM calculations (i.e. not requiring prior geometry optimisation at the chosen level of theory),<sup>136</sup> and the parametrisation of the atomistic models devised herein is thus done with this in mind. With reliable atomistic structures in hand, the electronic properties can then be investigated using, most often, DFT methods. For time-dependent properties such as molecular excitations, time-dependent DFT is used. It is built on linear response theory,<sup>137–139</sup> which relies on finding poles in the linear response equations that relate the frequency of an incoming field to the transition moments of the molecular system. This gives access to the transition energies and the oscillator strengths of the molecular excitations, which are important parameters for the interaction of organic functional materials with light.

Also the charge transfer processes in the materials studied herein are of great importance to the performance of the devices. Organic polymers and molecules can often be considered as weakly coupled to each other, and the charge transfer processes between them can thus be described by thermally activated "hopping" using Fermi's golden rule and Marcus theory.<sup>140</sup> The rate of "hopping" or charge transfer  $k_{\text{ET}}$  between sites  $i$  and  $j$  is in this framework proportional to the square of the electronic coupling strength  $J_{ij}$  as

$$k_{\text{ET}} = \frac{|J_{ij}^2|}{\hbar} \sqrt{\frac{\pi}{\lambda k_B T}} \exp - \frac{(\Delta E_{ij} + \lambda)^2}{4\lambda k_B T}, \quad (2.82)$$

where  $\lambda$  is the reorganisation energy cost associated with the rearrangement of the nuclei following the charge transfer,  $\Delta E_{ij}$  is the energy difference between the sites, and  $k_B T$  is the thermal energy. The electronic coupling between sites is hence decisive for the rate of charge transfer, and it can indirectly provide information about the ability of a material to conduct charges. In this thesis, we have used DFT and the projective method<sup>141,142</sup> to calculate the electronic couplings by evaluating the expectation value of the electronic Hamiltonian with respect to the electronic wave-functions of the molecules, which, in the frozen orbital approximation can be reduced to

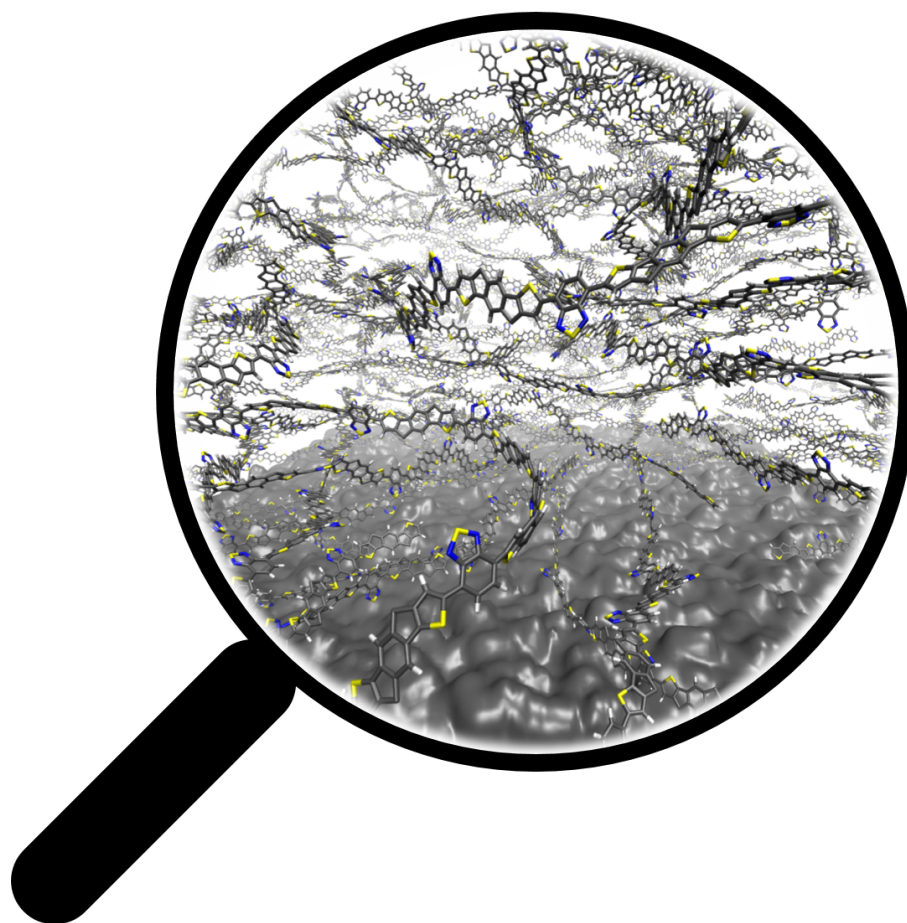
$$J_{ij} = \langle \phi_i^{\text{HOMO,LUMO}} | \hat{H}_e | \phi_j^{\text{HOMO,LUMO}} \rangle, \quad (2.83)$$

where  $\phi_i^{\text{HOMO,LUMO}}$  denotes either the highest occupied molecular orbital (HOMO) or the lowest unoccupied molecular orbital (LUMO) of molecule  $i$ , yielding the hole coupling strength for the HOMO-HOMO projections and the electron coupling strength for the LUMO-LUMO projections.<sup>142</sup> Along with the reorganisation energy and site energy

difference, these coupling can be used as input in kinetic Monte Carlo mobility simulations, which can link the scales all the way from the electronic, nanostructural properties, through the mesoscale coarse-grained structures, to macroscopic device properties.



### 3 Electronic coupling in neat, solution processed thin-films



This chapter is based on the published manuscript [II](#) and part of the work done in relation to manuscript [III](#), which is in preparation. It will here be described how multiscale modelling can be used to investigate the relationship between the nanostructure and the electronic properties of solution processed organic functional materials.

### 3.1 Introduction

Solution processable organic functional materials constitute the active layers of a promising generation of low-cost, scalable devices for a wide range of applications in photovoltaics, electronics, and bio-integration.<sup>39,143–147</sup> The majority of these materials are designed with conjugated backbones, often consisting of aromatic ring-systems, flanked by alkyl side-chains. Previously, alkyl side-chains were primarily regarded as a means of ensuring solubility of rigid polymers in organic solvents. It has since become strikingly clear that side-chain engineering represents an important way of tuning the solid state crystallinity of both polymer- and small molecule thin-films as well as their miscibility in blends.<sup>148–151</sup> The resulting structural changes can have vast implications for the electronic properties of the films, and elucidating these structure-property relationships is key to understanding and improving the devices.

Historically, the P3HT polymer has been the prototypical organic semiconductor for hole transport (*p*-type) applications.<sup>152–154</sup> P3HT readily forms well-ordered, lamellar structures when solution processed owing to its flat monomer structure. Modifying the morphology of P3HT thin-films via engineering of the solution processing parameters or by synthetically altering the regioregularity and molecular weight of the polymer batches can greatly affect their hole mobility,<sup>155,156</sup> but optimised conditions lead to a semicrystalline order and result in high hole mobilities of around  $0.1 \text{ cm}^2\text{V}^{-1}\text{s}^{-1}$ .<sup>157,158</sup> A high degree of long-range order was for some time accepted to be a prerequisite for high charge transport in polymer thin-films,<sup>159</sup> but in the late 2000's, new polymers emerged which exhibited high charge carrier mobilities but low order. First synthesised in 2010,<sup>160</sup> the IDTBT polymer (cf. Fig. 3.1), in particular the  $\text{C}_{16}$ -IDTBT polymer with hexadecyl side-chains, represents one of the best-performing organic materials for hole transport.<sup>161</sup> It has been studied rigorously since due to its seemingly contradictory high hole mobility of up to  $3.2 \text{ cm}^2\text{V}^{-1}\text{s}^{-1}$  and simultaneous low tendency to crystallise.<sup>162,163</sup> Its molecular design with flat torsional equilibrium angles between the electron donating indacenodithiophene (IDT) unit and the electron withdrawing benzothiadiazole (BT) unit as well as the parallel inter-monomer bonds results in a stiffness and low conformational disorder, which are believed to be some of the main causes for its high mobility.<sup>160,164,165</sup> Both amorphous and semicrystalline polymers have also been successfully employed as efficient electron-transport (*n*-type) materials in a range of applications,<sup>166–171</sup> but it is the emergence of *n*-type, small-molecule, non-fullerene acceptors such as ITIC<sup>172</sup> and IDTBR<sup>173</sup> that has accelerated especially the OPV field in recent years.<sup>174,175</sup>

Common for the IDTBT polymers and the ITIC and IDTBR acceptors are that their electron donating residues employ  $\text{sp}^3$  hybridised bridgehead carbons, i.e. the backbone carbons to which the side-chains are linked (cf. Fig. 3.1). This means that two side-chains are bonded to each linking carbon in a tetrahedral configuration, resulting in a bulkiness around these. In the case of IDTBT polymers, this hinders the  $\pi$ -stacking of parallel chains, in turn resulting in somewhat amorphous thin-film morphologies.<sup>160,162</sup> The  $\text{sp}^2$  hybridised linking carbons in P3HT leads to the single side-chain in each monomer being in the same plane as the thiophene ring, resulting in a propensity of P3HT chains to  $\pi$ -stack in parallel conformations. This conformation of parallel,  $\pi$ -stacking chains has also been suggested as a crystalline form of  $\text{C}_{16}$ -IDTBT,<sup>163,164,176</sup> but it seems unlikely to be a commonly occurring structure in solution processed thin-films.<sup>162</sup> At the same time, a strong dependence of the hole mobility on the length of side-chains is observed for IDTBT,<sup>148</sup> which further motivates coupling charge transport calculations

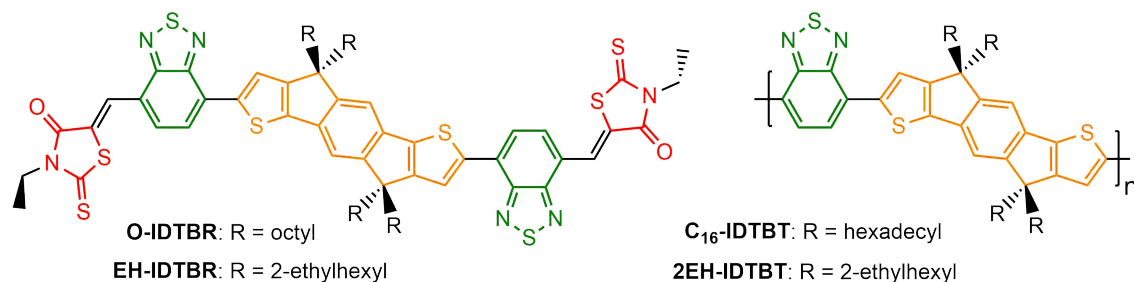


Figure 3.1: Structures of the O-IDTBR, EH-IDTBR, C<sub>16</sub>-IDTBT, and 2EH-IDTBT compounds discussed herein; orange marks the indacenodithiophene (IDT) residue, green marks the benzothiadiazole (BT), and red marks the rhodanine (RH).

and simulations of the morphologies of solution processed IDTBT thin-films.<sup>177</sup>

The IDTBR small-molecule acceptors are structurally very similar to the repeat units of IDTBT polymers (see Fig. 3.1). The central IDT unit is flanked by the electron withdrawing/accepting BT and rhodanine (RH) units, resulting in an acceptor-donor-acceptor (A-D-A) type structure. Originally synthesised as acceptor materials for organic photovoltaic (OPV) devices,<sup>173</sup> the IDTBR acceptors have also shown to be suitable as *n*-type materials in organic thin-film transistor (OTFT) devices.<sup>150</sup> Opposite to the IDTBT polymers, the packing motifs of both the 2-ethylhexyl- and octyl-substituted IDTBR molecules (EH-IDTBR and O-IDTBR, respectively) have been directly observed with X-ray crystallography of single crystals.<sup>150</sup> For the O-IDTBR crystals, an interdigitated columnar packing motif with close  $\pi$ -stacking between the peripheral electron withdrawing units was observed, yielding a 3D transport network. The EH-IDTBR crystals also exhibited close  $\pi$ -stacking between the RH and BT units, but in a 1D slipped stack packing motif. The solution processed thin-films of these yielded electron mobilities of  $0.12 \text{ cm}^2\text{V}^{-1}\text{s}^{-1}$  and  $0.05 \text{ cm}^2\text{V}^{-1}\text{s}^{-1}$ , respectively, in OTFT devices, emphasising the importance of side-chain engineering for organic functional materials.

Here, atomistic molecular dynamics force fields for IDTBT polymers and IDTBR molecules are presented. The structural properties of solution processed thin-films of these compounds deposited on silicon wafers are investigated based on solvent evaporation simulations, and the influence of the nanostructural packing on their intermolecular charge transfer properties is determined from quantum chemical electronic coupling calculations. We find that the  $\pi$ -stacking interactions of the electron withdrawing benzothiadiazole building blocks are key to high electron coupling in amorphous thin-films of *n*-type materials and that the  $\text{sp}^3$  hybridised bridgehead carbons facilitate these interactions by hindering parallel  $\pi$ -stacking of the backbones.

## 3.2 Methods

All simulations presented herein are performed in GROMACS 2018.3<sup>59,178</sup> using models based on the OPLS-AA force field.<sup>109,110</sup> The detailed parametrisation procedures of the models for IDTBT oligomers and IDTBR molecules can be found in the Appendix, Section 3.6.1, and additional validation can be found in Paper II, which is enclosed as an appendix to this thesis. Here, we will focus on the parametrisation of the torsional potentials, the solvent evaporation framework, and the analysis methods.



### 3.2.1 Torsions

The parametrisation of torsions in MD models is crucial, especially for polymers.<sup>179</sup> Here, dihedral parameters for the torsional potentials of the linking bonds between RH and BT in the IDTBR molecules as well as between IDT and BT and between IDT and the side-chains in both the IDTBR molecules and the IDTBT polymers were determined through an iterative Boltzmann inversion (IBI) procedure. This resulted in coefficients for Ryckaert-Bellemans (RB) functional forms (cf. Eq. 2.81) that, when included in the remainder of the force field, reproduce the corresponding torsional potentials obtained from density functional theory (DFT) calculations in GAUSSIAN 16<sup>180</sup> using the  $\omega$ B97X-D/6-311++G(d,p) level of theory. Using this specific level of theory is consistent with the recommendations in the most recent publication on the re-parametrisation of OPLS-AA peptide backbone torsions.<sup>115</sup> The IBI procedure was performed as follows:

- a) DFT relaxed scans at the  $\omega$ B97X-D/6-311++G(d,p) level of theory (i.e. geometry optimisations while constraining only the relevant torsional angle) of a methyl-substituted IDTBR and a methyl-substituted IDTBT dimer;
- b) MD relaxed scan (with a convergence criterion of a maximum force of  $10 \text{ kJ mol}^{-1} \text{ nm}^{-1}$ ) of the torsional angle of reduced systems (i.e. RH-BT for the RH-BT torsion, 4,4,9,9-tetramethyl-IDT-BT for the IDT-BT torsion, and 4,4-diethyl-9,9-dimethyl-IDT for the IDT-to-side-chain torsions) with the partial charges of the respective model determined as described in the Appendix, Section 3.6.1 with the potentials of the four dihedral quadruplets in question set to zero;
- c) non-linear least squares fitting of an RB functional form (Eq. 2.81) to the difference between the DFT scan and the MD scan, providing the initial RB parameter guesses;
- d) long vacuum simulation (10-50 ns depending on the iteration) in an NVT-ensemble at 600 K using 1 fs steps and subsequent collection of torsion statistics (using the `gmx angle` program);
- e) Boltzmann inversion of the statistics and fitting of RB parameters to the difference between the resulting potential and the  $\omega$ B97X-D potential - these RB parameters are then linearly combined with the ones from the previous step;
- f) iterations of steps d) and e) until convergence (which is defined by a root-mean-square deviation (RMSD) of  $< 1.0 \text{ kJ/mol}$  for the MD statistics to the DFT potential).

The resulting Boltzmann inverted statistics are compared to the DFT torsional potentials in Fig. 3.2, and the RB coefficients for the MD dihedrals can be found in the respective force field files `ffbonded_IDTBR.itp` and `ffbonded_IDTBT.itp` available at doi:10.11583/DTU.c.5254236. Note that due to the electron withdrawing RH unit on IDTBR, the IDT-BT torsional potential in IDTBR differs slightly from the corresponding torsional potential in IDTBT, and the two were thus parametrised independently (only the IDT-BT torsional potential for IDTBR is shown in Fig. 3.2).

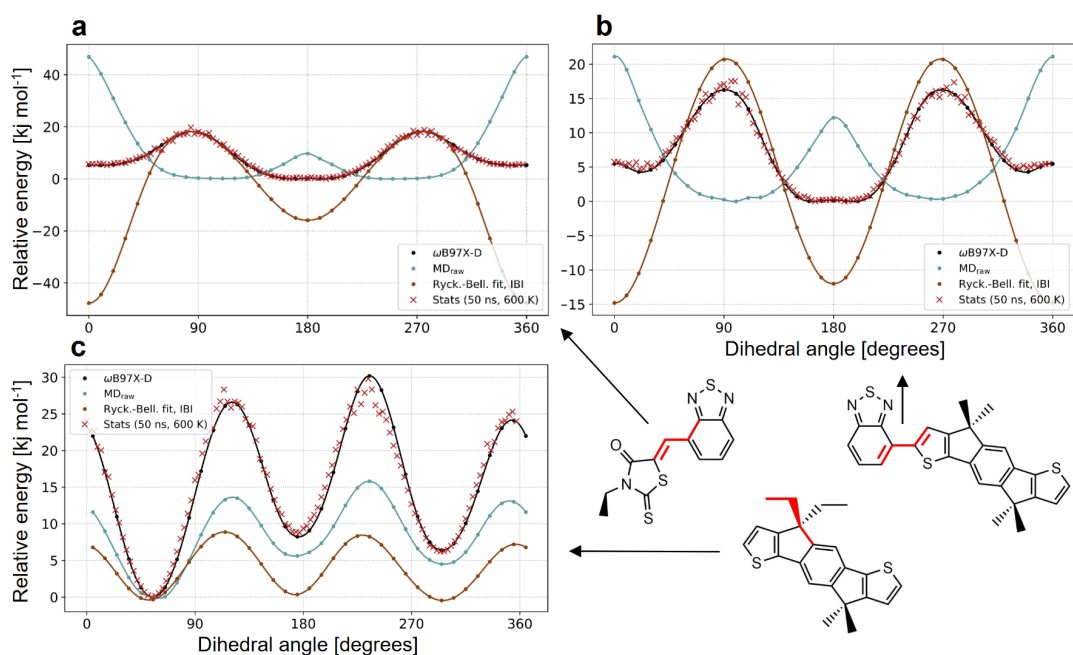


Figure 3.2: Visualisation of the parameterisation of a) the RH-BT, b) the IDT-BT, and c) the IDT-side-chain torsional potentials. The statistics are Boltzmann inverted to ensure comparability with the DFT torsional potentials. The red bonds on the molecular structures in the bottom right panel mark the dihedrals in question. Adapted from Paper II.

### 3.2.2 Solvent evaporation simulations

In order to study the structure of solution deposited organic thin-films on substrates, a solvent evaporation model has been devised, inspired by previous work.<sup>119,181</sup> This encompasses the inclusion of substrate effects, air-interface effects, and semi-isotropic pressure coupling in atomistic MD simulations with no periodic boundary conditions (PBC) in the z-direction. The substrate is modelled using an explicit  $\sim 2$  nm layer of amorphous silicon dioxide ( $\text{SiO}_2$ ). The parameters for  $\text{SiO}_2$  were based on the atomistic Clay force field<sup>182</sup> as adopted in Ref. 183, using exclusively non-bonded interactions between the silicon and oxygen atoms. The specific surface interactions between organic, conjugated molecules and  $\text{SiO}_2$  modelled using parameters from the Clay force field were validated by O. M. Roscioni, L. Muccioli, *et al.* in a study of pentacene crystal growth.<sup>184</sup> The substrate was held in place by an attractive interaction with a bottom potential wall of the 9-3 type in GROMACS, which is in essence a Lennard-Jones potential integrated over the volume behind the box boundary with an assigned density in atoms per  $\text{nm}^3$  of a given atom type. Here, a density of  $49.94 \text{ nm}^{-3}$ , similar to the experimental value for bulk, crystalline silicon, is used. The air-interface in the solvent evaporation simulations was also modelled using a potential wall of the 9-3 type with an assigned density of  $0.012 \text{ nm}^{-3}$ , corresponding to the experimental value for molecular nitrogen,  $\text{N}_2$ , in ambient conditions with the standard OPLS-AA parameters for nitrogen defining the interaction strengths with the rest of the system. Chloroform, modelled using the OPLS-AA parameters by C. Coleman, D. van der Spoel, and co-workers,<sup>114</sup> was used as the solvent in the simulations.

For the solvent evaporation simulations themselves, different rates of evaporation

were used for the IDTBR thin-films and the IDTBT thin-films. In order to simulate oligomers of a sufficient length to be able to somewhat compare their behaviour to the corresponding polymers, large box sizes are needed for the oligomers to not interact with themselves across the PBC. For both C<sub>16</sub>-IDTBT and 2EH-IDTBT, 12mers were used, meaning that the x- and y-dimensions of the simulation boxes needed to be 20x20 nm and the z-dimension around 150 nm to hit concentrations of approximately 40 mg/ml for 150 12mers of C<sub>16</sub>-IDTBT and 250 12mers of 2EH-IDTBT, which is close to the typical experimental concentration of 10 mg/ml used for spin-coating these polymers.<sup>162</sup> Whereas it is necessary to keep the initial concentrations low in MD simulations of polymers of a low solubility, these constraints can be relaxed for more soluble small molecules like IDTBR. The initial dimensions of the IDTBR boxes could thus be limited to 10x10x60 nm, yielding a concentration of around 200 mg/ml for 448 IDTBR molecules. This allowed an exponentially decreasing evaporation to be applied, removing 2.5 % of the remaining solvent every step randomly throughout the extent of the box until reaching the near-linear regime (defined as removing less than 0.025 % of the initial amount of solvent each step) after which the evaporation was continued linearly until a dry film was obtained. This amounts to a total of 132 steps. For the IDTBT simulations, it was only feasible to simulate a linear evaporation rate, removing 5.0 % of the *initial* solvent amount every step, amounting to a total of 20 steps. Physically, this is of course not a correct behaviour, and work on developing coarse-grained models to be able to simulate the thin-film formation on more realistic time and length scales is ongoing (see Section 3.4 and Chapter 4).

PBCs were only applied in the x- and y-directions, whereas potential walls were applied in the z-direction at  $z = 0$  and  $z = \text{box}_z$  as described above. The boxes were then equilibrated before initiating the solvent evaporation process. Both for the initial equilibration and for each step after solvent removal, the boxes were equilibrated for 0.2 ns in an NVT ensemble and 2.0 ns in an NPT ensemble using the Berendsen barostat ( $\tau = 2.0$  ps) before running a 3.0 ns production run in NPT ensemble using the Parrinello-Rahman barostat ( $\tau = 12.0$  ps), adding up to a total drying time of 0.7  $\mu\text{s}$  for the IDTBR systems and 0.1  $\mu\text{s}$  for the IDTBT systems. The V-rescale thermostat ( $\tau = 0.2$  ps) and a leap-frog integrator with 2 fs steps were used for all runs. Furthermore, semi-isotropic pressure coupling of 1.0 bar was used with an isothermal compressibility of  $4.5 \cdot 10^{-5} \text{ bar}^{-1}$  in the z-direction and  $0.0 \text{ bar}^{-1}$  in the x- and y-directions to facilitate shrinking of the box only in the z-direction to mimic the conditions in a drying thin-film. The particle mesh Ewald (PME) scheme was used to treat long-range electrostatics (short-range cutoff of 1.2 nm), whereas a cutoff of 1.2 nm was used for van der Waals interactions. All hydrogens were constrained with the LINCS algorithm to reduce computational time.

Having obtained dry thin-films, the IDTBR films were subjected to a 100 ns simulated annealing cycle in an NPT ensemble: 10 ns with a linear temperature increase from 300 K to 600 K, 70 ns at 600 K, 10 ns with a linear temperature decrease from 600 K to 300 K, and a final 10 ns at 300 K. The IDTBT films were annealed at 473 K (corresponding to the experimental annealing temperature for high mobility thin-films<sup>162</sup>) for 5 ns. The resulting annealed thin-films, having a thickness of approximately 10 nm<sup>3</sup>, were then used for analysis in addition to the as-cast thin-films. The evaporation process is visualised in Fig. 3.3.

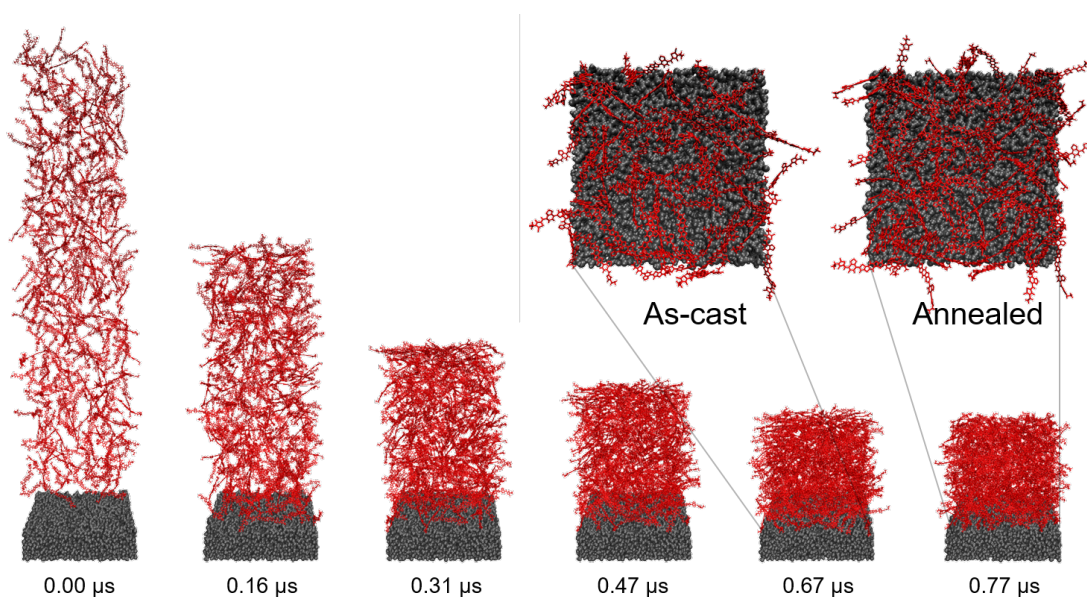


Figure 3.3: Visualisation of the solvent evaporation procedure for O-IDTBR (red) on an amorphous  $\text{SiO}_2$  substrate (dark grey). The final frames from five steps out of the total 133 steps are shown in addition to the annealed thin-film with their corresponding simulation times. Insets show the bottom layer of IDTBR molecules, i.e. molecules that are fully or partly within  $4.5 \text{ \AA}$  of the substrate, for the as-cast and annealed thin-films. Side-chains and solvent molecules are not shown for clarity. Reproduced from Paper II.

### 3.2.3 Persistence length

Quantifying the bending stiffness of a polymer can be done in terms of its persistence length, which is defined as the length over which the tangents to a chain are no longer correlated. The concept of persistence length was introduced in 1948 by Kratky and Porod<sup>185</sup> as a characteristic of what was dubbed the worm-like chain model, which was used to relate the scattering signatures of polymer chains in solution to their bending stiffness. The worm-like chain model is valid for the continuous curvature limit of polymers, i.e. when the contour length  $L$  is much longer than the monomer length  $l$ , and when the angles  $\Theta$  between neighbouring monomers do not deviate significantly from being parallel. The end-to-end length of the polymer,  $R$ , can then be related to the persistence length as<sup>185</sup>

$$\langle R^2 \rangle = 2Ll_p - 2l_p^2 \left( 1 - e^{-\frac{L}{l_p}} \right), \quad (3.1)$$

where the brackets  $\langle \rangle$  denote an average over a polymer chain's trajectory. This mean square end-to-end distance is not directly available from experiment, but it can be shown to be proportional to the mean square radius of gyration,  $\langle R_g^2 \rangle$ ,<sup>186</sup> which can be inferred from static light scattering or small-angle neutron or X-ray scattering.

Inferring the persistence length from MD simulations is more straightforward, as the full trajectory of the polymer or oligomer is directly available. Considering a chain of  $N$  rigid segments, for example monomers of conjugated ring-systems, its persistence length can, by definition, be computed as an angle correlation function quantifying the mean angle between segment tangents. If we represent these tangents by unit vectors

$\hat{\mathbf{v}}_i = \mathbf{v}_i/|\mathbf{v}_i|^{-1}$  across the  $i$ 'th segments, the angle  $\Theta_{ij}$  between segments  $i$  and  $j$  averaged over a trajectory is simply given as

$$\langle \cos(\Theta_{ij}) \rangle = \langle \hat{\mathbf{v}}_i \cdot \hat{\mathbf{v}}_j \rangle . \quad (3.2)$$

By definition,  $\langle \cos \Theta_{i=j} \rangle = 1$ , and keeping  $i$  constant as the first segment and letting  $j$  run across the remaining  $N - 1$  segments would thus give an estimate of the relative bending of the polymer or oligomer with length, *i.e.* its persistence length, with respect to its first repeat unit when the orientations of segment  $i$  and  $j$  lose correlation. This procedure can, however, potentially be prone to edge effects, and in order to minimise these, an additional averaging is introduced. Defining the index  $n = 0, 1, \dots, N - 1$  describing a pairwise "gap" between the segments, the arithmetic "gap"-means of the trajectory averages are given as

$$C(\Theta, n) = \frac{1}{N - n} \sum_{i=1}^{N-n} \langle \hat{\mathbf{v}}_i \cdot \hat{\mathbf{v}}_{i+n} \rangle , \quad (3.3)$$

where we finally introduce the angle correlation function  $C(\Theta, n)$ . To illustrate the implications of this extra averaging, letting  $n = 0$  corresponds to taking the angle auto-correlation function and will thus always lead to a value of 1. Effectively, this is the arithmetic mean of the trajectory averaged angle between segment 1 and itself, segment 2 and itself, segment 3 and itself, etc. (*i.e.* a repeat unit "gap" of 0). Letting  $n = 1$  will yield the arithmetic mean of the trajectory averaged angles between segments 1 and 2, segments 2 and 3, segments 3 and 4, etc. (*i.e.* a repeat unit "gap" of 1). This leads to a total of  $(N - n)T$  data-points being included in a single value of  $C(\Theta, n)$ , where  $T$  is the number of time frames that the trajectory is averaged over. Extrapolating this, we see that the last angle correlation function in the series will consist of only  $(N - (N - 1))T = T$  data-points, *i.e.* the same as had we used Eq. 3.2 - but note that the statistics are significantly improved for the rest of the data points. This motivates a discussion about the errors on the data points, which can be found in the Appendix, Section 3.6.

Turning our attention back to Eq. 3.3, a definition of how to extract a quantitative measure for persistence length from this angle correlation function is still needed. Assuming that the chain in question is only affected by thermal fluctuations, its motion can be considered Brownian, and the angle correlation function will thus decay exponentially.<sup>187</sup> The persistence length  $n_p$  (in units of segments) or, equivalently,  $l_p = n_p l$  (in units of distance) is then the characteristic scale of this decay, *i.e.*

$$C(\Theta, n) \approx e^{-n/n_p} , \quad (3.4)$$

which can simply be quantified as the value of  $n$  for which  $C(\Theta, n)$  intersects  $e^{-1}$ . An example can be found in Fig. 3.4.

Simulating the persistence length with MD can both serve as a validation of a force field in terms of *e.g.* torsional potentials when an experimental persistence length is known and as a way of predicting the relative stiffness of different polymers when experimental values are not available. The advantage of MD simulations are that they provide a direct link to the persistence length regardless of the type of polymer studied as well as to the radius of gyration and end-to-end lengths, which can be used in *e.g.* Eq. 3.1

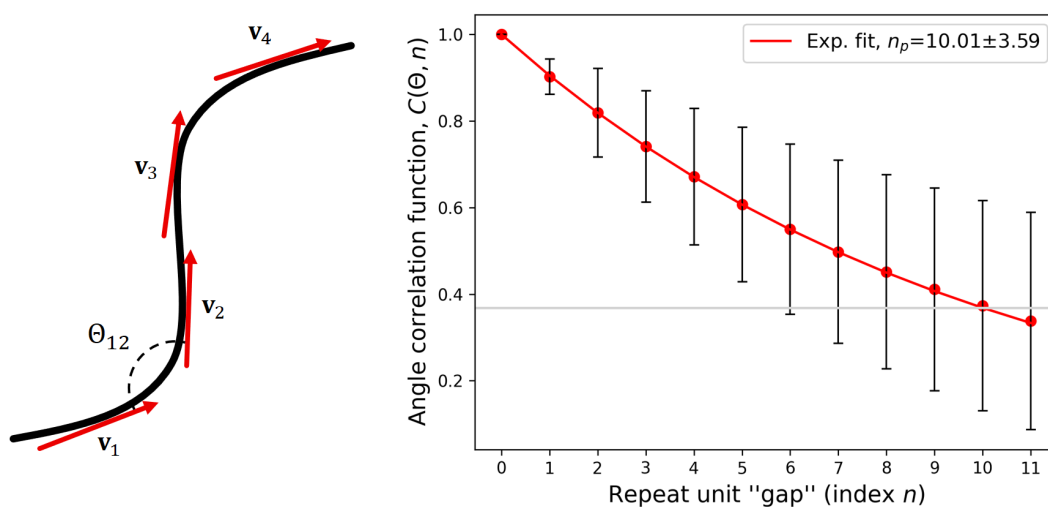


Figure 3.4: Visualisation of how the angles  $\Theta_{ij}$  between tangent vectors  $\mathbf{v}_i$  to an oligomer can be used to extrapolate a persistence length from Eqs. 3.3 and 3.4.

when the appropriate conditions are fulfilled. Furthermore, Eq. 3.4 allows the angle correlation function to be extrapolated and thus gives access to an approximate persistence length for simulations of chains that are shorter than their persistence length. This can especially be useful for very stiff polymers whose persistence length is longer than the chain lengths feasible to simulate.

### 3.2.4 Structural analysis

As the basis of the structural analysis of the simulations, the centre of mass (COM) of each of the conjugated ring-systems were defined as distance evaluation points: one for each of the RH units, one for each of the BT units, one for each of the thiophenes in the IDT unit, and one for the central benzene in the IDT unit, amounting to a total of seven evaluation points per IDTBR molecule and four evaluation points per IDTBT monomer (cf. Fig. 3.1). The normal vectors of the individual planes spanned by these ring systems were also computed to be able to evaluate the relative orientation of the molecular pairs. In addition, a vector along the dipole moment of the BT residues were defined to further quantify the orientation of interchain interactions for the IDTBT oligomers.

### 3.2.5 Electronic coupling

As described in Chapter 2, Section 2.4, the rate of charge transfer is proportional to the square of the electronic coupling between two molecules. In order to assess the influence of the neat films' structural characteristics on their charge transfer properties, the unique, closely interacting molecular pairs or oligomer segment pairs were thus extracted from the MD simulated thin-films and subjected to electronic structure calculations. In the case of the IDTBT oligomers, it is not feasible to perform electronic structure calculations on the full oligomers, and they were hence cropped to trimers centred around the interaction point prior to these. The choice of trimers is motivated by that the segment used in the coupling calculations should be large enough to encompass the delocalisation of an excited electron, which was found to extend across two monomers.<sup>160,163</sup>

For both the IDTBR molecules and the IDTBT oligomers, side-chains were substi-



tuted by methyl groups in order to reduce computational cost; a procedure which is justified by the insulating nature of alkyl side-chains as well as the negligible impact of their length on the backbone electronic structure.<sup>149</sup> With the pairs extracted, we then subjected these, as well as each of the molecules that the pairs consist of, to single point DFT calculations at the B3LYP/6-31G(d) level of theory. From these, their electronic couplings were calculated from the frontier orbitals (HOMO: highest occupied molecular orbital; LUMO: lowest unoccupied molecular orbital) using the projective method (as described in Chapter 2, Section 2.4).<sup>141,142</sup> The use of B3LYP/6-31G(d) is justified as a compromise between computational cost and accuracy in terms of the description of frontier orbital properties (see below). Note that incorporating diffuse functions in the basis set for the single point calculations of the pairs would lead to an over-complete basis because diffuse functions centred on one molecule would overlap with the other molecule in the pair, thus inhibiting the use of the projective method by causing the orthogonalisation of the overlap matrices to break down in the implementation used here.

## 3.3 Results

### 3.3.1 Persistence lengths of IDTBT polymers

IDTBT polymers are, as described above, considered very stiff. The molecular design with an extended, fused IDT ring-system, planar equilibrium torsional angles between IDT and BT, and, perhaps most importantly, parallel intermonomer bonds enables quite rigid polymer strands with long contour lengths. Using the formalism presented in Section 3.2.3, the persistence lengths of a C<sub>16</sub>-IDTBT 12mer in chloroform and a 2EH-IDTBT 12mer in chloroform were calculated based on 100 ns production runs. The vectors have to be carefully chosen, as naively selecting a vector that spans a monomer from the first to the last carbon in the backbone will introduce a periodic, artificial angle between subsequent monomers. Here, we have defined two sets of vectors: one with vectors extending across the BT units parallel to the intermonomer bonds and one with vectors going from the center-of-geometry (COG) of the IDT unit of one monomer to the next. For the first set of vectors, a persistence length of  $64.7 \pm 21.6$  nm was found for C<sub>16</sub>-IDTBT and one of  $52.3 \pm 16.1$  nm was found for 2EH-IDTBT, while the corresponding values were  $57.8 \pm 19.9$  nm and  $45.9 \pm 14.3$  nm, respectively, for the second set of vectors. These persistence lengths are very large compared to e.g. P3HT with an experimental persistence length of 2.9 nm,<sup>188</sup> and only few conjugated polymers are known to have persistence lengths of more than 30 nm.<sup>189,190</sup> For comparison, DNA has a persistence length of 50-70 nm,<sup>191</sup> and the calculated values for the IDTBT polymers thus seem quite high. However, preliminary analyses of small-angle neutron scattering (SANS) measurements on C<sub>16</sub>-IDTBT polymers in chloroform suggest that its persistence length is 30-60 nm (unpublished),<sup>a</sup> which renders the results from the MD simulations more reasonable.

It has previously been found that the oligomer lengths employed in MD simulations need to be several times longer than the persistence length of the given polymer in order to obtain converged values of the persistence length.<sup>179</sup> In this Ref. 179, however, the "gap" average of Eq. 3.3 was not employed, which significantly reduces the statistics.

<sup>a</sup>The SANS measurements are part of the work in preparation for Paper III.

It could be discussed whether it even makes sense to talk about persistence lengths of oligomers that are not longer than this and thus by definition behave as rigid rods, but as argued in Section 3.2.3, extrapolating the persistence length from an exponential decay (such as done here for the IDTBT 12mers) is often the only feasible strategy in simulations of very stiff oligomers. Nevertheless, the convergence of the calculated persistence lengths using the framework presented herein was sought validated with respect to both simulation time and oligomer length. Regarding the first concern, the extrapolated persistence lengths were only just converged after the 100 ns simulation time, meaning that longer simulations would have been preferable. However, the significant solvent volume that needs to be included in a simulation box of a size large enough to encompass an IDTBT 12mer quickly becomes a limiting factor for longer simulation times and in particular for longer oligomers. In an effort to address the second concern, a box with a  $C_{16}$ -IDTBT 24mer solvated in chloroform was simulated for 50 ns, but the extrapolated persistence length had not converged within this time. Instead, P3HT oligomers of 6, 12, and 24 repeat units were simulated for 100 ns in chloroform,<sup>b</sup> which all converged to approximately the same persistence length of around 2.4 nm, corresponding to six repeat units. This is slightly lower than the experimental persistence length of 2.9 nm,<sup>188</sup> but improving this is out of the scope of this chapter – it will, however, be addressed in Chapter 4 for a coarse-grained P3HT model. Nonetheless, it serves to validate the use of Eq. 3.3 and demonstrates the improved statistics of applying the "gap" average when comparing to the persistence length study of P3HT oligomers presented in Ref. 179.

### 3.3.2 Substrate effects

In order to validate the effects of the amorphous  $SiO_2$  substrate employed in the simulations, grazing incidence wide-angle X-ray scattering (GIWAXS) measurements of **O-IDTBR** and **EH-IDTBR** thin-films spin-cast from chloroform onto silicon wafers were performed (cf. Paper II). In Fig. 3.5, the relative orientations  $\omega$  of the normal vectors of the planes spanned by each of the seven ring-systems associated with an evaluation point in the IDTBR molecules (cf. Section 3.2.4) and the normal vector of the substrate xy-plane are shown alongside the experimental  $\pi$ -stack orientations extracted from the (010) peak of the GIWAXS measurements. Although the relative orientations from the simulations show a quantitative deviation from the corresponding GIWAXS data, the qualitative behaviours are very similar: a face-on stacking is favoured for both thin-films, i.e. highest intensities at low  $\omega$ -values, with a tendency for **O-IDTBR** to be more textured than **EH-IDTBR**, i.e. having a sharper orientation profile. Regarding the quantitative deviation, it is important to note that whereas the GIWAXS intensity depends strongly on the local order of several molecules and will thus not yield a signal for a disordered region, all molecules have equal weight in the analysis of the simulated thin-films regardless of the order of their surrounding molecules. This can explain the less sharp decrease of the signal from the simulated thin-films with higher angles compared to the measurements. Summarising, the substrate effects of amorphous  $SiO_2$  are satisfactorily modelled with the employed parameters in the context of this study. We note, however, that functional devices such as OPVs or OFETs are most often deposited directly on top of organic layers of polymers or small molecules that act as charge collection layers between the active layer and the solid state oxide or metal electrodes. Surface properties

<sup>b</sup>The P3HT force field was parametrised similarly to the IDTBT force field, following the procedure outlined in Section 3.2.1 and the Appendix, Section 3.6.1.



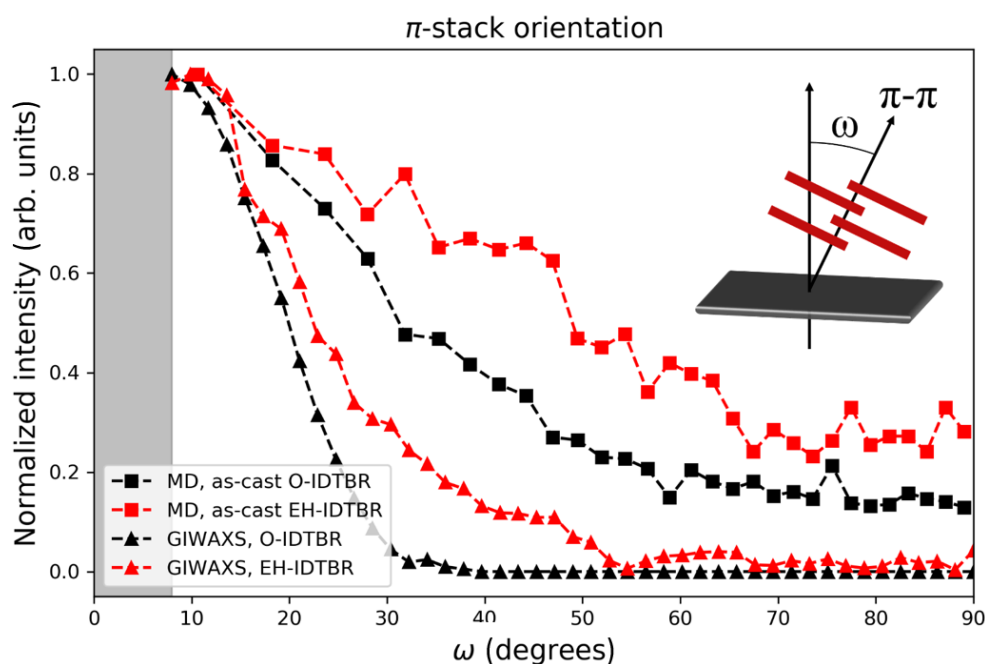


Figure 3.5: Orientational distribution of the  $\pi$ -stacks relative to the substrate (cf. inset) obtained from the (010) GIWAXS-peak for O-IDTBR and EH-IDTBR low-temperature cast thin-films (black and red squares, respectively) compared to the corresponding MD distributions computed as the angles between the normal vector of the substrate and those of each the evaluation point ring-systems in the as-cast thin-films (black and red triangles, respectively). The grey-shaded area from 0-8° represents the range of angles not probed due to the fixed grazing incidence angle. Reproduced from Paper II.

such as the hydrophobicity of these layers can vary significantly from that of amorphous  $\text{SiO}_2$ , which affects the thin-film growth.<sup>192</sup> In this study, a simple setup with few components was prioritised to enable a more direct comparison between simulations and experiments, but future studies should thus focus on implementing substrates that are more directly relevant for functional devices.

### 3.3.3 Thin-film morphologies

As described in Section 3.1, the crystal structure for O-IDTBR and EH-IDTBR has been solved.<sup>150</sup> It is thus possible to compare the nanostructure of thin-films inferred from solvent evaporation simulations to the ones of crystal supercell simulations. In addition, we performed GIWAXS measurements of IDTBR thin-films cast from chloroform on silicon wafers to be able to validate the simulation results further (see Paper II). In summary, we found that whereas the short-range structural properties, i.e.  $\pi$ -stacking, were described very well with quantitative precision, only minor indications of long-range order were present in the simulated thin-films. It was, however, indicated that the simulated annealing had, although to a low degree, increased the structural order in these, but it remained that the reasonably accessible simulation times for atomistic MD were not sufficient to induce a high long-range structural order in randomly initiated simulations of solution deposited small-molecule systems.

Polymers obviously behave very differently from small molecules, but given the struc-

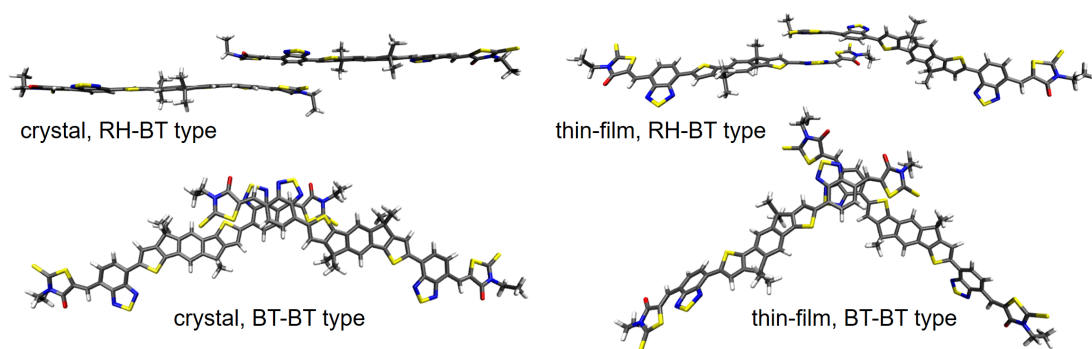


Figure 3.6: Representative pairs of different types of  $\pi$ -stacking interactions in an O-IDTBR crystal supercell and in an O-IDTBR thin-film processed from chloroform on amorphous  $\text{SiO}_2$ .

Table 3.1: Percentages of different interaction types relative to the total number of pairs with  $\pi - \pi$  interactions closer than 4.5 Å.

amount (%) type	O-IDTBR			EH-IDTBR			C <sub>16</sub> -IDTBT
	as-cast	anneal.	crystal	as-cast	anneal.	crystal	anneal.
RH-RH	8.6	4.3	-	12.0	8.8	-	-
BT-BT	27.5	32.4	35.1	35.1	35.0	-	27.9
IDT-IDT	0.9	3.2	-	-	-	-	16.4
RH-BT	33.3	25.9	61.4	42.9	41.9	100.0	-
RH-IDT	13.5	20.0	3.5	4.7	6.2	-	-
BT-IDT	16.2	14.1	-	5.2	8.1	-	55.7

tural similarity of the IDTBR molecules and the IDTBT monomers, the validation of the IDTBR force fields in Paper II in connection with the validation from the persistence length simulations described in Section 3.3.1 serve to validate the IDTBT force fields to some degree. The structural similarity also allows some comparison between the two. Both the IDTBR molecules and IDTBT polymers employ  $\text{sp}^3$  hybridised bridgehead carbons on the central IDT units, to each of which two side-chains are bonded (cf. 3.1). These side-chains thus have a preferential conformation which is normal to the plane of the backbone, i.e. pointing away from each other, which induces bulkiness around the IDT unit. This, in turn, means that the  $\pi$ -stacking is expected to occur between the terminal RH units and/or BT units in the thin-films and not between the IDT units (cf. Fig. 3.6). Indeed, close  $\pi$ -stacking intermolecular interactions between two IDT units are very rare according to the simulations. Neither O-IDTBR nor EH-IDTBR thin-films or crystals exhibit any significant fraction of this type of interactions as seen in Table 3.1, and the "lamellar" in-plane peaks in the GIWAXS spectra of IDTBR thin-film have been shown to arise from scattering between "columns" of these extended BT-RH and BT-BT  $\pi$ -stacks.<sup>150,193</sup>

C<sub>16</sub>-IDTBT polymers have, based on a molecular mechanics conformational search, previously been suggested to have a significantly different nanostructure with parallel,  $\pi$ -stacked chains organised in lamellae with interdigitated side-chains, which maximises the van der Waals interactions between chains.<sup>163</sup> The very low order observed in C<sub>16</sub>-IDTBT thin-films from GIWAXS measurements along with the coexistence of a  $\pi$ -stacking (010) peak and a side-chain length-dependent (200) peak in the out-of-plane direction<sup>162</sup> can,

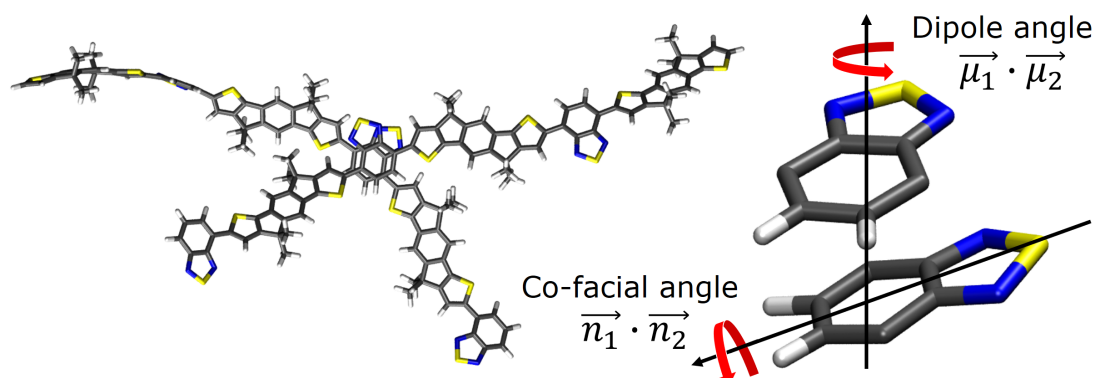


Figure 3.7: Example of a BT-BT type  $\pi$ -stacking interaction in a  $C_{16}$ -IDTBT thin-film processed from chloroform on amorphous  $SiO_2$  alongside a schematic of how the BT-BT co-facial and dipole angles are defined (used in Fig. 3.8).

however, not be fully explained with the crystal unit cell suggested in Ref. 163. In order to investigate other possible nanostructural conformations that could potentially coexist with the suggested crystalline form in solution processed thin-films, we simulated the amorphous phase of  $C_{16}$ -IDTBT and 2EH-IDTBT thin-films using the solvent evaporation scheme described in Section 3.2.2. A structural analysis (cf. Section 3.2.4) of the dry, annealed thin-films showed that, for the vast majority of the close interchain BT-BT type interactions, the two BT units were both co-facial and perpendicularly aligned with respect to their dipole vectors (cf. Fig. 3.7) as seen in Fig. 3.8. This effect is more pronounced for 2EH-IDTBT oligomers, which seems to be due to better statistics from more interactions owing to the shorter side-chains. Although this cannot explain the discrepancies between the suggested crystalline form of IDTBT and the measured GIWAXS spectra, it suggests that, in a solution processed IDTBT thin-film, the backbones are more likely to form perpendicular interchain crossings than to overcome the large energy barrier associated with orienting all side-chains from the minimum energy configuration at 70 degrees to the highest energy minima at 180 degrees (cf. Fig. 3.2) to be able to  $\pi$ -stack in lamellae along the backbone direction with interdigitated side-chains. The steric effects associated with the  $sp^3$  hybridised linking carbons thus lower the probability of extended  $\pi$ -stacking and promotes a grid-like backbone morphology with close interchain contacts primarily between perpendicular backbones. This is in contrast to highly ordered polymers such as P3HT whose  $sp^2$  hybridised linking carbons and linear alkane side-chains promote lamellar stacks separated by isolating side-chain domains, thus relying on amorphous domains to provide connections between the highly ordered crystalline domains.

It has previously been hypothesised that only few contacts between backbones are needed for facile charge transport in IDTBT films, as the interchain transport along the backbone becomes the dominant contributor to a high mobility due to the low torsional disorder and high rigidity of IDTBT polymers.<sup>162</sup> The preferential perpendicular alignment of the polymer backbones observed here can hence possibly be part of the explanation of why the predominantly amorphous films can exhibit such high mobilities, as a grid-like charge transport network provides the occasional contacts between backbones required to relay the charge carriers.

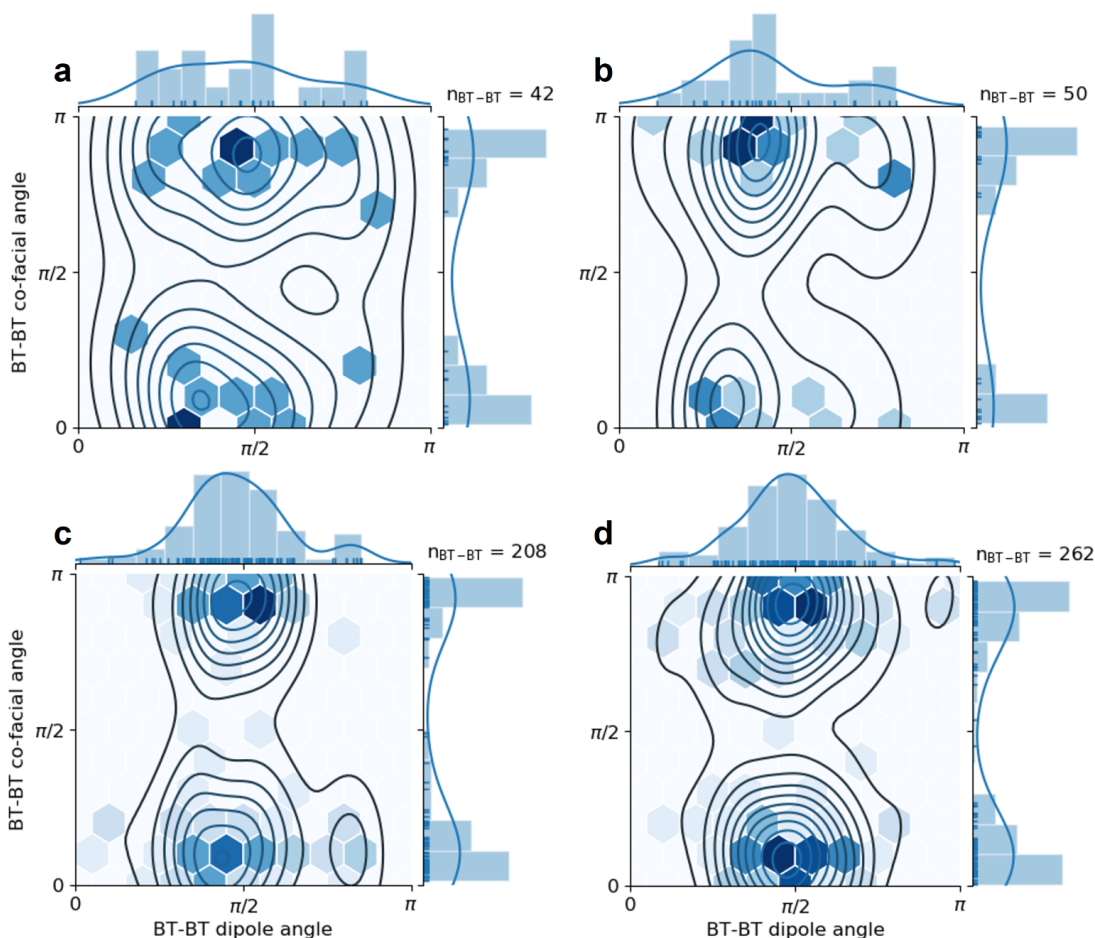


Figure 3.8: Relative orientations of the BT residues between closely interacting oligomers in a) as-cast and b) annealed  $C_{16}$ -IDTBT thin-films and in c) as-cast and d) annealed 2EH-IDTBT thin-films.

Recently, high-resolution scanning tunnelling microscopy (STM) images of a sub-monolayer of  $C_{16}$ -IDTBT deposited on an Au(111) surface by electrospray deposition were published.<sup>176</sup> These images clearly show that, on a gold surface under ultra-high vacuum, the  $C_{16}$ -IDTBT chains align face-on to the substrate with interdigitated side-chains. It is, however, also evident that in the few instances where a chain is deposited on top of other chains, their crossing are perpendicular. Further simulations including substrate and solvent effects on longer time scales than considered here are nonetheless needed to determine the evolution of the 3D morphology of solution processed IDTBT thin-films and to determine if the tendencies observed for 2D sub-monolayers are also relevant in the bulk of the films.

### 3.3.4 Electronic properties

In order to investigate how the above described nanostructure of the  $C_{16}$ -IDTBT thin-films influence their electronic properties, the closely interacting pairs were extracted from the simulations as described in Section 3.2.5. The different types of close interactions were analysed and listed in Table 3.1 as percentages relative to the total number of pairs extracted and in Table 3.2 and 3.3 as the mean electron and hole coupling strengths in meV, respectively. These are listed alongside the corresponding values for the IDTBR

Table 3.2: Mean electron coupling,  $\mu(J_e)$ , in meV of different interaction types of pairs with  $\pi - \pi$  interactions closer than 4.5 Å.

$\mu(J_e)$ [meV] type	O-IDTBR			EH-IDTBR			C <sub>16</sub> -IDTBT
	as-cast	anneal.	crystal	as-cast	anneal.	crystal	anneal.
RH-RH	16	6	-	9	13	-	-
BT-BT	23	20	25	18	20	-	18
IDT-IDT	15	8	-	-	-	-	7
RH-BT	16	17	31	15	14	15	-
RH-IDT	14	8	-	23	4	-	-
BT-IDT	13	12	-	15	16	-	11

Table 3.3: Mean hole coupling,  $\mu(J_h)$ , in meV of different interaction types of pairs with  $\pi - \pi$  interactions closer than 4.5 Å.

$\mu(J_h)$ [meV] type	O-IDTBR			EH-IDTBR			C <sub>16</sub> -IDTBT
	as-cast	anneal.	crystal	as-cast	anneal.	crystal	anneal.
RH-RH	8	4	-	7	10	-	-
BT-BT	13	12	16	8	7	-	5
IDT-IDT	26	1	-	-	-	-	4
RH-BT	9	9	32	9	9	13	-
RH-IDT	14	9	-	8	7	-	-
BT-IDT	9	7	-	11	7	-	4

thin-films and crystals for comparison; a further analysis of the IDTBR coupling can be found in Paper II.

Interestingly, the high fraction of close contacts involving a BT unit in the C<sub>16</sub>-IDTBT thin-films (cf. Table 3.1) is expected to be more beneficial to the electron transfer properties than to the hole transfer properties owing to the electron withdrawing nature of the BT unit. Similarly to the IDTBR acceptors, the LUMO of IDTBT is localised mainly on this BT unit,<sup>163</sup> and the electron coupling data in Table 3.2 are indeed consistent with this, showing stronger couplings for the BT-BT interactions than for the IDT-IDT and BT-IDT interactions. The magnitudes of the electron couplings are similar to those of the IDTBR simulations, but the calculated hole couplings for C<sub>16</sub>-IDTBT in Table 3.3 are significantly lower than both the corresponding electron couplings and the hole couplings of the IDTBR simulations. This seems inconsistent with the high measured hole mobilities in C<sub>16</sub>-IDTBT thin-films, and it is surprising that the IDT-IDT type interactions do not exhibit higher hole couplings.

## 3.4 Discussion

Due to the surprisingly low hole couplings in the C<sub>16</sub>-IDTBT thin-films, the procedure of extracting trimer pairs and calculating their electronic coupling was reviewed. When directly using MD geometries as input in quantum mechanical (QM) calculations, there is a risk that one or more of the different bonds and angles are in a stretched conformation, which can strongly impact the frontier orbitals calculation if an atom is very strained or is sufficiently far away to not be considered fully bonding. We thus performed five SCF iterations in a QM optimisation on each pair to ensure that all bond lengths were reasonable. As seen in Fig. 3.9, this mainly served to reduce a few strong electron coupling values and generally lower the hole coupling values relative to the pre-optimised

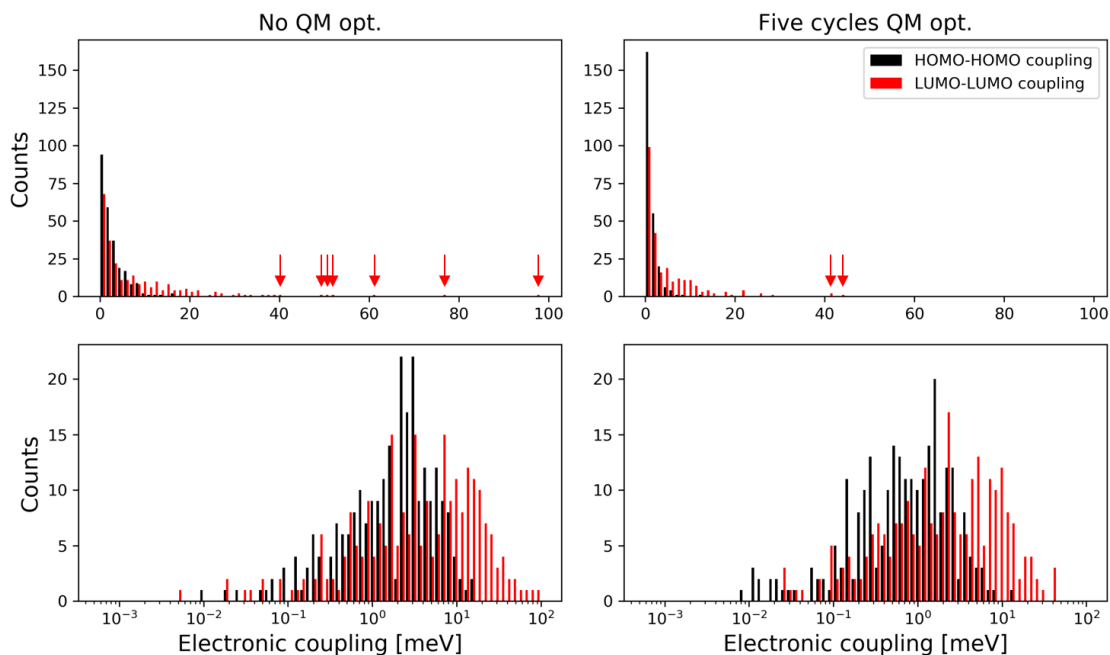


Figure 3.9: Comparison of the electronic coupling calculated before and after undergoing five cycles of QM optimisation of the 250 closest interacting  $C_{16}$ -IDTBT pairs extracted from the MD simulations. Top row is plotted on a linear scale, bottom row on a logarithmic scale. Arrows indicate single data points of high coupling to ease the view.

Table 3.4: Electron and hole coupling in meV as a function of chromophore size of the most closely interacting  $C_{16}$ -IDTBT pair in the annealed thin-film deposited on amorphous  $SiO_2$  from chloroform.

	trimers	dimers	IDT-BT-IDT	monomers
$\mu(J_e)$	76	211	348	63
$\mu(J_h)$	5	156	124	0

pairs listed in Tables 3.2 and 3.3, leading to average electron couplings of BT-BT, IDT-IDT, and BT-IDT types of interactions of 10, 2, and 6 meV, respectively, and corresponding average hole couplings of 2, 1, and 2 meV, respectively. This can be explained by the pairs moving further apart during the optimisation.

As a second check, the dependence of the coupling strengths on the chosen size of IDTBT chromophores (with the default being pairs of trimers) was evaluated. Choosing the most closely interacting pair of trimers having a BT-BT type interaction with an electron coupling of 76 meV and a hole coupling of 5 meV, it was cropped down to a pair of dimers, a pair of IDT-BT-IDT segments, and a pair of monomers. As seen in Table 3.4, the resulting couplings vary significantly with chromophore size, but which size that most closely reflects the actual coupling is difficult to say.

It is, however, more probable that the description of the structural properties is flawed. The solvent evaporation simulations presented for  $C_{16}$ -IDTBT are far from representative of the time scales relevant for the morphological evolution of solution processed polymers, but these are not accessible with atomistic models. In order to be able to simulate the behaviour of longer chains in solution as well as their packing in solution processed thin-



films, a coarse-grained model was thus developed for the C<sub>16</sub>-IDTBT polymer based on the MARTINI 3.0 model for IDTBR described in detail in Chapter 4. The work is preliminary, but it is feasible to run large simulations of thin-films, which confirm the tendencies of amorphous morphologies with very few close interchain interactions.

## 3.5 Conclusions

In this chapter, a molecular dynamics solvent evaporation procedure that includes substrate and air-interface effects to model solution deposition of organic thin-films has been devised. The procedure is general and can be used in combination with any given substrate and for both atomistic and coarse-grained MD simulations. Here, atomistic force-fields for IDBTR molecules and IDTBT polymers were developed and used to investigate the structure-property relationships in their thin-films.

It was found that the short-range structural properties, i.e.  $\pi$ -stacking, and the qualitative alignment effects relative to the substrate were accurately modelled, but it was, however, evident that the time scales feasible for atomistic MD, here on the order of 1  $\mu$ s, were not sufficient to induce significant longer range order in small-molecule thin-films. For the IDTBT polymer thin-films, a clear tendency of the close interchain interactions being predominantly between perpendicular backbones was observed, creating a grid-like charge transfer network which can potentially be part of the explanation for the high mobility observed experimentally.

Upon linking the structural findings to electronic properties, it was found that the  $\pi$ -stacking interactions of benzothiadiazole units were beneficial for the charge transport properties of IDTBR small-molecule thin-films, exhibiting high electronic transfer integrals even in amorphous films. This result is believed to be relevant for a range of *n*-type materials with similar molecular designs. This makes it all the more interesting that the C<sub>16</sub>-IDTBT polymers, which are known for their high hole mobility, exhibit the same tendencies of higher electron coupling than hole coupling as the IDTBR molecules, particularly for the  $\pi$ -stack interaction types involving BT units. It is thus hypothesised that IDTBT polymers could work well as *n*-type materials in organic bulk heterojunction solar cells.

## 3.6 Appendix

### 3.6.1 Detailed parametrisation procedure

**Partial charges** Atomic partial charges were determined from density functional theory (DFT) calculations at the B3LYP/6-311++G(d,p) level of theory using Gaussian 16.<sup>180</sup> For the IDTBR acceptors, the minimum energy conformation of a methyl-substituted IDTBR molecule was determined through a conformational search and energetically optimised in vacuum. The electrostatic potential (ESP) charges of the resulting structure (based on a population analysis using the `pop=ChelpG` keyword) were then symmetrised and included in the topology. Standard OPLS-AA charges were used for the alkane side-chains except for the first carbon, whose charge was modified to reflect the charge on the methyl substituent in the DFT calculations. The final charges are listed in the topology files `O-IDTBR.itp` and `EH-IDTBR.itp` available at doi:10.11583/DTU.c.5254236.

For the IDTBT polymers, a methyl-substituted trimer was optimised at the same level of theory as the IDTBR acceptor. The bond lengths, angles, and dihedrals of the internal monomer were then used to construct the seven internal monomers in a 9mer,

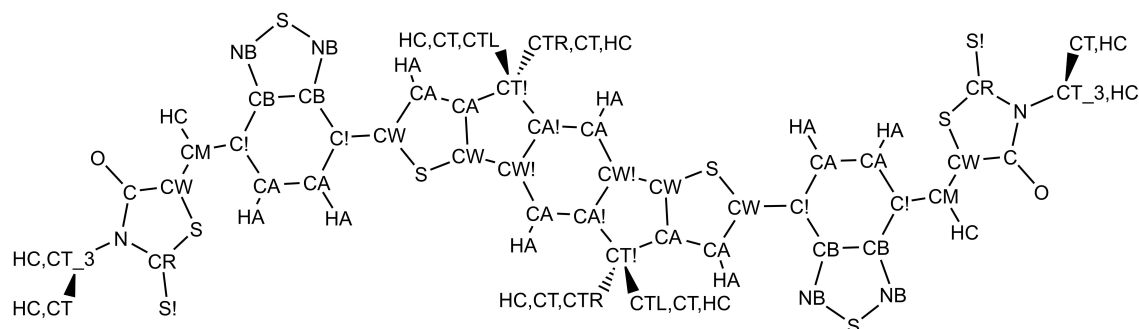


Figure 3.10: The `OPLS-AA` atom types assigned to IDTBR and IDTBT (the IDTBT atom types are identical to the IDTBR for the corresponding atoms, cf. Fig. 3.1).

Table 3.5: The assigned atom types (cf. Fig. 3.10) and their atom numbers, atomic masses, and Lennard-Jones parameters.

Atom type	Atom number	Mass (au)	$\sigma$ (nm)	$\epsilon$ (kJ/mol)
CA, CA!, C!	6	12.0110	0.355000	0.292880
CB, CW, CW!	6	12.0110	0.355000	0.292880
NB, N	7	14.0067	0.325000	0.711280
HA	1	1.00800	0.242000	0.125520
S, S!	16	32.0600	0.355000	1.046000
CT!	6	12.0110	0.380000	0.209200
CT, CTR, CTL	6	12.0110	0.350000	0.276144
CT_3, CR, CM	6	12.0110	0.350000	0.276144
C	6	12.0110	0.375000	0.439320
O	8	15.9994	0.296000	0.878640
HC	1	1.00800	0.250000	0.125520

whereas the terminal monomers in the 9mer were kept as the corresponding terminal monomers in the trimer. This 9mer was then subject to a single point energy calculation at the same level of theory, after which the resulting ESP charges of the seven internal monomers were symmetrised and scaled to yield a net charge of zero. This resulted in a three-residue model with different charges on either terminal monomer and on the internal monomer, allowing one to build oligomers of arbitrary length. The final charges are listed in the topology files `C16-IDTBT_12mer.itp` and `2EH-IDTBT_12mer.itp` available at doi:10.11583/DTU.c.5254236.

**Atom types** The atom types were assigned to IDTBR and IDTBT as depicted in Fig. 3.10. The native `OPLS-AA` atom types were used when applicable, while renamed copies of these were used where necessary (indicated by exclamation marks or R/L for the first sets of carbons in the sidechains). In Table 3.5, the masses and Lennard-Jones 12-6 parameters are listed for all atom types.

**Bonds** Parameters for bond types were, to the extent reasonable, taken from the `OPLS-AA` force field (explicitly stated from which `OPLS-AA` bond type in the force field files `ffbonded_IDTBR.itp` and `ffbonded_IDTBT.itp` available at doi:10.11583/



DTU.c.5254236 The few missing bond type parameters (for the BT unit) were taken from Ref. 194 in which B3LYP/6-311G(d,p) bond lengths combined with a modified Badger's rule was used to calculate the bond force constants. These are also listed in the force field files `ffbonded_IDTBR.itp` and `ffbonded_IDTBT.itp` available at doi:10.11583/DTU.c.5254236.

**Angles** The larger part of the backbone equilibrium angles were determined from the optimised B3LYP/6-311++G(d,p) structures, whereas the angle force constants were adopted from the OPLS-AA force field (explicitly stated from which angle type in the force field files `ffbonded_IDTBR.itp` and `ffbonded_IDTBT.itp` available at doi:10.11583/DTU.c.5254236 Great care was taken to capture the asymmetry of the IDT unit through specific atom type assignments, thus enabling the specification of distinct angle types where necessary (cf. Fig. 3.10). Both equilibrium angles and force constants for the alkane side-chains are taken from the OPLS-AA force field.

**Torsions** The general procedure for determining the RH-BT, IDT-BT, and IDT-to-sidechain torsional potentials is described in Section 3.2.1. Going a bit deeper into the details, it can be seen that the four possible definitions of dihedral quadruplets for each of the RH-BT and IDT-BT torsions are degenerate in pairs of two with a  $\sim 180^\circ$  phase shift: one pair of quadruplets (CB-C!-CW-CA and CA-C!-CW-S for IDT-BT) with an equilibrium angle of  $20^\circ$  or  $340^\circ$  and one pair (CB-C!-CW-S and CA-C!-CW-CA) with one of  $160^\circ$  or  $200^\circ$  (which of course corresponds to the exactly same structure). We thus employed an iterative Boltzmann inversion (IBI) fitting scheme (cf. Section 3.2.1) taking this symmetry into account by iterating the procedure simultaneously for each pair of degenerate quadruplets. The resulting converged Boltzmann inverted statistics collected through a 50 ns NVT simulation in vacuum at 600 K can be seen in Figs. 3.2a and 3.2b for the RH-BT and IDT-BT torsions, respectively, alongside the  $\omega$ B97X-D scans, the "raw" MD scans, and the fitted total RB torsional potentials. The RB parameters are listed explicitly in the force field files `ffbonded_IDTBR.itp` and `ffbonded_IDTBT.itp` available at doi:10.11583/DTU.c.5254236.

The IDT-to-side-chain torsions represent a slightly more complicated case. As seen in Fig. 3.10, it was necessary to assign different atom types (CTR and CTL) to the chemically identical first carbons of the side-chains as each dihedral quadruplet would otherwise partially define the torsions of both of the side-chains simultaneously, which are phase-shifted with respect to their equilibrium dihedral angles. By defining the CTR and CTL atom types, it is possible to distinguish these, and a pairwise degeneracy between the CA-CT!-CTR-CT and CA!-CT!-CTL-CT quadruplets and between the CA!-CT!-CTR-CT and CA-CT!-CTL-CT quadruplets will then be present. Note that the degeneracy is across different side-chains, hence requiring a slightly different approach than the above for the RH-BT and IDT-BT torsions. In order to probe only the relevant side-chain torsions, we employed a model system consisting of a 4,4-diethyl-9,9-dimethyl-IDT unit (with the respective IDTBR and IDTBT partial charges for the MD scans). Approximately half of the full potential for each side-chain torsion is assigned to each quadruplet in a degenerate pair with the asymmetry between the degenerate pairs accounted for in the different potentials assigned. The resulting converged Boltzmann inverted statistics collected through a 50 ns NVT simulation in vacuum at 600 K can be seen in Fig. 3.2c for one of the side-chains alongside the  $\omega$ B97X-D scan, the "raw"

MD scan, and the fitted total RB torsional potential (i.e. the linear combination of the two quadruplet potentials), both in the basis of the CA-CT!-CTL-CT dihedral. The RB parameters are listed explicitly in the force field files `ffbonded_IDTBR.itp` and `ffbonded_IDTBT.itp` available at doi:10.11583/DTU.c.5254236

**Improper dihedrals** For the flat backbone structures, improper dihedrals were defined manually for each atom to keep these, to a large extent, in plane. The standard OPLS-AA force constant for aromatic systems of 167.4 kJ/mol was used for all improper dihedrals defined in the systems. These are listed in the force field files `ffbonded_IDTBR.itp` and `ffbonded_IDTBT.itp` available at doi:10.11583/DTU.c.5254236

### 3.6.2 Error analysis of persistence length simulations

The errors on the simulated persistence lengths can seem excessively large. Below, an account of the error analysis will be given to shed some light on why they are found to be this big. From basic statistical analysis, we know that the corrected sample standard deviation for a sample with  $m$  measurements of a variable  $x$  is given as

$$s = \sqrt{\frac{1}{m-1} \sum_{i=1}^m (x_i - \bar{x})^2}, \quad (3.5)$$

where, in this notation, the arithmetic mean  $\bar{x}$  is defined as

$$\bar{x} = \frac{1}{m} \sum_{i=1}^m x_i. \quad (3.6)$$

Since we are combining several data-sets when taking the "gap"-mean of the trajectory averages of every alike pairwise combination of segments, the above definitions need to be extended. Taking  $k = 1, 2, \dots, K$  data-sets each consisting of  $m_k$  measurements of a variable  $x$  with a corrected sample standard deviation  $s_k$  and an arithmetic mean  $\bar{x}_k$ , the combined corrected sample standard deviation  $s_{\text{comb}}$  is given by

$$s_{\text{comb}} = \sqrt{\frac{\sum_{k=1}^K ((m_k - 1)s_k^2 + m_k(\bar{x}_k - \bar{x}_{\text{comb}})^2)}{\left(\sum_{k=1}^K m_k\right) - 1}}, \quad (3.7)$$

where the combined mean  $\bar{x}_{\text{comb}}$  of all  $K$  data-sets is calculated using

$$\bar{x}_{\text{comb}} = \frac{\sum_{k=1}^K m_k \bar{x}_k}{\sum_{k=1}^K m_k}. \quad (3.8)$$

Applying the above general expressions (Eqs. 3.5-3.8) to our specific case, we see that since  $m_k$  corresponds to the number of time frames for each measurement, it is equal to  $T$  for all  $k = 1, 2, \dots, K$  measurements and can thus be pulled out of the sum. It can then easily be shown that Eq. 3.8 can be reduced to

$$\bar{x}_{\text{comb}} = \frac{T \sum_{k=1}^K \bar{x}_k}{T \sum_{k=1}^K 1} = \frac{1}{K} \sum_{k=1}^K \bar{x}_k, \quad (3.9)$$

which, when letting  $k \rightarrow i = 1, 2, \dots, N - n$  and  $\bar{x}_k \rightarrow \langle \hat{\mathbf{v}}_i \cdot \hat{\mathbf{v}}_{i+n} \rangle$ , is exactly Eq. 3.3. When fitting an exponential decay to this angle correlation function as a function of the "gap" index  $n$ , we consider the calculated combined sample standard deviation (Eq. 3.7) for each point in the fit, thereby making sure that there is a higher relative weight of the fitting on the points with better statistics. Furthermore, we do so in an absolute manner to not artificially scale down the standard deviation of the fit itself. In general, the standard deviation of a fit with respect to  $p$  fitted parameters can be calculated from its (diagonal) covariance matrix  $\Sigma$ :

$$\Sigma = \begin{bmatrix} \sigma_{11} & \sigma_{12} & \dots & \sigma_{1p} \\ \sigma_{21} & \sigma_{22} & \dots & \sigma_{2p} \\ \vdots & \vdots & \ddots & \vdots \\ \sigma_{p1} & \sigma_{p2} & \dots & \sigma_{pp} \end{bmatrix}. \quad (3.10)$$

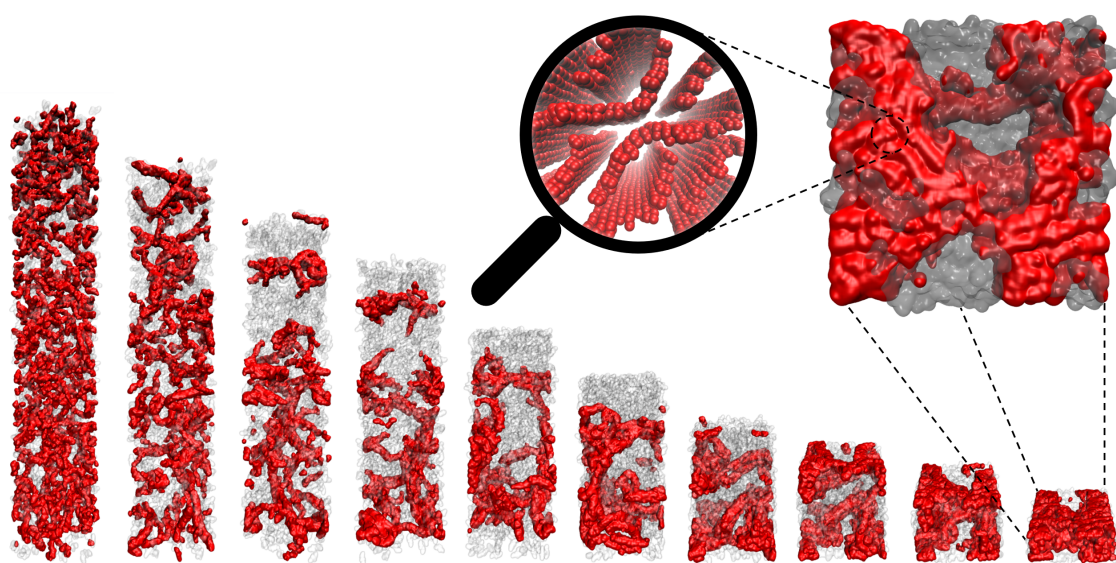
Using this, the variance of the  $i$ 'th fitted parameter is then simply given as

$$\sigma_i^2 = \Sigma_{ii}. \quad (3.11)$$

In our specific case, we are only fitting the parameter  $n_p$  in Eq. 3.4, and we can thus see that  $\Sigma$  is a single value  $\Sigma_{n_p}$  and that the standard deviation of our fit hence is

$$\sigma = \sqrt{\Sigma_{n_p}} = \sqrt{\text{cov}(n_p)}. \quad (3.12)$$

## 4 Morphology evolution in solution processed organic solar cell blends



This chapter is based on manuscript **IV**, which is in preparation. It will here be described how coarse-grained molecular dynamics simulations allow reaching the time and length scales necessary to study structural properties such as domain sizes and how to correlate these to experiments.

## 4.1 Introduction

The efficiency of organic photovoltaic (OPV) cells depends on a multitude of electronic and structural parameters. Whereas huge efforts are put into optimising the electronic properties of the donor and acceptor materials,<sup>195–201</sup> it is well known that subtle variations in processing parameters can give rise to rather large efficiency differences of devices based on exactly the same donor and acceptor materials.<sup>202–204</sup> This is generally believed to be directly related to the morphology of the active layer bulk heterojunction.<sup>205–207</sup> Although there is little doubt that the bulk heterojunction is a well-suited type of active layer morphology for high efficiency OPVs,<sup>208,209</sup> solution deposition leaves a vast processing parameter space to be optimised. Solvent, temperature, donor:acceptor composition, additives, and thickness are only a handful of the most important. Practically, optimising these is most often done in a trial-and-error manner by varying one processing parameter at a time to find an optimum, then varying the next processing parameter at the optimum of the first, and so on and so forth, in a prioritised sequence. Especially for scalable deposition methods,<sup>9,10,210</sup> this procedure is costly both in terms of time and resources.<sup>204</sup> Recently, Campoy-Quiles and co-workers have devised new, experimental frameworks for high-throughput evaluation of processing parameters in a continuous manner by blade coating active layers with gradients in e.g. composition, thickness, and annealing temperature.<sup>211,212</sup> This procedure can significantly reduce the necessary number of samples to find an optimum, and it furthermore increases the chance of finding *the* optimum, as processing parameter combinations not otherwise considered in the sequential trial-and-error procedure will be probed. However, and regardless of the sample preparation procedure, in order to obtain direct insight into the structural parameters of the active layers as a function of the processing parameters, advanced electron or X-ray techniques must be employed.

Although the electronic contrast between organic molecules is in general poor, the relatively high density of the fullerene phase in polymer:fullerene OPVs enables the use of grazing incidence small-angle X-ray or scattering (GISAXS) methods to determine average, long-range structural parameters such as the domain size.<sup>206,213</sup> The domain size is commonly believed to be highly influential on the performance of OPVs. This is due to the limited exciton diffusion length, which has been shown to be around 5–10 nm in a range of OPV donors and fullerene acceptors, including P3HT and PffBT4T-2OD.<sup>214,215</sup> Very recently, however, it has been shown that the exciton diffusion length in the acceptor-donor-acceptor (A-D-A) type of non-fullerene acceptors (NFA) is significantly longer, namely 20–45 nm for a range of the most frequently used acceptors in high performance OPVs.<sup>216</sup> The latter finding can potentially relax the constraints on domain sizes in NFA OPVs relative to the ones in fullerene OPVs, but the basic, physical principle that the domain size should be smaller than or close to the exciton diffusion length remains. However, the electronic contrast between donors and acceptors in NFA-based systems is even poorer than in fullerene-based systems due to the structural similarities between the donor polymers and the NFA acceptors, which can yield measurements with low signal-to-noise ratios. Furthermore, the signals from GISAXS measurements provide only average characteristic lengths, which depend on the fitting model used, and do not allow a qualitative insight into what exactly these lengths correspond to for real systems. Interpreting GISAXS results can thus be difficult without supportive structural models.

In order to gain a more detailed understanding of how OPV morphology is influenced by processing parameters and to be able to aid the interpretation of results from advanced

X-ray experiments, molecular dynamics (MD) simulations can prove useful.<sup>217</sup> Solution processing of organic functional materials has previously been modelled using MD solvent evaporation simulations with both atomistic<sup>193,218–220</sup> and coarse-grained (CG) models of varying resolution.<sup>119,133,181,221,222</sup> However, of the two, only CG models represent a computationally feasible framework to reach the time and length scales relevant for domain formation in donor:acceptor blends. In these previous CG MD studies of OPV material blends, only PCBM has been used as an acceptor,<sup>119,133,181,222</sup> but with the impressive device performance improvements realised with A-D-A NFAs,<sup>15,16,174,223,224</sup> studies of the structural evolution of OPV material blends with NFAs are called for. As demonstrated in Ref. 133, employing CG models with high relative chemical specificity allows reaching the length scales necessary to investigate large-scale structural information such as domain formation while at the same time retaining the necessary resolution of the materials to reliably backmap them to atomistic detail. Such a multiscale modelling framework can potentially help to elucidate the structure-property relationships of OPVs.

Here, we present molecular dynamics solvent evaporation simulations of organic solar cell blends using coarse-grained models based on the newly developed MARTINI 3.0 force field. The MARTINI force field relies on the building block approach where specific functional groups are mapped to specific bead types, resulting in transferable models with high chemical specificity despite the reduced representation. This also facilitates the building of new coarse-grained models of structurally complex donor polymers and non-fullerene acceptors. We have chosen to investigate the non-fullerene P3HT:O-IDTBR and PffBT4T-2OD:O-IDTBR systems and compare these to their fullerene analogues, namely P3HT:PCBM and PffBT4T-2OD:PCBM. The P3HT:PCBM system is the prototypical OPV material blend for fullerene systems, and the P3HT:O-IDTBR system is quickly becoming the prototypical P3HT-based non-fullerene material blend,<sup>173,225</sup> exhibiting efficiencies of more than 7 %<sup>203,226</sup> and being a promising candidate for low-cost OPV systems for large-scale fabrication.<sup>204,211,227–229</sup> The PffBT4T group of polymers<sup>230</sup> exhibit high efficiencies of up to 11 % when mixed with PCBM or IDTBR acceptors,<sup>223,231–234</sup> and these blends furthermore also represent some of the most promising candidates for high-efficiency, low-cost OPV systems.<sup>39</sup> For these systems, we simulate a range of processing conditions by varying the solvent and temperature of the simulation during the evaporation process and assess the influence of thermal annealing. We then analyse the influence of the processing parameters on structural properties such as domain- and crystallite sizes. In order to establish the structure-property relationships, we simulate the charge carrier mobilities in the donor and acceptor phases using kinetic Monte Carlo time-of-flight mobility simulations and compare the trends found to OPV device measurements.

## 4.2 Force field development

All simulations presented herein are performed in GROMACS 2018.3.<sup>59,178</sup> The coarse-grained models are based on the newly developed MARTINI 3.0 force field.<sup>a</sup> We have developed models for the polymer donors P3HT and PffBT4T-2OD as well as the small-molecule, non-fullerene acceptor (NFA) O-IDTBR. We furthermore present mod-

<sup>a</sup>A beta version of MARTINI 3.0 (v3.0.b.3.2) is available at <http://cgmartini.nl/index.php/martini3beta>; in this thesis, the final to-be-published version has been used (v3.0.b.4.27).

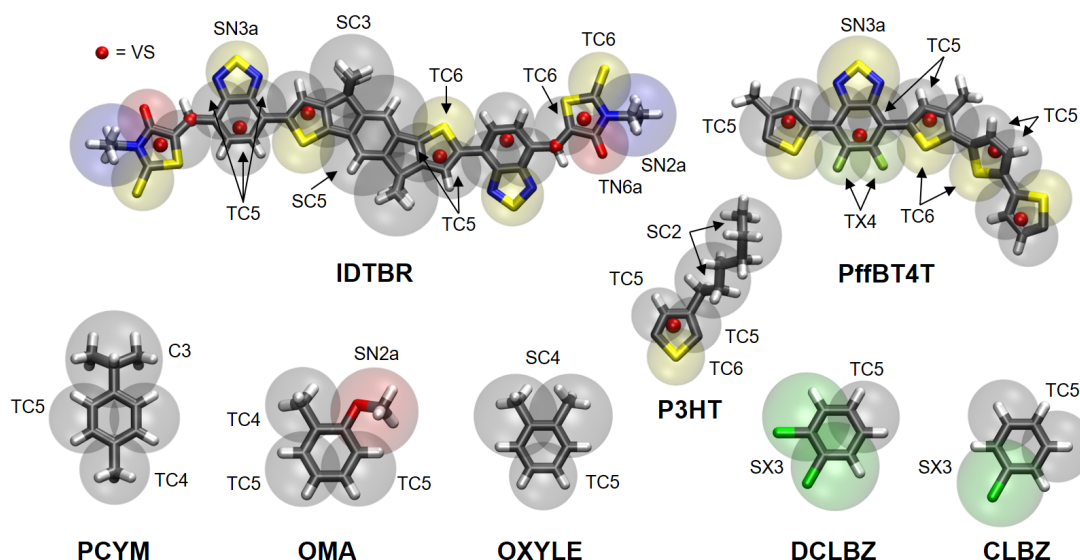


Figure 4.1: Mapping and MARTINI bead types for the molecular systems used in this work visualised on top of the atomistic structures (grey: carbon, white: hydrogen, red: oxygen, blue: nitrogen, yellow: sulphur, bright green: chlorine, yellowish green: fluorine). For clarity, longer alkane side-chains are not shown - each of the four octyl side-chains on O-IDTBR are modelled by two SC2 beads, and each of the two branched 2-octyldodecyl side-chains per PffBT4T-2OD monomer are modelled by six SC2 beads. Virtual sites (VS) are marked with small, opaque red beads. The beads are not visualised to scale.

els of five organic solvents commonly used for solution processing of organic functional materials: chlorobenzene (CLBZ), *o*-xylene (OXYLE), *o*-dichlorobenzene (DCLBZ), *o*-methylanisole (OMA), and *p*-cymene (PCYM). The latter two have been developed for this work, as the use of non-halogenated or "green" solvents<sup>235,236</sup> has proven beneficial for optimal morphology evolution in the material blends considered herein,<sup>202,223</sup> whereas the former three have been developed previously.<sup>237</sup> Additionally, we have used an updated MARTINI 3.0 version of the MARTINI 2.2 PCBM model<sup>133,238</sup> in order to compare the NFA systems to their fullerene analogues.

All of the presented models include aromatic ring-systems, and the procedure presented in Ref. 237 thus forms the basis for this work. In the MARTINI spirit, the models have been parametrised using a combined bottom-up and top-down approach, with the bonded parameters being determined by mapping the bead-representation onto atomistic models and the bead types (in essence, the non-bonded parameters) being chosen to reproduce the liquid densities of the molecules as well as their free energies of transfer between water and 1-octanol. In addition, the solvent accessible surface area (SASA) method has been used to compare the effective sizes of the coarse-grained models to the atomistic models in cases where the densities were not ideal for this. The chosen mapping and the final bead types for the models can be seen in Fig. 4.1. To allow the reader to manually inspect the models and use them in further work, they have been made available at doi:10.11583/DTU.c.5254236.



### 4.2.1 Mapping

The CG models were mapped onto our atomistic (OPLS-AA based) models for P3HT, PffBT4T-2OD, and O-IDTBR and onto OPLS-AA models by Coleman *et al.*<sup>114</sup> for the organic solvents using a centre of geometry (COG) bead representation. The general parametrisation procedure of the atomistic models is described in Chapter 3, Section 3.6.1. The CG Builder tool by J. Barnoud<sup>239</sup> was used to visualise the mapping process and generate the necessary mapping files describing which atoms should be described by which bead. To obtain a statistically representative mapping, the CG bonded parameters were determined as averages over 100 ns atomistic trajectories using the `gmx traj`, `gmx distance`, and `gmx angle` programs. The bonded parameters of the atomistic models were validated by density functional theory (DFT) calculations at the B3LYP/6-311++G(d,p) level of theory, and the O-IDTBR model is furthermore validated from the experimentally determined crystal structure.<sup>150,193</sup> A detailed description of the parametrisation of the atomistic models can be found in Chapter 3 and Paper II. Here, we focus on the further validation of the MARTINI models.

#### P3HT

A MARTINI 2.2 model for P3HT has previously been published,<sup>133</sup> but we have here made significant updates to this model. First of all, a thiophene monomer is now mapped in a COG basis with three tiny beads instead of a centre of mass (COM) basis with three small beads. Secondly, the torsion potential has been updated to reproduce the experimental persistence length (see below Section 4.2.3 as well as Chapter 3, Section 3.2.3). Constraints are used between beads in the rigid, aromatic backbone monomers, which are connected through harmonic bonds via virtual sites placed at the bead COG (cf. Fig. 4.1). The side-chains are modelled by two small beads connected by an harmonic bond, one of which is connected to the backbone with an harmonic bond. When mapping the bead representation directly onto atomistic polymers, short interbead distances can arise for conjugated ring-systems, which has been shown to be problematic for the balance of the MARTINI non-bonded interactions, causing overly attractive interactions in regions of high bead density.<sup>240</sup> These non-bonded interactions are mainly parametrised against single monomer units or residues of these in which the terminal hydrogens in the COG basis serve to keep the CG bead density sufficiently low, but with these not being present in the backbones of conjugated polymers, it is often necessary to manually elongate the distances between beads. Here, it was found that increasing the mapped interbead distances by 20 % in the constrained triangle representing thiophene (the intermonomer distances were kept equal to the mapped value) improved both the simulated 3HT (monomer) liquid density and the P3HT crystal density to relative deviations from the experimental values of 8 % and 5 %, respectively (using the final bead types, see Section 4.2.2). The final P3HT model is available from doi:10.11583/DTU.c.5254236.

#### PffBT4T-2OD

A procedure similar to that for P3HT was used, also treating inter-unit connections through harmonic bonds between virtual sites and elongating the interbead distances in the constrained ring-systems by 20 % (including the 5,6-difluoro-2,1,3-benzothiadiazole, ffBT, unit). The thiophene units are represented as for the P3HT model (although with small differences in interbead distances between the side-chain substituted thiophene units and the non-substituted ones), and the ffBT unit is represented by five constrained beads kept in plane with impropers. The thiadiazole part is described by a small bead and the difluoro-substituted benzene by four tiny beads with a virtual site at the COG



of these (cf. Fig. 4.1) through which it is bonded to the neighbouring thiophenes with harmonic potentials. The branched 2-octyldecyl (2OD) side-chains are modelled by six small beads. The final model can be found at doi:10.11583/DTU.c.5254236.

## O-IDTBR

Modelling fused, conjugated ring-systems with the MARTINI force field is challenging due to the constraints usually applied to ring-system constructions.<sup>237,240</sup> The O-IDTBR model represents a particularly complicated case with five fused ring-systems in its central IDT unit, and maintaining both the symmetry of the molecule as well as its terminal group's torsional freedom in the mapping while at the same time ensuring numerical stability of the model is not straightforward. To ensure symmetry, the central six-membered ring was mapped to two small beads, and the fused thiophenes were mapped with the same construction as isolated thiophenes to maintain transferability of the model. The side-chain linking carbons and the first carbon of each side-chain were mapped to a small bead, and the whole construction of the indacenodithiophene (IDT) central unit was constrained in a grid of triangles with impropers to keep it planar. Some of the interbead distances are borderline too short, but due to the ring-systems in the IDT unit being fused, it is not possible to elongate these bonds post-mapping without elongating the whole molecule. The BT units were mapped as three tiny beads (the benzo-part) and one small bead (the thiadiazole-part), all constrained, and the 3-ethylrhodanine (RH) terminal groups were mapped to three constrained tiny beads and one small bead (cf. Fig. 4.1), with the small bead (representing the ethylamine part) being bonded to the rhodanine ring-system through harmonic potentials and an angle slightly out of plane of the rhodanine to mimic the orientational effect of the ethyl group. Similar to the polymer systems, the inter-unit links were handled through harmonic bonds between virtual sites. The RH-BT link in O-IDTBR goes through an ethylene linker, which was assigned a virtual site to allow torsional rotation of the RH unit around an axis approximately along the same bond as in the atomistic model. The remaining seven carbons in each of the octyl side-chains (the first carbon is included in the small bead representing the side-chain linker) were modelled by two small beads, i.e. sharing seven heavy atoms between two beads, each bead with a size corresponding to a 3-to-1 mapping. Despite the mapping being off by one carbon, this was deemed to be the best choice in order to ensure consistency with the alkane side-chain descriptions of the polymers in terms of bead types and sizes. The bond lengths between the backbone and the first side-chain beads were slightly elongated to account for this, and the volume of the model was validated by comparing the unit cell parameters of the experimental crystal structure<sup>150</sup> to those of the atomistic and coarse-grained models (simulated under the same conditions as the experiment), yielding relative deviations of +2.5 % and -7.3 %, respectively. SASA calculations showed that the difference in volume between the atomistic and coarse-grained were almost exclusively related to the side-chain construction.

As a side note, the O-IDTBR model described here showed substantial numerical instabilities for in trial NVT runs, and surprisingly it was found that these could be completely eliminated by switching to the Berendsen thermostat instead of the V-rescale thermostat.<sup>b</sup> As of now, we have no further explanation of this, but we speculate that

---

<sup>b</sup>The problem occurred for several versions of GROMACS at two different systems. It appears to be related to the specific O-IDTBR model used, as other molecules do not, to our knowledge, suffer from the same problems, but it might also hint towards some implications for the use of the V-rescale thermostat with MARTINI in general.

extended, fused ring-systems modelled with grids of triangular constraints and/or exotic virtual site constructions could be the cause of this instability. However, the described construction is kept for the final MARTINI model for O-IDTBR, and we hence note that it might not be numerically stable with other thermostats than the Berendsen. The model can be found at doi:10.11583/DTU.c.5254236.

## Solvents

The models for the organic solvents used herein were mapped directly onto the OPLS-AA atomistic models<sup>114</sup> in a COG basis, and the bead sizes and interbead constraint lengths were, guided by SASA calculations, slightly refined to reproduce the liquid densities of the solvents. Note that all of the solvents are modelled using only constraints between beads and, in the case of PCYM and OMA, an improper dihedral to keep all four beads in plane.

### 4.2.2 Free energies of transfer

After having determined suitable mappings of the compounds, the bead types were chosen as to reproduce the free energies of transfer between water and 1-octanol. The free energies of transfer were calculated using the standard alchemical procedure of gradually turning off interactions between the solute and the solvent through intermediate  $\lambda$ -states and analysing the associated free energy changes with the multi-state Bennett's Acceptance Ratio (MBAR) formalism<sup>241</sup> as implemented in the `alchemlyb` Python package.<sup>242</sup> Doing this for two different solvents will allow one to connect the two alchemical, thermodynamic paths through the vacuum state of the solute and thus calculate the free energy change upon going from one solvent to the other. In terms of experimental data, water-octanol partitioning coefficients LogP are by far the most accessible due to their importance in drug discovery. These can be related to the free energy of transfer  $\Delta\Delta G_{W\rightarrow OCO}^0$  between water (W) and 1-octanol (OCO) at standard conditions as

$$\log P = \frac{-\Delta\Delta G_{W\rightarrow OCO}^0}{2.303RT} = \frac{\Delta G_{OCO}^{\text{sol}} - \Delta G_W^{\text{sol}}}{2.303RT}, \quad (4.1)$$

where  $\Delta G_W^{\text{sol}}$  and  $\Delta G_{OCO}^{\text{sol}}$  are the solvation free energies of a given solute in water and 1-octanol, respectively, and  $RT$  is the product of the gas constant and temperature. It is worth noting that a hydrated 1-octanol phase contains approximately 20 mol% water in partitioning experiments, and we thus simulate the 1-octanol phase accordingly (the water phase is almost completely pure). The simulated values for the full range of solvents and for the individual units that the donor and acceptor compounds consist of are compared to the experimental values in Table 4.1 for the final choices of bead types (as visualised in Fig. 4.1). As seen, the correspondence to experiment is good with most of the simulated values being within a couple of kJ/mol of the experimental values. The choices of bead types are a compromise between quantitative agreement of the free energies of transfer and the transferability of the model in terms of that specific substituents and functional groups should, in most cases, be able to be described by specific bead types, thus allowing for the use of chemical intuition in the building of MARTINI models. For example, the fluoro-substituted carbons in ffBT were chosen to be TX4 beads, as it was deemed important for the transferability and user-friendliness of the force field to maintain the logical X2-X3-X4 relationship of the halogen bead types for Br-Cl-FI containing compounds (i.e. more polar halogen beads for more electronegative halogens, cf. e.g. the use of SX3 in chlorobenzene).

Table 4.1: Comparison of experimental logP values and their corresponding free energies of transfers to the calculated free energies of transfer of the water-to-octanol thermodynamic path.

compound	MARTINI model	logP	$\Delta\Delta G_{W\rightarrow OCO}^{exp.}$	$\Delta\Delta G_{W\rightarrow OCO}^{MARTINI}$
<i>o</i> -methylanisole	SN2a-TC5 <sub>2</sub> -TC4	2.7 <sup>243</sup>	-15.4	-17.4
chlorobenzene	SX3-TC5 <sub>2</sub>	2.9 <sup>244</sup>	-16.6	-15.5
<i>o</i> -xylene	SC4 <sub>2</sub> -TC5	3.1 <sup>243</sup>	-17.7	-19.8
<i>o</i> -dichlorobenzene	SX3 <sub>2</sub> -TC5	3.4 <sup>243</sup>	-19.4	-18.3
<i>p</i> -cymene	C3-TC5 <sub>2</sub> -TC4	4.1 <sup>243</sup>	-23.4	-25.8
3-ethylrhodanine* <sup>a</sup>	TC6 <sub>2</sub> -TN6a-SN2a	-1.2 <sup>†</sup>	6.9	6.9
thiophene* <sup>d</sup>	TC4-TC5 <sub>2</sub>	1.8 <sup>243</sup>	-10.2	-11.7
2,1,3-benzothiadiazole* <sup>d</sup>	TC5 <sub>3</sub> -SN3a	2.0 <sup>245</sup>	-11.4	-11.0
5,6-difluoro-BT* <sup>d</sup>	TC5 <sub>2</sub> -TX4 <sub>2</sub> -SN3a	2.0 <sup>†</sup>	-11.4	-12.9
benzene	TC5 <sub>3</sub>	2.1 <sup>243</sup>	-12.0	-12.5
hexane	SC2 <sub>2</sub>	3.9 <sup>243</sup>	-22.3	-19.0

\*Using bonded parameters identical to those in d) donor oligomers and a) acceptor molecules;

<sup>†</sup> predicted XLogP3 values<sup>246</sup>

### 4.2.3 Torsions

Especially for the polymers, an accurate description of the torsional potentials is critical, as they greatly influence the structural properties of these. The torsional potentials are usually determined from density functional theory (DFT) or other quantum chemical calculations, but even small variations in the energetic profile arising from different choices of methods, functionals, and basis-sets can have a large impact on the behaviour of polymers in solution in some cases. P3HT represents a notoriously difficult case, as the local minima of the torsion are very close in energy and, due to the non-parallel intermonomer bonds, correspond to different degrees of bending of the backbone. We have thus based our choice of computational level of theory used to describe the torsion on its ability to reproduce the experimental persistence length of P3HT. The persistence length  $l_p$  of highly regio-regular (RR > 97 %), low number-average molar mass ( $M_n = 7.4$  kg/mol) P3HT with a low poly-dispersity index (PDI = 1.08) was determined to be  $l_p = 2.9 \pm 0.1$  nm in dichlorobenzene.<sup>188</sup> This sample corresponds very well to the "idealised" P3HT 48mers used in the simulations with PDI = 1.00,  $M_n = 8.1$  kg/mol, and RR = 100 %. Using the MARTINI 2.2 P3HT construction and torsional profile, the simulated persistence length was 8.5 nm, whereas it for the new MARTINI 3.0 model developed herein was determined to be 3.9 nm when using a torsional profile for 2,2'-bithiophene derived from wB97X-D/6-311++G(d,p) and 3.2 nm when using a torsional profile derived from MP2/aug-cc-pVTZ. The great correspondence of the persistence length calculated using MP2/aug-cc-pVTZ torsions to the experimental persistence length strongly motivates the use of these. For consistency, this MP2/aug-cc-pVTZ torsional profile was used for the thiophene-thiophene torsions in the PffBT4T model as well, whereas the MP2/aug-cc-pVTZ level of theory was also to determine the ffBT-thiophene torsional profiles.

Due to the size of the central IDT unit in IDTBR, using the MP2/aug-cc-pVTZ level of theory to calculate the IDT-BT torsion is not feasible, and we thus applied the wB97X-D/6-311++G(d,p) level of theory to calculate this and the RH-BT torsional

profiles.

Finally, it should be noted that the non-bonded interactions between beads in neighbouring ring-systems are consistently excluded in the models presented herein, meaning that the quantum chemically derived torsional profiles can be used "directly" after conversion to a Ryckaert-Bellemans functional form (cf. Eq. 2.81).

### 4.3 Solvent evaporation simulations

With the parametrised models at hand, initial systems for solvent evaporation simulations were prepared as follows:

- P3HT:O-IDTBR: A 1:1 weight ratio of 210 P3HT 48mers and 1279 O-IDTBR molecules were randomly inserted in a box of size 25x25x136 nm (using `gmx insert-molecules`) and solvated (using `gmx solvate`), yielding concentrations of 20 mg/ml of each component (40 mg/ml total), which corresponds to the concentration used for slot-die coating of the thin-films used in the OPV devices. In total, 15 different types of solvent evaporation runs were computed for this material system, namely at three different processing temperatures (298 K, 333 K, and 363 K) for each of the five different solvents (OMA, CLBZ, OXYLE, DCLBZ, and PCYM).
- PffBT4T-2OD:O-IDTBR: A 1:1 weight ratio of 140 PffBT4T-2OD 12mers and 1342 O-IDTBR molecules were randomly inserted in a box of size 25x25x142 nm, yielding concentrations of 20 mg/ml of each component (40 mg/ml total). For this material system, only three solvents were used (CLBZ, OXYLE, and PCYM), and the three different processing temperatures were shifted up compared to the P3HT-based systems to 333 K, 363 K, and 393 K due to the lower solubility of PffBT4T-2OD. This yields a total of nine different types of solvent evaporation runs (plus an extra at 298 K for CLBZ).
- Donor:PCBM: In order to compare the above NFA systems to their fullerene analogues, 1:1 weight ratio systems at 40 mg/ml of 210 P3HT 48mers and 1862 PCBM molecules as well as 140 PffBT4T-2OD 12mers and 1954 PCBM molecules, respectively, were prepared in CLBZ and simulated at the same temperatures as for the respective NFA systems. This yields three P3HT-based types of solvent evaporation runs as well as four PffBT4T-2OD-based ones.

Before evaporating any solvent, the systems were equilibrated for 0.5 ns in an NVT ensemble and for 4.0 ns in an NPT ensemble. After this, the evaporation run was started, evaporating 1.25 % of the remaining solvent every step randomly throughout the extent of the box at each step. When reaching the near-linear regime, which is defined as removing less than 0.0125 % of the initial amount of solvent each step, the evaporation was continued linearly until a dry film was obtained, amounting to a total of 264 steps. At each step, the system was equilibrated for 0.5 ns in an NVT ensemble (Berendsen thermostat,  $\tau = 2$  ps) and for 4.0 ns in an NPT ensemble (Berendsen thermostat,  $\tau = 2$  ps, and Berendsen barostat,  $\tau = 4$  ps) before undergoing a production run of 3.0 ns in an NPT ensemble (Berendsen thermostat,  $\tau = 2$  ps, Parrinello-Rahman barostat,  $\tau = 15$  ps), adding up to a total evaporation time of around 2  $\mu$ s. A 20 fs time step was used for the leap-frog integrator, and semi-isotropic pressure coupling was applied with a pressure

of 1 bar, a compressibility of  $4.5 \cdot 10^{-5} \text{ bar}^{-1}$  in the z-direction, and one of  $0.0 \text{ bar}^{-1}$  in the x- and y-directions to facilitate shrinking of the box only in the z-direction, hence mimicking the conditions in a drying thin-film. No charges were present in the systems, meaning that the electrostatics could be ignored. The van der Waals interactions were treated with the potential-shift Verlet scheme with a cut-off of 1.1 nm as recommended with MARTINI.

### 4.3.1 Methodological considerations

#### Run parameters

Some numerical instabilities were experienced during the trial solvent evaporation runs, which caused a not insignificant number of crashes per run. It was found that specifying the following settings in the run parameter ( `.mdp` ) file suppresses these instabilities:

`nsttcouple = 10` and `lincs-order = 6`. The former explicitly sets the frequency of temperature coupling to every 10 steps instead of the default, which is the same value as the neighbour list update frequency, `nstlist`. `nstlist` is usually set automatically by the program to 20 or more to optimise performance, but only updating the temperature coupling every 20 steps or less resulted in the simulations blowing up. Setting `lincs-order = 6` specifically increases the numerical stability of the virtual site constructions in large time step simulations. Furthermore, the `-normvsbds` flag has to be passed to `gmx grompp` for simulations with models where virtual sites are bonded to each other in order to keep them bonded.

#### Interface effects

This solvent evaporation scheme is similar to ones previously published (see Refs. 247 and 133 and Paper II), but it should be noted that it is a simple scheme ignoring potentially important effects related to vertical mass transfer of solvent up towards the air interface of drying films. This effect can potentially play a role in the morphological evolution, and for example skinning effects, i.e. the formation of a dry layer of solutes at the air interface trapping residual solvent in the film, are well known experimentally and have also been shown in simulations.<sup>220</sup> Whereas these air-interface effects are likely to be more important for thick films requiring solvent mass transfer over larger distances, alignment effects due to the substrate interface become increasingly important for thinner films. With the solvent evaporation scheme applied herein, we aim to simulate the bulk morphology evolution of drying OPV thin-films, which are usually more than 300 nm thick when slot-die coated.

#### Evaporation rates

Although it is in principle possible to consider differences in evaporation rate of different solvents in the framework of the applied solvent evaporation scheme, we have here chosen to keep the evaporation rate equal for all solvents in order to keep the drying times constant and thus allowing us to analyse the effects of specific solvent-solute interactions and their resulting effects on the aggregation behaviour of the donor polymers and acceptor molecules. Further work considering these effects is ongoing.

#### Oligomer lengths

The mass-average molar mass,  $M_w$ , of the P3HT 48mers and PffBT4T-2OD 12mers used in the simulations are 8.1 kg/mol and 12.7 kg/mol, respectively, which are approximately an order of magnitude lighter than the ones of the batches used for experiments (60.2 kg/mol and 118.0 kg/mol, respectively). First of all, it is not feasible to simulate a large number of polymer strands of this length, and secondly, the length of an oligomer strand

in a simulation should preferably not exceed the side length of the box in order for it to not interact with itself. This constraint is, however, not fulfilled for the z-dimension in the solvent evaporation simulations for the more dry stages, but the artificial self-interactions potentially arising from this are expected to be negligible due to the alignment effect resulting from the anisotropic shrinkage of the box during evaporation as well as the large number of oligomers and molecules in the blends.

#### Computational cost

Even with the coarse-grained models employed here, simulating solution processing of the blends from initial concentrations corresponding to the experimental ones (20 mg/ml of each component) puts a constraint on the length scales we are able to simulate at a reasonable computational cost. Using the P3HT:O-IDTBR systems described above as examples, the simulation time of systems this size amounts to around 12,500 CPU hours for a 2  $\mu$ s evaporation run (including annealing and cooling runs), which add up to almost half a million CPU hours in total for all CG simulations presented in this chapter. Although longer evaporation times and more refined evaporation schemes including interface effects are desirable, the many processing parameter combinations explored herein limits us to studying the evolution of bulk morphologies.

## 4.4 Analysis methods

The main goals of this work are to a) aid the interpretation of experiments, b) make sense of and predicting macroscopic properties from a detailed understanding of atomic scale behaviour, and c) visualise blend, mesoscale structures to improve our understanding of domain formation. A framework for analysing MD simulations of organic solar cell blends (or, in practice, any type of material blends exhibiting phase separation) has thus been devised below, allowing one to follow the morphology evolution during post-deposition drying and annealing as well as to extract important structural parameters such as domain sizes, specific interface areas, and percolating pathways. The former two can aid the interpretation of (*in situ*) GISAXS experiments, and the latter two can be used to explain trends in the structure-property relationships of organic solar cells.

### 4.4.1 Close contacts

The evolution of the blends during the drying process is followed by looking at the number of close contacts formed between donor oligomers, between acceptor molecules, and between donors and acceptors as a function of time using the `gmx mindist` program. A close contact is defined as two backbones coming within 0.6 nm of each other, i.e. with a high probability exhibiting a  $\pi$ -stacking interaction, utilising the virtual sites of the donor and acceptor models as evaluation points for this analysis. By extracting the number of close contacts between the different components for every  $n$ 'th step of a solvent evaporation simulation, their aggregation behaviour at different temperatures and concentrations and in different solvents can be studied *in situ*. The number of close contacts are normalised with respect to simulations of neat films and relative number of contacts in interface regions as follows: taking a P3HT:O-IDTBR blend as an example, the maximum number of P3HT $\leftrightarrow$ P3HT contacts is given by the number of contacts in a dry, neat P3HT thin-film (processed from CLBZ at 333 K; all other simulation parameters are identical to the blend simulations) normalised to the number of analysis points. The maximum number of O-IDTBR $\leftrightarrow$ O-IDTBR contacts is computed similarly, whereas the maximum number of P3HT $\leftrightarrow$ O-IDTBR contacts is computed as the number

of interface contacts in a blend (processed from CLBZ at 333 K) normalised to the number of interface beads. This essentially corresponds to assuming that every donor and acceptor is part of an interface, i.e. randomly distributed in a completely intermixed blend. Figures visualising the results of this analysis are presented in Section 4.5.1.

#### 4.4.2 Spatial discretisation

Several of the analyses presented are based on spatially discretised versions of the dry films (both as-cast and annealed). The spatial discretisation scheme is implemented in Python 3 and makes use of the `MDAnalysis`<sup>248,249</sup> package to import the MD morphologies. It spans a grid of cubic voxels of a given side length across the system and assigns a phase to the  $i$ 'th voxel depending on the relative number of donor (D) and acceptor (A) particles that it encloses ( $n_{D,i}$  and  $n_{A,i}$ , respectively, which are determined using the `matplotlib.path`<sup>250</sup> module). The phases are assigned as follows:

- Donor phase:  $\frac{1}{3}n_{D,i} \geq n_{A,i}$
- Acceptor phase:  $\frac{1}{3}n_{A,i} \geq n_{D,i}$
- Mixed phase:  $0 \neq \frac{1}{3}n_{D,i} < n_{A,i} \wedge 0 \neq \frac{1}{3}n_{D,i} < n_{A,i}$
- Empty phase:  $n_{D,i} = 0 \wedge n_{A,i} = 0$

As a general guideline, the voxel side length should be chosen to be larger than the maximum bond length and double the usual van der Waals (vdW) radii of the particles in the MD model to ensure that most voxels contain more than one particle. In this work, a voxel side length of 0.5 nm was thus chosen, as it respects these guidelines for the MARTINI beads and at the same time provides a decent resolution for the box sizes of the dry films (ca. 50x50x15 voxels). However, using a small voxel size means that a few empty voxels can be present in areas of low density, which can have unwanted, artificial effects on analyses relying on the connectivity of phases or voxels. To mitigate this, a nearest-neighbour search algorithm was implemented. It reads every  $j$ 'th empty voxel and assigns it to either a donor, acceptor, or mixed (M) phase based on the number of (non-diagonal) neighbouring voxels  $m_{k,j}$  with a respective phase  $k = D, A, M$  using the following rules:

- Donor phase:  $m_{D,j} > 3$
- Acceptor phase:  $m_{A,j} > 3$
- Empty phase:  $\sum_k m_{k,j} \leq 3$
- Mixed phase: All other

In Fig. 4.2, examples of 3D discretised morphologies before and after assigning phases to empty voxels are presented. Note that the PBC are accounted for and that all voxels hence are evaluated based on six nearest-neighbours.

We stress that allowing the algorithm to recognise both mixed and empty phases can be crucial for some analyses; the former especially for voxel sizes that are significantly larger than the characteristic bond lengths and the latter especially for voxel sizes on the order of the bond lengths or for systems where empty pores are expected.



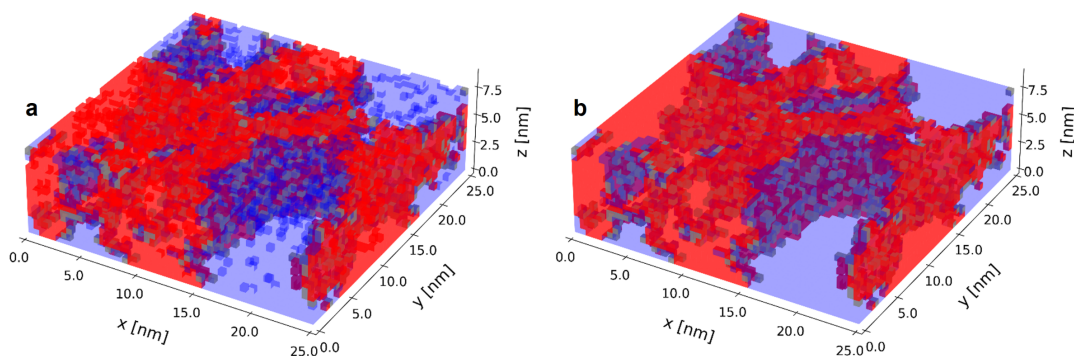


Figure 4.2: Example visualisations of 3D discretised P3HT:O-IDTBR morphology, where **a)** is before and **b)** is after applying the nearest-neighbour search-based voxel filling routine. The red voxels are donor phases, the blue voxels are acceptor phases, and the grey voxels are mixed phases.

#### 4.4.3 Domain sizes and purity

The spatial discretisation scheme described above allows the use of image processing algorithms to analyse the morphologies. Here, a fast-Fourier transform (FFT) algorithm from the PoreSpy<sup>251</sup> package is employed to calculate the pair correlation function of the morphologies. It is possible to perform this analysis in 3D, but due to the small thickness ( $z$ -dimension) of the dry film morphologies presented herein compared to their  $x$ - and  $y$ -dimensions, a 3D analysis will be skewed and limited. Instead, we present pair correlation functions averaged over  $xy$ -slices, which makes sure that the full size of the simulation box is considered, although only in a pseudo-3D fashion.

The pair correlation function is defined as the probability that two sites picked at random and separated by a distance  $r$  will be of the same type. At long distances, it will probe the bulk blend composition and thus statistically go towards the volume fraction of a given phase, whereas it at shorter distances is indicative of the size and purity of the domains. It is thus possible to infer a characteristic length of a phase, i.e. an average domain size, from the distance at which it first drops to the volume fraction of that given phase.<sup>252</sup> In Fig. 4.3, an example of a calculated set of pair correlation functions are presented for a P3HT:O-IDTBR system with indications of the respective volume fractions and domain sizes. Theoretically, these two domain sizes should coincide for a binary system, but as some voxels are assigned to a mixed phase, a small deviation is expected. The domain sizes presented in Section 4.5.2 are hence arithmetic averages of the donor and acceptor domain sizes.

As mentioned, qualitative tendencies of the domain purity can also be extracted from the pair correlation functions: the purer the domains (and equivalently the sharper the interface), the higher the initial value of the pair correlation function. This follows directly from its definition: the shortest distance will be that to the neighbouring voxels, and if these are all of the same phase as the voxel in question, the pair correlation will be 1, whereas it will decrease with an increasing number of different neighbouring phases. These results are presented and discussed in Section 4.5.2.



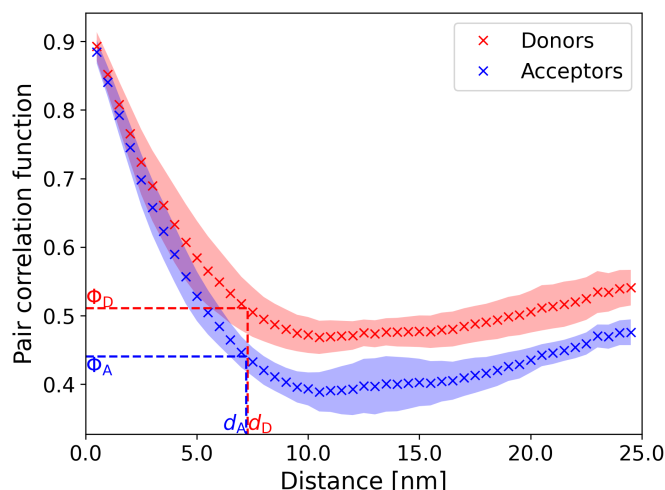


Figure 4.3: Example of a set of pair correlation functions and how to infer the domain size  $d = \frac{1}{2}(d_D + d_A)$  from this and the donor and acceptor volume fractions ( $\Phi_D$  and  $\Phi_A$ , respectively). The shaded areas mark the standard deviation and the x's the mean values of the pair correlation function for the collection of xy-slices.

#### 4.4.4 Percolating pathways and mobility simulations

The charge extraction efficiency is an important parameter in photovoltaic devices. It depends on a multitude of structural and electronic parameters, but most importantly on whether pathways from the generation site to the respective electrodes are present. The simplest way of defining such a percolating pathway in a spatially discretised morphology is by checking if two opposite box boundaries are connected through a continuous path of nearest neighbour voxels of the same phase. Whereas this method can be very useful, especially for interpreting experimental images or tomograms of limited resolution, it does not directly consider the molecular structure of the phases. In the case of organic semiconducting materials, the molecular structure and packing are decisive, as the charges travel intramolecularly in the conjugated backbones and jump between neighbouring polymers or molecules via close intermolecular  $\pi$ - $\pi$  interactions. The full (coarse-grained) molecular resolution is utilised in the kinetic Monte Carlo (kMC) simulations presented in Section 4.5.3, where time-of-flight mobilities are simulated using the ToFeT program.<sup>253,c</sup> Here, the virtual sites (cf. Fig. 4.1) are used as evaluation points (with an extra evaluation point added in the COG of the central benzene unit of O-IDTBR as well as for each triangular construction in the PCBM cage). All intramolecular connections are generated as having a coupling strength of 1 eV, whereas intermolecular coupling strengths are assigned as an exponentially decreasing function of the distance  $r_{ij}$  between the two evaluation points. Only intermolecular connections with coupling strengths  $> 10^{-6}$  eV are considered (ca. for  $r_{ij} < 1$  nm). The hopping rates between sites are determined using semi-classical Marcus theory with a site energy of 0 eV for all sites and a reorganisation energy of 0.1 eV. The time-of-flight hole mobilities are then simulated for the donor phases and the time-of-flight electron mobilities for the acceptor phases at a temperature of 300 K and from charges generated only at interfaces between the donors and acceptors. We stress that the choices of equal

<sup>c</sup>ToFeT is an in-house, open-source software package from the Department of Physics, Imperial College London; see [code.google.com/archive/p/tofet](https://code.google.com/archive/p/tofet) and Ref. 253.

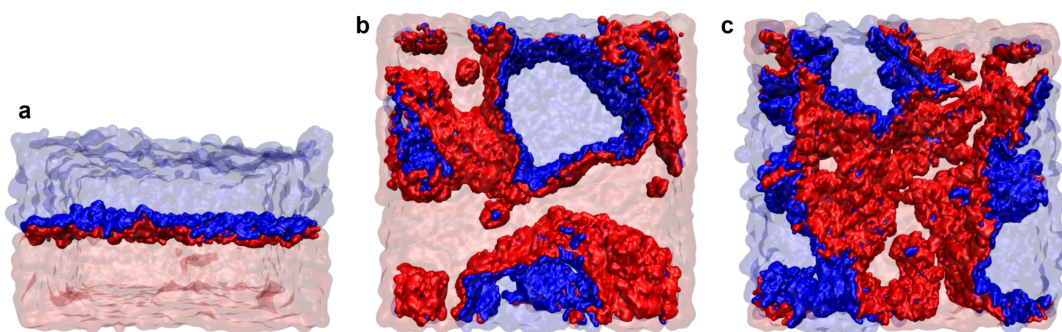


Figure 4.4: Example visualisation of donor:acceptor interfaces in **a)** a P3HT:O-IDTBR bilayer with  $\gamma = 0.24 \text{ nm}^{-1}$ , **b)** a P3HT:PCBM bulk heterojunction with  $\gamma = 0.37 \text{ nm}^{-1}$ , and **c)** a P3HT:O-IDTBR bulk heterojunction with  $\gamma = 0.54 \text{ nm}^{-1}$ . The red phases are donors, the blue phases are acceptors, the opaque parts mark the beads within 0.6 nm of an interface, and the transparent parts mark the bulk phases.

coupling strengths and energies represent a simplified approach and that it can only be used to evaluate the relative carrier mobilities of the simulated morphologies.

In the case of high-throughput simulations, simpler approximations of the interpenetrating networks might be desirable. As a quick estimate of the fraction of donor and acceptor units that are part of a percolating pathway, we generate a spatial discretisation of the simulation boxes where all voxels containing a donor virtual site are assigned to a donor phase and all voxels containing an acceptor virtual site (as above, an extra point is added in the COG of the central benzene unit of O-IDTBR as well as for each triangular construction in the PCBM cage to ensure intramolecular connections) are assigned to an acceptor phase. The two phases are assigned separately, meaning that a given voxel is not necessarily exclusively assigned to only one phase. The voxel side length is kept as 0.5 nm, ensuring that intramolecular pathways and close intermolecular contacts are preserved as nearest-neighbour voxels. This spatial discretisation thus (approximately) only considers charge transport pathways in conjugated backbones and between closely interacting oligomers or molecules. Using `scipy.ndimage`,<sup>254</sup> a 3D image processing algorithm, the connectivity of all voxels of a given phase is evaluated. A connection is assigned between nearest-neighbour (including diagonal) voxels of the same phase, and if such a connected domain extends across the simulation box (i.e. to two opposite surfaces), all voxels in that domain are considered part of a percolating pathway. By relating all such voxels to the total number of voxels of a given phase, the percolation fraction can be computed. These are presented in Section 4.5.3.

#### 4.4.5 Specific interface areas

The charge separation process in organic solar cells, i.e. the dissociation of excitons into free charges, happens at the donor:acceptor interfaces, and the specific interface area of a bulk heterojunction thus represents an important measure for coupling the morphology to the properties of devices. Whereas other analyses in literature have made use of spatially discretised morphologies to infer specific interface areas from the voxel interfaces,<sup>255</sup> we have here utilised the full resolution of the CG model (i.e. *not* the spatially discretised morphologies). The specific interface area can, from a geometrical perspective, be difficult to define on a nanoscale with interpenetrating molecular and polymeric phases, but

as the electronic coupling between donors and acceptors at interfaces is a distance- and orientation dependent parameter ultimately relying on wave-function overlap, considering the molecular shapes represents a more physically motivated approach. The double cubic lattice method by Eisenhaber *et al.*,<sup>256</sup> as implemented in the `gmx sasa` program, has been used to evaluate the surface area  $A_k$  of a given phase  $k$  which is accessible to a spherical probe of radius 0.191 nm (corresponding to the vdW-radius of a T-T bead interaction). By doing this for each phase separately (yielding  $A_D$  and  $A_A$ ) and for both phases together (yielding  $A_{D:A}$ ), the specific interface area  $\gamma$  can be calculated as

$$\gamma = \frac{1}{2} (A_D + A_A - A_{D:A}) V^{-1}, \quad (4.2)$$

where  $V$  is the volume of the system. The specific interface areas for the full set of systems can be found in Section 4.5.4, and in Fig. 4.4, example visualisations of interfaces in different systems are shown.

#### 4.4.6 Crystallinity and crystallite sizes

Quantifying crystallinity and crystallite sizes in MD morphologies is not straightforward, but as especially crystallite sizes are readily available from simple analyses of GIWAXS spectra, it would be beneficial to be able to directly compare simulation and experiment. Inspired by Lee, Pao, and Chen,<sup>257</sup> we have used a formalism based on second order Legendre polynomials to probe the local order of the donor phase and quantify its crystallinity. Commonly used in the field of liquid crystals, the local order parameter can for the purposes herein be defined as

$$\langle P_2(r) \rangle_i = \frac{1}{2} \langle 3 \cos^2 \Theta_{ij} - 1 \rangle_r = \frac{1}{2N_r} \sum_{j=1}^{N_r} 3 \cos^2 \Theta_{ij} - 1, \quad (4.3)$$

where  $\Theta_{ij}$  is the angle between the normal to the plane spanned by a given monomer (or generally a flat residue)  $i$  and the corresponding normal vector of the  $j$ 'th monomer in a collection of  $N_r$  monomers within a sphere of radius  $r$  surrounding monomer  $i$  (cf. Fig. 4.5a and inset in Fig. 4.6a). The brackets  $\langle \rangle$  signify that the local order parameter is an average quantity. Usually, Eq. 4.3 will be evaluated with the subscript  $i$  denoting a global director, e.g. the z-axis or a field, but in a bulk heterojunction where crystallites can have any orientation and where one is mainly interested in the local order, the director should be chosen to reflect this, e.g. by being represented by the normal vectors of monomers.

In Fig. 4.5a, a non-averaged order parameter  $P_2$  is plotted as a function of  $\Theta_{ij}$ . As seen, it takes on values between 1.0 (i.e. parallel or anti-parallel vectors) and -0.5 (i.e. perpendicular vectors), which, respectively, corresponds to perfect face-on crystalline order and a type of perfect "negative" or edge-on crystalline order for an ensemble (not to be confused with the concepts of face-on and edge-on used in GIWAXS analysis, which are relative to the substrate). The average in Eq. 4.3 will be close to zero for an amorphous (isotropic) ensemble and will for ordered, semi-crystalline (smectic) phases or grains be somewhere between 0.5 and 1.0 (see Fig. 4.5b for an illustrative schematic). The local order parameter thus holds information about how aligned different polymer chains in a sample are, and by integrating a histogram of local order parameters, each evaluated at different monomers,  $i$ , from a chosen cut-off to 1.0, the degree of order

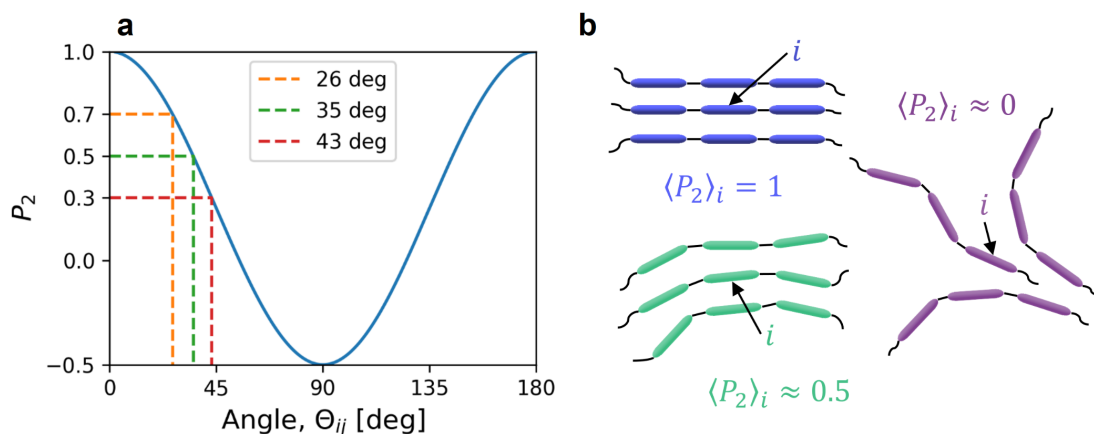


Figure 4.5: Schematics of **a)** the relation between a non-averaged order parameter and the angle between two normal vectors, and **b)** a perfectly crystalline phase (blue), an ordered phase (green), and an amorphous phase (purple).

(or, loosely speaking, the degree of crystallinity) in the sample can be estimated. Here, we have chosen  $\langle P_2(r) \rangle_i = 0.5$  as the lower limit for the definition of crystallinity, as it corresponds to an average deviation of 35 degrees from perfect (anti-)alignment (cf. Fig. 4.5a). In Fig. 4.6a, histograms for a range of different evaluation sphere radii are plotted, and the integrals for the respective local order parameters in the range  $[0.5, 1.0]$  are marked as shaded areas. The degree of crystallinity within a given evaluation sphere is then given as the ratio of this area,  $\int_{0.5}^{1.0} \langle P_2(r) \rangle_i$ , to the total area,  $\int_{-0.5}^{1.0} \langle P_2(r) \rangle_i$ .

From the above, it is clear that any quantification of crystallinity from an MD-generated morphology is dependent on the choice made for the cut-off, but it is a very useful tool to extract qualitative tendencies for different processing parameters. To allow a more direct comparison to GIWAXS measurements, the degrees of crystallinity inferred from the integrated local order parameters can be plotted against the evaluation sphere radius as seen in Fig. 4.6b. The average size of donor crystallites in the MD simulated thin-film can then be estimated as  $L_D = 2r$  for the radius at which the crystallinity drops below 50 %. These data are presented in Section 4.5.5 for the full set of systems studied. It should be noted that the degrees of crystallinity for the acceptor phases were not sufficiently large to perform a crystallite size analysis using the formalism described in this section.

## 4.5 Results

### 4.5.1 Close contacts

Following the procedure outlined in Section 4.4.1, the close contacts were analysed and shown as a function of drying, annealing, and cooling time for the P3HT:O-IDTBR systems in Fig. 4.7 and for the PffBT4T-2OD:O-IDTBR and donor:PCBM systems in Fig. 4.8. Here, the data sets are shown both as a function of solvent at each processing temperature and as a function of processing temperature in each solvent in order to uncover potential trends specific to either of these.

Looking at the P3HT:O-IDTBR systems (Fig. 4.7), it is first of all seen that the number of P3HT  $\leftrightarrow$  P3HT contacts rises steeply in the first couple of hundred nanoseconds of the drying process; this is due to aggregation. The initial P3HT concentration was 20

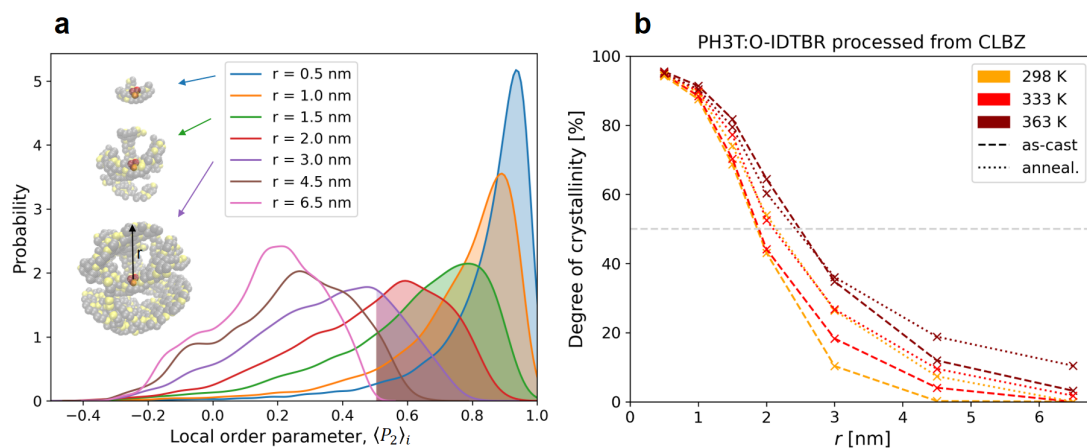


Figure 4.6: **a)** Illustration of the method behind the crystallinity analysis: example histograms of local order parameters evaluated at different monomers and for different evaluation sphere radii (inset) with the shaded areas representing the crystalline fractions of the sample for a given radius. The histograms are smoothed with a kernel density estimate for visualisation purposes only. **b)** Example of the determination of average donor crystallite sizes from the value of  $r$  at which the crystallinity degree goes below 50 % (grey, dashed line).

Table 4.2: Selected solubilities of P3HT, O-IDTBR, and PCBM in different solvents at different temperatures in units of mg/ml taken from Ref. 202.

$T_{\text{process.}}$	P3HT			IDTBR			PCBM		
	298 K	348 K	363 K	298 K	348 K	363 K	298 K	348 K	363 K
OMA	0.3	3.1	14.7	10.9	40.8	> 50			
CLBZ	18.3	> 100	> 100	45.8	> 80	> 100	69.0	> 80	> 100
OXYLE	1.2	76.3		18.9	98.9				

mg/ml, which, depending on temperature and molecular weight of the chains, is well below the experimental solubility limit in the chlorinated solvents (cf. Table 4.2),<sup>202,258</sup> and aggregation is thus not expected to be quite as pronounced as seen early in the drying process for CLBZ and DCLBZ. A strong aggregation behaviour is, however, expected for P3HT in OMA at all considered temperatures and for OXYLE at low temperatures.<sup>202</sup> Given that the models are parametrised based on free energies of transfer (cf. Table 4.1), it is no surprise that the trend from these is reproduced (i.e. quicker aggregation for more polar solvents), but it seems that some specific halogen-related interactions are not captured with the MARTINI force field despite the X-beads being parametrised exclusively for halogens. Secondly, it can be seen that the number of P3HT $\leftrightarrow$  P3HT contacts increases only slightly with increasing temperature, differing by a few percent for the as-cast films. During the annealing, the low-temperature processed films (298 K) form more P3HT $\leftrightarrow$  P3HT contacts, whereas it stays more or less constant during annealing of the high-temperature processed films (363 K). Regardless of solvent or temperature, the number of P3HT $\leftrightarrow$  P3HT contacts in the annealed and cooled films ends up at close to 80 % of the normalised, maximum number of contacts in a neat P3HT film (processed from CLBZ at 333 K), suggesting that the P3HT aggregation through  $\pi$ -stacking is not affected significantly by the presence of O-IDTBR in the blends.

Due to the high solubility of O-IDTBR in all of the solvents (cf. Table 4.2),<sup>202</sup> no particular aggregation is expected for these. As seen in Fig. 4.7, the number of O-IDTBR $\leftrightarrow$ O-IDTBR contacts evolves exponentially, more or less as the inverse of the solvent fraction, suggesting that the domain formation in P3HT:O-IDTBR films is exclusively controlled by aggregation of donor oligomers during the drying process. Lower polarity solvent and higher temperature keeps O-IDTBR slightly more solvated for slightly longer in the drying process as expected, but the number of O-IDTBR $\leftrightarrow$ O-IDTBR contacts end up at almost exactly the same values of 50 % of the normalised maximum (relative to a neat O-IDTBR film processed from CLBZ at 333 K) for all solvents and temperatures after only a slight increase during annealing.

Regarding the number of P3HT $\leftrightarrow$ O-IDTBR contacts, there is in general a clear trend of the number of contacts decreasing with increasing processing temperature during drying, an effect which is particularly pronounced in OMA and DCLBZ. The effect of annealing is also dependent on the processing temperature, with a larger number of P3HT $\leftrightarrow$ O-IDTBR contacts being lost during annealing and cooling for lower processing temperatures during drying. This suggests that the phases are more intermixed in the as-cast films and that annealing seems to "purify" the respective domains. On average, the final number of interfacial contacts in the dried, annealed, and cooled films decreases slightly with temperature, taking values of around 30-35 % relative to the normalised number of contacts in a completely intermixed blend.

The PffBT4T-2OD:O-IDTBR blends (Fig. 4.8) exhibit the same tendencies for O-IDTBR $\leftrightarrow$ O-IDTBR contacts as the P3HT:O-IDTBR blends, but a very clear temperature dependence is seen for the PffBT4T-2OD $\leftrightarrow$ PffBT4T-2OD contacts. Experimentally, the PffBT4T group of polymers show highly temperature-dependent aggregation,<sup>230,259–262</sup> an effect which is captured very well with the present MARTINI model. A strong aggregation is seen in the simulated films processed at low temperatures, whereas the chains will stay fully solvated for longer at high processing temperatures. Solvent polarity also increasingly influences the aggregation with increasing temperature: all three solvents give rise to only small differences at low processing temperature, but for CLBZ and PCYM, the aggregation is suppressed significantly more than for OXYLE at high processing temperatures. For all solvents and temperatures, the number of PffBT4T-2OD $\leftrightarrow$ PffBT4T-2OD contacts converge to slightly less than 60 % of the normalised maximum inferred from a neat PffBT4T-2OD film processed from CLBZ at 363 K – a significantly lower fraction than for the P3HT-based films – suggesting that the presence of O-IDTBR disturbs the packing of the PffBT4T-2OD phase. Annealing does not have a significant effect on this.

Regarding the interfacial contacts in the PffBT4T-2OD:O-IDTBR blends, no clear trends for neither temperature nor solvent polarity can be seen, but interestingly, the number of interfacial contacts rise more quickly during drying at high processing temperatures than at low processing temperatures. This is due to more PffBT4T-2OD chains being "caught" in the O-IDTBR phases when the donor aggregation has a later onset, meaning that the donors have a higher probability of finding themselves kinetically trapped in an acceptor phase as the solvent fraction decreases.

Finally, the donor:PCBM blends (bottom row of Fig. 4.8) show the same trends for the respective donor $\leftrightarrow$ donor contacts as the NFA blends, but the number of PCBM $\leftrightarrow$ PCBM contacts rises more linearly with decreasing solvent fraction due to aggregation initiated at concentrations of around 60-100 mg/ml. This finding correlates very well



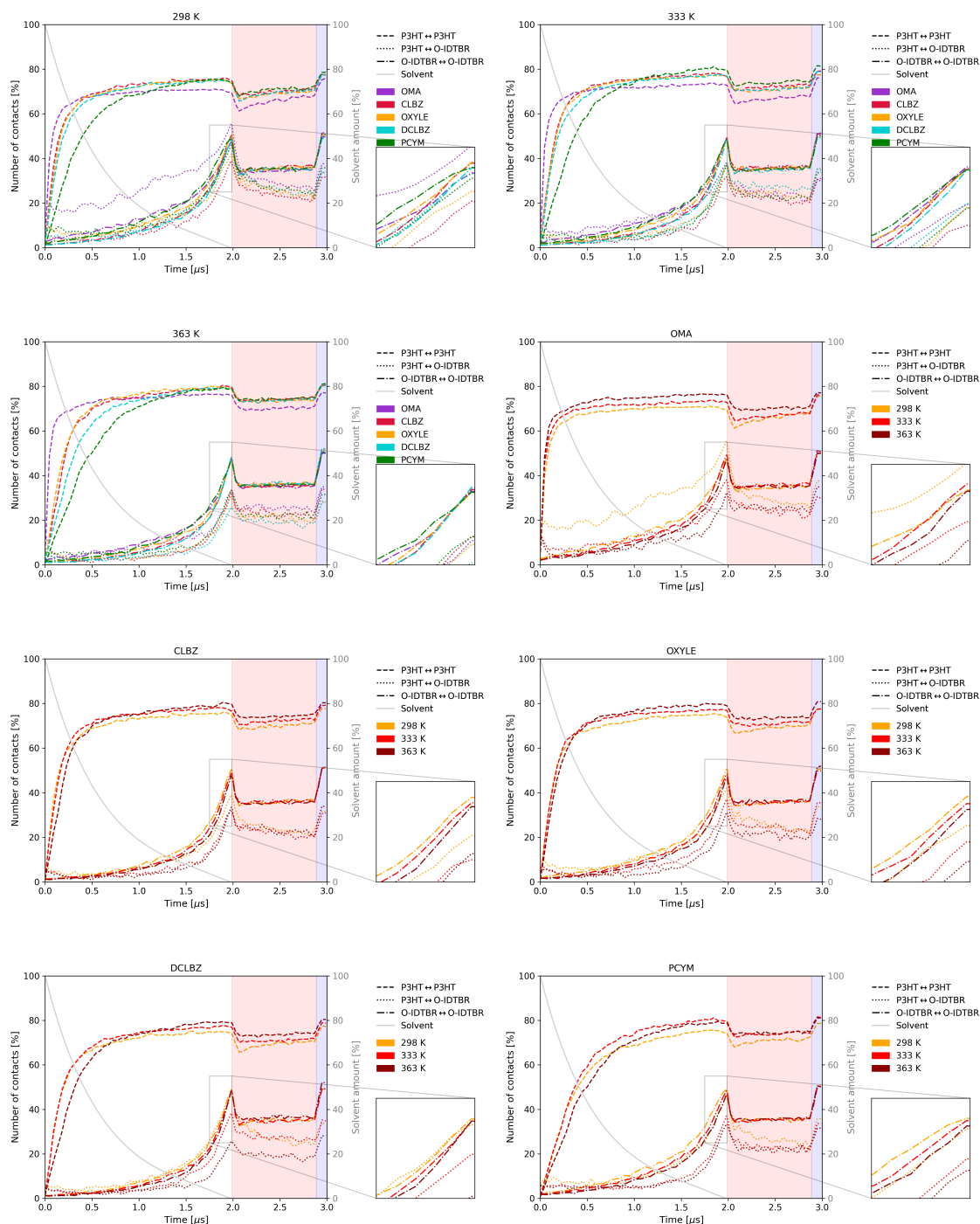


Figure 4.7: Close contacts in the P3HT:O-IDTBR blends as a function of time compared both across temperatures and solvents. Red- and blue-shaded areas correspond to annealing at 498 K and cooling to 298 K, respectively.

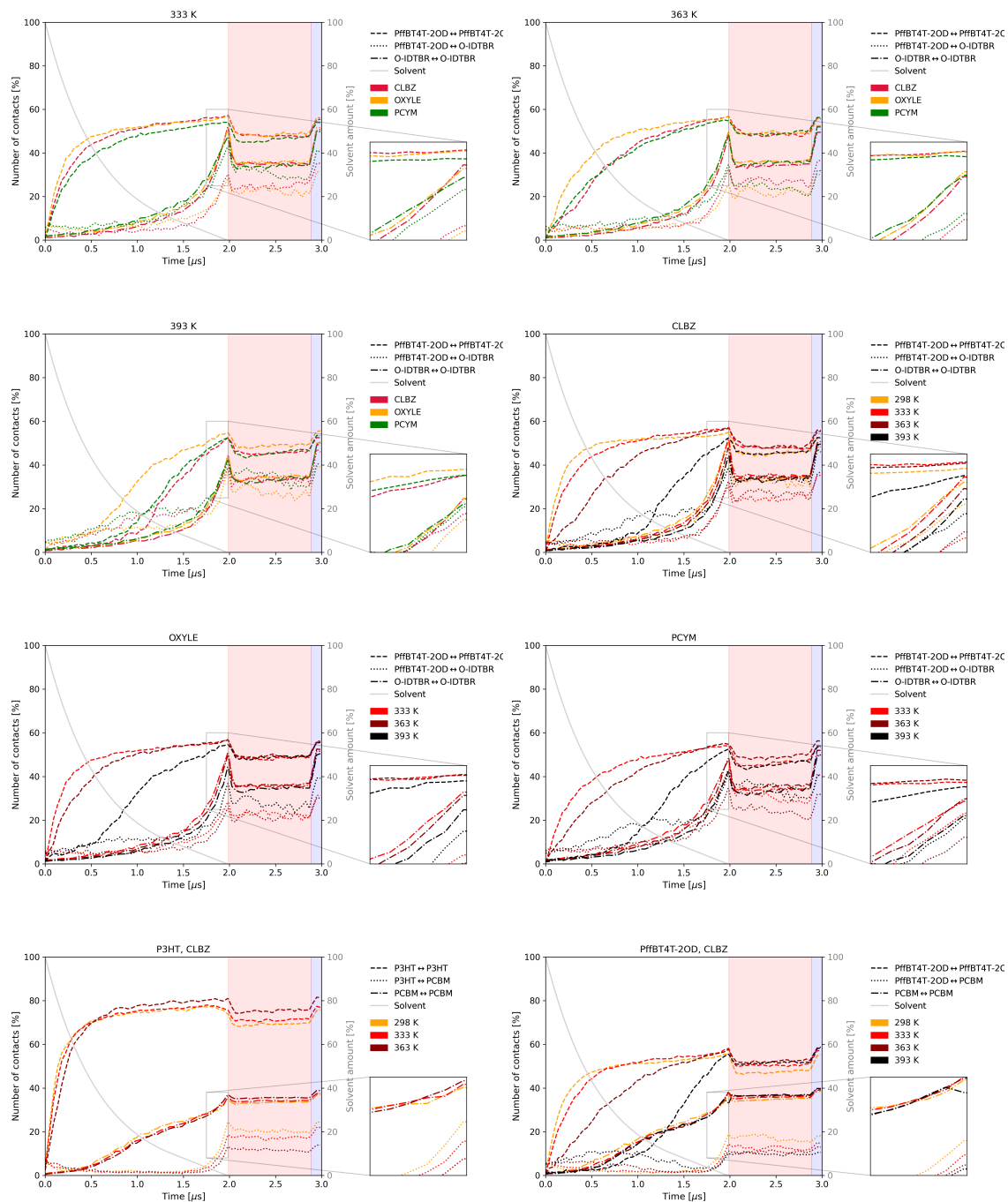


Figure 4.8: Close contacts in the PffBT4T-2OD:O-IDTBR (top three rows) and donor:PCBM blends (bottom row) as a function of time compared across both temperatures and solvents. Red- and blue-shaded areas correspond to annealing at 498 K and cooling to 298 K, respectively.



to the experimental solubility limits presented in Table 4.2. The effect of temperature on PCBM aggregation is negligible, and annealing does not have any significant effect either. The number of interfacial contacts are on the other hand quite influenced by temperature, with a clear trend of fewer contacts in the dry films at lower temperatures, suggesting that the domain purity and/or size is increased with increasing temperature. Similarly to the PffBT4T-2OD:O-IDTBR systems, the number of interfacial contacts in the PffBT4T-2OD:PCBM systems increases more during evaporation at higher processing temperatures due to the donor chains being less aggregated. Whereas the increased number of contacts for the highest processing temperature is maintained in the dry PffBT4T-2OD:O-IDTBR films, it decreases towards the end of the drying process in the PffBT4T-2OD:PCBM systems, leading to the reversed trend of fewer interfacial contacts at higher temperatures. This suggests, in line with the expectations, that the PCBM molecules are less miscible with the donor phases than the O-IDTBR molecules and that the former can more easily diffuse out of the donor phase at higher processing temperatures.

Already from the close contact analysis, it can thus be concluded that films processed from lower temperatures are impacted more by annealing, which serves to purify domains. Furthermore, changing the processing temperature and solvent mainly influences the donor polymer aggregation and not the O-IDTBR acceptor domain formation, which seems to be exclusively controlled by spatial constriction when solvent evaporates and not by aggregation. PCBM acceptors, on the other hand, show signs of aggregation at low CLBZ solvent fractions, meaning that domain formation for fullerene blends is aggregation controlled by both acceptors and donors. We, however, note that the simulations do not take differences in drying time (or, equivalently, evaporation rate) as a function of temperature into account, i.e. that a low-temperature processed film would dry slower than a high-temperature processed film, which means that a potentially crucial effect is not considered. One would expect a quick drying to result in a more kinetically trapped morphology, but this effect is counterbalanced by the higher solubility and higher kinetic energy of the components at higher temperatures, allowing them to explore more configurations. This results in them having a higher probability of finding a low-energy conformation, e.g.  $\pi$ -stacking of donor polymers, around the critical concentration in the drying process. Furthermore, different solvents evaporate with different rates, which is also not considered, and including the evaporation rates of different solvents at different temperatures in the simulations thus represent the logical next step. This is discussed in more detail in Section 4.6.

### 4.5.2 Domain sizes and purity

In order to visualise the morphologies in a way that allows easy comparison across the different processing conditions applied, the spatially discretised 3D volumes of the annealed films were projected down onto the xy-plane and coloured according to the amount of donors or acceptors present in the projected pixel areas. These 2D visualisations are presented in Figs. 4.9-4.11 for the P3HT:O-IDTBR, the PffBT4T-2OD:O-IDTBR, and the donor:PCBM systems, respectively. These can, in an illustrative sense, be seen as an analogue of energy-filtered transmission electron microscope images. In this work, they can be used as a visual reference point for the results of the structural analyses presented in this and the following sections.

As described in Section 4.4.3, pair correlation functions of the donor and acceptor

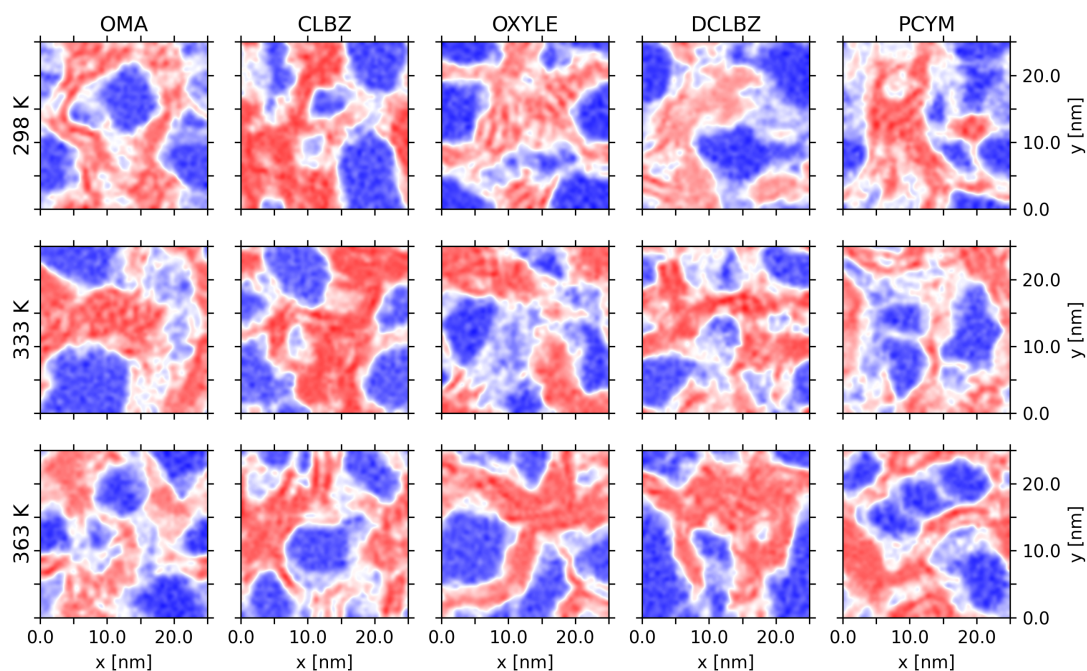


Figure 4.9: 2D projections of the spatially discretised P3HT:O-IDTBR morphologies processed from different solvents (columns) and at different temperatures (rows); colors indicate the phases (more red corresponds to a higher donor fraction and more blue to a higher acceptor fraction); the pixel boundaries are smoothed using a bicubic interpolation.

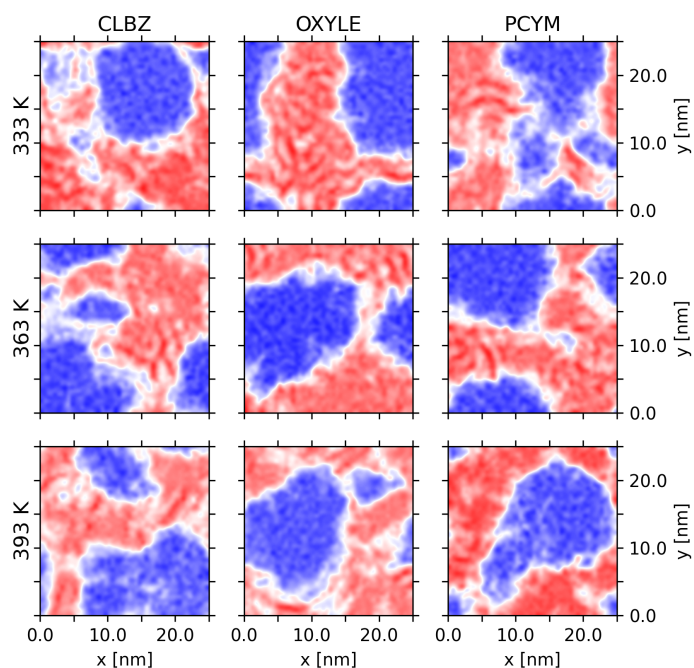


Figure 4.10: 2D projections of the spatially discretised PffBT4T-2OD:O-IDTBR morphologies processed from different solvents (columns) and at different temperatures (rows); colors indicate the phases (more red corresponds to a higher donor fraction and more blue to a higher acceptor fraction); the pixel boundaries are smoothed using a bicubic interpolation.

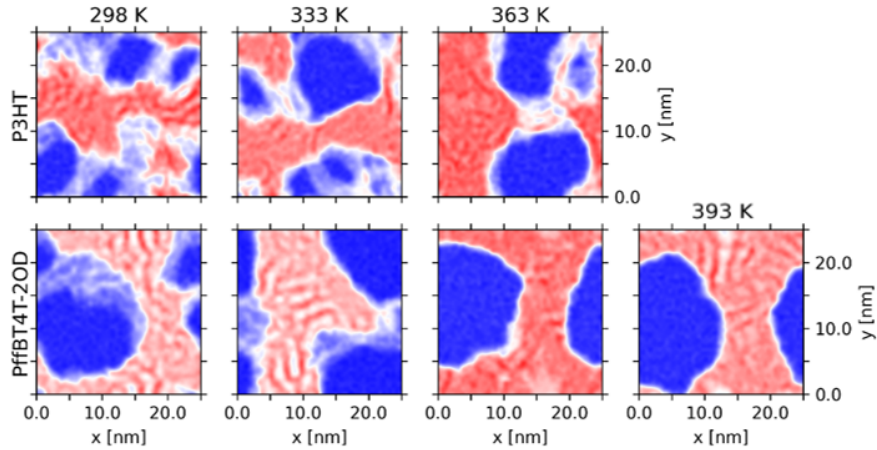


Figure 4.11: 2D projections of the spatially discretised donor:PCBM morphologies processed from chlorobenzene at different temperatures (columns); colors indicate the phases (more red corresponds to a higher donor fraction and more blue to a higher acceptor fraction); the pixel boundaries are smoothed using a bicubic interpolation.

Table 4.3: P3HT:O-IDTBR: Average domain sizes,  $d$ , inferred from pair correlation functions of as-cast and annealed thin-films processed from different solvents and at different temperatures.

$T_{\text{process.}}$	domain size, as-cast [nm]			domain size, annealed [nm]		
	298 K	333 K	363 K	298 K	333 K	363 K
OMA	$5.88 \pm 2.00$	$6.85 \pm 1.69$	$6.79 \pm 2.07$	$6.28 \pm 1.13$	$7.69 \pm 1.42$	$6.35 \pm 1.37$
CLBZ	$7.96 \pm 1.82$	$6.53 \pm 1.12$	$6.69 \pm 1.26$	$7.95 \pm 0.83$	$7.25 \pm 0.89$	$6.99 \pm 1.27$
OXYLE	$7.39 \pm 1.82$	$7.56 \pm 1.83$	$7.26 \pm 1.57$	$6.53 \pm 0.84$	$7.31 \pm 1.48$	$6.76 \pm 1.43$
DCLBZ	$5.63 \pm 1.13$	$9.71 \pm 4.12$	$9.60 \pm 2.50$	$6.80 \pm 0.91$	$6.93 \pm 1.91$	$9.38 \pm 1.23$
PCYM	$5.93 \pm 1.05$	$6.73 \pm 2.15$	$5.69 \pm 0.90$	$9.04 \pm 3.07$	$7.15 \pm 1.98$	$5.98 \pm 0.97$

Table 4.4: PffBT4T-2OD:O-IDTBR: Average domain sizes,  $d$ , inferred from pair correlation functions of as-cast and annealed thin-films processed from different solvents and at different temperatures.

$T_{\text{process.}}$	domain size, as-cast [nm]			domain size, annealed [nm]		
	333 K	363 K	393 K	333 K	363 K	393 K
CLBZ*	$8.69 \pm 2.98$	$8.55 \pm 3.14$	$7.48 \pm 0.37$	$9.36 \pm 2.08$	$9.46 \pm 1.18$	$7.96 \pm 0.99$
OXYLE	$9.17 \pm 1.23$	$9.37 \pm 0.77$	$7.13 \pm 0.92$	$9.46 \pm 0.35$	$9.53 \pm 0.50$	$8.99 \pm 1.16$
PCYM	$8.11 \pm 2.03$	$8.78 \pm 1.47$	$6.69 \pm 1.02$	$8.95 \pm 1.09$	$9.22 \pm 0.39$	$7.63 \pm 0.84$

\*At 298 K: as-cast:  $8.82 \pm 1.65$  nm, annealed:  $9.35 \pm 0.64$  nm

Table 4.5: Donor:PCBM: Average domain sizes,  $d$ , inferred from pair correlation functions of as-cast and annealed thin-films processed from CLBZ at different temperatures.

$T_{\text{process.}}$	domain size [nm]			
	298 K	333 K	363 K	393 K
P3HT, as-cast	$8.07 \pm 2.04$	$8.29 \pm 1.82$	$9.40 \pm 1.65$	n/a
P3HT, anneal.	$7.92 \pm 1.45$	$8.31 \pm 1.87$	$9.44 \pm 1.42$	n/a
PffBT4T-2OD, as-cast	$7.93 \pm 1.05$	$9.09 \pm 1.34$	$9.23 \pm 0.37$	$9.52 \pm 0.30$
PffBT4T-2OD, anneal.	$8.41 \pm 1.14$	$9.21 \pm 1.14$	$9.22 \pm 0.27$	$9.56 \pm 0.09$

Table 4.6: Domain purity (in arb. units) inferred from pair correlation functions of as-cast and annealed thin-films processed from different solvents and at different temperatures.

$T_{\text{process.}}$	domain purity, as-cast				domain purity, annealed			
	298 K	333 K	363 K	393 K	298 K	333 K	363 K	393 K
P3HT:O-IDTBR								
OMA	0.81	0.85	0.85	n/a	0.86	0.89	0.86	n/a
CLBZ	0.86	0.87	0.85	n/a	0.88	0.89	0.87	n/a
OXYLE	0.84	0.85	0.86	n/a	0.88	0.87	0.89	n/a
DCLBZ	0.82	0.84	0.87	n/a	0.87	0.86	0.89	n/a
PCYM	0.84	0.83	0.85	n/a	0.87	0.86	0.87	n/a
PffBT4T-2OD:O-IDTBR								
CLBZ	0.83	0.86	0.84	0.84	0.85	0.87	0.87	0.85
OXYLE	n/a	0.88	0.89	0.84	n/a	0.90	0.89	0.86
PCYM	n/a	0.82	0.85	0.81	n/a	0.86	0.89	0.86
Donor:PCBM in CLBZ								
P3HT	0.90	0.92	0.94	n/a	0.91	0.92	0.94	n/a
PffBT4T-2OD	0.92	0.93	0.95	0.96	0.94	0.95	0.96	0.96

phases in the spatially discretised morphologies were used to infer the domain sizes. The domain size is generally considered *the* structural figure of merit for OPVs. With the measured exciton diffusion lengths being around 10 nm in neat P3HT and PffBT4T-2OD thin-films<sup>263,264</sup> and around 15 nm in thin-films of the 2-ethylhexyl substituted IDTBR,<sup>216</sup> the optimal domain size for the systems studied herein is assumed to be on the order of 10 nm.

In Table 4.3, the calculated domain sizes for the P3HT:O-IDTBR systems can be found. The typical values range from 6-8 nm, but no clear, general trends are seen. In most cases, annealing increases the domain size slightly and/or decreases the standard deviation of the calculated domain sizes. The standard deviations are, due to the pseudo-3D implementation of analysing slice by slice in the xy-plane, related to the variation of the domain sizes and composition in the vertical z-direction, meaning that the 2D projections of the morphologies in Figs. 4.9-4.11 provide visual representations of the errors; the more "messy" or the more white areas, the larger the standard deviation of the domain sizes. Indeed, looking at Fig. 4.9, the domains are not well defined and the phases not well separated, which is also reflected in the relatively large standard deviations of the domain sizes. The P3HT chains form long, thin,  $\pi$ -stacked nanofibrils during the initial, quick aggregation described above in Section 4.5.1 that do not aggregate much further during the evaporation and hence extend in a random network with small acceptor domains as "pores". The purity of the individual domains is around 85 % for the as-cast films as seen in Table 4.6, which increases slightly to around 88 % on average upon annealing.

Looking at the PffBT4T-2OD:O-IDTBR domain sizes in Table 4.4, the trends are more clear: larger domains are formed when the films are processed at 333 K and 363 K than when they are processed at 393 K, and annealing increases the domain sizes for all systems, but to a larger extent for the high-temperature processed films. The domains seem to be bigger for the 363 K processed films, although within error of the 333 K processed films. As seen in Fig. 4.10, the domains are more well defined

than for the P3HT-based films, which is also reflected in lower relative errors of the domain sizes. Generally, the PffBT4T-2OD:O-IDTBR films exhibit larger domains ( $\sim 9$  nm) than the P3HT:O-IDTBR films ( $\sim 7$  nm) but with approximately similar domain purities and a similar trend of increased purity with annealing (cf. Table 4.6). The CLBZ processed films seem to benefit more from annealing than the OXYLE and PCYM processed films, showing increased domain sizes and reduced standard deviations. The strongly temperature dependent aggregation properties of the PffBT4T polymers seem to be beneficial for controlling the domain size through processing temperature. It is noteworthy that PffBT4T-2OD does not seem to form the same long, thin nanofibrils as P3HT early in the drying phase but instead aggregates more continuously, allowing the chains to form thicker fibrils and thus larger "pores" of acceptor domains.

As seen in Table 4.5, the donor:PCBM systems exhibit a clear trend of larger domain sizes with increasing processing temperature. The domains are furthermore well separated, having purities of 90-96 % (cf. Table 4.6). In general, annealing does not have a significant effect on neither the domain sizes nor the purity of the domains, as the domains are already quite large and pure for the as-cast films. The trends described in the above Section 4.5.1 regarding the relative miscibility of the polymer donors and the acceptor molecules and the relative diffusivity of the acceptor molecules are substantiated by the results here, and employing PCBM acceptors indeed result in a more distinct phase separation as seen in Fig. 4.11.

### 4.5.3 Percolating pathways and mobility simulations

As a quick estimate of the connectivity of the donor and acceptor domains, the fraction of donor backbone units being part of a percolating pathway in each principal direction was extracted for the systems alongside the corresponding fraction of acceptor backbone units. This was done in accordance with the description in Section 4.4.4. In all of the P3HT:O-IDTBR simulations (both as-cast and annealed), more than 97 % of the donor backbone units were part of a percolating pathway spanning the z-direction *and* the x- and y-directions. Similarly, more than 95 % of the acceptor backbone units were part of a percolating pathway spanning the z-direction, but a few simulations (CLBZ at 298 K and DCLBZ at 363 K) only formed a percolating pathway in one of the x- and y-directions in the acceptor domains (cf. Fig. 4.9 – note that these are 2D projections and hence not true representations of the full 3D network analysed in this section), leading to average in-plane percolation fractions of 35-50 %. The rest formed percolating acceptor pathways in both the x- and y-directions with average percolation fractions of more than 88 %. For all PffBT4T-2OD:O-IDTBR systems, both donor and acceptor domains exhibited high percolation fractions of more than 95 % in all directions except for PCYM at 363 K, which only formed a percolating pathway in one of the x- and y-directions in the acceptor domains, leading to an average in-plane percolation fraction of 37 %. The donor:PCBM systems showed donor percolation fractions of 99 % or more in all directions, whereas the acceptor domains had equally high percolation fractions in the z-direction. The acceptor domains, however, did not exhibit percolation in both the x- and y-directions simultaneously for any of the donor:PCBM simulations, leading to in-plane acceptor percolation fractions of 35-50 % for all of the P3HT:PCBM systems. The PffBT4T-2OD:PCBM systems had no acceptor percolation in neither of the in-plane directions except for the 333 K processed system (cf. Fig. 4.11), which had an average in-plane percolation fraction of 50 %.

With these quick estimates of the percolation fractions, it is straightforward to predict that the kMC time-of-flight mobility simulations will yield zero-mobilities in the directions with no percolation. For the rest of the directions and systems, the percolation fractions are all close to unity, and the differences in mobilities for these systems are thus expected to be directly related to the degree of local order between donor oligomers and between acceptor molecules: closer  $\pi$ -stacking will result in higher coupling (as a distance dependence is implemented for these), and a larger number of intermolecular interactions will result in more well-connected networks, leading to a higher charge carrier mobility. The connectivity between ordered donor crystallites mediated by less ordered oligomer chains will also be a determining factor,<sup>177</sup> as two perfect lamellar stacks will not be able to communicate due to the insulating layer of side-chains between them.

In Fig. 4.12, the results of the kMC time-of-flight mobility simulations are presented.<sup>d</sup> The mobilities are reported as normalised quantities with respect to the corresponding mobilities of the neat, annealed P3HT, PffBT4T-2OD, and O-IDTBR thin-films processed from CLBZ at 333 K, 363 K, and 333 K, respectively. Note that no mobility simulation of a neat PCBM film was available and that the PCBM mobilities are hence normalised relative to three times the simulated mobilities of the neat O-IDTBR film, approximately corresponding to the difference in experimental organic thin-film transistor mobilities of neat PCBM ( $\sim 0.20\text{--}0.42\text{ cm}^2\text{V}^{-1}\text{s}^{-1}$ ) and neat O-IDTBR ( $\sim 0.12\text{ cm}^2\text{V}^{-1}\text{s}^{-1}$ ).<sup>150,265</sup> For the P3HT:O-IDTBR systems (Fig. 4.12, top row), the simulated charge carrier mobilities are quite similar across all of the investigated solvents and temperatures and exhibit no clear trends. The out-of-plane hole mobility (i.e. charge transport in the donor phase) for the OMA processed films seems to be higher at lower temperatures, whereas it is significantly lower for the OXYLE processed film at 333 K. The out-of-plane hole mobilities for the rest of the systems are centred around 15 %. This is also the case for most of the in-plane hole mobilities except for a significant outlier for CLBZ at 298 K, which reaches 30 %, as well as OMA at 333 K and PCYM at 363 K, which reach around 21 % and 23 %, respectively. Looking at the electron mobilities (i.e. charge transport in the acceptor phase), these are fairly steady around 10–15 % in the out-of-plane direction but drops to around 4–8 % for the in-plane directions. Again, CLBZ at 298 K deviates significantly from the trend, reaching 15 %, along with OXYLE at 298 K, which reaches around 12 %.

Moving on to the PffBT4T-2OD:O-IDTBR films, the out-of-plane hole and electron mobilities seem to increase slightly with increasing temperature for CLBZ processed films, whereas the opposite trend is present for the OXYLE processed films – these trends are then somewhat reversed for the in-plane directions. The PCYM processed films seem to have an overall optimum at 363 K for both the out-of-plane and in-plane directions. In general, the same trend as for the P3HT:O-IDTBR films of fairly similar hole mobilities both across solvents, temperatures, and directions is seen alongside the trend of lower relative electron mobilities in the in-plane directions than in the out-of-plane direction.

For the P3HT:PCBM systems processed from CLBZ, the mobilities seem to find a minimum for a processing temperature of 333 K and a maximum for 363 K. A trend of increasing mobilities with increasing temperature is seen for the PffBT4T-2OD:PCBM systems, although with zero electron mobilities in the in-plane directions for 298 K, 363

<sup>d</sup>The kMC simulations are carried out by Jack Coker, Department of Physics, Imperial College London on the annealed thin-films presented herein. Data analysis and plotting are carried out by the author of this thesis.

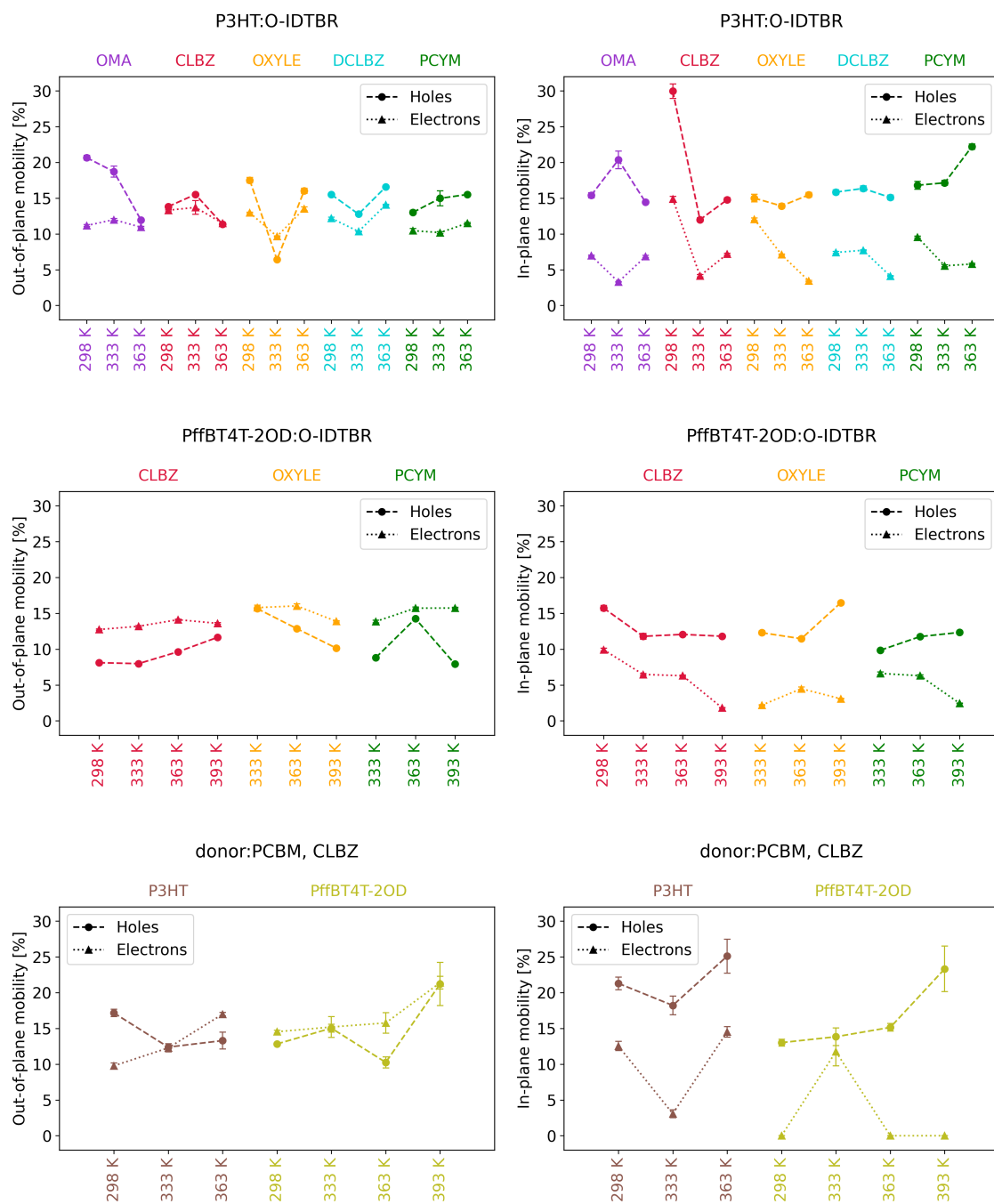


Figure 4.12: Normalised time-of-flight charge carrier mobilities from kMC simulations in the out-of-plane direction (z-direction; left column) and in the in-plane direction (average of x- and y-directions; right column) for annealed P3HT:O-IDTBR systems (top row) and annealed PffBT4T-2OD:O-IDTBR systems (middle row) processed from different solvents and at different temperatures and for annealed donor:PCBM systems (bottom row) processed from CLBZ at different temperatures. The data points are averages of 6-9 individual mobility simulations (identical structures, different initial seeds for charge generation), and error bars indicate the standard deviation of these.

K, and 393 K due to no percolating pathways being present.

The general trend of lower electron mobilities in the in-plane directions relative to the out-of-plane direction can be directly explained by the lower percolation fractions of the acceptor phases in the xy-plane. Correspondingly, the almost unity percolation fractions of the donor phases in all directions can explain the similar hole mobilities for the in-plane and out-of-plane directions. However, as the  $\pi$ -stacking of donor chains is mainly in the out-of-plane direction due to the drying causing the wet film to shrink in this direction, the out-of-plane hole mobilities rely to a higher degree on interchain couplings, whereas the in-plane mobility is mainly governed by intrachain transport. With the charge transport in a standard OPV device being perpendicular to the substrate, i.e. in the out-of-plane direction, a well-connected network of  $\pi$ -stacked chains in a face-on orientation to the substrate is crucial for efficient hole extraction. For all of the simulations, such networks indeed seem to have been present in the blend films, as the out-of-plane mobilities are similar in relative magnitude (and within a factor of two in absolute magnitude) to the in-plane mobilities despite the intermolecular couplings being several orders of magnitude weaker than the intramolecular couplings.

#### 4.5.4 Specific interface areas

The interfacial area per unit volume, i.e. the specific interface area, can yield information about the density of potential sites for exciton dissociation. The specific interface area of a system is inversely related to its average domain size, and an optimal relation between these, which necessarily depends on the exciton diffusion length, must therefore be present. Following the procedure outlined in Section 4.4.5, the specific interface areas are calculated for all systems and listed in Table 4.7. First of all, comparing the specific interface areas to the domain sizes in Tables 4.3-4.5 and the domain purities in Table 4.6, the expected inverse correlation is observed (bigger and purer domains correspond to smaller specific interface areas). Assuming that the optimal domain size of the blends is around 10 nm and a high purity is desirable, the specific interface areas would have an optimum around  $0.18 \text{ nm}^{-1}$  as inferred from the PffBT4T-2OD:PCBM system processed at 393 K in CLBZ (cf. Fig. 4.11). Secondly, the trend of increasing domain size with annealing is substantiated by the specific interface area calculations, which clearly show a significant decrease upon annealing. It is also clear from the donor:PCBM calculations that increasing processing temperature decreases the specific interface areas, leading to very well-separated domains. The O-IDTBR-based systems again do not show any clear trends across the processing solvents, but it seems that the PffBT4T-2OD:O-IDTBR systems in general have minimum specific interface areas around 363 K for OXYLE and PCBM and around 333 K for CLBZ. For P3HT:O-IDTBR, the specific interface areas are smallest around 333 K for OMA and CLBZ and around 363 K for DCLBZ, suggesting that these could be some of the better processing conditions considered. However, with the trends being as vague as they are, nothing conclusive can be said.

#### 4.5.5 Crystallite sizes

Based on the analysis methods described in Section 4.4.6, the average donor crystallite sizes were extracted for all simulations and presented in Table 4.8. In general, annealing is found to increase the crystallite sizes, and for some systems quite significantly. Looking at the P3HT:O-IDTBR systems first, there are again no clear trends across processing temperatures or solvents. For the as-cast films, the crystallite sizes are generally between 3.5 nm and 4.5 nm, which grow to around 4.5-5.2 nm for most of the processing



Table 4.7: Specific interface areas,  $\gamma$ , in as-cast and annealed thin-films processed from different solvents and at different temperatures.

$T_{\text{process.}}$	$\gamma$ , as-cast [ $\text{nm}^{-1}$ ]				$\gamma$ , annealed [ $\text{nm}^{-1}$ ]			
	298 K	333 K	363 K	393 K	298 K	333 K	363 K	393 K
P3HT:O-IDTBR								
OMA	0.90	0.73	0.75	n/a	0.65	0.54	0.67	n/a
CLBZ	0.70	0.65	0.74	n/a	0.56	0.54	0.63	n/a
OXYLE	0.77	0.71	0.70	n/a	0.60	0.62	0.55	n/a
DCLBZ	0.87	0.78	0.62	n/a	0.61	0.69	0.53	n/a
PCYM	0.80	0.80	0.73	n/a	0.64	0.69	0.61	n/a
PffBT4T-2OD:O-IDTBR								
CLBZ	0.80	0.63	0.74	0.76	0.72	0.60	0.62	0.71
OXYLE	n/a	0.56	0.52	0.78	n/a	0.50	0.50	0.65
PCYM	n/a	0.85	0.69	0.87	n/a	0.67	0.52	0.66
Donor:PCBM in CLBZ								
P3HT	0.48	0.39	0.29	n/a	0.42	0.37	0.27	n/a
PffBT4T-2OD	0.41	0.32	0.23	0.20	0.30	0.25	0.20	0.18

conditions upon annealing. Two significant outliers are, however, present, namely for OMA at 333 K and for OXYLE at 298 K, exhibiting average crystallite sizes of 6.5 and 7.8 nm, respectively, for the annealed films. The expectation is for this to be reflected in the hole mobilities presented above (cf. Fig. 4.12, top row), and the OMA processed films indeed have high hole mobilities both out-of-plane and in-plane around 333 K, and the OXYLE processed films also have higher out-of-plane hole mobilities at 298 K.

The PffBT4T-2OD:O-IDTBR follow the same trend of growing donor crystallites upon annealing, but other than that, no clear trends are present across processing solvent or temperature. The PffBT4T-2OD crystallites are in general found to be larger than the P3HT crystallites, and two significant outliers are also present for the annealed PffBT4T-2OD:O-IDTBR films, namely for CLBZ at 298 K and for OXYLE at 393 K. Counter-intuitively, these seem to coincide with minima of the out-of-plane hole mobilities (cf. Fig. 4.12, middle row). This can, however, be explained by the smaller domain sizes, lower domain purity, and higher specific interface areas for exactly these processing conditions. For the film processed from OXYLE at 333 K, quite high average crystallite sizes were found, extending past the limit for the analysis framework (i.e. the analysis sphere radius  $r$  becoming larger than the simulation box in the  $z$ -direction). Manual inspection of the film reveals that it is indeed very crystalline, which is also reflected in the high out-of-plane hole mobility (cf. Fig. 4.12, middle row).

For the P3HT:PCBM systems, a small increase in crystallite sizes seems to be present with increasing processing temperature. A further increase is seen for the annealed film with the crystallites reaching average sizes of 4.2 nm for the annealed film processed at 363 K. The PffBT4T-2OD:PCBM films in general exhibit larger crystallites than the P3HT:PCBM films, and the effect of annealing is significantly bigger. For the as-cast films, the largest crystallites are found for a processing temperature of 363 K, but after annealing, the 333 K processed films exhibit the largest crystallites of an average size of 8 nm.

Table 4.8: Average donor crystallite sizes,  $L_D$ , inferred from integration of radially averaged local order parameters at different distances (cf. Fig. 4.6) in as-cast and annealed thin-films processed from different solvents and at different temperatures.

$T_{\text{process.}}$	$L_D$ , as-cast [nm]				$L_D$ , annealed [nm]			
	298 K	333 K	363 K	393 K	298 K	333 K	363 K	393 K
P3HT:O-IDTBR								
OMA	3.53	4.17	4.10	n/a	5.14	6.48	4.76	n/a
CLBZ	3.73	3.78	4.98	n/a	4.29	4.20	4.85	n/a
OXYLE	3.96	4.10	4.68	n/a	7.82	4.67	5.08	n/a
DCLBZ	3.84	4.22	3.92	n/a	5.04	4.72	4.37	n/a
PCYM	3.74	4.65	4.64	n/a	4.88	5.20	5.04	n/a
PffBT4T-2OD:O-IDTBR								
CLBZ	5.59	5.02	5.42	5.25	8.73	5.67	6.14	5.41
OXYLE	n/a	5.07	4.86	6.39	n/a	*	5.72	8.26
PCYM	n/a	4.93	5.54	5.09	n/a	6.57	6.05	5.58
Donor:PCBM in CLBZ								
P3HT	3.34	3.53	3.85	n/a	3.84	3.78	4.19	n/a
PffBT4T-2OD	4.13	4.56	4.86	4.77	5.22	8.01	6.15	5.62

\*degree of crystallinity did not go below 50 % for  $2r < 2\text{box}_z$

## 4.6 Discussion

### 4.6.1 Comparison to device measurements

As one of the goals of this work is to be able to predict optimal processing conditions for the systems in question, a range of P3HT:O-IDTBR devices processed from the five different solvents considered at 333 K and 363 K was fabricated.<sup>e</sup> The devices were fabricated using the procedure outlined in Ref. 204, employing an ITO-free flexible<sup>266</sup> substrate and fully open-air, roll-processed active layers and electrodes in a PET/Ag/PEDOT:PSS/ZnO/ P3HT:O-IDTBR/PEDOT:PSS/Ag stack. The active layers were slot-die coated using dual temperature control, ensuring that both the slot-die coating head and the substrate bed had the desired temperatures. Here, both are kept at either 333 K or 363 K (the inks were not viscous enough for printing at 298 K). The properties of the resulting devices are listed in Table 4.9.

As seen, the devices processed at a temperature of 333 K are significantly more efficient than the ones processed at 363 K. Furthermore, processing the active layers from non-halogenated solvents yield better efficiencies than when processing from halogenated solvents, with an average PCE of  $3.19 \pm 0.17$  for the OMA-processed devices being the highest. Looking back through Section 4.4, no analysis single-handedly reflects this trend. It can be mentioned that the domain size seems to decrease from 333 K to 363 K for all of the solvents except DCLBZ, but these are all well within error of each other. Naively constructing a structural figure of merit (s-FoM) for the analysis by multiplying the domain size, domain purity, specific interface area, and donor crystallite size (cf. Appendix, Section 4.8.1) does not capture the correct trends either. It hence seems that either the models or the solvent evaporation scheme and the assumptions

<sup>e</sup>OPV devices were fabricated by Marcial Fernández Castro and Moises Espindola Rodrigues, who also carried out all device measurements.

Table 4.9: Average device properties (six cells or more) of 1 cm<sup>2</sup>, flexible P3HT:O-IDTBR organic solar cells with slot-die coated active layers processed from different solvents and at different temperatures.

	$T_{\text{process.}}$	OMA	CLBZ	OXYLE	DCLBZ	PCYM*
PCE [%]	333 K	3.19 ± 0.17	1.84 ± 0.07	2.63 ± 0.18	2.14 ± 0.21	2.79 ± 0.08
	363 K	1.39 ± 0.18	1.46 ± 0.06	1.52 ± 0.21	1.70 ± 0.18	1.97 ± 0.43
FF [%]	333 K	59.2 ± 1.2	38.6 ± 1.3	49.7 ± 2.5	44.6 ± 4.2	56.9 ± 1.8
	363 K	36.8 ± 2.1	33.2 ± 1.2	36.8 ± 2.2	40.1 ± 1.9	43.1 ± 9.2
$J_{\text{sc}}$ [ $\frac{\text{mA}}{\text{cm}^2}$ ]	333 K	7.54 ± 0.35	6.66 ± 0.12	7.35 ± 0.48	6.68 ± 0.21	6.90 ± 0.00
	363 K	5.28 ± 0.40	6.06 ± 0.27	5.92 ± 0.35	5.76 ± 0.44	6.38 ± 0.32
$V_{\text{oc}}$ [V]	333 K	0.72 ± 0.00	0.71 ± 0.01	0.72 ± 0.00	0.72 ± 0.01	0.72 ± 0.00
	363 K	0.71 ± 0.01	0.72 ± 0.01	0.73 ± 0.01	0.73 ± 0.01	0.72 ± 0.01

\*values for PCYM at 333 K are averages of only three cells

made for this do not describe the formation of blend OPV morphologies sufficiently well.

#### 4.6.2 Impact of evaporation rate and statistics

No significant differences in simulated domain sizes are seen for the P3HT:O-IDTBR systems as a function of processing temperature and solvent. From the large differences in device performance seen experimentally depending on these processing conditions (cf. Table 4.9 and Refs. 202,<sup>204</sup>, and<sup>203</sup>), a difference in domain size is, however, expected. As the difference in evaporation rate between solvents has not been considered in the above simulations, it is speculated that this can impact the domain formation. To test the influence of simulated evaporation rate on the quantities presented above, a fast 1  $\mu\text{s}$  and a slow 4  $\mu\text{s}$  evaporation run in CLBZ at 333 K were set up in addition to the medium 2  $\mu\text{s}$  evaporation run presented above. A close contact analysis (cf. left panel of Fig. 4.13) revealed that the P3HT aggregation did not depend on evaporation rate and was equally fast for all three runs (thus the shifted trends on the normalised axis), meaning that the quick P3HT aggregation in the above (medium evaporation time) runs was not a result of too fast evaporation rates not leaving sufficient time for diffusion controlled aggregation but rather of a very low solubility or too strong interchain interactions and thus a possible model failure. Conversely, the O-IDTBR $\leftrightarrow$ O-IDTBR contacts and the interfacial contacts follow identical trends on a normalised axis (i.e. with the increase in contacts uniformly spread out across the drying phase relative to evaporation rate on an absolute time axis), confirming the observation in Section 4.5.1 of them being inversely proportional to the remaining solvent fraction. This also indicates that the dynamics of the acceptors are well accounted for even in a 1  $\mu\text{s}$  evaporation run and confirms that O-IDTBR acceptor domain formation is not aggregation controlled in the solvents considered – however also with the caveat that the O-IDTBR model may be too soluble. In general, all three runs showed only very slight differences in total number of respective types of contacts both for the as-cast and annealed films, indicating that short-range structural order had sufficient time to relax in the 2  $\mu\text{s}$  runs. The only noteworthy difference was a 3 % increase in interfacial contacts from the fast evaporation to the slow evaporation which could very well just be a statistical variation (see below).

With it being established that the short range order is not significantly affected by evaporation time, the longer range structural order was investigated; the results of the structural analyses are compared in Table 4.10. Although the different domain sizes are within error of each other, it seems that a longer evaporation time results in larger

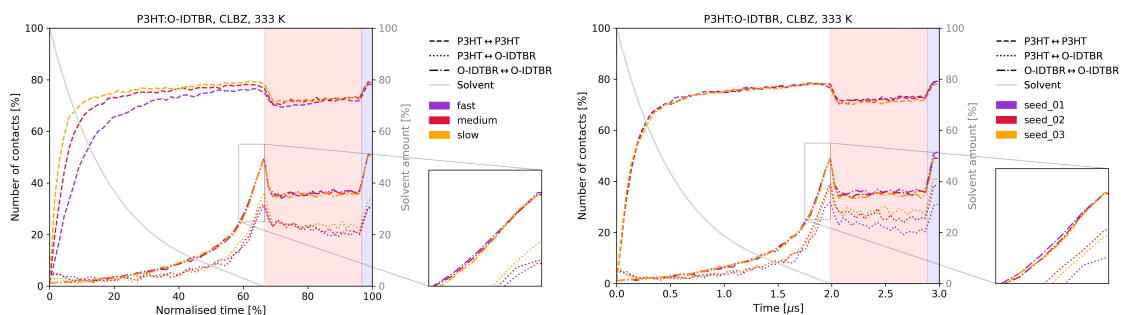


Figure 4.13: Close contacts in P3HT:O-IDTBR blends processed from CLBZ at 333 K as a function of evaporation rate (left) and initial seed (right). Note that the x-axis in the left panel is normalised in order to directly compare trends. Red- and blue-shaded areas correspond to annealing at 498 K and cooling to 298 K, respectively.

Table 4.10: Structural parameters as a function of evaporation time (fast: 1  $\mu\text{s}$ ; medium: 2  $\mu\text{s}$ ; slow: 4  $\mu\text{s}$ ) as well as statistics for medium evaporation rate runs (different initial seeds, seed\_01-03) for a P3HT:O-IDTBR system processed from CLBZ at 333 K. Note that the "medium" row corresponds to the "seed\_01" row (identical to each other and to the equivalent run presented in Section 4.5).

	as-cast				annealed			
	$d$ [nm]	purity	$\gamma$ [nm <sup>-1</sup> ]	$L_D$ [nm]	$d$ [nm]	purity	$\gamma$ [nm <sup>-1</sup> ]	$L_D$ [nm]
fast	$8.11 \pm 0.66$	0.87	0.64	3.87	$7.22 \pm 0.64$	0.89	0.53	5.26
medium	$6.53 \pm 1.12$	0.87	0.65	3.78	$7.25 \pm 0.89$	0.89	0.54	4.20
slow	$8.62 \pm 1.84$	0.85	0.74	4.62	$8.57 \pm 2.03$	0.87	0.62	5.12
seed_01	$6.53 \pm 1.12$	0.87	0.65	3.78	$7.25 \pm 0.89$	0.89	0.54	4.20
seed_02	$6.98 \pm 2.08$	0.84	0.78	4.39	$6.59 \pm 1.65$	0.85	0.70	4.78
seed_03	$5.63 \pm 1.03$	0.84	0.80	3.96	$5.97 \pm 1.30$	0.85	0.74	4.47

domains. Furthermore, the crystallite sizes are also bigger for the slow evaporation than for the medium evaporation, although the annealed film for the fast evaporation also exhibits an equally large crystallite size. The slight increase in interfacial contacts is also reflected here with a small increase in specific interface area. In order to investigate the impact of statistics on the structural parameters, two additional evaporation runs for the medium evaporation time initiated with different seeds for the velocity generation were set up (P3HT:O-IDTBR processed from CLBZ at 333 K). The results are also presented in Table 4.10. Some variation is seen for all the parameters, and it is thus clear that presenting average values of at least three equivalent simulations for the long-range structural parameters would have been preferable, but this would have been too computationally costly for the amount of simulations presented herein. Looking at the close contacts for these equivalent simulations in the right panel of Fig. 4.13, it is clear that the number of P3HT ↔ P3HT contacts and O-IDTBR ↔ O-IDTBR contacts evolve almost identically but that the interfacial contacts reflect the statistical differences in domain size seen in Table 4.10.

### 4.6.3 Impact of simulation box size

When discussing domain sizes, the simulation box size becomes an important parameter. As seen in the 2D projections in Figs. 4.10 and 4.11, the two phases are almost completely separated for most of the processing conditions, which indicates that the simulation box size has already become a limiting factor in the domain formation for PffBT4T-2OD:O-IDTBR and donor:PCBM blends; logically, the domains in an MD simulation can never get bigger than a characteristic size defined by the relative volume fraction of the respective phases and the absolute volume of the box. To conceptualise this, a 2D square of side length  $x$  can be considered. The biggest domain size  $d_{\max}$  for a 0.5:0.5 area fraction blend would approximately be the radius  $r$  of a circle with an area corresponding to half the total area of the square, namely

$$d_{\max} \approx \frac{x}{\sqrt{2\pi}}. \quad (4.4)$$

This can easily be extended to 3D for a cubic simulation box of side length  $x$  and a sphere of radius  $r$  when keeping the assumption of equal donor and acceptor volume fractions as

$$d_{\max} \approx \frac{x}{2} \left( \frac{3}{\pi} \right)^{1/3}. \quad (4.5)$$

For a 25x25x25 nm<sup>3</sup> simulation box, the maximum domain size would thus be just above 12 nm, but as the simulation boxes for the dry films presented herein are thinner in the z-direction, the domains exhibit more of a cylindrical shape in 3D (cf. Fig. 4.11). Approximating the maximum domain size with the 2D version is thus more fitting – also considering the pseudo-3D slice-by-slice implementation of the domain size analysis – which leads to a maximum domain size of around 10 nm. The limit thus seems to have been reached for some of the simulations presented in this work, and future simulations should carefully consider this point; regrettably, the computational resources have not been available in time to include larger simulation boxes in this study. Nevertheless, the computational cost would likely be limiting for significantly larger simulation box sizes: increasing the dry film thickness to 15 nm while doubling the x- and y-dimensions to 50 nm would correspond to an eight-fold increase in the number of particles but only a two-fold increase in maximum domain size.

## 4.7 Conclusions

In this chapter, new coarse-grained MARTINI 3.0 models for molecular dynamics simulations of solution deposition of organic solar cell blends were presented. The models presented include the ubiquitous P3HT donor polymer, the PffBT4T-2OD donor polymer, and the O-IDTBR non-fullerene acceptor as well as a range of organic solvents commonly used in OPV fabrication. The models were validated using the standard MARTINI procedures as well as an extra validation of the polymer flexibilities to experimental persistence length measurements. Employing a simple solvent evaporation scheme, the dependence of the structure-property relationships of the material systems were sought investigated as a function of processing solvents, processing temperature, and annealing. The morphology evolution of the material systems during post-deposition drying was analysed, followed by an extensive analysis of the structural parameters of the dry films both before and after annealing, including domain sizes and purity, percolating

pathways, specific interface areas, and crystallite sizes. These were related to kinetic Monte Carlo simulations of time-of-flight charge carrier mobilities as well as OPV device measurements.

It was found that the phase separation and domain formation in the donor:O-IDTBR systems were exclusively controlled by donor aggregation, whereas they in donor:PCBM systems were also partly controlled by acceptor aggregation. The experimentally observed temperature dependent aggregation of the PffBT4T-2OD donor polymers was captured nicely by the model, whereas the P3HT aggregation propensity was similar across all processing temperatures and seemed too high when comparing to experimental solubilities. The expected trend of slower aggregation in less polar solvents was, however, captured. For the dry, as-cast donor:O-IDTBR films, it was difficult to identify any general trends in structural parameters as a function of processing temperature and solvent, but the PffBT4T-2OD:O-IDTBR blends in general seemed to form larger domains than the P3HT:O-IDTBR blends. In general, and fully in line with the expectations, annealing was found to increase domain sizes, domain purities, and crystallite sizes while decreasing the specific interface areas for all of the investigated combinations of material systems and processing parameters. The donor:PCBM systems furthermore showed clear trends of increased domain sizes and domain purities with increasing processing temperature. The general picture was the same for the simulated charge carrier mobilities, from which no general trends could be extracted either except for the donor:PCBM systems, which tended to have higher mobilities for increased processing temperature.

Although it was not possible to conclusively suggest optimal OPV processing parameters based on the simulations presented in this chapter, the methods outlined are expected to be useful for analysing simulations of material blends going forward. Furthermore, the presented framework as a whole can be used to investigate and visualise the effects of e.g. processing additives on organic solar cell morphologies and aid the interpretation of advanced structural measurements and their relation to device properties. However, three potential deficiencies of the framework would need to be addressed in future simulations. First, differences in evaporation rate depending on solvent and processing temperature should be considered. This could simply be done by extending the drying time according to the relative vapour pressures of the solvents, but a more physically motivated approach would be to model actual solvent evaporation from the film surface after deposition on a substrate.<sup>181,220,221</sup> Secondly, when considering self-assembly processes such as domain formation during solvent evaporation, the models should be parametrised to reproduce experimental solubilities, as their aggregation properties might otherwise be wrongly accounted for. Finally, larger simulation box sizes are needed in order to reliably extract structural parameters such as domain size. This can of course be reduced to a question of available computational resources, but for high-throughput screening of several processing conditions, simulating boxes even half an order of magnitude larger than the expected domain size is not feasible for most systems. Although simulations using more coarse-grained models, most notably the one for the P3HT:PCBM system by Lee, Pao, and Chu,<sup>255</sup> have shown to yield convincing morphologies and related structural properties,<sup>119,247,267</sup> the vast amount of new, structurally complex non-fullerene acceptors and donor polymers being synthesised for OPVs calls for more transferable models that are not specifically parametrised only for single systems. The building block approach, such as the one employed for the MARTINI force field, thus represents a more practical solution, retaining chemical specificity and

transferability and allowing direct backmapping to atomistic resolution.<sup>45</sup> A potential strategy for reducing the computational cost of MARTINI simulations could be to use implicit solvation models (as already seen for water in the "DRY MARTINI" model<sup>130</sup>), although solvent evaporation simulations could prove conceptually difficult with these. Alternatively, true multiscale simulations employing adaptive resolution schemes could be explored, coarse-graining the systems even further on-the-fly.

## 4.8 Appendix

### 4.8.1 Structural figure of merit

Table 4.11: Structural figures of merit (s-FoM) for the as-cast and annealed thin-films processed from different solvents and at different temperatures.

$T_{\text{process.}}$	s-FoM, as-cast [nm]				s-FoM, annealed [nm]			
	298 K	333 K	363 K	393 K	298 K	333 K	363 K	393 K
P3HT:O-IDTBR								
OMA	0.56	0.66	0.66	n/a	0.67	0.89	0.65	n/a
CLBZ	0.66	0.52	0.78	n/a	0.62	0.54	0.69	n/a
OXYLE	0.70	0.69	0.76	n/a	1.00	0.68	0.62	n/a
DCLBZ	0.57	1.00	0.75	n/a	0.67	0.72	0.72	n/a
PCYM	0.55	0.77	0.61	n/a	0.91	0.82	0.59	n/a
PffBT4T-2OD:O-IDTBR								
CLBZ	0.66	0.47	0.58	0.50	1.00	0.55	0.63	0.52
OXYLE	n/a	0.46	0.42	0.60	n/a	*	0.49	0.83
PCYM	n/a	0.56	0.57	0.48	n/a	0.68	0.52	0.48
Donor:PCBM in CLBZ								
P3HT	1.00	0.90	0.85	n/a	1.00	0.91	0.86	n/a
PffBT4T-2OD	0.71	0.70	0.56	0.50	0.72	1.00	0.62	0.53

## 5 Outreach projects



This chapter showcases two of the outreach projects that have been arranged by the author of this thesis along with Michael Korning Sørensen. The importance of communicating research to the broad public will be described here.



## 5.1 Motivation

The Technical University of Denmark (DTU) was founded in 1829 with the mission of creating value for the benefit of society. The strategy of DTU is thus to foster sustainable value and welfare in society through education, research, research-based advice and innovation. Clear and understandable communication of forefront research to governmental institutions, private businesses, and the broad public thus constitutes an important aspect of the responsibilities that we have as university employees. Addressing the latter two, outreach initiatives represent the most important means of attracting external collaborators and new students that allow us to fulfil this strategy.

With these outreach projects, we have tried to stimulate an interactive dialogue about our research in organic solar cells with the public. The initiatives and activities presented below aim to enhance the understanding of sustainable energy technologies and their value to society by meeting the public in public.

## 5.2 Science Pavilion at Roskilde Festival

The Science Pavilion<sup>a</sup> is an outreach project initiated by The Big Bang Collective<sup>b</sup> in collaboration with the European Organization for Nuclear Research (CERN) and the Niels Bohr Institute at the University of Copenhagen. The Science Pavilion was part of the official programme of Roskilde Festival 2019, one of Europe's biggest music events with more than 130,000 people attending during the week-long festival. Various shows, panel discussions on sustainable energy, and workshops were hosted during the four warm-up days of Roskilde Festival, and the camping sites were toured with the Science Show on Wheels. Specifically, our team from DTU Energy hosted the "Make a Solar Charger" workshop and had the responsibility of engaging and attracting people for the shows and workshops. If the current pandemic allows, the Science Pavilion has been confirmed as part of the programme at Roskilde Festival 2021.

As the eye-catcher of the Science Pavilion, the Solar Tree Project was initiated. The Solar Tree was, as the name implies, an installation built in the shape of a tree that provided solar power, shade, and seating for the users (see Fig. 5.1). The overarching aim of the installation was to spark curiosity amongst young festival goers towards sustainable energy and to invite dialogue about emerging solar cell technologies being researched at DTU Energy through incorporating these in the installation. The huge success of the Solar Tree and the Science Pavilion in general earned us an invitation back to the next edition of the Roskilde Festival, and we thus set out to rethink the concept and improve the design. We teamed up with three student from the DTU Design and Innovation study line and their supervisor to build a new version of the Solar Tree. This can be seen in Fig. 5.2, and a small catalogue enclosed in Appendix A, Section 5.4 presents the concept, the design, and the stakeholders in the project.

The new version of the Solar Tree was built to better resemble the shape of a tree to further signal sustainability and could again provide power, shade, and seating. As opposed to the first version, which relied on a crystalline silicon solar panel, the power to charge user electronics is generated from organic solar cells, which, due to their semi-transparency, additionally provides a pleasant shade for the users relaxing in the seats associated with the installation. The tree also features an interactive user experience that

---

<sup>a</sup><https://sciencepavilion.nbi.dk/>

<sup>b</sup><https://www.lancaster.ac.uk/physics/outreach/big-bang-collective/>



Figure 5.1: The first version of the Solar Tree installed at Roskilde Festival 2019.



Figure 5.2: The new version of the Solar Tree to be installed at Roskilde Festival 2021; the left panel shows a scale model of the design and the right panel shows the first build of the wooden skeleton for the new Solar Tree.

seeks to inform about the technology behind organic solar cells as well as sustainability as a broader concept through easily comprehensible illustrations and videos.

With the Solar Tree, we hope to catch the attention of the young festival goers with an appealing design and in turn to spark their curiosity with the fascinating properties of organic solar cells such as flexibility and semi-transparency. A prerequisite for this is to communicate advanced research topics in an accessible manner, and the installation is designed exactly with this in mind. Running out of power, whether it's you or your phone, is always a problem at a busy festival, and by providing a solution with recharging, shade, and seating will buy us the time it takes for the users to look around and get curious. The combination of light explanatory text and a touch screen directly incorporated in the tree with illustrations and videos will maintain the attention of the users and fulfil the purpose of creating awareness of both emerging solar cell technologies and the science and study programs at DTU.

Roskilde Festival brands itself on having a sustainable profile and has a focus on art and activism in addition to the music. The Solar Tree installation embraces both of these profiles, being a functional art installation that runs solely on green energy. It also



Figure 5.3: Pictures from the DTU Energy tent at the Grand Opening of Amager Bakke/CopenHill.

adds value for both the festival and the festival goers by providing a place for recharging user electronics and learning about sustainable energy technologies. Already with the Science Pavilion at Roskilde Festival 2019 and the first version of the Solar Tree, it was demonstrated that we could reach thousands of people who did not proactively seek out science in a matter of days. This project is, as a now recurring installation at Roskilde Festival, thus an excellent opportunity for DTU Energy to continuously reach out to especially young people in the ages of 16-25 years and communicate the research we are involved in.

### 5.3 Grand Opening of Amager Bakke/CopenHill

Amager Bakke<sup>c</sup> is a combined heat and power waste-to-energy plant in Copenhagen. Famously designed by the Bjarke Ingels Group (BIG) architects, it houses a multi-sports facility with an artificial hiking and skiing slope on top and the world's tallest climbing wall on the side. The organisers of the Grand Opening<sup>d</sup> of Amager Bakke to the public had heard about our workshops at Roskilde Festival in the summer of 2019 and contacted us to ask if we would like to host similar activities for the families attending the opening weekend. With the waste-to-energy plant being an integral part of Copenhagen's 2025 climate strategy, a strong focus on sustainable technologies was desired, with DTU Energy representing future solutions. Given the very broad target audience, from young kids to pensioners, we designed a collection of explanatory posters and organised a quiz alongside the "Make a Solar Charger" workshop. These posters and the quiz are enclosed Appendix B, Section 5.5 (in Danish). Particularly the young kids of age 10-16 years were excited for the workshop and the quiz, whereas their parents showed great interest in the organic solar cell technology and its potential to reduce the embedded energy in solar cells by roll-to-roll fabrication and solution processing. Attending events like these thus represents an excellent opportunity for DTU Energy to reach out to different age groups than the ones usually present at e.g. music festivals.

<sup>c</sup><https://a-r-c.dk/amager-bakke/>

<sup>d</sup><https://www.copenhill.dk/en/news/presse-materiale-copenhill-grand-opening>



## 5.4 Appendix A: Solar Tree catalogue



Department of Energy Conversion and Storage  
Department of Mechanical Engineering

A photograph of a 'Solar Tree' installation in a grassy field. The tree has a central vertical pole with several blue, curved solar panels attached to it, resembling leaves. The base of the tree is made of several brown, cylindrical logs arranged in a circular pattern. The background shows a green lawn and trees.

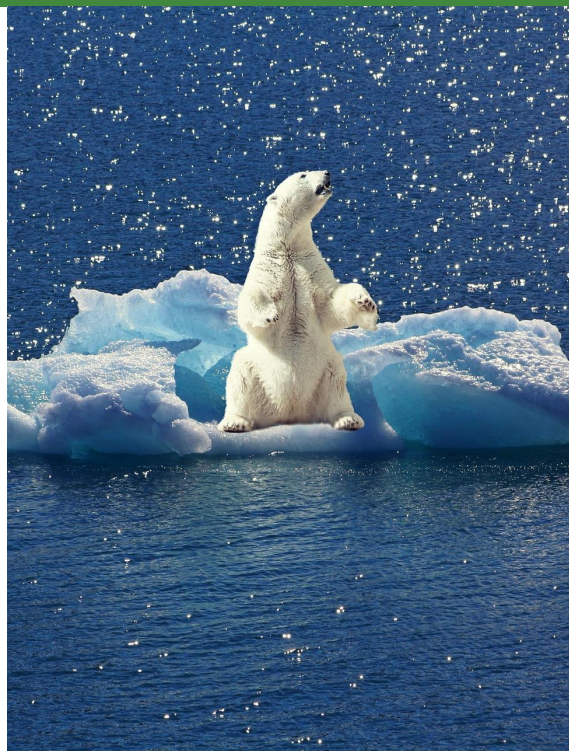
# The Solar Tree

### Our mission

Global warming is one of the most pressing challenges of the current century. In order to mitigate the consequences of climate change, each of us must do our best to reduce our emissions and to recycle.

We believe that the best way of motivating environmentally friendly behaviour is through the sharing of knowledge about sustainable energy technologies in an accessible manner.

This project aims to spark curiosity by showcasing organic solar cells in an innovative, interactive installation and to inform about the potential of this novel technology.



## Our technology

Organic solar cells consist of, as the name suggests, organic materials in the form of small molecules and polymers that convert photons from the sun to electrical current. These materials enable low-energy fabrication on flexible substrates, and organic solar cells can literally be printed on rolls of plastic such as what soda bottles are made of. This means that organic solar cells can compensate for the energy consumed during fabrication in only a few months once operational – less than ten times the time it takes for conventional silicon solar cells!

Organic solar cells are flexible, very thin, ultra low-weight, and can even be made semi-transparent and in a variety of colors. This enables high architectural freedom in building integrations and artistic installations.



## Our value

The *Solar Tree* provides power, shade and seating in addition to educating curious minds. It allows charging of electronic devices directly from 100 % green energy through high-output USB charging hubs.

The *Solar Tree* aims to inspire, educate, and engage festival guests in sustainable energy, the potential of novel solar cell technologies, as well as engineering in general.

The *Solar Tree* showcases the architectural possibilities of organic solar cells through an aesthetically pleasing design inspired by palm trees. This enables a seamless blend into a festival environment and encourages innovation and creativity as tools to combat climate change.



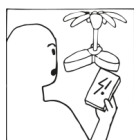


## User scenarios

### *Power, shade, seating – and education*

The most probable user scenarios are driven by either running out of power, finding the solar tree visually attractive, or by being curious about the technology and engineering behind the *Solar Tree*. The aim is for the *Solar Tree* to be self-explanatory and for the greeters to chip in with expert knowledge if the users are interested in learning more.

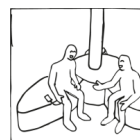
### Need-driven interaction



a) The user requires a charging facility for his/her phone and sees the *Solar Tree*

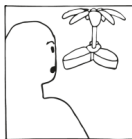


b) The user spots the USB-ports and charges his/her phone whilst admiring the installation



c) The user is met by a greeter and is interested in hearing more about the *Solar Tree* during charging

### Visually driven interaction



a) The user sees the *Solar Tree* and becomes interested in its biologically inspired design



b) The user adjusts the leaves and observes that the power output of the tree is increased

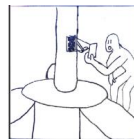


c) The user is inspired and willing to engage in conversation with the greeters

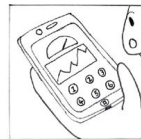
### Curiosity-driven interaction



a) The user interacts with the *Solar Tree* and is inspired to know more



b) The user notices the QR code on the stem and scans it to get access to the online app



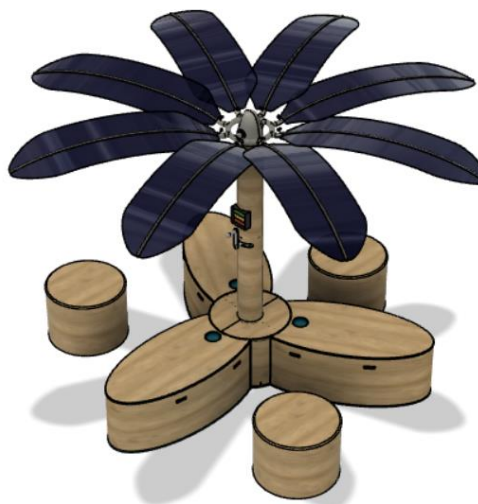
c) The user can see power output, number of available ports, and read about the project at any time

## Components

The *Solar Tree* is designed to enable easy installation and transportation, and it can thus be readily assembled from the following components:

- i. Hub
- ii. Benches
- iii. Stem
- iv. Mechanism
- v. Crown
- vi. Stools and games
- vii. Leaves
- viii. Electronics

These will all be described in detail on the following pages.



# Components

## i. Hub

The hub is centre of the solar tree in which all electronic components are connected and stored. It is made from plywood supported by a steel framework. A cylindrical tube provides a stable base for the stem and allows for easy assembly. Lids on hinges can be locked to allow easy access as well as prevent theft. A concave rotation base allows the mechanism (see point iv.) to rotate like a spinning top.



## ii. Benches

The three benches are built from plywood and provides seating whilst the guests charge their phones from high-output USB charging hubs integrated in the sides. The benches are also equipped with LED projectors which illuminate the solar panels from below at night, making the *Solar Tree* a round-the-clock gathering spot. The benches can easily be attached and fixed to the hub with locking rods.



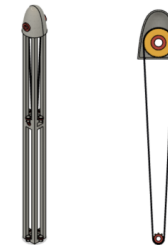
## iii. Stem

The stem of the solar tree is made of plywood. The stem features a handle controlling the angle and rotation of the crown (see point v.), which allows the user to easily change the relative orientation of the solar cells to the sun. A built-in power meter displays the solar cells' output as a function of this angle. Furthermore, a QR code is placed on the side of the stem for easy access to the online app that shows information about the project – go ahead, try it!



## iv. Mechanism

The mechanism controls the rotation and angle of the crown through the rotation and sliding of the handle on the stem (cf. point iii.), enabling the *Solar Tree* to smoothly rotate on two axes. The mechanism is built from a strong stainless steel frame, which supports the gears and the crown (see point v.). With a gearing of 1:6, two sprockets and a chain transfers the rotational force of the handle to the crown, while eight ball bearings provide stable rotation of the stem.



# Components

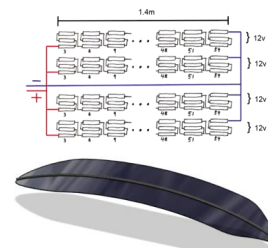
## v. Crown

The crown of the solar tree is a stainless steel structure that supports and connects the leaves to the electronics running through the stem through two-pin cable connectors. The eight connection points to the leaves are designed to enable easy attachment and securing of the leaves using screws. The crown is connected to the tilt mechanism through a chain with a 1:6 gearing and to the rotation mechanism through ball bearings as described in point iv.



## vii. Leaves

The leaves are made from organic solar cells that are laser cut into the shape of palm tree leaves. Owing to the unique properties of organic solar cells, the leaves are semi-transparent and flexible, giving them a natural bend and providing a pleasant shade. The solar cells are supported by PVC plastic tubing, through which the wiring is also run. This results in an elegant and simple design.



## vi. Stools and games

Three stools built from plywood are placed around the solar tree, providing seating for varying group sizes. The stools are secured to the hub by a long steel wire to prevent theft. We envisage that small games that require no or only improvised pieces can be engraved in the stools to entertain users whilst they charge their phones. The stools can thus also be used as small tables. Furthermore, a trash bin voting game will be set up to encourage users to properly dispose of their litter.



## viii. Electronics

The output of the organic solar cell leaves (see point vii.) depends strongly on the weather, so an inverter is used to ensure a steady output voltage before storing the energy in a battery. The USB charging hubs are then connected to the battery, allowing users to charge their electronics at all times. An internet-of-things system is connected to an Arduino microcontroller, which updates the online app with live information about the power output and number of available charging ports.

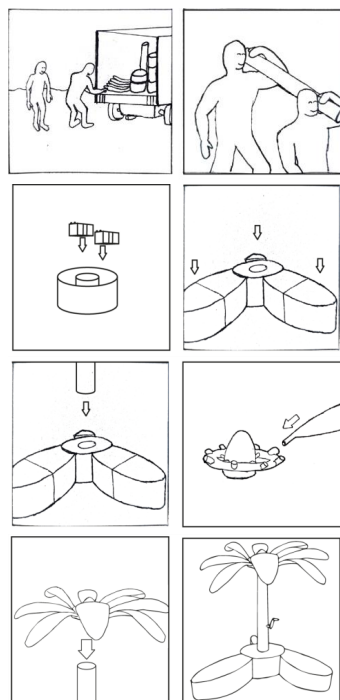


## Installation

The *Solar Tree* is designed to be easy to transport, install, and disassemble. Each of the components will weigh less than 70 kg, allowing them to be carried by two persons.

After securing the hub with ground spikes, the benches are attached to this with locking rods. The benches themselves can also be secured to the ground with spikes. Then, the stem and the mechanism are secured in the hub, and the electrical components are connected. Finally, the crown with the attached leaves can be put on and secured.

In fact, assembling the *Solar Tree* is so simple that we could have let our small cartoon speak for itself.



## Materials

The *Solar Tree* will be built from commonly available materials – only the organic solar cells are not readily available for purchase. To the right, we have listed all materials needed for the main structure (i.e. excluding the organic solar cells, the inverter, and the battery, which will all be provided by the Technical University of Denmark, DTU).

As described in the previous pages, the individual components are built to be sturdy and to be able to withstand typical use, light misuse, and weather conditions at a festival. All electrical components are shielded, and the leaves are designed with a weakest link in the PVC tube close to the connection point to the crown so that the easily replaceable PVC tube breaks before any valuable components.

Part number	Part name	Quantity
<b>Arduino</b>		
1.1	Current + voltage sensor	1
1.2	Micro controller	1
1.3	USB charging hub	3
1.4	USB cable	12
1.5	Wiring	1
1.6	SD card	1
1.7	SD card reader	1
1.8	LED lamps	1
1.9	LED power output screen	1
1.10	Current sensor	12
1.11	USB-port LED indicator	3
<b>Structure</b>		
2.2	Base cylinder	1
2.3	Ply wood 18x1220x2440 mm	5
2.4	Ply wood 9x1220x2440 mm	5
2.5	Steel profiles 20x20x2x6000 mm	3
2.6	Steel tubes 1500 mm, Ø50 mm	1
2.7	Screws 4 x 45 mm (100 stk)	2
2.8	PVC tubes 20x1.4x5000 mm	5
2.9	Large ball bearing	2
2.10	Small ball bearing	10
2.11	60 tooth sprocket	1
2.12	9 tooth sprocket	1
2.13	96 link chain	3
<b>Wiring</b>		
4.1	Cable 1m	120
4.2	5 x 2 pin cable connectors	4
4.3	200 x nail-in cable clips	1
4.4	100 x strips	1
<b>Miscellaneous</b>		
5.1	Steel wire 1m	12
5.2	Lock	4
5.3	Hinge	4
5.4	Wood protection	2



## Our team and partners

The idea of the *Solar Tree* was first conceived in 2019 by Anders and Michael as an eye-catcher for *Science Pavilion* at *Roskilde Festival 2019*. The first version of the *Solar Tree* was indeed a success, but much could still be improved – a collaboration with Lasse, Nikolaj, and Oskar and their supervisor Torben was hence started, and what you see today is the result of their hard work during their Bachelor's projects at DTU.



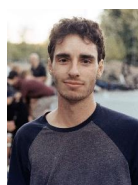
**Anders S. Gertsen**  
Ph.D. student  
Modelling of organic  
solar cells  
DTU Energy



**Michael K. Sørensen**  
Ph.D. student  
X-ray measurements  
of organic solar cells  
DTU Energy



**Torben A. Lenau**  
Assoc. Prof.  
Eng. design and  
product develop.  
DTU Mech. Eng.



**Lasse P. S. Hansen**  
B.Sc. student  
Design and  
innovation  
DTU Mech. Eng.



**Nikolaj C. C. Brun**  
B.Sc. Student  
Design and  
innovation  
DTU Mech. Eng.



**Oskar H. Møller**  
B.Sc. Student  
Design and  
innovation  
DTU Mech. Eng.

### Contact

Technical University of Denmark  
Department of Energy Conversion and  
Storage (DTU Energy)

Fysikvej  
Building 310  
2800 Kgs. Lyngby  
[www.energy.dtu.dk](http://www.energy.dtu.dk)

### Questions

Anders S. Gertsen, DTU Energy  
Phone +45 30 70 64 42  
[askov@dtu.dk](mailto:askov@dtu.dk)

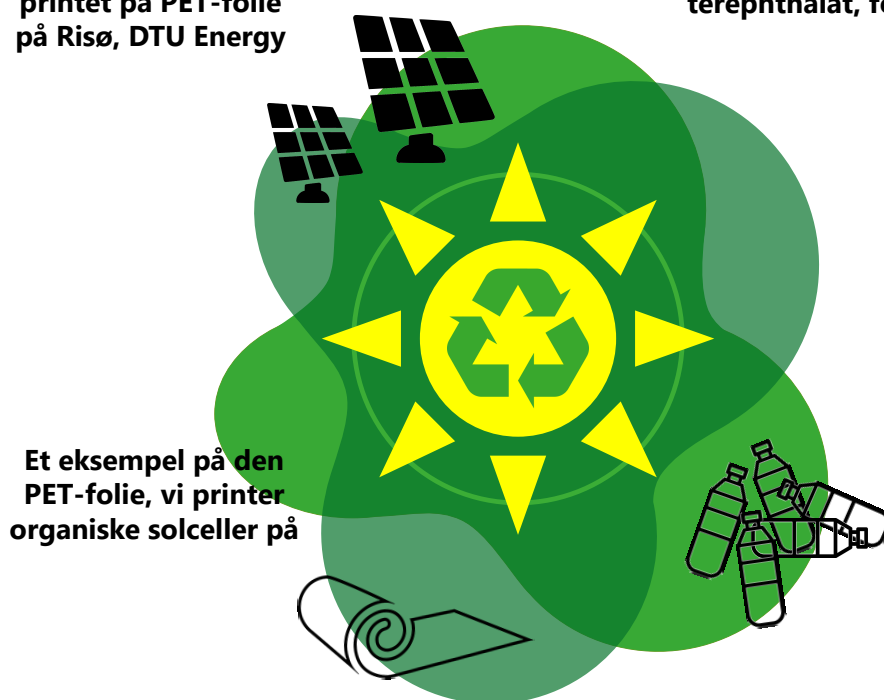
## 5.5 Appendix B: Explanatory posters and quiz



**Plastikaffald er et stort problem, hvis det ender i verdenshavene – så hvorfor ikke genbruge plast og printe organiske solceller på det i stedet?**

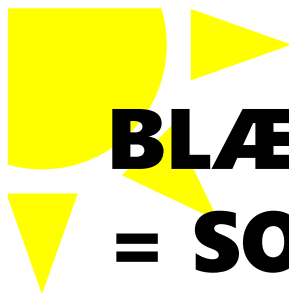
Organiske solceller  
printet på PET-folie  
på Risø, DTU Energy

Plastflasker er oftest lavet  
af polymeren polyethylen-  
terephthalat, forkortet PET



Et eksempel på den  
PET-folie, vi printer  
organiske solceller på





# BLÆK+PRINTER = SOLCELLER



Tænk, hvis vi bare kunne printe meter efter meter af solceller... det kan vi faktisk! Organiske solceller kan printes på store ruller af plastik ved hjælp af de samme teknikker, som vi kender fra printeren på kontoret og fra industriel printning af ugeblade



Først printes en gennemsigtig elektrode på PET-folien – den blæk, der bruges, består blandt andet af polymerer, der kan lede strøm



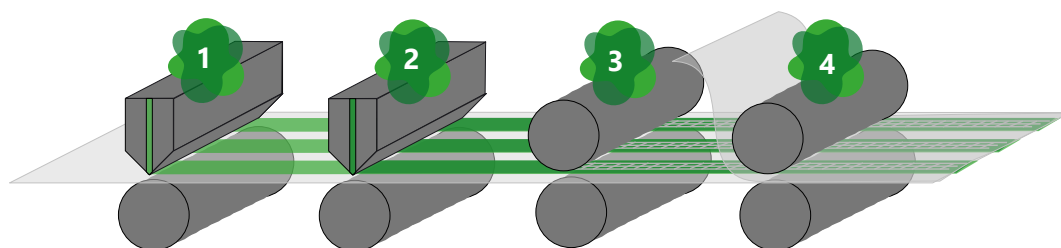
I tredje trin bliver top-elektroderne trykt på – de består ofte af en tyk pasta af sølv



Dernæst printes det aktive lag med en blæk bestående af polymerer og små molekyler – der findes hundredvis af forskellige typer blæk



Til sidst limes et lag PET-folie ovenpå stakken, så solcellen beskyttes mod luft og vand

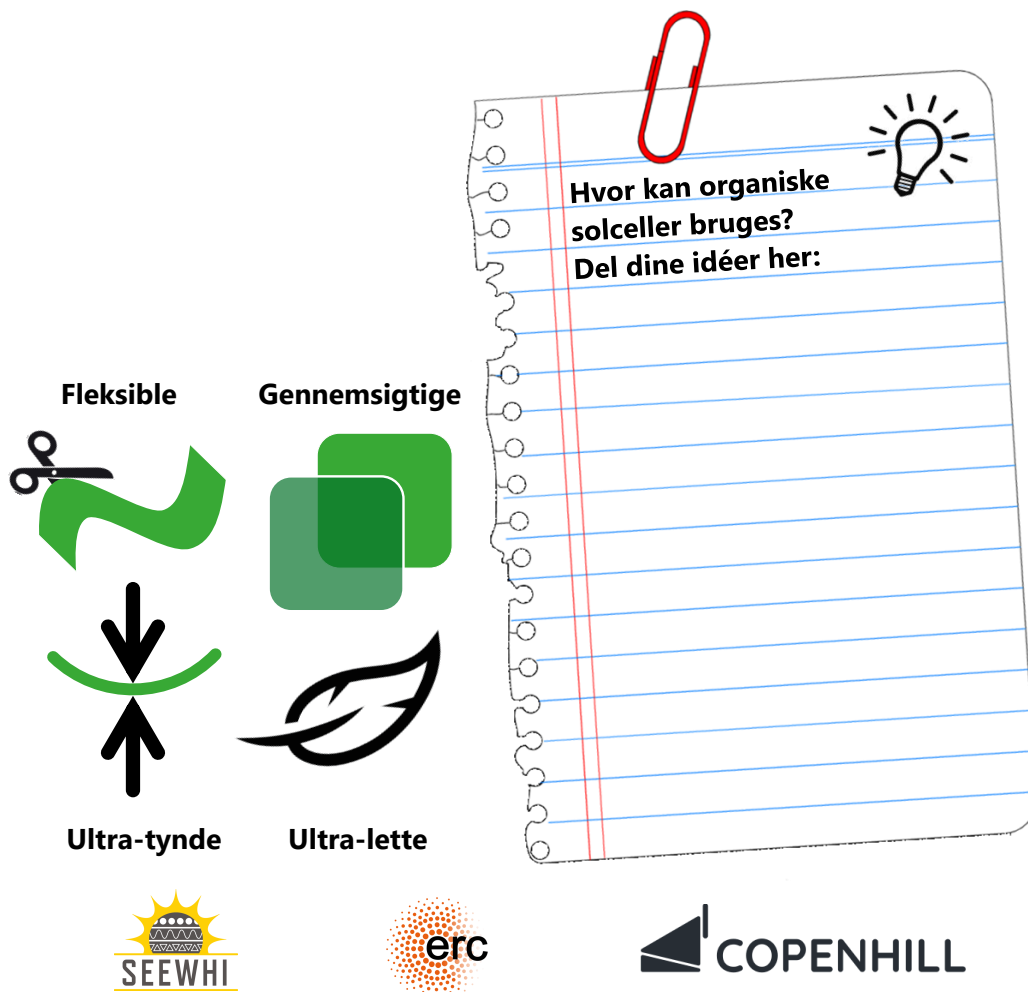




# FLEKSIBLE OG GENNEMSIGTIGE



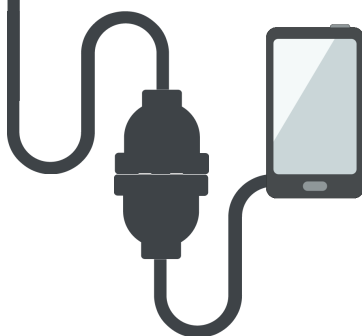
Ved at printe på plastik kan organiske solceller gøres både fleksible og gennemsigtige – og så kan de tilmed klippes til lige præcis den form, du ønsker! Kombineret med den lille tykkelse og lette vægt gør det organiske solceller ideelle til bygningsintegrering



# WORKSHOP: BYG EN SOLCELLE



Har du før stået og manglet en stikkontakt? Her kan du bygge din egen solcelleoplader til powerbanks og smartphones – lige til at tage med dig hjem!



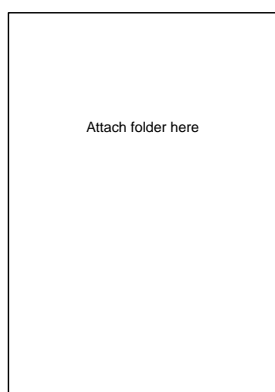
Kobber-  
tape

USB-port

Attach demonstration  
solar charger here

Silicium-  
solceller

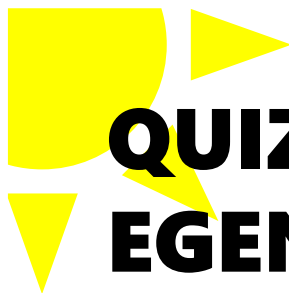
**Snup en guide her!**



## Hvad er forskellen på organiske solceller og silicium-solceller?

Det aktive lag i en solcelle er det lag, der omdanner solens stråler til strøm. I organiske solceller består det aktive lag af polymerer og molekyler, mens det aktive lag i silicium-solceller er krystaller af silicium. Silicium-krystallerne kan ikke printes og er hverken gennemsigtige eller fleksible. Til gengæld er silicium-solceller stadig mere effektive og stabile end de organiske – og tilmed billigere.





# QUIZ: VIND DIN EGEN SOLCELLE



**Deltag i vores quiz om organiske solceller og vær med i lodtrækningen om 12 laser-pointere drevet af organiske solceller! Vi trækker én ny vinder hver time fra kl. 12-17 – vinderne får direkte besked**

Det er sådan én,  
du kan vinde!



Attach  
laser-  
pointer  
here



**Snup en quiz her!**

**Aflevér din quiz her!**

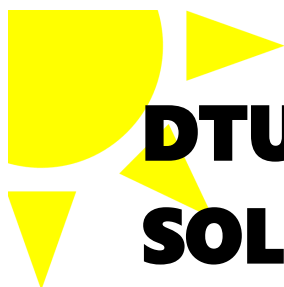
Attach folder here

Er vi løbet tør  
for kuglepenne?  
Spørg en i en DTU  
t-shirt efter flere!

Attach pen  
holder here

Attach folder here





# DTU ENERGIS SOLCELLEQUIZ



1

Hvor meget vejer 1 m<sup>2</sup> organiske solceller cirka?

- ☐ 50 g
- ☐ 500 g
- ☐ 5 kg

2

Hvor mange gram af det aktive materiale skal bruges til at printe 1 m<sup>2</sup> organiske solceller?

- ☐ 0.1 g/m<sup>2</sup>
- ☐ 1 g/m<sup>2</sup>
- ☐ 5 g/m<sup>2</sup>

3

Hvor tykt er det aktive lag typisk i organiske solceller?

Hint: et hår er ca. 100 µm tykt

- ☐ 0.1 µm
- ☐ 10 µm
- ☐ 100 µm

4

Hvad er verdensrekorden for effektivitet af organiske solceller?

- ☐ Under 8 %
- ☐ Omkring 14 %
- ☐ Over 17 %

5

Hvad effektiviteten af masseproducerede, fleksible organiske solceller typisk?

- ☐ Under 4 %
- ☐ Omkring 7 %
- ☐ Over 10 %

Hvis du har lyst til at deltage i lodtrækningen om en laser-pointer drevet af organiske solceller, kan du skrive dine kontaktoplysninger\* her - vi trækker lod hver time:

Navn: \_\_\_\_\_

E-mail: \_\_\_\_\_

\*Bruges udelukkende til at kontakte vindere



## 6 Outlook

The organic solar cell technology has experienced a remarkable development in the last five years. With the record efficiencies of lab-scale devices now being above 18 %, <sup>15,16</sup> the projected lifetimes closing in on double digit years, <sup>37,38</sup> and highly encouraging reports of large-scale modules breaking the 10 % efficiency barrier emerging, <sup>35,36</sup> the technology is edging towards commercialisation. Although the gap between lab-scale and large-scale efficiencies is significant, the scientific literature remains focused on the synthesis of new materials and reaching the 20 % efficiency mark. Whereas this is obviously the main driver for the rapid development seen in recent years, accompanying these efforts by an increased focus on scalable deposition methods, stability test, and on reducing the synthetic complexity of the active materials is believed to be crucial for maturing the technology. <sup>39,210,227,268</sup>

The continuously increasing number of exciting new materials being synthesised for organic solar cells, however, complicates the modelling aspects of the field. With the state-of-the-art changing almost by the month, highly transferable, coarse-grained models based on building block approaches constitute the most promising strategy towards feasibly simulating the effects of varying processing parameters on relevant time and length scales. The MARTINI force field currently represents the most accessible framework of this kind with comprehensive tutorials, open-source extensions, and an upcoming new version 3.0 tailored to conjugated ring-systems. <sup>237</sup> Using this, it was shown in Chapter 4 how the morphology evolution in solution processed organic solar cell blends could be simulated. However, as discussed both in this and in Chapter 3, modelling substrate effects as well as a more physically correct solvent evaporation process with diffusion of solvent towards an air-interface is believed to be important, <sup>181</sup> and it should be addressed in combination with coarse-grained models that allow reaching the necessary time and length scales for phase separation. Work on this is currently ongoing.

In addition to being able to simulate the morphologies of solution processed organic functional materials, the main goal of this work was to establish methods for relating the simulations to advanced X-ray measurements. A rigorous and general analysis framework has been outlined, enabling the extraction of structural parameters with relevance to experimental measurables. Furthermore, the combined simulation and analysis procedure allows visualisation of the morphology formation, yielding valuable insight into the processes governing the structural evolution, and the bridging of scales allow the calculation of electronic properties as a function of the structures.

Finally, the importance of communicating science and research to the broad public was underlined. Not only the universities, but also private companies and society as a whole can benefit from improved communication, as potential research and collaboration opportunities are more easily uncovered and the future bright minds more easily attracted.





# Bibliography

- [1] "Paris agreement to the united nations framework convention on climate change." Dec. 12, 2015, T.I.A.S. No. 16-1104.
- [2] UN General Assembly, "Transforming our world: the 2030 agenda for sustainable development." Oct. 21, 2015, A/RES/70/1, overview at <https://sdgs.un.org/goals> (accessed on November 23, 2020).
- [3] IEA, "Renewables 2019: Analysis and forecast to 2024," Report, International Energy Agency, 2019. Overview at <https://www.iea.org/reports/renewables-2019> (accessed on November 23, 2020).
- [4] EIA, "Annual energy outlook 2020 – with projections to 2050," Report, U.S. Energy Information Administration, 2020. Overview at <https://www.eia.gov/outlooks/aeo/> (accessed on November 23, 2020).
- [5] P. C. K. Vesborg and T. F. Jaramillo, "Addressing the terawatt challenge: scalability in the supply of chemical elements for renewable energy," *RSC Adv.*, vol. 2, pp. 7933–7947, 2012.
- [6] C. C. Pavel, R. Lacal-Arántegui, A. Marmier, D. Schöler, E. Tzimas, M. Buchert, W. Jenseit, and D. Blagoeva, "Substitution strategies for reducing the use of rare earths in wind turbines," *Resour. Policy*, vol. 52, pp. 349 – 357, 2017.
- [7] A. Bonou, A. Laurent, and S. I. Olsen, "Life cycle assessment of onshore and offshore wind energy-from theory to application," *Appl. Energy*, vol. 180, pp. 327 – 337, 2016.
- [8] J. Peng, L. Lu, and H. Yang, "Review on life cycle assessment of energy payback and greenhouse gas emission of solar photovoltaic systems," *Renew. Sustainable Energy Rev.*, vol. 19, pp. 255 – 274, 2013.
- [9] F. C. Krebs, "Fabrication and processing of polymer solar cells: A review of printing and coating techniques," *Sol. Energy Mater. Sol. Cells*, vol. 93, no. 4, pp. 394 – 412, 2009.
- [10] R. Söndergaard, M. Hösel, D. Angmo, T. T. Larsen-Olsen, and F. C. Krebs, "Roll-to-roll fabrication of polymer solar cells," *Mater. Today*, vol. 15, no. 1, pp. 36 – 49, 2012.
- [11] N. Espinosa, M. Hösel, D. Angmo, and F. C. Krebs, "Solar cells with one-day energy payback for the factories of the future," *Energy Environ. Sci.*, vol. 5, pp. 5117–5132, 2012.
- [12] O. Almora, D. Baran, G. C. Bazan, C. Berger, C. I. Cabrera, K. R. Catchpole, S. Erten-Ela, F. Guo, J. Hauch, A. W. Y. Ho-Baillie, T. J. Jacobsson, R. A. J. Janssen, T. Kirchartz, N. Kopidakis, Y. Li, M. A. Loi, R. R. Lunt, X. Mathew, M. D. McGehee, J. Min, D. B. Mitzi, M. K. Nazeeruddin, J. Nelson, A. F. Nogueira, U. W. Paetzold, N.-G. Park, B. P. Rand, U. Rau, H. J. Snaith, E. Unger, L. Vaillant-Roca, H.-L. Yip, and C. J. Brabec, "Device performance of emerging photovoltaic materials (version 1)," *Adv. Energy Mater.*, p. 2002774, 2020.
- [13] M. Green, E. Dunlop, J. Hohl-Ebinger, M. Yoshita, N. Kopidakis, and X. Hao, "Solar cell efficiency tables (version 57)," *Prog. Photovolt. Res. Appl.*, vol. 29, no. 1, pp. 3–15, 2021.
- [14] NREL, "Best research cell efficiency," Chart, National Renewable Energy Laboratory, U.S. Department of Energy, 2020.
- [15] Q. Liu, Y. Jiang, K. Jin, J. Qin, J. Xu, W. Li, J. Xiong, J. Liu, Z. Xiao, K. Sun, S. Yang,

- X. Zhang, and L. Ding, "18 % efficiency organic solar cells," *Sci. Bull.*, vol. 65, no. 4, pp. 272 – 275, 2020.
- [16] Y. Lin, Y. Firdaus, F. H. Isikgor, M. I. Nugraha, E. Yengel, G. T. Harrison, R. Hallani, A. El-Labban, H. Faber, C. Ma, X. Zheng, A. Subbiah, C. T. Howells, O. M. Bakr, I. McCulloch, S. D. Wolf, L. Tsetseris, and T. D. Anthopoulos, "Self-assembled monolayer enables hole transport layer-free organic solar cells with 18% efficiency and improved operational stability," *ACS Energy Lett.*, vol. 5, no. 9, pp. 2935–2944, 2020.
- [17] A. Gambhir, P. Sandwell, and J. Nelson, "The future costs of OPV - a bottom-up model of material and manufacturing costs with uncertainty analysis," *Sol. Energy Mater. Sol. Cells*, vol. 156, pp. 49 – 58, 2016.
- [18] M. P. Tsang, G. W. Sonnemann, and D. M. Bassani, "Life-cycle assessment of cradle-to-grave opportunities and environmental impacts of organic photovoltaic solar panels compared to conventional technologies," *Sol. Energy Mater. Sol. Cells*, vol. 156, pp. 37 – 48, 2016.
- [19] L. Ma, S. Zhang, J. Wang, Y. Xu, and J. Hou, "Recent advances in non-fullerene organic solar cells: from lab to fab," *Chem. Commun.*, vol. 56, pp. 14337–14352, 2020.
- [20] F. C. Krebs, S. A. Gevorgyan, and J. Alstrup, "A roll-to-roll process to flexible polymer solar cells: model studies, manufacture and operational stability studies," *J. Mater. Chem.*, vol. 19, pp. 5442–5451, 2009.
- [21] B. Roth, R. Søndergaard, and F. Krebs, "7 - roll-to-roll printing and coating techniques for manufacturing large-area flexible organic electronics," in *Handbook of Flexible Organic Electronics* (S. Logothetidis, ed.), pp. 171 – 197, Oxford: Woodhead Publishing, 2015.
- [22] J. E. Carlé, M. Helgesen, M. V. Madsen, E. Bundgaard, and F. C. Krebs, "Upscaling from single cells to modules - fabrication of vacuum- and ito-free polymer solar cells on flexible substrates with long lifetime," *J. Mater. Chem. C*, vol. 2, pp. 1290–1297, 2014.
- [23] P. Cheng, Y. Lin, N. K. Zawacka, T. R. Andersen, W. Liu, E. Bundgaard, M. Jørgensen, H. Chen, F. C. Krebs, and X. Zhan, "Comparison of additive amount used in spin-coated and roll-coated organic solar cells," *J. Mater. Chem. A*, vol. 2, pp. 19542–19549, 2014.
- [24] Y.-C. Huang, H.-C. Cha, C.-Y. Chen, and C.-S. Tsao, "Morphological control and performance improvement of organic photovoltaic layer of roll-to-roll coated polymer solar cells," *Sol. Energy Mater. Sol. Cells*, vol. 150, pp. 10 – 18, 2016.
- [25] Y.-C. Huang, H.-C. Cha, C.-Y. Chen, and C.-S. Tsao, "A universal roll-to-roll slot-die coating approach towards high-efficiency organic photovoltaics," *Prog. Photovoltaics*, vol. 25, no. 11, pp. 928–935, 2017.
- [26] L. Lucera, P. Kubis, F. W. Fecher, C. Bronnbauer, M. Turbiez, K. Forberich, T. Ameri, H. Egelhaaf, and C. J. Brabec, "Guidelines for closing the efficiency gap between hero solar cells and roll-to-roll printed modules," *Energy Technol.*, vol. 3, no. 4, pp. 373–384, 2015.
- [27] T. R. Andersen, H. F. Dam, M. Hösel, M. Helgesen, J. E. Carlé, T. T. Larsen-Olsen, S. A. Gevorgyan, J. W. Andreasen, J. Adams, N. Li, F. Machui, G. D. Spyropoulos, T. Ameri, N. Lemaître, M. Legros, A. Scheel, D. Gaiser, K. Kreul, S. Berny, O. R. Lozman, S. Nordman, M. Välimäki, M. Vilkmann, R. R. Søndergaard, M. Jørgensen, C. J. Brabec, and F. C. Krebs, "Scalable, ambient atmosphere roll-to-roll manufacture of encapsulated large area, flexible organic tandem solar cell modules," *Energy Environ. Sci.*, vol. 7, pp. 2925–2933, 2014.
- [28] N. K. Zawacka, T. R. Andersen, J. W. Andreasen, L. H. Rossander, H. F. Dam, M. Jørgensen, and F. C. Krebs, "The influence of additives on the morphology and stability of roll-to-roll processed polymer solar cells studied through ex situ and in situ X-ray scattering," *J. Mater. Chem. A*, vol. 2, pp. 18644–18654, 2014.
- [29] A. P. L. Böttiger, M. Jørgensen, A. Menzel, F. C. Krebs, and J. W. Andreasen, "High-throughput roll-to-roll X-ray characterization of polymer solar cell active layers," *J. Mater. Chem.*, vol. 22, pp. 22501–22509, 2012.
- [30] L. H. Rossander, N. K. Zawacka, H. F. Dam, F. C. Krebs, and J. W. Andreasen, "In situ

monitoring of structure formation in the active layer of polymer solar cells during roll-to-roll coating," *AIP Adv.*, vol. 4, no. 8, 2014. 087105.

- [31] L. H. Rossander, H. F. Dam, J. E. Carle, M. Helgesen, I. Rajkovic, M. Corazza, F. C. Krebs, and J. W. Andreasen, "In-line, roll-to-roll morphology analysis of organic solar cell active layers," *Energy Environ. Sci.*, vol. 10, pp. 2411–2419, 2017.
- [32] W. Chen and Q. Zhang, "Recent progress in non-fullerene small molecule acceptors in organic solar cells (OSCs)," *J. Mater. Chem. C*, vol. 5, pp. 1275–1302, 2017.
- [33] S.-I. Na, Y.-H. Seo, Y.-C. Nah, S.-S. Kim, H. Heo, J.-E. Kim, N. Rolston, R. H. Dauskardt, M. Gao, Y. Lee, and D. Vak, "High performance roll-to-roll produced fullerene-free organic photovoltaic devices via temperature-controlled slot die coating," *Adv. Mater.*, vol. 29, no. 6, p. 1805825, 2019.
- [34] Y. Lin, Y. Jin, S. Dong, W. Zheng, J. Yang, A. Liu, F. Liu, Y. Jiang, T. P. Russell, F. Zhang, F. Huang, and L. Hou, "Printed nonfullerene organic solar cells with the highest efficiency of 9.5 %," *Adv. Energy Mater.*, vol. 8, no. 13, p. 1701942, 2018.
- [35] G. Wang, J. Zhang, C. Yang, Y. Wang, Y. Xing, M. A. Adil, Y. Yang, L. Tian, M. Su, W. Shang, K. Lu, Z. Shuai, and Z. Wei, "Synergistic optimization enables large-area flexible organic solar cells to maintain over 98% pce of the small-area rigid devices," *Adv. Mater.*, vol. 32, no. 49, p. 2005153, 2020.
- [36] A. Distler, C. J. Brabec, and H.-J. Egelhaaf, "Organic photovoltaic modules with new world record efficiencies," *Prog. Photovolt. Res. Appl.*, vol. 29, no. 1, pp. 24–31, 2021.
- [37] X. Du, T. Heumueller, W. Gruber, A. Classen, T. Unruh, N. Li, and C. J. Brabec, "Efficient polymer solar cells based on non-fullerene acceptors with potential device lifetime approaching 10 years," *Joule*, vol. 3, no. 1, pp. 215 – 226, 2019.
- [38] X. Xu, J. Xiao, G. Zhang, L. Wei, X. Jiao, H.-L. Yip, and Y. Cao, "Interface-enhanced organic solar cells with extrapolated T80 lifetimes of over 20 years," *Sci. Bull.*, vol. 65, no. 3, pp. 208 – 216, 2020.
- [39] C. J. Brabec, A. Distler, X. Du, H.-J. Egelhaaf, J. Hauch, T. Heumueller, and N. Li, "Material strategies to accelerate OPV technology toward a GW technology," *Adv. Energy Mater.*, vol. 10, no. 43, p. 2001864, 2020.
- [40] C. W. Tang, "Two-layer organic photovoltaic cell," *Appl. Phys. Lett.*, vol. 48, no. 2, pp. 183–185, 1986.
- [41] J. J. M. Halls, C. A. Walsh, N. C. Greenham, E. A. Marseglia, R. H. Friend, S. C. Moratti, and A. B. Holmes, "Efficient photodiodes from interpenetrating polymer networks," *Nature*, vol. 376, pp. 498–500, 1995.
- [42] G. Yu and A. J. Heeger, "Charge separation and photovoltaic conversion in polymer composites with internal donor/acceptor heterojunctions," *J. Appl. Phys.*, vol. 78, no. 7, pp. 4510–4515, 1995.
- [43] G. Yu, J. Gao, J. C. Hummelen, F. Wudl, and A. J. Heeger, "Polymer photovoltaic cells: Enhanced efficiencies via a network of internal donor-acceptor heterojunctions," *Science*, vol. 270, no. 5243, pp. 1789–1791, 1995.
- [44] L. D. Site, "What is a multiscale problem in molecular dynamics?," *Entropy*, vol. 16, no. 1, pp. 23–40, 2014.
- [45] T. A. Wassenaar, K. Pluhackova, R. A. Böckmann, S. J. Marrink, and D. P. Tieleman, "Going backward: A flexible geometric approach to reverse transformation from coarse grained to atomistic models," *J. Chem. Theory Comput.*, vol. 10, no. 2, pp. 676–690, 2014.
- [46] W. Pezeshkian, M. König, T. A. Wassenaar, and S. J. Marrink, "Backmapping triangulated surfaces to coarse-grained membrane models," *Nat. Commun.*, vol. 11, p. 2296, 2020.
- [47] A. Warshel and M. Levitt, "Theoretical studies of enzymic reactions: Dielectric, electrostatic and steric stabilization of the carbonium ion in the reaction of lysozyme," *J. Mol. Biol.*, vol. 103, no. 2, pp. 227 – 249, 1976.

- [48] E. Brunk and U. Rothlisberger, "Mixed quantum mechanical/molecular mechanical molecular dynamics simulations of biological systems in ground and electronically excited states," *Chem. Rev.*, vol. 115, no. 12, pp. 6217–6263, 2015.
- [49] M. Praprotnik, L. Delle Site, and K. Kremer, "Adaptive resolution molecular-dynamics simulation: Changing the degrees of freedom on the fly," *J. Chem. Phys.*, vol. 123, no. 22, p. 224106, 2005.
- [50] C. Krekeler, A. Agarwal, C. Junghans, M. Praprotnik, and L. Delle Site, "Adaptive resolution molecular dynamics technique: Down to the essential," *J. Chem. Phys.*, vol. 149, no. 2, p. 024104, 2018.
- [51] M. Praprotnik, R. Cortes-Huerto, R. Potestio, and L. Delle Site, "Adaptive resolution molecular dynamics technique," in *Handbook of Materials Modeling: Methods: Theory and Modeling* (W. Andreoni and S. Yip, eds.), pp. 1443–1457, Cham: Springer International Publishing, 2020.
- [52] L. Zhigilei, "Lecture notes for mse 4270/6270: Introduction to atomistic simulations." <http://www.people.virginia.edu/~lz2n/mse627/>. Accessed on November 11, 2020.
- [53] Y. G. Yingling, "Lecture notes: Potential energy surface and molecular dynamics simulations." [http://hybrid3.duke.edu/sites/hybrid3.duke.edu/files/u63/Duke\\_workshop\\_PES\\_MD\\_final\\_send.pdf](http://hybrid3.duke.edu/sites/hybrid3.duke.edu/files/u63/Duke_workshop_PES_MD_final_send.pdf). Accessed on November 5, 2020.
- [54] M. Teschner, "Lecture notes for simulation in computer graphics: Particles." [https://cg.informatik.uni-freiburg.de/course\\_notes/sim\\_02\\_particles.pdf](https://cg.informatik.uni-freiburg.de/course_notes/sim_02_particles.pdf). Accessed on November 13, 2020.
- [55] F. Jensen, *Introduction to Computational Chemistry*. John Wiley & Sons Ltd, second ed., 2007.
- [56] J. H. Jensen, *Molecular Modeling Basics*. CRC Press, Taylor & Francis Group, first ed., 2010.
- [57] M. P. Allen, "Introduction to molecular dynamics simulation," in *NIC Series Volume 23: Computational Soft Matter: From Synthetic Polymers to Proteins, Lecture Notes* (N. Attig, K. Binder, H. Grubmüller, and K. Kremer, eds.), pp. 1–28, Jülich: John von Neumann Institute for Computing, 2004.
- [58] A. S. Gertsen, *Closed-cycle molecular thermal solar energy storage and triplet-triplet annihilation photon upconversion*. PhD thesis, University of Copenhagen, 2017.
- [59] M. J. Abraham, D. van der Spoel, E. Lindahl, B. Hess, and the GROMACS development team, "GROMACS User Manual version 2018." [www.gromacs.org](http://www.gromacs.org), 2018.
- [60] E. Schrödinger, "Über das verhältnis der heisenberg-born-jordanschen quantenmechanik zu der meinem," *Ann. Phys.*, vol. 384, no. 8, pp. 734–756, 1926.
- [61] E. Schrödinger, "Quantisierung als eigenwertproblem," *Ann. Phys.*, vol. 384, no. 4, pp. 361–376, 1926.
- [62] E. Schrödinger, "Quantisierung als eigenwertproblem," *Ann. Phys.*, vol. 385, no. 13, pp. 437–490, 1926.
- [63] M. Born and R. Oppenheimer, "Zur quantentheorie der molekeln," *Ann. Phys.*, vol. 389, no. 20, pp. 457–484, 1927.
- [64] B. Wardle, *Principles and Applications of Photochemistry*. John Wiley & Sons Ltd, first ed., 2009.
- [65] D. R. Hartree, "The wave mechanics of an atom with a non-coulomb central field. part i. theory and methods," *Math. Proc. Camb. Philos. Soc.*, vol. 24, no. 1, p. 89–110, 1928.
- [66] J. C. Slater, "The self consistent field and the structure of atoms," *Phys. Rev.*, vol. 32, pp. 339–348, 1928.
- [67] J. C. Slater, "Note on hartree's method," *Phys. Rev.*, vol. 35, pp. 210–211, 1930.
- [68] V. Fock, "Näherungsmethode zur lösung des quantenmechanischen mehrkörperproblems," *Z. Phys.*, vol. 61, pp. 126–148, 1930.
- [69] D. R. Hartree, "The wave mechanics of an atom with a non-coulomb central field. part ii. some results and discussion," *Math. Proc. Camb. Philos. Soc.*, vol. 24, no. 1, p. 111–132, 1928.

- [70] W. Pauli, "Über den zusammenhang des abschlusses der elektronengruppen im atom mit der komplexstruktur der spektren," *Z. Phys.*, vol. 31, pp. 765–783, 1925.
- [71] D. L. Strout and G. E. Scuseria, "A quantitative study of the scaling properties of the hartree–fock method," *J. Chem. Phys.*, vol. 102, no. 21, pp. 8448–8452, 1995.
- [72] P. Hohenberg and W. Kohn, "Inhomogeneous electron gas," *Phys. Rev.*, vol. 136, pp. B864–B871, 1964.
- [73] D. J. Tozer, "Density functional theory," in *European Summer School in Quantum Chemistry 2013 Book II* (R. Bast and P.-O. Widmark, eds.), pp. 529–563, Palermo: ESQC Committee, eight ed., 2013.
- [74] W. Kohn and L. J. Sham, "Self-consistent equations including exchange and correlation effects," *Phys. Rev.*, vol. 140, pp. A1133–A1138, 1965.
- [75] J. P. Perdew, J. Tao, V. N. Staroverov, and G. E. Scuseria, "Meta-generalized gradient approximation: Explanation of a realistic nonempirical density functional," *J. Chem. Phys.*, vol. 120, no. 15, pp. 6898–6911, 2004.
- [76] J. P. Perdew and K. Schmidt, "Jacob's ladder of density functional approximations for the exchange-correlation energy," *AIP Conference Proceedings*, vol. 577, no. 1, 2001.
- [77] J. P. Perdew, K. Burke, and M. Ernzerhof, "Generalized gradient approximation made simple," *Phys. Rev. Lett.*, vol. 77, pp. 3865–3868, 1996.
- [78] A. D. Becke, "Density-functional exchange-energy approximation with correct asymptotic behavior," *Phys. Rev. A*, vol. 38, pp. 3098–3100, 1988.
- [79] C. Lee, W. Yang, and R. G. Parr, "Development of the Colle-Salvetti correlation-energy formula into a functional of the electron density," *Phys. Rev. B*, vol. 37, pp. 785–789, 1988.
- [80] A. D. Becke, "Density functional thermochemistry. III. The role of exact exchange," *J. Chem. Phys.*, vol. 98, no. 7, pp. 5648–5652, 1993.
- [81] C. Adamo and V. Barone, "Toward reliable density functional methods without adjustable parameters: The PBE0 model," *J. Chem. Phys.*, vol. 110, pp. 6158–6169, 1999.
- [82] P. J. Stephens, F. J. Devlin, C. F. Chabalowski, and M. J. Frisch, "Ab initio calculation of vibrational absorption and circular dichroism spectra using density functional force fields," *J. Phys. Chem.*, vol. 98, pp. 11623–11627, 1994.
- [83] S. H. Vosko, L. Wilk, and M. Nusair, "Accurate spin-dependent electron liquid correlation energies for local spin density calculations: A critical analysis," *Can. J. Phys.*, vol. 58, no. 8, pp. 1200–1211, 1980.
- [84] J. P. Dombroski, S. W. Taylor, and P. M. W. Gill, "KWIK: Coulomb energies in O(N) work," *J. Phys. Chem.*, vol. 100, no. 15, pp. 6272–6276, 1996.
- [85] P. M. Gill and R. D. Adamson, "A family of attenuated coulomb operators," *Chem. Phys. Lett.*, vol. 261, no. 1, pp. 105 – 110, 1996.
- [86] H. Iikura, T. Tsuneda, T. Yanai, and K. Hirao, "A long-range correction scheme for generalized-gradient-approximation exchange functionals," *J. Chem. Phys.*, vol. 115, no. 8, pp. 3540–3544, 2001.
- [87] Y. Tawada, T. Tsuneda, S. Yanagisawa, T. Yanai, and K. Hirao, "A long-range-corrected time-dependent density functional theory," *J. Chem. Phys.*, vol. 120, no. 18, pp. 8425–8433, 2004.
- [88] T. Yanai, D. P. Tew, and N. C. Handy, "A new hybrid exchange–correlation functional using the Coulomb-attenuating method (CAM-B3LYP)," *Chem. Phys. Letters*, vol. 393, pp. 51–57, 2004.
- [89] A. D. Laurent and D. Jacquemin, "TD-DFT benchmarks: A review," *Int. J. Quantum Chem.*, vol. 113, no. 17, pp. 2019–2039, 2013.
- [90] D. Jacquemin, E. A. Perpète, G. E. Scuseria, I. Ciofini, and C. Adamo, "TD-DFT performance for the visible absorption spectra of organic dyes: Conventional versus long-range hybrids," *J. Chem. Theo. Comp.*, vol. 4, no. 1, pp. 123–135, 2008.

- [91] S. Grimme, "Density functional theory with london dispersion corrections," *Wiley Interdiscip. Rev. Comput. Mol. Sci.*, vol. 1, no. 2, pp. 211–228, 2011.
- [92] A. D. Becke, "Density-functional thermochemistry. V. systematic optimization of exchange-correlation functionals," *J. Chem. Phys.*, vol. 107, pp. 8554–8560, 1997.
- [93] J.-D. Chai and M. Head-Gordon, "Systematic optimization of long-range corrected hybrid density functionals," *J. Chem. Phys.*, vol. 128, no. 8, p. 084106, 2008.
- [94] J.-D. Chai and M. Head-Gordon, "Long-range corrected hybrid density functionals with damped atom-atom dispersion corrections," *Phys. Chem. Chem. Phys.*, vol. 10, pp. 6615–6620, 2008.
- [95] N. Mardirossian and M. Head-Gordon, "Thirty years of density functional theory in computational chemistry: an overview and extensive assessment of 200 density functionals," *Mol. Phys.*, vol. 115, no. 19, pp. 2315–2372, 2017.
- [96] R. Eisenschitz and F. London, "Über das verhältnis der van der waalsschen kräfte zu den homöopolaren bindungskräften," *Z. Phys.*, vol. 60, pp. 491–527, 1930.
- [97] F. London, "The general theory of molecular forces," *Trans. Faraday Soc.*, vol. 33, pp. 8b–26, 1937.
- [98] J. E. Lennard-Jones, "Cohesion," *Proc. Phys. Soc.*, vol. 43, no. 5, pp. 461–482, 1931.
- [99] C. M. Baker, "Polarizable force fields for molecular dynamics simulations of biomolecules," *WIREs Comput. Mol. Sci.*, vol. 5, no. 2, pp. 241–254, 2015.
- [100] P. Ren and J. W. Ponder, "Consistent treatment of inter- and intramolecular polarization in molecular mechanics calculations," *J. Comput. Chem.*, vol. 23, no. 16, pp. 1497–1506, 2002.
- [101] J. W. Ponder, C. Wu, P. Ren, V. S. Pande, J. D. Chodera, M. J. Schnieders, I. Haque, D. L. Mobley, D. S. Lambrecht, R. A. DiStasio, M. Head-Gordon, G. N. I. Clark, M. E. Johnson, and T. Head-Gordon, "Current status of the AMOEBA polarizable force field," *J. Phys. Chem. B*, vol. 114, no. 8, pp. 2549–2564, 2010.
- [102] Z. Jing, C. Liu, S. Y. Cheng, R. Qi, B. D. Walker, J.-P. Piquemal, and P. Ren, "Polarizable force fields for biomolecular simulations: Recent advances and applications," *Annu. Rev. Biophys.*, vol. 48, no. 1, pp. 371–394, 2019.
- [103] D. A. Pearlman, D. A. Case, J. W. Caldwell, W. S. Ross, T. E. Cheatham, S. DeBolt, D. Ferguson, G. Seibel, and P. Kollman, "AMBER, a package of computer programs for applying molecular mechanics, normal mode analysis, molecular dynamics and free energy calculations to simulate the structural and energetic properties of molecules," *Compu. Phys. Commun.*, vol. 91, no. 1, pp. 1 – 41, 1995.
- [104] W. D. Cornell, P. Cieplak, C. I. Bayly, I. R. Gould, K. M. Merz, D. M. Ferguson, D. C. Spellmeyer, T. Fox, J. W. Caldwell, and P. A. Kollman, "A second generation force field for the simulation of proteins, nucleic acids, and organic molecules," *J. Am. Chem. Soc.*, vol. 117, no. 19, pp. 5179–5197, 1995.
- [105] B. R. Brooks, R. E. Bruccoleri, B. D. Olafson, D. J. States, S. Swaminathan, and M. Karplus, "CHARMM: A program for macromolecular energy, minimization, and dynamics calculations," *J. Comput. Chem.*, vol. 4, no. 2, pp. 187–217, 1983.
- [106] B. R. Brooks, C. L. Brooks III, A. D. Mackerell Jr., L. Nilsson, R. J. Petrella, B. Roux, Y. Won, G. Archontis, C. Bartels, S. Boresch, A. Caflisch, L. Caves, Q. Cui, A. R. Dinner, M. Feig, S. Fischer, J. Gao, M. Hodoscek, W. Im, K. Kuczera, T. Lazaridis, J. Ma, V. Ovchinnikov, E. Paci, R. W. Pastor, C. B. Post, J. Z. Pu, M. Schaefer, B. Tidor, R. M. Venable, H. L. Woodcock, X. Wu, W. Yang, D. M. York, and M. Karplus, "CHARMM: The biomolecular simulation program," *J. Comput. Chem.*, vol. 30, no. 10, pp. 1545–1614, 2009.
- [107] W. F. van Gunsteren and H. J. C. Berendsen, "Groningen molecular simulation (GROMOS) library manual." Biomos, Groningen, The Netherlands, 1987.
- [108] W. R. P. Scott, P. H. Hünenberger, I. G. Tironi, A. E. Mark, S. R. Billeter, J. Fennen, A. E. Torda, T. Huber, P. Krüger, and W. F. van Gunsteren, "The GROMOS biomolecular simulation program package," *J. Phys. Chem. A*, vol. 103, no. 19, pp. 3596–3607, 1999.

- [109] W. L. Jorgensen, D. S. Maxwell, and J. Tirado-Rives, "Development and testing of the OPLS all-atom force field on conformational energetics and properties of organic liquids," *J. Am. Chem. Soc.*, vol. 118, no. 45, pp. 11225–11236, 1996.
- [110] G. A. Kaminski, R. A. Friesner, J. Tirado-Rives, and W. L. Jorgensen, "Evaluation and reparametrization of the OPLS-AA force field for proteins via comparison with accurate quantum chemical calculations on peptides," *J. Phys. Chem. B*, vol. 105, no. 28, pp. 6474–6487, 2001.
- [111] W. Damm, A. Frontera, J. Tirado-Rives, and W. L. Jorgensen, "OPLS all-atom force field for carbohydrates," *J. Comput. Chem.*, vol. 18, no. 16, pp. 1955–1970, 1997.
- [112] N. A. McDonald and W. L. Jorgensen, "Development of an all-atom force field for heterocycles. properties of liquid pyrrole, furan, diazoles, and oxazoles," *J. Phys. Chem. B*, vol. 102, no. 41, pp. 8049–8059, 1998.
- [113] W. L. Jorgensen, J. P. Ulmschneider, and J. Tirado-Rives, "Free energies of hydration from a generalized born model and an all-atom force field," *J. Phys. Chem. B*, vol. 108, no. 41, pp. 16264–16270, 2004.
- [114] C. Caleman, P. J. van Maaren, M. Hong, J. S. Hub, L. T. Costa, and D. van der Spoel, "Force field benchmark of organic liquids: Density, enthalpy of vaporization, heat capacities, surface tension, isothermal compressibility, volumetric expansion coefficient, and dielectric constant," *J. Chem. Theory Comput.*, vol. 8, no. 1, pp. 61–74, 2012.
- [115] M. J. Robertson, J. Tirado-Rives, and W. L. Jorgensen, "Improved peptide and protein torsional energetics with the OPLS-AA force field," *J. Chem. Theory Comput.*, vol. 11, no. 7, pp. 3499–3509, 2015.
- [116] P. Carbone, H. A. K. Varzaneh, X. Chen, and F. Müller-Plathe, "Transferability of coarse-grained force fields: The polymer case," *J. Chem. Phys.*, vol. 128, no. 6, p. 064904, 2008.
- [117] D. M. Huang, R. Faller, K. Do, and A. J. Moulé, "Coarse-grained computer simulations of polymer/fullerene bulk heterojunctions for organic photovoltaic applications," *J. Chem. Theory Comput.*, vol. 6, no. 2, pp. 526–537, 2010.
- [118] W. G. Noid, "Perspective: Coarse-grained models for biomolecular systems," *J. Chem. Phys.*, vol. 139, no. 9, p. 090901, 2013.
- [119] C.-K. Lee and C.-W. Pao, "Nanomorphology evolution of P3HT/PCBM blends during solution-processing from coarse-grained molecular simulations," *J. Phys. Chem. C*, vol. 118, no. 21, pp. 11224–11233, 2014.
- [120] J. Barnoud and L. Monticelli, "Coarse-grained force fields for molecular simulations," in *Molecular Modeling of Proteins* (A. Kukol, ed.), pp. 125–149, New York, NY: Springer New York, 2015.
- [121] S. J. Marrink, A. H. de Vries, and A. E. Mark, "Coarse grained model for semiquantitative lipid simulations," *J. Phys. Chem. B*, vol. 108, no. 2, pp. 750–760, 2004.
- [122] S. J. Marrink, H. J. Risselada, S. Yefimov, D. P. Tieleman, and A. H. de Vries, "The MARTINI force field: Coarse grained model for biomolecular simulations," *J. Phys. Chem. B*, vol. 111, no. 27, pp. 7812–7824, 2007.
- [123] S. J. Marrink and D. P. Tieleman, "Perspective on the martini model," *Chem. Soc. Rev.*, vol. 42, pp. 6801–6822, 2013.
- [124] B. M. H. Bruininks, P. C. T. Souza, and S. J. Marrink, "A practical view of the martini force field," in *Biomolecular Simulations: Methods and Protocols* (M. Bonomi and C. Camilloni, eds.), pp. 105–127, New York, NY: Springer New York, 2019.
- [125] L. Monticelli, S. K. Kandasamy, X. Periole, R. G. Larson, D. P. Tieleman, and S.-J. Marrink, "The MARTINI coarse-grained force field: Extension to proteins," *J. Chem. Theory Comput.*, vol. 4, no. 5, pp. 819–834, 2008.
- [126] D. H. de Jong, G. Singh, W. F. D. Bennett, C. Arnarez, T. A. Wassenaar, L. V. Schäfer, X. Periole, D. P. Tieleman, and S. J. Marrink, "Improved parameters for the martini coarse-grained protein force field," *J. Chem. Theory Comput.*, vol. 9, no. 1, pp. 687–697, 2013.



- [127] C. A. López, A. J. Rzepiela, A. H. de Vries, L. Dijkhuizen, P. H. Hünenberger, and S. J. Marrink, "Martini coarse-grained force field: Extension to carbohydrates," *J. Chem. Theory Comput.*, vol. 5, no. 12, pp. 3195–3210, 2009.
- [128] J. J. Uusitalo, H. I. Ingólfsson, P. Akhshi, D. P. Tieleman, and S. J. Marrink, "Martini coarse-grained force field: Extension to DNA," *J. Chem. Theory Comput.*, vol. 11, no. 8, pp. 3932–3945, 2015.
- [129] J. J. Uusitalo, H. I. Ingólfsson, S. J. Marrink, and I. Faustino, "Martini coarse-grained force field: Extension to RNA," *Biophys. J.*, vol. 113, no. 2, pp. 246 – 256, 2017.
- [130] C. Arnarez, J. J. Uusitalo, M. F. Masman, H. I. Ingólfsson, D. H. de Jong, M. N. Melo, X. Periole, A. H. de Vries, and S. J. Marrink, "Dry martini, a coarse-grained force field for lipid membrane simulations with implicit solvent," *J. Chem. Theory Comput.*, vol. 11, no. 1, pp. 260–275, 2015.
- [131] G. Rossi, L. Monticelli, S. R. Puisto, I. Vattulainen, and T. Ala-Nissila, "Coarse-graining polymers with the MARTINI force-field: polystyrene as a benchmark case," *Soft Matter*, vol. 7, pp. 698–708, 2011.
- [132] M. Vögele, C. Holm, and J. Smiatek, "Coarse-grained simulations of polyelectrolyte complexes: MARTINI models for poly(styrene sulfonate) and poly(diallyldimethylammonium)," *J. Chem. Phys.*, vol. 143, no. 24, p. 243151, 2015.
- [133] R. Alessandri, J. J. Uusitalo, A. H. de Vries, R. W. A. Havenith, and S. J. Marrink, "Bulk heterojunction morphologies with atomistic resolution from coarse-grain solvent evaporation simulations," *J. Am. Chem. Soc.*, vol. 139, no. 10, pp. 3697–3705, 2017.
- [134] J. Liu, L. Qiu, R. Alessandri, X. Qiu, G. Portale, J. Dong, W. Talsma, G. Ye, A. A. Sengrhan, P. C. T. Souza, M. A. Loi, R. C. Chiechi, S. J. Marrink, J. C. Hummelen, and L. J. A. Koster, "Enhancing molecular n-type doping of donor–acceptor copolymers by tailoring side chains," *Adv. Mater.*, vol. 30, no. 7, p. 1704630, 2018.
- [135] R. Alessandri, S. Sami, J. Barnoud, A. H. de Vries, S. J. Marrink, and R. W. A. Havenith, "Resolving donor–acceptor interfaces and charge carrier energy levels of organic semiconductors with polar side chains," *Adv. Funct. Mater.*, vol. 30, no. 46, p. 2004799, 2020.
- [136] S. Sami, R. Alessandri, R. Broer, and R. W. A. Havenith, "How ethylene glycol chains enhance the dielectric constant of organic semiconductors: Molecular origin and frequency dependence," *ACS Appl. Mater. Interfaces*, vol. 12, no. 15, pp. 17783–17789, 2020.
- [137] J. Olsen and P. Jørgensen, "Linear and nonlinear response functions for an exact state and for an MCSCF state," *J. Chem. Phys.*, vol. 82, pp. 3235–3264, 1985.
- [138] P. Salek, O. Vahtras, T. Helgaker, and H. Ågren, "Density-functional theory of linear and non-linear time-dependent molecular properties," *J. Chem. Phys.*, vol. 117, pp. 9630–9645, 2002.
- [139] S. T. Olsen, T. Hansen, and K. V. Mikkelsen, "A theoretical approach to molecular single-electron transistors," *Theor. Chem. Acc.*, vol. 130, no. 4-6, pp. 839–850, 2011.
- [140] R. A. Marcus, "Chemical and electrochemical electron-transfer theory," *Annu. Rev. Phys. Chem.*, vol. 15, no. 1, pp. 155–196, 1964.
- [141] J. Kirkpatrick, *Calculating Intermolecular Charge Transport Parameters in Conjugated Materials*. PhD thesis, Imperial College London, 2007.
- [142] E. Rice, *Computational Modelling of Electronic States, Charge Transfer and Charge Transport in Organic Semiconductors*. PhD thesis, Imperial College London, 2018.
- [143] L. Torsi, M. Magliulo, K. Manoli, and G. Palazzo, "Organic field-effect transistor sensors: a tutorial review," *Chem. Soc. Rev.*, vol. 42, pp. 8612–8628, 2013.
- [144] J. Rivnay, S. Inal, A. Salleo, R. M. Owens, M. Berggren, and G. G. Malliaras, "Organic electrochemical transistors," *Nat. Rev. Mater.*, vol. 3, p. 17086, 2018.
- [145] H. Xu, L. Yin, C. Liu, X. Sheng, and N. Zhao, "Recent advances in biointegrated optoelectronic devices," *Adv. Mater.*, vol. 30, no. 33, p. 1800156, 2018.
- [146] E. Pascual-San-José, G. Sadoughi, L. Lucera, M. Stella, E. Martínez-Ferrero, G. E. Morse,

- M. Campoy-Quiles, and I. Burgués-Ceballos, "Towards photovoltaic windows: scalable fabrication of semitransparent modules based on non-fullerene acceptors via laser-patterning," *J. Mater. Chem. A*, pp. –, 2020.
- [147] A. M. Zeidell, D. S. Filston, M. Waldrip, H. F. Iqbal, H. Chen, I. McCulloch, and O. D. Jurchescu, "Large-area uniform polymer transistor arrays on flexible substrates: Towards high-throughput sensor fabrication," *Adv. Mater. Technol.*, vol. 5, no. 8, p. 2000390, 2020.
- [148] H. Bronstein, D. S. Leem, R. Hamilton, P. Woebkenberg, S. King, W. Zhang, R. S. Ashraf, M. Heeney, T. D. Anthopoulos, J. d. Mello, and I. McCulloch, "Indacenodithiophene-co-benzothiadiazole copolymers for high performance solar cells or transistors via alkyl chain optimization," *Macromol.*, vol. 44, no. 17, pp. 6649–6652, 2011.
- [149] Z. Ma, H. Geng, D. Wang, and Z. Shuai, "Influence of alkyl side-chain length on the carrier mobility in organic semiconductors: herringbone vs. pi-pi stacking," *J. Mater. Chem. C*, vol. 4, pp. 4546–4555, 2016.
- [150] H. Bristow, K. J. Thorley, A. J. P. White, A. Wadsworth, M. Babics, Z. Hamid, W. Zhang, A. F. Paterson, J. Kosco, J. Panidi, T. D. Anthopoulos, and I. McCulloch, "Impact of nonfullerene acceptor side chain variation on transistor mobility," *Adv. Electron. Mater.*, vol. 5, p. 1900344, 2019.
- [151] L. Ye, K. Weng, J. Xu, X. Du, S. Chandrabose, K. Chen, J. Zhou, G. Han, S. Tan, Z. Xie, Y. Yi, N. Li, F. Liu, J. M. Hodgkiss, C. J. Brabec, and Y. Sun, "Unraveling the influence of non-fullerene acceptor molecular packing on photovoltaic performance of organic solar cells," *Nat. Commun.*, vol. 11, no. 1, p. 6005, 2020.
- [152] A. Marrocchi, D. Lanari, A. Facchetti, and L. Vaccaro, "Poly(3-hexylthiophene): synthetic methodologies and properties in bulk heterojunction solar cells," *Energy Environ. Sci.*, vol. 5, pp. 8457–8474, 2012.
- [153] M. T. Dang, L. Hirsch, and G. Wantz, "P3HT:PCBM, best seller in polymer photovoltaic research," *Adv. Mater.*, vol. 23, no. 31, pp. 3597–3602, 2011.
- [154] C. Tanase, E. J. Meijer, P. W. M. Blom, and D. M. de Leeuw, "Unification of the hole transport in polymeric field-effect transistors and light-emitting diodes," *Phys. Rev. Lett.*, vol. 91, p. 216601, 2003.
- [155] H. Sirringhaus, P. J. Brown, R. H. Friend, M. M. Nielsen, K. Bechgaard, B. M. W. Langeveld-Voss, A. J. H. Spiering, R. A. J. Janssen, E. W. Meijer, P. Herwig, and D. M. de Leeuw, "Two-dimensional charge transport in self-organized, high-mobility conjugated polymers," *Nature*, vol. 401, pp. 685–688, 1999.
- [156] J.-F. Chang, H. Sirringhaus, M. Giles, M. Heeney, and I. McCulloch, "Relative importance of polaron activation and disorder on charge transport in high-mobility conjugated polymer field-effect transistors," *Phys. Rev. B*, vol. 76, p. 205204, 2007.
- [157] Z. Bao, A. Dodabalapur, and A. J. Lovinger, "Soluble and processable regioregular poly(3-hexylthiophene) for thin film field-effect transistor applications with high mobility," *Appl. Phys. Lett.*, vol. 69, no. 26, pp. 4108–4110, 1996.
- [158] H. Sirringhaus, N. Tessler, and R. H. Friend, "Integrated optoelectronic devices based on conjugated polymers," *Science*, vol. 280, no. 5370, pp. 1741–1744, 1998.
- [159] A. Salleo, "Charge transport in polymeric transistors," *Mater. Today*, vol. 10, no. 3, pp. 38 – 45, 2007.
- [160] W. Zhang, J. Smith, S. E. Watkins, R. Gysel, M. McGehee, A. Salleo, J. Kirkpatrick, S. Ashraf, T. Anthopoulos, M. Heeney, and I. McCulloch, "Indacenodithiophene semiconducting polymers for high-performance, air-stable transistors," *J. Am. Chem. Soc.*, vol. 132, no. 33, pp. 11437–11439, 2010.
- [161] A. Wadsworth, H. Chen, K. J. Thorley, C. Cendra, M. Nikolka, H. Bristow, M. Moser, A. Salleo, T. D. Anthopoulos, H. Sirringhaus, and I. McCulloch, "Modification of indacenodithiophene-based polymers and its impact on charge carrier mobility in organic thin-film transistors," *J. Am.*

- Chem. Soc.*, vol. 142, no. 2, pp. 652–664, 2020.
- [162] X. Zhang, H. Bronstein, A. J. Kronemeijer, J. Smith, Y. Kim, R. J. Kline, L. J. Richter, T. D. Anthopoulos, H. Sirringhaus, K. Song, M. Heeney, W. Zhang, I. McCulloch, and D. M. DeLongchamp, "Molecular origin of high field-effect mobility in an indacenodithiophene-benzothiadiazole copolymer," *Nat. Commun.*, vol. 4, p. 2238, 2013.
  - [163] D. Venkateshvaran, M. Nikolka, A. Sadhanala, V. Lemaure, M. Zelazny, M. Kepa, M. Hurhangee, A. J. Kronemeijer, V. Pecunia, I. Nasrallah, I. Romanov, K. Broch, I. McCulloch, D. Emin, Y. Olivier, J. Cornil, D. Beljonne, and H. Sirringhaus, "Approaching disorder-free transport in high-mobility conjugated polymers," *Nature*, vol. 515, pp. 384–388, 2014.
  - [164] V. Lemaure, J. Cornil, R. Lazzaroni, H. Sirringhaus, D. Beljonne, and Y. Olivier, "Resilience to conformational fluctuations controls energetic disorder in conjugated polymer materials: Insights from atomistic simulations," *Chem. Mater.*, vol. 31, no. 17, pp. 6889–6899, 2019.
  - [165] M. Nikolka, K. Broch, J. Armitage, D. Hanifi, P. J. Nowack, D. Venkateshvaran, A. Sadhanala, J. Saska, M. Mascal, S.-H. Jung, J. Lee, I. McCulloch, A. Salleo, and H. Sirringhaus, "High-mobility, trap-free charge transport in conjugated polymer diodes," *Nat. Commun.*, vol. 10, p. 2122, 2019.
  - [166] H. Yan, Z. Chen, Y. Zheng, C. Newman, J. R. Quinn, F. Dötz, M. Kastler, and A. Facchetti, "A high-mobility electron-transporting polymer for printed transistors," *Nature*, vol. 457, pp. 679–686, 2009.
  - [167] Z. Genene, W. Mammo, E. Wang, and M. R. Andersson, "Recent advances in n-type polymers for all-polymer solar cells," *Adv. Mater.*, vol. 31, no. 22, p. 1807275, 2019.
  - [168] H. Sun, X. Guo, and A. Facchetti, "High-performance n-type polymer semiconductors: Applications, recent development, and challenges," *Chem*, vol. 6, no. 6, pp. 1310 – 1326, 2020.
  - [169] H. Sun, H. Yu, Y. Shi, J. Yu, Z. Peng, X. Zhang, B. Liu, J. Wang, R. Singh, J. Lee, Y. Li, Z. Wei, Q. Liao, Z. Kan, L. Ye, H. Yan, F. Gao, and X. Guo, "A narrow-bandgap n-type polymer with an acceptor-acceptor backbone enabling efficient all-polymer solar cells," *Adv. Mater.*, vol. 32, no. 43, p. 2004183, 2020.
  - [170] H. Yu, Z. Qi, J. Yu, Y. Xiao, R. Sun, Z. Luo, A. M. H. Cheung, J. Zhang, H. Sun, W. Zhou, S. Chen, X. Guo, X. Lu, F. Gao, J. Min, and H. Yan, "Fluorinated end group enables high-performance all-polymer solar cells with near-infrared absorption and enhanced device efficiency over 14 %," *Adv. Energy Mater.*, p. 2003171, 2021.
  - [171] Z. Luo, T. Liu, R. Ma, Y. Xiao, L. Zhan, G. Zhang, H. Sun, F. Ni, G. Chai, J. Wang, C. Zhong, Y. Zou, X. Guo, X. Lu, H. Chen, H. Yan, and C. Yang, "Precisely controlling the position of bromine on the end group enables well-regular polymer acceptors for all-polymer solar cells with efficiencies over 15%," *Adv. Mater.*, vol. 32, no. 48, p. 2005942, 2020.
  - [172] Y. Lin, J. Wang, Z.-G. Zhang, H. Bai, Y. Li, D. Zhu, and X. Zhan, "An electron acceptor challenging fullerenes for efficient polymer solar cells," *Adv. Mater.*, vol. 27, no. 7, pp. 1170–1174, 2015.
  - [173] S. Holliday, R. S. Ashraf, A. Wadsworth, D. Baran, S. A. Yousaf, C. B. Nielsen, C.-H. Tan, S. D. Dimitrov, Z. Shang, N. Gasparini, M. Alamoudi, F. Laquai, C. J. Brabec, A. Salleo, J. R. Durrant, and I. McCulloch, "High-efficiency and air-stable P3HT-based polymer solar cells with a new non-fullerene acceptor," *Nat. Comm.*, vol. 7, p. 11585, 2016.
  - [174] A. Wadsworth, M. Moser, A. Marks, M. S. Little, N. Gasparini, C. J. Brabec, D. Baran, and I. McCulloch, "Critical review of the molecular design progress in non-fullerene electron acceptors towards commercially viable organic solar cells," *Chem. Soc. Rev.*, pp. –, 2019. Advance Article.
  - [175] P. Cheng, G. Li, X. Zhan, and Y. Yang, "Next-generation organic photovoltaics based on non-fullerene acceptors," *Nat. Photonics*, vol. 12, no. 3, pp. 131–142, 2018.
  - [176] H. Chen, A. Wadsworth, C. Ma, A. Nanni, W. Zhang, M. Nikolka, A. M. Luci, L. M. A. Perdigo, K. J. Thorley, C. Cendra, B. Larson, G. Rumbles, T. D. Anthopoulos, A. Salleo, G. Costantini, H. Sirringhaus, and I. McCulloch, "The effect of ring expansion in

- thienobenzo[b]indacenodithiophene polymers for organic field-effect transistors," *J. Am. Chem. Soc.*, vol. 141, no. 47, pp. 18806–18813, 2019.
- [177] K. Gu and Y.-L. Loo, "The polymer physics of multiscale charge transport in conjugated systems," *J. Polym. Sci. Part B: Polym. Phys.*, vol. 57, no. 23, pp. 1559–1571, 2019.
- [178] M. J. Abraham, T. Murtola, R. Schulz, S. Páll, J. C. Smith, B. Hess, and E. Lindahl, "GROMACS: High performance molecular simulations through multi-level parallelism from laptops to supercomputers," *SoftwareX*, vol. 1-2, pp. 19 – 25, 2015.
- [179] J. Wildman, P. Repiščák, M. J. Paterson, and I. Galbraith, "General force-field parametrization scheme for molecular dynamics simulations of conjugated materials in solution," *J. Chem. Theory Comput.*, vol. 12, no. 8, pp. 3813–3824, 2016.
- [180] M. J. Frisch, G. W. Trucks, H. B. Schlegel, G. E. Scuseria, M. A. Robb, J. R. Cheeseman, G. Scalmani, V. Barone, G. A. Petersson, H. Nakatsuji, *et al.*, "Gaussian 16 Revision A.03," 2016. Gaussian Inc. Wallingford CT.
- [181] V. Negi, A. Lyulin, and P. Bobbert, "Solvent-dependent structure formation in drying P3HT:PCBM films studied by molecular dynamics simulations," *Macromol. Theory Simul.*, vol. 25, no. 6, pp. 550–558, 2016.
- [182] R. T. Cygan, J.-J. Liang, and A. G. Kalinichev, "Molecular models of hydroxide, oxyhydroxide, and clay phases and the development of a general force field," *J. Phys. Chem. B*, vol. 108, no. 4, pp. 1255–1266, 2004.
- [183] S. Leroy and M. Wendland, "Simulation of forces between humid amorphous silica surfaces: A comparison of empirical atomistic force fields," *J. Phys. Chem. C*, vol. 116, no. 50, pp. 26247–26261, 2012.
- [184] O. M. Roscioni, G. D'Avino, L. Muccioli, and C. Zannoni, "Pentacene crystal growth on silica and layer-dependent step-edge barrier from atomistic simulations," *J. Phys. Chem. Lett.*, vol. 9, no. 23, pp. 6900–6906, 2018.
- [185] O. Kratky and G. Porod, "Röntgenuntersuchung gelöster fadenmoleküle," *Rec. Trav. Chim.*, vol. 68, no. 12, pp. 1106–1122, 1949.
- [186] S. R. Zhao, C. P. Sun, and W. X. Zhang, "Statistics of wormlike chains. I. Properties of a single chain," *J. Chem. Phys.*, vol. 106, no. 6, pp. 2520–2529, 1997.
- [187] M. Doi, *Introduction to Polymer Physics*. Oxford University Press, fifth ed., 2004.
- [188] B. McCulloch, V. Ho, M. Hoarfrost, C. Stanley, C. Do, W. T. Heller, and R. A. Segalman, "Polymer chain shape of poly(3-alkylthiophenes) in solution using small-angle neutron scattering," *Macromol.*, vol. 46, no. 5, pp. 1899–1907, 2013.
- [189] C. L. Gettinger, A. J. Heeger, J. M. Drake, and D. J. Pine, "A photoluminescence study of poly(phenylene vinylene) derivatives: The effect of intrinsic persistence length," *J. Chem. Phys.*, vol. 101, no. 2, pp. 1673–1678, 1994.
- [190] B. Kuei and E. D. Gomez, "Chain conformations and phase behavior of conjugated polymers," *Soft Matter*, vol. 13, pp. 49–67, 2017.
- [191] Y. Lu, B. Weers, and N. C. Stellwagen, "DNA persistence length revisited," *Biopolymers*, vol. 61, no. 4, pp. 261–275, 2002.
- [192] B. Kang, M. Jang, Y. Chung, H. Kim, S. K. Kwak, J. H. Oh, and K. Cho, "Enhancing 2D growth of organic semiconductor thin films with macroporous structures via a small-molecule heterointerface," *Nat. Commun.*, vol. 5, no. 1, p. 4752, 2014.
- [193] A. S. Gertsen, M. K. Sørensen, and J. W. Andreasen, "Nanostructure of organic semiconductor thin films: Molecular dynamics modeling with solvent evaporation," *Phys. Rev. Mater.*, vol. 4, p. 075405, 2020.
- [194] A. A. Y. Guilbert, J. M. Frost, T. Agostinelli, E. Pires, S. Lilliu, J. E. Macdonald, and J. Nelson, "Influence of bridging atom and side chains on the structure and crystallinity of cyclopentadithiophene–benzothiadiazole polymers," *Chem. Mater.*, vol. 26, no. 2, pp. 1226–1233,

2014.

- [195] J. Hou, O. Inganäs, R. H. Friend, and F. Gao, "Organic solar cells based on non-fullerene acceptors," *Nat. Mater.*, vol. 17, pp. 119–128, 2018.
- [196] G. Zhang, J. Zhao, P. C. Y. Chow, K. Jiang, J. Zhang, Z. Zhu, J. Zhang, F. Huang, and H. Yan, "Nonfullerene acceptor molecules for bulk heterojunction organic solar cells," *Chem. Rev.*, vol. 118, no. 7, pp. 3447–3507, 2018.
- [197] H. Sun, F. Chen, and Z.-K. Chen, "Recent progress on non-fullerene acceptors for organic photovoltaics," *Mater. Today*, vol. 24, pp. 94 – 118, 2019.
- [198] Y. Cai, L. Huo, and Y. Sun, "Recent advances in wide-bandgap photovoltaic polymers," *Adv. Mater.*, vol. 29, no. 22, p. 1605437, 2017.
- [199] L. Sun, X. Xu, S. Song, Y. Zhang, C. Miao, X. Liu, G. Xing, and S. Zhang, "Medium-bandgap conjugated polymer donors for organic photovoltaics," *Macromol. Rapid Commun.*, vol. 40, no. 14, p. 1900074, 2019.
- [200] H. Sun, T. Liu, J. Yu, T.-K. Lau, G. Zhang, Y. Zhang, M. Su, Y. Tang, R. Ma, B. Liu, J. Liang, K. Feng, X. Lu, X. Guo, F. Gao, and H. Yan, "A monothiophene unit incorporating both fluoro and ester substitution enabling high-performance donor polymers for non-fullerene solar cells with 16.4 % efficiency," *Energy Environ. Sci.*, pp. –, 2019.
- [201] J. Wu, G. Li, J. Fang, X. Guo, L. Zhu, B. Guo, Y. Wang, G. Zhang, L. Arunagiri, F. Liu, H. Yan, M. Zhang, and Y. Li, "Random terpolymer based on thiophene-thiazolothiazole unit enabling efficient non-fullerene organic solar cells," *Nat. Commun.*, vol. 11, p. 4612, 2020.
- [202] S. Strohm, F. Machui, S. Langner, P. Kubis, N. Gasparini, M. Salvador, I. McCulloch, H.-J. Egelhaaf, and C. J. Brabec, "P3HT: non-fullerene acceptor based large area, semi-transparent PV modules with power conversion efficiencies of 5 %, processed by industrially scalable methods," *Energy Environ. Sci.*, vol. 11, pp. 2225–2234, 2018.
- [203] K. An, W. Zhong, and L. Ying, "Enhanced performance of P3HT-based non-fullerene polymer solar cells by optimizing film morphology using non-halogenated solvent," *Org. Electron.*, vol. 82, p. 105701, 2020.
- [204] M. Fernández Castro, E. Mazzolini, R. R. Søndergaard, M. Espindola-Rodriguez, and J. W. Andreasen, "Flexible ITO-free roll-processed large-area nonfullerene organic solar cells based on P3HT:O-IDTBR," *Phys. Rev. Applied*, vol. 14, p. 034067, 2020.
- [205] H. Hoppe and N. S. Sariciftci, "Morphology of polymer/fullerene bulk heterojunction solar cells," *J. Mater. Chem.*, vol. 16, pp. 45–61, 2006.
- [206] W. Wang, S. Guo, E. M. Herzig, K. Sarkar, M. Schindler, D. Magerl, M. Philipp, J. Perlich, and P. Müller-Buschbaum, "Investigation of morphological degradation of p3ht:pcbm bulk heterojunction films exposed to long-term host solvent vapor," *J. Mater. Chem. A*, vol. 4, pp. 3743–3753, 2016.
- [207] F. Zhao, C. Wang, and X. Zhan, "Morphology control in organic solar cells," *Adv. Energy Mater.*, vol. 8, no. 28, p. 1703147, 2018.
- [208] L. Lu, T. Zheng, Q. Wu, A. M. Schneider, D. Zhao, and L. Yu, "Recent advances in bulk heterojunction polymer solar cells," *Chem. Rev.*, vol. 115, no. 23, pp. 12666–12731, 2015.
- [209] A. Wadsworth, Z. Hamid, J. Kosco, N. Gasparini, and I. McCulloch, "The bulk heterojunction in organic photovoltaic, photodetector, and photocatalytic applications," *Adv. Mater.*, vol. 32, no. 38, p. 2001763, 2020.
- [210] A. S. Gertsen, M. F. Castro, R. R. Søndergaard, and J. W. Andreasen, "Scalable fabrication of organic solar cells based on non-fullerene acceptors," *Flex. Print. Electron.*, vol. 5, p. 014004, 2020.
- [211] E. Pascual-San-José, X. Rodríguez-Martínez, R. Adel-Abdelaleim, M. Stella, E. Martínez-Ferrero, and M. Campoy-Quiles, "Blade coated P3HT:non-fullerene acceptor solar cells: a high-throughput parameter study with a focus on up-scalability," *J. Mater. Chem. A*, vol. 7, pp. 20369–20382, 2019.

- [212] A. Harillo-Baños, X. Rodríguez-Martínez, and M. Campoy-Quiles, "Efficient exploration of the composition space in ternary organic solar cells by combining high-throughput material libraries and hyperspectral imaging," *Adv. Energy Mater.*, vol. 10, no. 1, p. 1902417, 2020.
- [213] L. J. Richter, D. M. DeLongchamp, and A. Amassian, "Morphology development in solution-processed functional organic blend films: An in situ viewpoint," *Chem. Rev.*, vol. 117, no. 9, pp. 6332–6366, 2017.
- [214] P. E. Shaw, A. Ruseckas, and I. D. W. Samuel, "Exciton diffusion measurements in poly(3-hexylthiophene)," *Adv. Mater.*, vol. 20, no. 18, pp. 3516–3520, 2008.
- [215] O. V. Mikhnenko, P. W. M. Blom, and T.-Q. Nguyen, "Exciton diffusion in organic semiconductors," *Energy Environ. Sci.*, vol. 8, pp. 1867–1888, 2015.
- [216] Y. Firdaus, V. M. Le Corre, S. Karuthedath, W. Liu, A. Markina, W. Huang, S. Chattopadhyay, M. M. Nahid, M. I. Nugraha, Y. Lin, A. Seitkhan, A. Basu, W. Zhang, I. McCulloch, H. Ade, J. Labram, F. Laquai, D. Andrienko, L. J. A. Koster, and T. D. Anthopoulos, "Long-range exciton diffusion in molecular non-fullerene acceptors," *Nat. Commun.*, vol. 11, p. 5220, 2020.
- [217] M. L. Jones and E. Jankowski, "Computationally connecting organic photovoltaic performance to atomistic arrangements and bulk morphology," *Mol. Simul.*, vol. 43, no. 10-11, pp. 756–773, 2017.
- [218] G. Han, Y. Guo, X. Ma, and Y. Yi, "Atomistic insight into donor/acceptor interfaces in high-efficiency nonfullerene organic solar cells," *Solar RRL*, vol. 2, no. 11, p. 1800190, 2018.
- [219] A. F. Marmolejo-Valencia, Z. Mata-Pinzón, L. Dominguez, and C. Amador-Bedolla, "Atomistic simulations of bulk heterojunctions to evaluate the structural and packing properties of new predicted donors in OPVs," *Phys. Chem. Chem. Phys.*, vol. 21, pp. 20315–20326, 2019.
- [220] T. Lee, A. V. Sanzogni, P. L. Burn, and A. E. Mark, "Evolution and morphology of thin films formed by solvent evaporation: An organic semiconductor case study," *ACS Appl. Mater. Interfaces*, vol. 0, no. 0, p. null, 2020.
- [221] S. Peter, H. Meyer, and J. Baschnagel, "Molecular dynamics simulations of concentrated polymer solutions in thin film geometry.II. solvent evaporation near the glass transition," *J. Chem. Phys.*, vol. 131, no. 1, p. 014903, 2009.
- [222] C.-K. Lee and C.-W. Pao, "Multiscale molecular simulation of solution processing of SMDPPEH:PCBM small-molecule organic solar cells," *ACS Appl. Mater. Interfaces*, vol. 8, no. 32, pp. 20691–20700, 2016.
- [223] A. Wadsworth, R. S. Ashraf, M. Abdelsamie, S. Pont, M. Little, M. Moser, Z. Hamid, M. Neophytou, W. Zhang, A. Amassian, J. R. Durrant, D. Baran, and I. McCulloch, "Highly efficient and reproducible nonfullerene solar cells from hydrocarbon solvents," *ACS Energy Lett.*, vol. 2, no. 7, pp. 1494–1500, 2017.
- [224] Y. Lin, B. Adilbekova, Y. Firdaus, E. Yengel, H. Faber, M. Sajjad, X. Zheng, E. Yarali, A. Seitkhan, O. M. Bakr, A. El-Labban, U. Schwingenschlögl, V. Tung, I. McCulloch, F. Laquai, and T. D. Anthopoulos, "17 % efficient organic solar cells based on liquid exfoliated WS<sub>2</sub> as a replacement for PEDOT:PSS," *Adv. Mater.*, vol. 31, no. 46, p. 1902965, 2019.
- [225] A. Wadsworth, Z. Hamid, M. Bidwell, R. S. Ashraf, J. I. Khan, D. H. Anjum, C. Cendra, J. Yan, E. Rezasoltani, A. A. Y. Guilbert, M. Azzouzi, N. Gasparini, J. H. Bannock, D. Baran, H. Wu, J. C. de Mello, C. J. Brabec, A. Salleo, J. Nelson, F. Laquai, and I. McCulloch, "Progress in poly (3-hexylthiophene) organic solar cells and the influence of its molecular weight on device performance," *Adv. Energy Mater.*, vol. 8, no. 28, p. 1801001, 2018.
- [226] Q. Liang, X. Jiao, Y. Yan, Z. Xie, G. Lu, J. Liu, and Y. Han, "Separating crystallization process of P3HT and O-IDTBR to construct highly crystalline interpenetrating network with optimized vertical phase separation," *Adv. Funct. Mater.*, vol. 29, no. 47, p. 1807591, 2019.
- [227] N. Li, I. McCulloch, and C. J. Brabec, "Analyzing the efficiency, stability and cost potential for fullerene-free organic photovoltaics in one figure of merit," *Energy Environ. Sci.*, vol. 11, pp. 1355–1361, 2018.

- [228] N. Gasparini, M. Salvador, S. Strohm, T. Heumueller, I. Levchuk, A. Wadsworth, J. H. Bannock, J. C. de Mello, H.-J. Egelhaaf, D. Baran, I. McCulloch, and C. J. Brabec, "Burn-in free nonfullerene-based organic solar cells," *Adv. Energy Mater.*, vol. 7, no. 19, p. 1700770, 2017.
- [229] D. Baran, R. S. Ashraf, D. A. Hanifi, M. Abdelsamie, N. Gasparini, J. A. Röhr, S. Holliday, A. Wadsworth, S. Lockett, M. Neophytou, C. J. M. Emmott, J. Nelson, C. J. Brabec, A. Amassian, A. Salleo, T. Kirchartz, J. R. Durrant, and I. McCulloch, "Reducing the efficiency-stability-cost gap of organic photovoltaics with highly efficient and stable small molecule acceptor ternary solar cells," *Nat. Mater.*, vol. 16, pp. 363–370, 2017.
- [230] Y. Liu, J. Zhao, Z. Li, C. Mu, W. Ma, H. Hu, K. Jiang, H. Lin, H. Ade, and H. Yan, "Aggregation and morphology control enables multiple cases of high-efficiency polymer solar cells," *Nat. Commun.*, vol. 5, no. 1, p. 5293, 2014.
- [231] J. Zhao, Y. Li, G. Yang, K. Jiang, H. Lin, H. Ade, W. Ma, and H. Yan, "Efficient organic solar cells processed from hydrocarbon solvents," *Nat. Energy*, vol. 1, p. 15027, 2016.
- [232] H. Cha, J. Wu, A. Wadsworth, J. Nagitta, S. Limbu, S. Pont, Z. Li, J. Searle, M. F. Wyatt, D. Baran, J.-S. Kim, I. McCulloch, and J. R. Durrant, "An efficient, "burn in" free organic solar cell employing a nonfullerene electron acceptor," *Adv. Mater.*, vol. 29, no. 33, p. 1701156, 2017.
- [233] Z. Hamid, A. Wadsworth, E. Rezasoltani, S. Holliday, M. Azzouzi, M. Neophytou, A. A. Y. Guilbert, Y. Dong, M. S. Little, S. Mukherjee, A. A. Herzing, H. Bristow, R. J. Kline, D. M. DeLongchamp, A. A. Bakulin, J. R. Durrant, J. Nelson, and I. McCulloch, "Influence of polymer aggregation and liquid immiscibility on morphology tuning by varying composition in PffBT4T-2DT/nonfullerene organic solar cells," *Adv. Energy Mater.*, vol. 10, no. 8, p. 1903248, 2020.
- [234] D. Baran, T. Kirchartz, S. Wheeler, S. Dimitrov, M. Abdelsamie, J. Gorman, R. S. Ashraf, S. Holliday, A. Wadsworth, N. Gasparini, P. Kaienburg, H. Yan, A. Amassian, C. J. Brabec, J. R. Durrant, and I. McCulloch, "Reduced voltage losses yield 10 % efficient fullerene free organic solar cells with >1 V open circuit voltages," *Energy Environ. Sci.*, vol. 9, pp. 3783–3793, 2016.
- [235] S. Zhang, L. Ye, H. Zhang, and J. Hou, "Green-solvent-processable organic solar cells," *Mater. Today*, vol. 19, no. 9, pp. 533 – 543, 2016.
- [236] Y.-Y. Yu, T.-W. Tsai, C.-C. Yang, and C.-P. Chen, "Highly efficient non-fullerene organic photovoltaics processed from o-xylene without using additives," *J. Phys. Chem. C*, vol. 121, no. 40, pp. 21969–21974, 2017.
- [237] R. Alessandri, *Multiscale modeling of organic materials: from the Morphology Up*. PhD thesis, University of Groningen, 2019.
- [238] L. Monticelli, "On atomistic and coarse-grained models for c60 fullerene," *J. Chem. Theory Comput.*, vol. 8, no. 4, pp. 1370–1378, 2012.
- [239] J. Barnoud, "CG Builder." <https://jbarnoud.github.io/cgbuilder/>.
- [240] R. Alessandri, P. C. T. Souza, S. Thallmair, M. N. Melo, A. H. de Vries, and S. J. Marrink, "Pitfalls of the MARTINI model," *J. Chem. Theory Comput.*, vol. 15, no. 10, pp. 5448–5460, 2019.
- [241] M. R. Shirts and J. D. Chodera, "Statistically optimal analysis of samples from multiple equilibrium states," *J. Chem. Phys.*, vol. 129, no. 12, p. 124105, 2008.
- [242] O. Beckstein, D. Mobley, M. Shirts, D. Dotson, *et al.*, "alchemlyb: the simple alchemistry library." <https://github.com/alchemistry/alchemlyb>.
- [243] C. Hansch, A. Leo, D. Hoekman, and D. Livingstone, *Exploring QSAR: hydrophobic, electronic, and steric constants*, vol. 48. American Chemical Society, 1995.
- [244] J. Sangster, "Octanol-water partition coefficients of simple organic compounds," *J. Phys. Chem. Ref. Data*, vol. 18, no. 3, pp. 1111–1229, 1989.
- [245] R. Calvino, A. Gasco, and A. Leo, "An analysis of the lipophilicity of furazan and furoxan derivatives using the CLOGP algorithm," *J. Chem. Soc., Perkin Trans. 2*, pp. 1643–1646, 1992.
- [246] T. Cheng, Y. Zhao, X. Li, F. Lin, Y. Xu, X. Zhang, Y. Li, R. Wang, and L. Lai, "Computation

- of octanol-water partition coefficients by guiding an additive model with knowledge," *J. Chem. Inf. Model.*, vol. 47, no. 6, pp. 2140–2148, 2007.
- [247] C.-K. Lee, O. Wodo, B. Ganapathysubramanian, and C.-W. Pao, "Electrode materials, thermal annealing sequences, and lateral/vertical phase separation of polymer solar cells from multiscale molecular simulations," *ACS Appl. Mater. Interfaces*, vol. 6, no. 23, pp. 20612–20624, 2014.
  - [248] N. Michaud-Agrawal, E. J. Denning, T. B. Woolf, and O. Beckstein, "MDAnalysis: A toolkit for the analysis of molecular dynamics simulations," *J. Comput. Chem.*, vol. 32, no. 10, pp. 2319–2327, 2011.
  - [249] R. J. Gowers, M. Linke, J. Barnoud, T. J. E. Reddy, M. N. Melo, S. L. Seyler, J. Domanski, D. L. Dotson, S. Buchoux, I. M. Kenney, and O. Beckstein, "MDAnalysis: A Python package for the rapid analysis of molecular dynamics simulations," in *Proceedings of the 15th Python in Science Conference* (S. Benthall and S. Rostrup, eds.), pp. 98–105, United States, Austin, TX: SciPy, 2016.
  - [250] J. D. Hunter, "Matplotlib: A 2D graphics environment," *Comput. Sci. Eng.*, vol. 9, no. 3, pp. 90–95, 2007.
  - [251] J. Gostick, Z. A. Khan, T. G. Tranter, M. D. R. Kok, M. Agnaou, M. A. Sadeghi, and R. Jarvis, "PoreSpy: A Python toolkit for quantitative analysis of porous media images," *J. Open Source Softw.*, 2019.
  - [252] B. P. Lyons, N. Clarke, and C. Groves, "The relative importance of domain size, domain purity and domain interfaces to the performance of bulk-heterojunction organic photovoltaics," *Energy Environ. Sci.*, vol. 5, pp. 7657–7663, 2012.
  - [253] J. Nelson, J. J. Kwiatkowski, J. Kirkpatrick, and J. M. Frost, "Modeling charge transport in organic photovoltaic materials," *Acc. Chem. Res.*, vol. 42, no. 11, pp. 1768–1778, 2009.
  - [254] P. Virtanen, R. Gommers, T. E. Oliphant, M. Haberland, T. Reddy, D. Cournapeau, E. Burovski, P. Peterson, W. Weckesser, J. Bright, S. J. van der Walt, M. Brett, J. Wilson, K. J. Millman, N. Mayorov, A. R. J. Nelson, E. Jones, R. Kern, E. Larson, C. J. Carey, Í. Polat, Y. Feng, E. W. Moore, J. VanderPlas, D. Laxalde, J. Perktold, R. Cimrman, I. Henriksen, E. A. Quintero, C. R. Harris, A. M. Archibald, A. H. Ribeiro, F. Pedregosa, P. van Mulbregt, and SciPy 1.0 Contributors, "SciPy 1.0: Fundamental algorithms for scientific computing in Python," *Nat. Methods*, vol. 17, pp. 261–272, 2020.
  - [255] C.-K. Lee, C.-W. Pao, and C.-W. Chu, "Multiscale molecular simulations of the nanoscale morphologies of P3HT:PCBM blends for bulk heterojunction organic photovoltaic cells," *Energy Environ. Sci.*, vol. 4, pp. 4124–4132, 2011.
  - [256] F. Eisenhaber, P. Lijnzaad, P. Argos, C. Sander, and M. Scharf, "The double cubic lattice method: Efficient approaches to numerical integration of surface area and volume and to dot surface contouring of molecular assemblies," *J. Comput. Chem.*, vol. 16, no. 3, pp. 273–284, 1995.
  - [257] C.-K. Lee, C.-W. Pao, and C.-W. Chen, "Correlation of nanoscale organizations of polymer and nanocrystals in polymer/inorganic nanocrystal bulk heterojunction hybrid solar cells: insights from multiscale molecular simulations," *Energy Environ. Sci.*, vol. 6, pp. 307–315, 2013.
  - [258] M. Roesing, J. Howell, and D. Boucher, "Solubility characteristics of poly(3-hexylthiophene)," *J. Polym. Sci. Part B: Polym. Phys.*, vol. 55, no. 14, pp. 1075–1087, 2017.
  - [259] J. Zhao, Y. Li, H. Lin, Y. Liu, K. Jiang, C. Mu, T. Ma, J. Y. Lin Lai, H. Hu, D. Yu, and H. Yan, "High-efficiency non-fullerene organic solar cells enabled by a difluorobenzothiadiazole-based donor polymer combined with a properly matched small molecule acceptor," *Energy Environ. Sci.*, vol. 8, pp. 520–525, 2015.
  - [260] M. Reichenberger, D. Kroh, G. M. M. Matrone, K. Schötz, S. Pröller, O. Filonik, M. E. Thordardottir, E. M. Herzig, H. Bässler, N. Stingelin, and A. Köhler, "Controlling aggregate formation in conjugated polymers by spin-coating below the critical temperature of the disorder–order transition," *J. Polym. Sci. B: Polym. Phys.*, vol. 56, no. 6, pp. 532–542, 2018.



- [261] H. Hu, P. C. Y. Chow, G. Zhang, T. Ma, J. Liu, G. Yang, and H. Yan, "Design of donor polymers with strong temperature-dependent aggregation property for efficient organic photovoltaics," *Acc. Chem. Res.*, vol. 50, no. 10, pp. 2519–2528, 2017.
- [262] J. Zhang, W. Liu, M. Zhang, S. Xu, F. Liu, and X. Zhu, "PCE11-based polymer solar cells with high efficiency over 13 % achieved by room-temperature processing," *J. Mater. Chem. A*, vol. 8, pp. 8661–8668, 2020.
- [263] H. Ohkita, Y. Tamai, H. Benten, and S. Ito, "Transient absorption spectroscopy for polymer solar cells," *IEEE J. Sel. Top. Quantum Electron.*, vol. 22, no. 1, pp. 100–111, 2016.
- [264] H. Cha, S. Wheeler, S. Holliday, S. D. Dimitrov, A. Wadsworth, H. H. Lee, D. Baran, I. McCulloch, and J. R. Durrant, "Influence of blend morphology and energetics on charge separation and recombination dynamics in organic solar cells incorporating a nonfullerene acceptor," *Adv. Funct. Mater.*, vol. 28, no. 3, p. 1704389, 2018.
- [265] W.-Y. Sit, F. D. Eisner, Y.-H. Lin, Y. Firdaus, A. Seitzhan, A. H. Balawi, F. Laquai, C. H. Burgess, M. A. McLachlan, G. Volonakis, F. Giustino, and T. D. Anthopoulos, "High-efficiency fullerene solar cells enabled by a spontaneously formed mesostructured CuSCN-nanowire heterointerface," *Adv. Sci.*, vol. 5, no. 4, p. 1700980, 2018.
- [266] M. Hösel, R. R. Søndergaard, M. Jørgensen, and F. C. Krebs, "Fast inline roll-to-roll printing for indium-tin-oxide-free polymer solar cells using automatic registration," *Energy Technol.*, vol. 1, no. 1, pp. 102–107, 2013.
- [267] J.-M. Y. Carrillo, R. Kumar, M. Goswami, B. G. Sumpter, and W. M. Brown, "New insights into the dynamics and morphology of P3HT:PCBM active layers in bulk heterojunctions," *Phys. Chem. Chem. Phys.*, vol. 15, pp. 17873–17882, 2013.
- [268] J. Min, Y. N. Luponosov, C. Cui, B. Kan, H. Chen, X. Wan, Y. Chen, S. A. Ponomarenko, Y. Li, and C. J. Brabec, "Evaluation of electron donor materials for solution-processed organic solar cells via a novel figure of merit," *Adv. Energy Mater.*, vol. 7, no. 18, p. 1700465, 2017.

# Publications

## Paper I

**Title:**

Scalable fabrication of organic solar cells based on non-fullerene acceptors

**Authors:**

Anders S. Gertsen<sup>†</sup>, Marcial Fernández Castro<sup>†</sup>, Roar R. Søndergaard, and Jens W. Andreasen\*

**Published in:**

Flexible and Printed Electronics, vol. 5, 014004, 2020.

**Digital object identifier:**

10.1088/2058-8585/ab5f57

©2020 The Author(s). Published by IOP Publishing Ltd under the Creative Commons Attribution 3.0 licence.

---

<sup>†</sup>Equal contributions; \*corresponding authorship

## Flexible and Printed Electronics



## PAPER

## OPEN ACCESS

RECEIVED  
3 October 2019

ACCEPTED FOR PUBLICATION  
31 October 2019

PUBLISHED  
9 January 2020

Original content from this work may be used under the terms of the [Creative Commons Attribution 3.0 licence](#).

Any further distribution of this work must maintain attribution to the author(s) and the title of the work, journal citation and DOI.



## Scalable fabrication of organic solar cells based on non-fullerene acceptors

Anders S Gertsen<sup>1</sup> , Marcial Fernández Castro<sup>1</sup> , Roar R Søndergaard and Jens W Andreasen

Department of Energy Conversion and Storage, Technical University of Denmark, Frederiksborgvej 399, DK-4000 Roskilde, Denmark

<sup>1</sup> These authors contributed equally to the work.

E-mail: [jewa@dtu.dk](mailto:jewa@dtu.dk)

**Keywords:** organic photovoltaics, scalable fabrication, printing and coating, non-fullerene acceptors, polymer solar cells

## Abstract

Organic solar cells have recently experienced a substantial leap in power conversion efficiency, in part driven by formulations with new non-fullerene acceptors. This has brought the technology past the psychologically important mark of 15% efficiency for unscaled laboratory devices, and the results are stimulating another burst of research activity. Whether this will propel the technology into a viable commercial contender has yet to be determined, but to realize the potential of organic solar cells for utility scale application, fabrication using scalable processing techniques has to be demonstrated—otherwise, the passing of the 15% mark will eventually leave no more lasting impact than what the passing of the 10% mark did. Thus, addressing the scaling lag between the 15% cell efficiencies of lab-scale devices on rigid glass substrates fabricated using non-scalable techniques and the 7% efficiencies of scalably fabricated devices on flexible substrates is key. Here, we discuss the concept of scalability and give an account of the literature on non-fullerene acceptor devices fabricated with scalable methods and materials. On the basis of this, we identify three crucial focus points for overcoming the lab-to-fab challenge: (i) dual temperature control, i.e. simultaneous control of the ink and substrate temperatures during deposition, (ii) systematic *in situ* morphology studies of active layer inks with new, green solvent formulations during continuous deposition, and (iii) development of protocols for continuous solution processing of smooth, transparent interfacial layers with efficient charge transfer to the active layer. Combining these efforts and in general accompanying such studies with stability analyses and fabrication of large-area, scalably processed devices are believed to accelerate the relevance of organic solar cells for large-scale energy supply.

## 1. Broader context

Climate change is arguably one of the biggest challenges currently faced by human kind. Honouring the Paris Agreement and thus keeping the average global temperature rise in this century below 2 °C relative to pre-industrial levels demands an ambitious effort to replace fossil fuels with sustainable energy sources in our electricity production. Silicon solar cells are experiencing a rapid increase in worldwide installed capacity, but also new generations of solar cell technologies have the potential to reach maturity as a sustainable technology in the near future and thus to aid this transition. The key to the sustainability in terms of energy and materials use of these emerging technologies is scalability. Although silicon solar cell technologies have proven that upscaling fabrication also

leads to significant cost reductions, their fabrication remains very energy consuming. Organic solar cells could prove to be a viable alternative with projected energy payback times of only fractions of those of silicon modules. Already now, organic solar cells are used for niche applications owing to their semi-transparency, flexibility, low weight, and possibilities of custom designs in terms of colors and shapes. In addition, utility scale competitiveness of organic solar cells with mature thin-film technologies is edging closer in current years with researchers pushing laboratory cell efficiencies beyond 15% using novel non-fullerene acceptor materials and several companies continuously improving large-scale fabrication; bridging these efforts and thus addressing the lab-to-fab challenge remains the most significant hurdle for the sustainable scalability of organic solar cells.

## 2. Introduction

Organic photovoltaics (OPVs) are often cited as one of the most promising third generation solar cell technologies because of their compatibility with solution processed roll-to-roll fabrication, enabling a fast and continuous fabrication [1–3]. Whereas the projected energy payback times of roll-to-roll fabricated OPVs are as short as weeks [4], at least an order of magnitude better than those of silicon technologies [5], the large-scale, grid-connected installations of OPVs continue to be halted by economical inferiority. In order to overcome this, improvements of especially stabilities, but also efficiencies, of flexible OPV modules are needed [6, 7]. However, properties that are beneficial for building integration such as low weight and partial transparency have given OPVs an advantage, and a number of companies are focusing on these alternative applications.

With the surpassing of the psychologically important 15% power conversion efficiency (PCE) mark for single junction cells earlier this year [8], it is clear that the field of OPVs is experiencing a revitalization which can mainly be attributed to the emergence of non-fullerene acceptor materials [9, 10]. The advantages of these over fullerene-based acceptor materials do not only comprise higher efficiencies, but also improved optical absorption and tunability as well as superior cell stabilities [11–16]. Combined with the recently reported low dependence of the PCE on active layer thicknesses and areas for high-efficiency systems [8, 17, 18], many prerequisites for the upscaling of organic solar cells are nearly fulfilled.

In accordance with previous endeavors related to fullerene-based OPVs [1, 19–23], we believe that it is paramount for the continued growth of the research field as well as a sustainable scaleup of the technology that the current focus on high PCEs and material development within fullerene-free OPVs is accompanied by:

- (a) the use of roll-to-roll compatible or other scalable deposition methods in addition to spin coating,
- (b) efficiencies of larger cells ( $\geq 1 \text{ cm}^2$ ) or even modules alongside the small scale champion devices which are often only on the order of  $\text{mm}^2$ , and
- (c) stability analyses.

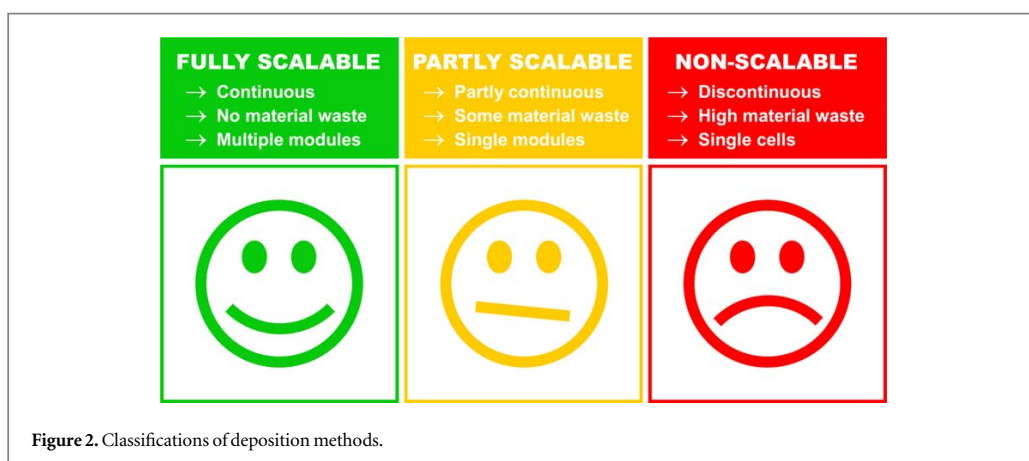
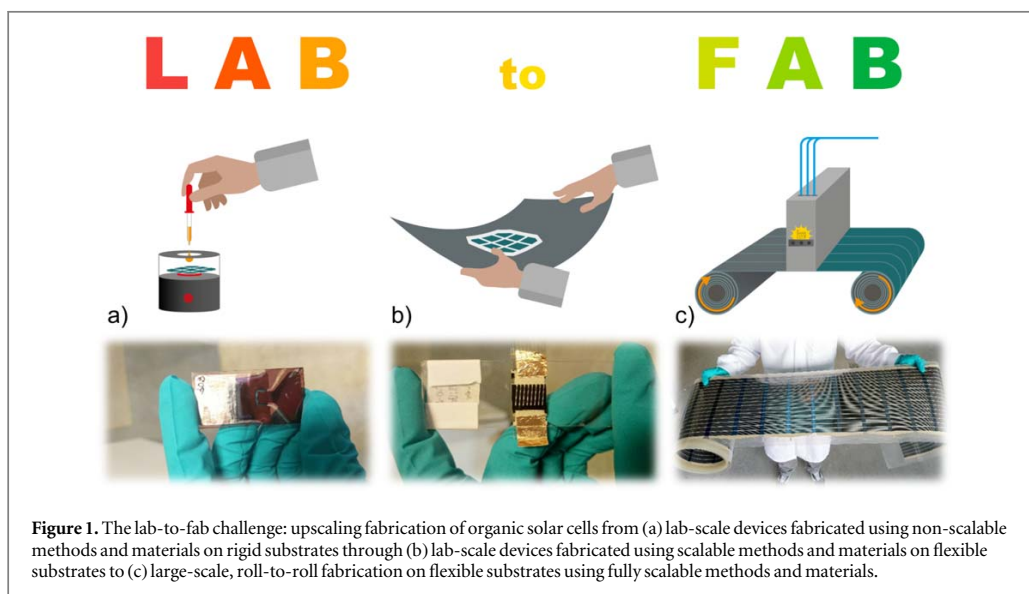
If these parameters were to be consistently reported, it would enable a more concentrated effort towards addressing the lab-to-fab challenges (visualized in figure 1) and meeting the 10-10 targets for flexible organic solar cell modules of 10% efficiency and 10 years stability [1]. Held up against extensive economical analyses based on flexible OPV modules with 7% PCE and stabilities of 5–10 years that predict superior leveled costs of electricity compared to mature solar

technologies such as e.g. crystalline silicon [7, 24], the 10-10 targets almost seem like a conservative estimate for sustainable scalability of organic solar cells. This further motivates overcoming the lab-to-fab challenges: in recent years, efficiencies well above 10% have consistently been reported for fullerene-free, spin-coated, small-area laboratory devices on glass substrates [17, 25–30], and 10% has also been reached using partly or fully scalable active layer deposition techniques (see section 3 for a discussion of scalability) [31, 32]. Even flexible devices with scalably deposited fullerene-free active layers are exhibiting efficiencies above 7% [33, 34], which, coupled with recent reports of 10 year lifetimes (extrapolated from 200 h stabilities) in fullerene-free, laboratory-scale devices by Du, Brabec *et al* [16], indicates that the 10-10 targets are within immediate reach.

The current limitations in upscaling of OPVs are complex and involve a series of challenges, including materials' compatibility, choice of non-toxic solvents, choice of compatible interface materials and, most importantly, stability and costs. Evaluating and seeking to overcome these limitations in devices processed using non-scalable deposition techniques such as spin-coating is inherently problematic, and they should instead be evaluated in the framework of fully scalably deposited OPVs. In this perspective, we review state-of-the-art fullerene-free, single junction OPV devices and the extent to which scalable techniques and materials are used in the fabrication. Aided by a discussion of the terminology related to the concept of scalability as it is used in connection with fabrication of organic solar cells, we aim to assess the potential of organic solar cells for sustainable scalability, to evaluate which material systems are the most promising for upscaling, and to suggest focus points for overcoming the lab-to-fab challenges currently faced. We note that a similar deserved attention is given to the closely related field of upscaling of perovskite solar cells in a recent publication, underlining the relevance of this challenge for third generation solar cells in general [35].

## 3. Scalability: a note on semantics

The word 'scalable' can generally be interpreted as the capability of a process to handle a larger workload without significantly compromising functionality and cost. However, formulating a clear cut definition of scalability in the context of organic solar cell fabrication is at best a very difficult task and not the purpose of this section. Instead, we seek a discussion and eventually a community-wide consensus on a terminology, allowing for a higher degree of transparency in the reporting of OPV devices. As a first iteration, and for categorizing fabrication processes reviewed in the



present article, we suggest the following three classifications (illustrated in figure 2).

- Fully scalable: high throughput deposition techniques that are directly compatible with continuous roll-to-roll setups and are linked to no material waste.
- Partly scalable: deposition techniques that can be made compatible with continuous roll-to-roll setups with some modifications and/or are linked to some material waste.
- Non-scalable: low throughput deposition techniques that are incompatible with continuous roll-to-roll setups and/or are linked to a high material waste.

These can be used to classify deposition techniques of both active layers and electrodes as well as interfacial

layers such as hole- and electron-transport layers. The arguments for the placement of specific deposition techniques in these categories will be given in section 4 alongside descriptions of these.

Defining scalability of the actual active layers based on non-fullerene acceptors is yet more complex. A material can have properties that allow for the use of scalable deposition methods without being scalable itself, simply because the material synthesis or manufacture is too elaborate and thus too expensive to use in an upscaling process. In this context, we would like to highlight the recent work by Li *et al* on an industrial figure of merit for the cost potential of fullerene-free OPVs [36], an extension of previous work by Min *et al* from 2017 [23], which in turn is inspired by the work of Bundgaard *et al* from 2015 [37]. By taking the synthetic complexity of the donor and acceptor materials into account alongside the PCE and the photostability of a device, this industrial figure of merit, i-FoM,

allows for a quantitative comparison of viability for upscaling across different active layers and the resulting devices. The synthetic complexity reflects the number of synthetic steps, the yield, the isolation/purification process, and the number of hazardous chemicals used, and it is therefore indirectly a qualitative estimation of both cost and sustainability of the donor and acceptor materials, making it a strong indicative measure of the scalability of the active layer itself. Taking the current rapid development of increasingly complex donor polymers and non-fullerene acceptors into account [14, 38–40], we believe that this i-FoM value could serve as an important tool in the evaluation of their scalability going forward. This, however, should not stand alone when discussing the potential for upscaling fabrication, since it does not incorporate the scalability of the fabrication as discussed above.

It is important to underline that scalability encompasses more than what is related to deposition techniques and active layers. Especially broader economical considerations regarding materials, processing conditions, and solvents are important for sustainable scalability of organic solar cell modules, but also environmental concerns should be taken into account. A number of significant contributions to the discussion of OPV scalability in terms of these parameters have been published throughout the years in the form of economical analyses [6, 7], life-cycle assessments [6, 41–43] and analyses of energy payback times [4, 5]. Although indeed interesting, these analyses are outside of the scope of this work, and we thus refer the interested reader to the cited articles.

## 4. Deposition techniques

In order to discuss scalability from a device fabrication point of view, it is important to understand the general working principles of how the different layers are deposited. Traditionally, the focus in the field has been on varying the active layer deposition, but here we will also try to incorporate interfacial layer deposition as well as electrode deposition. Comprehensive reviews of the different deposition techniques themselves have been published elsewhere [1, 44, 45], and we will hence refrain from extensive descriptions in the present paper and instead emphasize the discussion of their individual applicability to large-scale fabrication setups.

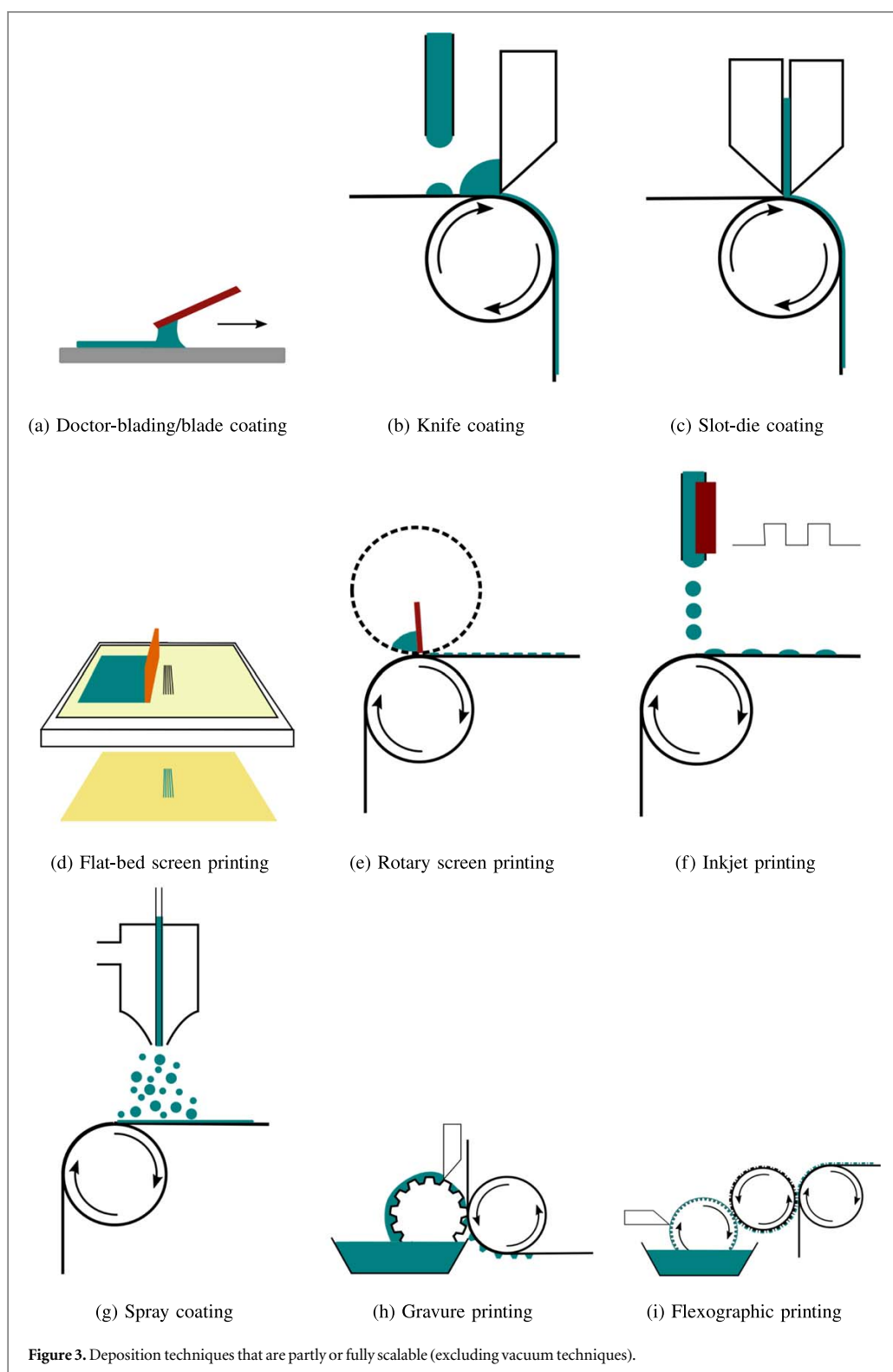
### 4.1. Coating and printing

We will here distinguish between coating and printing techniques—the former are used to deposit continuous layers along the translational direction of the substrate without direct contact to the surface of this, whereas the latter often are associated with the possibility to perform complex patterning through direct contact with the surface of the substrate, e.g. via a stamp, through the use of masks, or through control

of the flow as is the case for inkjet printing. Because of the ability of printing techniques to deposit well defined patterns, they are highly applicable for electrode deposition in semi-transparent devices, whereas coating techniques are most often used for active and interfacial layer deposition given their continuous nature and possibilities to control film thicknesses by varying flow rates and/or web speed. All scalable techniques mentioned in the below paragraphs are illustrated in figure 3.

**Spin-coating** 😞 Spin-coating is a thin-film deposition technique relying on the dispensing of a solution onto a rotating substrate. The centrifugal ‘force’ will distribute the dispensed solution across the substrate surface, and combined with simultaneous evaporation of the solvent(s), a uniform thin-film of the solute(s) is obtained. This technique allows for easy control of the thin-film thickness from tens of nanometers to several micrometers by varying the angular spin-speed (the thickness,  $d$ , is proportional to the inverse of the square root of the angular velocity,  $\omega$ :  $d \propto \frac{1}{\sqrt{\omega}}$ ) [44], which, coupled with the possibility of spin-coating on very small areas, provides a powerful lab-scale technique for testing wide ranges of processing parameters. However, there are significant drawbacks for large-scale implementations such as a high material waste (most of the dispensed material is slung off of the substrate and onto the walls of the spin-coater) and the lack of possibilities to engineer a continuous version of this. Although commercial implementations of spin-coating in e.g. the LED industry enables deposition on areas of up to 1 m<sup>2</sup>, the inherent batch process nature of spin-coating combined with the high material waste has made us label it non-scalable (see section 3 and figure 2). Spin-coating is thus one of the only deposition techniques that can not be used in scalable fabrication of OPVs, however, it remains to be the most widely used technique in literature for active layer and interfacial layer deposition due to the low equipment requirements and easy operation. The many years of experience with spin-coating deposition and historically the record device efficiencies achieved are obviously also significant drivers for the widespread use of this technique.

**Doctor-blading/blade coating** 😊 Because of its minimal equipment requirements and easy transferability to a roll-to-roll setup (as knife coating, see below), doctor-blading is often employed as the first step towards a more scalable deposition of active layers compared to spin-coating. By depositing an ink directly onto a substrate and subsequently dragging a sharp knife or a blade across it at a fixed distance, a wet thin-film with a well-defined thickness is obtained (see figure 3(a)). The empirical relationship defining the dry thickness,  $d$ , of this film is given by  $d = \frac{1}{2}g\frac{c}{\rho}$ , where  $g$  is the distance between the blade and the substrate,  $c$  the ink concentration, and  $\rho$  the dry film density [44]. This technique is accompanied by some



material waste, but with the possibility of obtaining coatings using only small amounts of material, it is a strong technique for laboratory scale testing. As the main limitation, formation of the thin-film using

doctor-blading is slow compared to spin-coating, and volatile solvents combined with highly concentrated inks can thus lead to non-uniform films if aggregation has time to occur. In general, however, the longer



solvent evaporation times for doctor-blading are more comparable to the ones of other scalable deposition techniques.

A variation of the doctor-blading technique that deserves mentioning is the fluid-enhanced crystal engineering (FLUENCE) technique developed by Diao *et al* in 2013 [46]. By patterning the ink contact side of the blade with micropillar arrays, a flow-induced extensional strain facilitates increased crystallinity while simultaneously reducing domain sizes in all-polymer solar cells, in turn improving the device characteristics [47]. This principle could readily be applied to other deposition techniques described herein.

**Knife coating** 😊 Knife coating (or knife-over-edge coating) can be regarded as the continuous, roll-to-roll compatible analog to doctor-blading: an ink supplier gradually adds excess ink to a bath downstream of a knife, which controls the thickness of the wet film through its proximity to the substrate (see figure 3(b)). It is in essence a zero-dimensional technique, but the inherent lack of control of the width of the deposited layer can in part be solved by adding barriers to the ink bath and thus prohibit material waste, whereas also viscous inks allow for well-defined widths. The somewhat unknown width can furthermore complicate the calculation of the dry thickness (which is defined in a similar way to the one of doctor-blading, see above). In spite of knife coating being a fully scalable technique, the higher degree of patterning control in e.g. slot-die coating for active layer deposition will probably limit the applicability of knife coating in commercial setups.

**Slot-die coating** 😊 Slot-die coating enables a continuous, roll-to-roll compatible deposition of many varieties of inks and not least a one-dimensional control of coating patterns in the form of one or more stripes with well-defined widths. In slot-die coating, the ink is supplied via a pump to a slot-die coating head through which the ink is deposited onto a moving substrate (illustrated in figure 3(c)). There is practically almost no material waste, and the thickness of the dry film can thus easily be calculated as  $d = \frac{c}{\rho} \frac{f}{vw}$ , where  $f$  is the ink flow rate,  $v$  the coating velocity (i.e. the speed of the substrate or of the coating head), and  $w$  the width of the deposited ink [44].

The limitations of this technique are mainly related to the fluid dynamics defining the so-called coating window, i.e. the range of parameters for which a stable meniscus can be obtained, which relies on a range of properties, including flow rate, ink viscosity, distance of the coating head to the substrate, and coating velocity [48]. Slot-die coating is, however, a forgiving technique in the sense that a broad range of ink viscosities can be used and that its continuous nature allows for visual feedback while fine-tuning the above mentioned mechanical parameters until a stable meniscus is formed.

One of the drawbacks of conventional slot-die coating is the lack of temperature control in the tubing and the slot-die head. Compared to spin-coating, where the time from removal of the ink from a heat-bath to the deposition onto a heated substrate can be very short, the longer time needed for slot-die coating can cause problems for inks that undergo gelation below certain temperatures. This can in part be solved by hot slot-die coating in which the slot-die head is heated and connected to a thermo-couple, providing an extra temperature control in addition to substrate hot-plates—this deposition method has also proven to be very beneficial in terms of device efficiency as demonstrated in [33, 49].

**Flat-bed screen printing** 😊 Especially applicable for electrode deposition owing to its full two-dimensional patterning control, flat-bed screen printing employs a mask through which the ink is pushed into contact with the substrate using a moving squeegee (see figure 3(d)). Because of the nature of this process, there are significant limitations in terms of the ink properties: it should have a high viscosity to avoid deviations from the patterning and the solvent should have a low volatility to avoid evaporation causing concentration gradients and thus differences in dry film thickness along the squeegee translational direction. As the thickness of the deposited layer is defined by the mask thickness, screen printing techniques are mostly applicable when thick layers (wet layer thicknesses of 10–500  $\mu\text{m}$ ) are needed; [1] the dry thickness can be estimated by  $d = k_p V_{\text{screen}} \frac{c}{\rho}$ , where  $V_{\text{screen}}$  is the paste volume of the screen (theoretical volume of wet ink deposited per area of mask hole) and  $k_p$  is the ratio of this wet ink that practically remains on the substrate [44]. There is potentially only a low material waste connected to this technique, and with it being a sheet-to-sheet process easily applicable for large areas, it is labeled partly scalable. This, however, makes it a strong technique for laboratory scale testing, and with the possibility to adapt it to fully continuous roll-to-roll setups through rotary screen printing (see below), observations and results from flat-bed screen printing are readily transferable to fully scalable fabrication.

**Rotary screen printing** 😊 Developed as a roll-to-roll compatible version of screen printing, rotary screen printing makes use of a stationary squeegee around which a mask rotates (see figure 3(e)). An ink bath supplies material, which in a similar fashion to flat-bed screen printing is pushed through the holes in the mask onto the substrate to reproduce the pattern of the mask. The limitations related to the ink viscosity are the same as in flat-bed screen printing, but the volatility of the solvent can be higher, as the ink is somewhat protected from the surroundings inside the screen.

**Inkjet printing** 😊 Inkjet printing is a digitally controlled patterning technique known from standard printers. Using a nozzle with a piezoelectric stage or a thermal unit to eject ink droplets that are then



electrostatically charged and accelerated towards the substrate by an electric field, a digital pattern can be reproduced with high resolution and no material loss (illustrated in figure 3(f)). Although indeed attractive for niche applications where complex or varying patterning as well as aesthetics are necessary, the slow speeds, relative to slot-die coating, with which inkjet printing can coat large areas are a potential limitation for its use in large-scale fabrication of organic solar cells. We have hence, despite its apparent compatibility with a continuous roll-to-roll setup, labeled it partly scalable. Furthermore, restrictions on the ink to have a low viscosity to be able to form droplets can be prohibitive for inkjet printing of some layers. The thickness of a dry film deposited by inkjet printing can be calculated as  $d = N_d V_d \frac{\epsilon}{\rho}$ , where  $N_d$  is the number of droplets with volume  $V_d$  deposited per unit area [44].

**Spray coating** 😊 Like inkjet printing, spray coating relies on droplet formation of the ink. However, the requirements to the ink are more lenient compared to inkjet printing, facilitating the use of inks with a wide variety of rheologies and viscosities [50]. The most common spray coating technique is airbrush spray coating, where an aerosol is formed by forcing the ink out of the nozzle using a gas flow, usually  $N_2$  (see figure 3(g)). Whereas inkjet printing is a two-dimensional patterning technique, spray coating is essentially zero-dimensional, although with the possibility of some one-dimensional control if variations in the stripe edges can be accepted. This sacrifice of patterning control, however, enables a significant speedup of the deposition, allowing for a more meaningful roll-to-roll implementation, but the relatively high surface roughness and thus the need for thicker layers to prevent pinholes can in practice lead to low-efficiency or even defect cells and in turn to material waste. We have therefore categorized this technique as only partly scalable despite its roll-to-roll compatibility.

**Gravure printing** 😊 Known from commercial printing, gravure printing is based on a gravure roller transferring ink from a bath via its engraved cavities to the substrate when pressed into contact (visualized in figure 3(h)). This allows for high speed processing and two-dimensional patterning in a continuous roll-to-roll setup with the shape and thickness of the obtained patterns defined by the engravings in the gravure roller. As the main limitation of gravure printing, the necessary optimization of the ink's surface tension should be mentioned, since factors such as the ink rheology and the pressure of the gravure roller on the substrate affect the quality of the print significantly [1].

**Flexographic printing** 😊 In flexographic printing, the ink is transferred from the bath via an anilox roller, which is a cylinder with ink-collecting micro-cavities, to the relief of a printing roller that then 'stamps' its pattern onto the substrate when pressed into contact (see figure 3(i)). Like for gravure printing, this allows

for two-dimensional patterning control in continuous roll-to-roll setups, and the remaining advantages and limitations are very similar to this too.

## 4.2. Vacuum deposition

Previously, vacuum steps have been regarded as being non-compatible with large-scale fabrication of organic solar cells, and 'vacuum-free' has often been used in literature as a precondition for scalability [21, 44, 51–53]. We would, however, like to challenge that position with reference to the numerous commercial photovoltaic technologies incorporating vacuum deposition steps such as organic light emitting diodes and silicon solar cells. Furthermore, Heliatek has demonstrated with their HeliaFilm® pilot line in 2016 and later with a small-scale fabrication line that a full roll-to-roll setup in inert atmosphere and with several vacuum steps is indeed realizable and not least commercially promising [54]. Very recently, the group led by M Madsen at the University of Southern Denmark also demonstrated roll-to-roll vacuum sputtering using their in-house setup [55]. Vacuum steps are thus not prohibitive for the upscaling of the fabrication itself, and if the costs related to material use and processing conditions, amongst these high-temperature steps, can be kept down as indicated by the commercial nature of the HeliaFilm® project, vacuum- and inert steps are likely to be part of the future large-scale fabrication of organic solar cells because of the efficiency gains usually seen compared to solution processing in ambient conditions.

**Thermal evaporation** 😊 Also known as vapor deposition, thermal evaporation relies on resistive heating of an evaporation source, for example silver in the case of electrode deposition, under vacuum until a vapor pressure is reached and the evaporated silver is deposited on a substrate, forming a thin-film. Thermal evaporation allows for a precise control of the layer thickness and produces highly uniform layers, and patterning control is achievable through the use of shadow masks: for one-dimensional control, a stationary mask would be sufficient, whereas two-dimensional patterning in a continuous setup would demand a mask moving with the same speed as the substrate. The requirement of shadow masks for patterning control is, however, linked to a not insignificant material waste, but the material deposited on the shadow mask could potentially be recycled. Even though this is a significant challenge, especially in terms of economy when using expensive materials such as silver, we have in the evaluation of this deposition method chosen to put emphasis on the possibility to integrate it into a roll-to-roll setup for continuous deposition and thus labeled it partly scalable.

**Sputtering** 😊 In sputter deposition, material is eroded off of a target source, e.g. molybdenum, using, in most cases, argon plasma. The sputtered material will then deposit on the substrate to form a thin-film. The atmosphere in the sputtering chamber can be

tuned to need—for example in the case of  $\text{MoO}_x$  hole-transport layers, molybdenum atoms are sputtered in a controlled oxygen atmosphere to obtain a stoichiometrically desired  $\text{MoO}_x$  layer. Like for thermal evaporation, the uniformity of the deposited layer is high, and its thickness can be controlled with a very high precision down to single nanometres. The need for shadow masks poses problems identical to the ones for thermal evaporation, but it should be noted that the amount of material needed per area is usually significantly lower for vacuum deposition than for solution processing because of the homogeneity of the vacuum deposited layers.

## 5. Overview of scalably fabricated, fullerene-free OPVs from literature

The availability of equipment and especially the ease of use are important explanatory factors for the relatively few studies published on fully scalable fabrication of organic solar cells. However, as discussed above, techniques like blade coating and flat-bed screen printing are optimal for laboratory-scale optimization and readily transferable to continuous roll-to-roll setups, but whereas blade coating has recently been used routinely for active layer deposition, top electrodes and interfacial layers are still, almost exclusively, thermally evaporated.

Opposed to scalable deposition techniques, the use of non-fullerene acceptor materials is not a prerequisite for commercial fabrication of organic solar cells, but they have to a large extent simply out-competed fullerene acceptors. Fullerene acceptors have historically been widely used in the active layers of organic solar cells owing to their favorable properties such as high electron affinities, high electron mobilities, and easy solution processing [56]. However, the low-energy transitions in fullerenes are dipole forbidden owing to their high molecular symmetry, in turn leading to weak optical absorbance in the visible spectrum, which is a significant limitation for further improvements in the efficiencies of fullerene-based organic solar cells. The optical properties of non-fullerene acceptors can to a higher degree be tuned by chemically engineering their molecular structure. The most widely used design principle for small-molecule, non-fullerene acceptor materials is to utilize a conjugated internal acceptor–donor–acceptor structure in which two electron withdrawing units (internal acceptors) are separated by a central electron donating unit (internal donor) and potential bridging units [57, 58]. In this way, the low-energy transitions are red-shifted due to a promotion of charge-transfer states, in turn facilitating an optical absorption profile dominant in the red part of the visible spectrum, complementary to most polymer donor materials, which

absorb in the blue and green parts of the spectrum. A second way to achieve this is by employing polymeric, non-fullerene acceptor materials with internally alternating donor–acceptor structures [38, 59, 60], similarly facilitating low-energy charge-transfer absorptions. Like for the fullerene acceptors, high electron affinities of both small-molecule and polymer non-fullerene acceptors are obviously paramount, but the active layer processing conditions for which optimal microphase separation and domain purity occur to ensure high electron mobilities can vary greatly for the three types of acceptors and not least for different deposition techniques. These considerations will be discussed below.

Another important consideration for scalable processing relates to the device architecture. On flexible substrates, and especially in a roll-to-roll context, the inverted device architecture has proven to be the most practical given the available materials and processing methods. In particular, hole-transport layers have shown to be problematic in normal device architecture solar cells, as they have to be both highly transparent (all light has to pass through it to reach the active layer) and mechanically robust (being the first layer processed on top of the transparent electrode, it is subject to high stress). The commonly used materials like PEDOT:PSS and hole-conducting metal oxides have so far not proven processable in a way where these demands are fulfilled. On the other hand, the materials for electron-transport layers have not suffered from the same problems. Highly transparent materials like  $\text{ZnO}$  and  $\text{TiO}_x$  are routinely used and have proven themselves as good front materials in inverted architecture solar cells while simultaneously allowing the use of less transparent and less robust hole-transport materials such as the above mentioned at the back of the solar cell. The dominance of the inverted architecture, as will be obvious from the following sections, is thus predominately a consequence of the availability of suitable materials. If new hole-transport materials with the right properties are found, there is in principle no reason why normal architecture solar cells could not be used in the future.

Throughout the coming sections, we have highlighted groundbreaking works and their resulting devices in figures 4–8. The molecular structures of all donor polymers mentioned in these sections are shown in figure 9, of all non-fullerene acceptors in figure 10, and of all molecular interfacial layers in figure 11. The device parameters for all mentioned devices, including short-circuit currents, open-circuit voltages, and fill-factors (FF), as well as qualitative estimates of the scalability of the materials and deposition techniques are summarized in table 1. Further details regarding this table can be found in section 5.5.



**Figure 4.** Flexible, ITO-free, vacuum-free OPV module fabricated using continuous roll-to-roll deposition techniques at the Technical University of Denmark.

### 5.1. Devices fabricated using solely roll-to-roll compatible deposition methods and no vacuum steps 😊

Only a few studies on fully roll-to-roll compatible, vacuum-free processing of non-fullerene systems have been reported. The first effort in this respect was published in 2013 by Liu *et al* [64], where they investigated the effect of upscaling small area devices on glass substrates with spin-coated active and interfacial layers and thermally evaporated electrodes to a complete roll-to-roll fabrication of large-area modules on flexible substrates. For the flexible devices, an inverted structure of indium tin oxide (ITO)/ZnO (NP)/PDI-DTT:PSBTBT/PEDOT:PSS/Ag was used; the polyethylene terephthalate (PET) substrate with ITO was purchased from a commercial supplier, the zinc oxide nanoparticles (ZnO(NP)), active layer (PDI-DTT:PSBTBT, see figures 9 and 10, respectively), and PEDOT:PSS (see figure 11) were slot-die coated, and the silver back electrode was deposited using a roll-to-roll integrated flat-bed screen printer. The average efficiencies of the resulting  $4.2 \text{ cm}^2$  modules were 0.20%, a factor of three lower than the small-area, spin-coated devices on glass substrates, leaving notable room for improvement. The effect of the substrate (PET versus glass) was concluded to be a decisive factor, but probably most problematic for upscaling (disregarding the low performance) was the use of ITO. ITO has been shown to be both economically and environmentally critical, and in addition, the significant fraction of more than 80% of the embedded energy in similar modules stemming from the ITO coated PET posed a significant impediment for the projected energy payback times [6, 41].

This problematic use of ITO had already been addressed in fullerene-based OPVs at several occasions [65, 66], but the first study of roll-to-roll compatible processing of non-fullerene OPVs on flexible substrates without ITO was not published until 2014

by Chen *et al* [67]. This was additionally the first study looking to replace the fullerenes in the well-known model system P3HT:PC<sub>61</sub>BM (see figure 9) with small-molecule, non-fullerene acceptors in fully roll-to-roll processed OPVs, but the efficiencies reached were lower than 0.1%. However, the deposition techniques and the device structure used therein have been the dominant in literature since. The processing equipment was introduced in 2012 by Dam and Krebs, who reported a laboratory-scale coating/printing machine enabling the fully scalable processing of all layers in a stand-alone setup [68], and the device structure was introduced by Carlé *et al* later that year [69]. Using an inverted architecture of PET/Ag/PEDOT:PSS/ZnO(NP)/D:A/PEDOT:PSS/Ag (D: donor, A: acceptor), ITO- and vacuum-free devices could be realized, allowing for lab-scale assessment of new active layers in the context of large-scale fabrication. The processing is, in principle, straightforward: flexographic printing of a silver paste onto the PET substrate, slot-die coating of a ZnO nanoparticle solution, slot-die coating of a PEDOT:PSS ink, slot-die coating of an active layer ink, slot-die coating of a second PEDOT:PSS ink, and lastly flexographic printing of a silver paste as the top electrode. This also enables the use of pre-processed substrate foils with bottom electrodes and ZnO electron-transport layers already applied, making the testing of new systems simple as well as minimizing material waste.

The above procedure has been used in almost all studies of fully roll-to-roll compatible, non-fullerene acceptor OPVs published subsequently. In 2014, Cheng *et al* aimed to study the effects of the 1,8-diiodooctane (DIO) high boiling-point additive and to compare spin-coating on glass substrates with slot-die coating on flexible substrates in this type of setup for both fullerene-based systems and all-polymer systems [70]. Of the four combinations, the scalable processed, flexible, all-polymer cells with an

inverted Ag/PEDOT:PSS/ZnO(NP)/PBDDTTT-C-T:PDIDTT/PEDOT:PSS/Ag structure (see figure 9 for structures; note that PDIDTT is only shown in here despite of its applicability as an acceptor too) showed the lowest average PCEs of 0.67% for 1 cm<sup>2</sup> devices. This was followed by a paper from the same authors in 2015 [11], using identical device structures and deposition techniques but with a small-molecule, non-fullerene acceptor (active layer: PBDDTTT-C-T:DC-IDT2T, see figures 9 and 10). This led to a champion efficiency of 1.0% for a 1 cm<sup>2</sup> device, which was, however, still a factor of two lower than the PC<sub>71</sub>BM analog. On the other hand, the non-fullerene devices showed a far superior stability under continuous AM 1.5G illumination, maintaining more than 80% of their initial efficiency compared to the mere 50% of the fullerene-based device. This increased stability has later been shown to be a somewhat general characteristic for small-molecule, non-fullerene acceptors [12, 13, 16], giving them a significant advantage over fullerene acceptors for commercial viability.

The following year in 2016, Liu *et al* investigated devices based on the PTB7-Th:IEIC active layer (see figures 9 and 10 for molecular structures) [71]. With champion efficiencies of 6.31% in lab-scale, spin-coated devices on glass substrates with evaporated electrodes, it was a good candidate for upscaling to flexible devices deposited with fully scalable methods. They employed two types of flexible device structures on PET foil: an ITO-free one, namely Ag/PEDOT:PSS/ZnO(NP)/PTB7-Th:IEIC/PEDOT:PSS/Ag, and an ITO-containing one, namely ITO/ZnO(NP)/PTB7-Th:IEIC/PEDOT:PSS/Ag. As described above, the ITO-free devices were deposited using flexographic printing for the electrodes and slot-die coating for the remainder of the layers, whereas the PET/ITO foil was purchased and the remainder of the layers were processed as for the ITO-free devices. For the ITO-free devices, an average PCE of 1.60% with a champion efficiency of 1.79% was obtained for 1 cm<sup>2</sup> cells, whereas the ITO containing devices reached an average PCE of 2.05% and a champion efficiency of 2.26% for 0.7 cm<sup>2</sup> cells—all of these were slightly lower than their fullerene (PC<sub>61</sub>BM) counterparts, but were at the time the highest reported efficiencies for flexible, non-fullerene devices. All cells in this study were suffering from low FF of around 35%, but the fullerene-free cells exhibited slightly higher FF than the fullerene cells, whereas the fullerene cells had significantly higher short-circuit currents. Stability tests were also performed, showing increased stability in the fullerene-free devices, in turn supporting the statement made in the previous paragraph.

Later that year, Brandt *et al* reported the only second work on combining P3HT and non-fullerene

acceptors using roll-to-roll compatible processing [52]. Here, they investigated variations in absorption, crystallinity, and device performance based on the geometrical effects of three diketopyrrolopyrrole acceptors with different degrees of ground state planarity in a combined study between quantum chemical calculations, X-ray experiments, and device characterization. Obtaining only low efficiencies of 0.54% for the best roll-coated device (using the same device structure as described above), the most important conclusion drawn from this study was that the less crystalline system performed better in roll-coating, whereas the more crystalline system performed better in spin-coating. This underlines the need for *in situ* morphological studies of active layer deposition to probe the microstructure evolution during solvent evaporation [72–75].

For a couple of years after this, no studies on fully scalably fabricated, fullerene-free devices were published, but from 2016 onwards, significant effort has been put into synthesis of new and improved non-fullerene acceptors. The impressive efficiencies exceeding 10% reached in lab-scale devices using IDTBR small-molecule acceptors [13, 76–78] has, in 2018, motivated Strohm *et al* to produce P3HT:O-IDTBR modules using fully scalable deposition methods (see figure 10 for the structure of IDTBR) [61]. Although the modules were deposited on ITO coated glass substrates, which prohibits a true industrial fabrication as discussed above, we have chosen to include their work in this section because of their effort to upscale both the interfacial layers themselves and their deposition as well as the deposition of the top electrode. Using a device structure of ITO/ZnO(NP)/P3HT:O-IDTBR/PEDOT:PSS/AgNW (AgNW: silver nanowires), doctor-bladed 0.1 cm<sup>2</sup> cells with an average PCE of 5.25% and an average FF of 66.6% were fabricated using a solvent formulation of chlorobenzene with 5% 4-bromoanisole additive for the active layer processing. 59.5 cm<sup>2</sup> modules using the same device structure and processing conditions exhibited efficiencies of an impressive 5.0% (see figure 5), whereas exchanging doctor-blading for slot-die coating yielded modules with efficiencies of up to 4.4%. This system is thus indeed interesting for further studies on flexible, ITO-free substrates using true roll-to-roll deposition.

From this limited number of works on scalably fabricated, non-fullerene OPVs, it is clear that there is room for significant progress in the field. In line with our recommendations in the introduction, we urge an increased effort to demonstrate scalability both in terms of deposition techniques and materials. As will be evident from the below sections, promising material systems and solvent formulations as well as important considerations regarding interfacial layers





**Figure 5.** Rigid OPV module with P3HT:O-IDTBR active layers fabricated using roll-to-roll compatible deposition techniques by S Strohm, F Machui, and co-workers. Reproduced from [61] with permission from The Royal Society of Chemistry.

have been put forth, which, combined, will surely lead to advances for fully scalably fabricated OPVs.

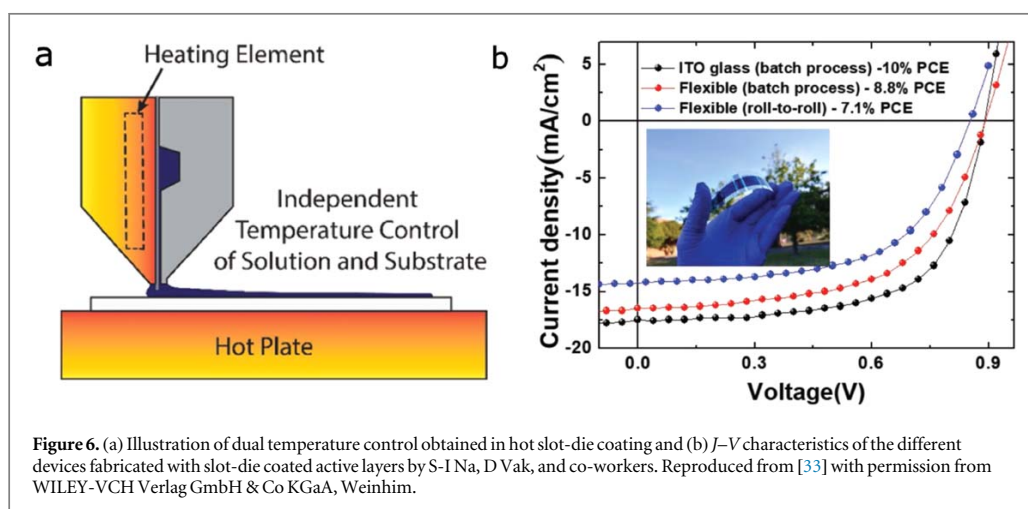
### 5.2. Devices fabricated using solely roll-to-roll compatible deposition methods but vacuum steps 😊

As discussed in section 4.2, vacuum deposition techniques are likely to play a role in future large-scale fabrication of organic solar cells if the processing costs can be kept low; the techniques themselves are not incompatible with roll-to-roll setups. In this section, we will thus highlight studies utilizing vacuum deposition for the top electrodes and hole-transport layers but using continuous roll-to-roll deposition techniques for the active layers.

In 2017, Gu *et al* were the first to reach the 5% efficiency mark for fullerene-free organic solar cells using roll-to-roll deposition of the active layer [3]. In this study, different all-polymer active layers were studied in a PET/ITO/ZnO(NP)/D:A/MoO<sub>3</sub>/Ag device structure, where the ZnO(NP) and active layers were slot-die coated onto a pre-produced PET/ITO foil in a custom-built roll-to-roll setup and the MoO<sub>3</sub> hole-transport layers as well as the silver top electrodes were thermally evaporated. Using sidechain engineering to control crystallinity, the two donor polymers PII2T and PII2T-PS (see figure 9) were synthesized and categorized as crystalline and low-crystalline, respectively, using grazing-incidence X-ray scattering. They were then paired with the two acceptor polymers PNDIT and PPDIT (see figure 10), similarly categorized as crystalline and low-crystalline, respectively. Spin-coated, lab-scale devices were then fabricated for each

of the four pairs, showing that suppressing crystallinity led to higher device efficiencies caused by lower phase-separation sizes. The low-crystalline PII2T-PS:PPDIT pair was hence identified as the best candidate for upscaling, and cells were fabricated using the device structure described above. A small module with a combined area of 10 cm<sup>2</sup> was characterized, showing an average PCE of 4.1% with a champion PCE of 4.24% measured over 12 of the 0.12 cm<sup>2</sup> cells that were connected to form the 10 cm<sup>2</sup> module. With these impressive results in mind, they extended the study to encompass the PTB7-Th:PPDIE active layer (see figure 10 for molecular structures of PPDIE), which exhibited even lower crystallinity and phase-separation sizes than the PII2T-PS:PPDIT combination. The roll-to-roll coated devices based on this PTB7-Th:PPDIE active layer showed an average PCE of 5.0% with a champion PCE of 5.1%, at the time a record for flexible organic solar cells with continuously printed active layers. This work furthermore substantiates the findings of Brandt *et al* [52] described in the previous section, putting additional emphasis on the importance of morphological studies and showcasing the strength of developing design principles.

Very recently, in 2019, Na *et al* reported the current record efficiency of 7.11% for non-fullerene organic solar cells with roll-to-roll deposited active layers [33]. Extending their previous work on fullerene-based OPVs [49], their novel modification of a slot-die coater was used to investigate the effects of deposition temperature on device parameters of fullerene-free OPVs. By implementing a heating element in the slot-die head of a modified 3D printer,



independent temperature control of the solution and the substrate was achieved (see figure 6(a)). Optimization showed large deviations of several percentage points in PCE with varying substrate temperature, whereas fixing the substrate at its optimum temperature of 120 °C and varying the slot-die head temperature showed a couple of percentage points difference with an optimum around 90 °C. They used an ITO/ZnO(NP)/PEIE/PBDB-T:ITIC/MoO<sub>3</sub>/Ag device structure (see figures 9–11 for the structures) with pre-produced ITO-coated substrates, slot-die coating of the ZnO nanoparticles, the PEIE electron-transport layers, and the active layers, and thermal evaporation of MoO<sub>3</sub> and the silver top electrodes. PCEs of 10.0% on glass substrates with slot-die batch processing, 8.77% on PET substrates with slot-die batch processing, and 7.11% on PET substrates with full roll-to-roll, continuous slot-die processing were achieved for 0.07 cm<sup>2</sup> areas (see figure 6(b)). The latter is close to the current efficiency record for flexible OPV devices with roll-to-roll processed active layers of 7.32%, which was reached using an ITO/AZO:PEIE/PTB7:PC<sub>71</sub>BM/MoO<sub>3</sub>/Ag structure (AZO: aluminum-doped zinc oxide) in 2017 [34]. The discrepancy between the batch process and the roll-to-roll process for flexible substrates is explained by the physical contact between the coated film and the backside of the substrate on the rewinder roll, but this contact will be avoided in commercial roll-to-roll setups before the addition of the remainder of the layers or even before encapsulation. These results thus strongly indicate that dual temperature control can be key in overcoming the lab-to-fab challenge and realizing large-scale fabrication of flexible OPVs with high efficiencies.

### 5.3. Devices fabricated using partly scalable active layer deposition methods ☺

The vast majority of fully scalable deposition techniques are not straightforward to adopt in small-scale laboratory testing of costly material systems of which only small amounts are available. In particular, doctor-

blading has been a popular choice as the first stepping stone towards scalable fabrication of organic solar cells because of its easy transferability to continuous processing. This makes it a strong technique for optimization of active layer solutions in terms of solvents, additives, material composition, and processing conditions in batch processes prior to upscaling. Hence, in this section, we will keep a principal focus on the active layers and review the most notable works using doctor-blading or other partly scalable techniques for the active layer deposition. Unless otherwise mentioned, ZnO(NP) electron-transport layers were spin-coated and MoO<sub>3</sub> hole-transport layers and Al or Ag top electrodes thermally evaporated for all reviewed devices below.

In the doctor-blading paragraph of section 4, we briefly touched upon the FLUENCE technique. In 2015, Diao *et al* used this variation of the doctor-blading technique to alter the morphology of all-polymer active layers [47]. It was found that the flow design with a microstructured blade increased the crystallinity of neat donor PII-tT-PS5 thin-films while concurrently reducing domain sizes in blend PII-tT-PS5:PPDIT thin-films (PPDIT is also denoted P(TP); see figures 9 and 10, respectively, for structures). Additionally, the surface roughness was also reduced significantly compared to regular, unstructured doctor-blading, in turn improving the reproducibility of device efficiencies. The combined effect of these properties led to a champion PCE of 3.2% in an inverted glass/ITO/ZnO(NP)/PII-tT-PS5:PPDIT/MoO<sub>3</sub>/Al structure, the record efficiency for blade-coated, all-polymer organic solar cells at the time.

The following year in 2016, Ye *et al* reached a new record efficiency for blade-coated, all-polymer OPVs [79]. By doctor-blading a PBDT-TS1:PPDIOT active layer (see figures 9 and 10) in a green solvent, namely 2-methylanisole, in an inverted glass/ITO/ZnO(NP)/MoO<sub>3</sub>/Al architecture, a champion PCE of 5.21% was achieved. This was one of the earlier efforts to replace the halogenated solvents regularly used for a green solvent, allowing for a more environmentally friendly

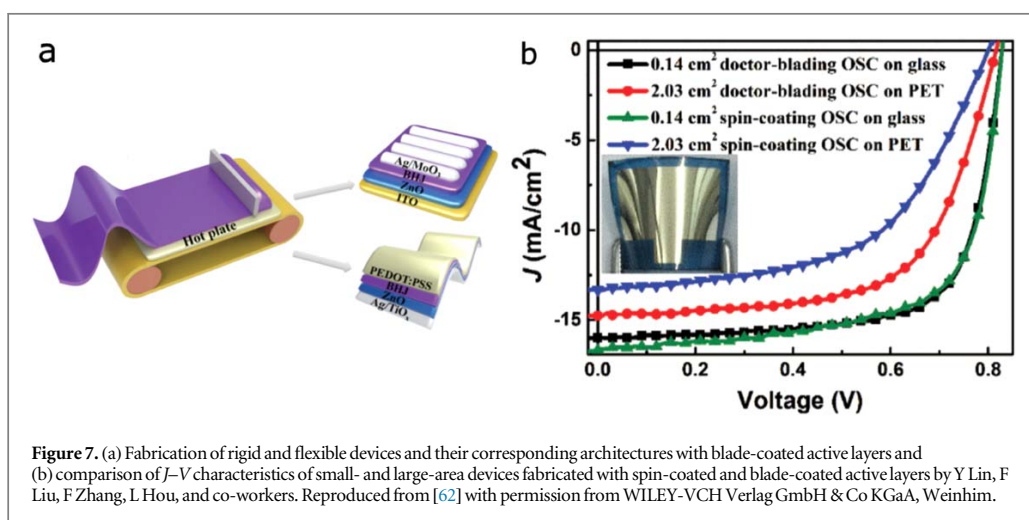


**Figure 7.** (a) Fabrication of rigid and flexible devices and their corresponding architectures with blade-coated active layers and (b) comparison of  $J$ - $V$  characteristics of small- and large-area devices fabricated with spin-coated and blade-coated active layers by Y Lin, F Liu, F Zhang, L Hou, and co-workers. Reproduced from [62] with permission from WILEY-VCH Verlag GmbH & Co KGaA, Weinheim.

processing, which is particularly desirable for large-scale fabrication. More recently in 2019, Lin *et al* also focused on the use of non-halogenated solvents to control the morphology of all-polymer OPVs based on PTzBI: N2200 active layers (see figures 9 and 10, respectively, for structures) [80]. Using 2-methyltetrahydrofuran as the processing solvent, a champion PCE of 8.36% was achieved, whereas devices processed from chlorobenzene only reached 2.92% (both in glass/ITO/ZnO(NP)/D:A/MoO<sub>3</sub>/Al inverted structures). This significant difference underlines the importance of exploring alternative—and preferably green—solvent formulations.

Moving to small-molecule acceptors, the ITIC non-fullerene acceptor and derivatives hereof have dominated the scene of blade-coated devices since late 2017. In December, Zhao *et al* investigated a methylated ITIC derivative, IT-M, in conjunction with the polymeric donor PBTA-TF (see figures 9 and 10) processed in green solvent formulations [81]. By comparing spin-coating and blade-coating of this active layer using both a low-boiling point solvent blend, namely tetrahydrofuran/isopropanol, and a high-boiling point solvent blend, namely *o*-xylene/1-phenylnaphthalene, it was found that the spin-coated devices performed slightly better when processed from the high-boiling point blend, whereas the blade-coated devices performed significantly better when processed from the low-boiling point blend. For these tetrahydrofuran/isopropanol processed, blade-coated devices, a record PCE of 11.7% was obtained in a conventional glass/ITO/PEDOT:PSS/D:A/PFN-Br/Al architecture (see figure 11 for PFN-Br structure) and 11.3% in an inverted glass/ITO/ZnO(NP)/D:A/MoO<sub>3</sub>/Al architecture, both for 0.04 cm<sup>2</sup> devices. Impressively, large-area conventional devices of 1.0 cm<sup>2</sup> maintained a high efficiency of 10.6%, showing great promise for both this material system and the tetrahydrofuran/isopropanol solvent formulation for blade-coating.

In January 2018, Ye *et al* also investigated IT-M in an active layer with the FTAZ donor (see figure 9) similarly using a conventional glass/ITO/PEDOT:PSS/D:A/PFN-Br/Al architecture [31]. Once more, chlorobenzene processing, even with additives, was shown to be inferior to processing in additive-free, non-halogenated solvents, exemplified by pure toluene yielding a champion PCE of 11.0% for a 0.07 cm<sup>2</sup> cell, close to the above mentioned record at the time for blade-coated OPVs. For an area of 0.56 cm<sup>2</sup>, an impressive PCE of 9.80% was reached, and with a dark stability of 85% of the initial PCE after 1000 hours in nitrogen atmosphere as well as only minimal FF reductions with longer annealing times at 150 °C, the morphological stability of this material system shows promise for adoption to commercial fabrication.

Simultaneously in January 2018, Lin *et al* published their efforts on doctor-blading flexible, large-area devices based on ITIC [62]. In a comparative study, they investigated the difference of spin-coated and blade-coated active layers as well as that of rigid substrates and flexible substrates (see figure 7). In addition, they worked with ITO-free PET for the flexible substrates, yielding the overall most scalable cells reviewed in this section. Starting from the glass substrates, doctor-blading the active layer in an ITO/ZnO(NP)/PTB7-Th:ITIC/MoO<sub>3</sub>/Ag inverted structure, a champion PCE of 9.54% was achieved, slightly higher than the 9.31% of the spin-coated analog. For the flexible substrates, this difference was more pronounced with a champion PCE of 7.60% for doctor-blading and 5.86% for spin-coating in an inverted Ag/TiO<sub>x</sub>/PTB7-Th:ITIC/PEDOT:PSS devices with large areas of 2.03 cm<sup>2</sup>—the former 7.60% a record for large-area, flexible, ITO-free, non-fullerene OPVs with blade-coated active layers.

Later in 2018, Zhang *et al*, investigated the dependence of device characteristics on DIO additive content in chlorobenzene active layer processing solution for spin- and blade-coated glass/ITO/ZnO(NP)/PBDB-T:ITIC/MoO<sub>3</sub>/Al cells [32]. Historically, DIO has been

key to achieving high efficiencies in devices deposited from halogenated solutions, but the difficulty of removing residual DIO content due to its high boiling-point has been shown to lead to accelerated morphology evolution [82] and degradation of device performance caused by iodine radicals formed under irradiation [83]. Using processing solvent formulations not dependent on DIO additives, as in the above described work of Ye *et al* [31], is thus the most obvious solution, although decreasing the DIO content would also be a step in the right direction. In the work mentioned in this paragraph by Zhang *et al* [32], it was found that blade-coated devices exhibited an optimum PCE of 10.0% for a DIO content of 0.25%, whereas the optimum PCE of 9.41% for spin-coated devices was achieved for a DIO content of 1.00%. This was reflected in the stability studies of unencapsulated devices, where the blade-coated cells with 0.25% DIO outperformed the spin-coated with 1.00% DIO on all parameters, both under illumination in ambient and in the dark under nitrogen atmosphere, indicating that both of the discussed degradation pathways were indeed relevant. These findings motivate morphological studies on residual additive content in dry OPV thin-films and in particular studies on alternative, additive-free processing solutions.

Jumping to 2019, Ji *et al* set out to investigate and optimize the surface morphology of ZnO electron-transport layers, leading to some of the highest efficiencies both for blade-coated OPVs in general of 12.88% for 0.12 cm<sup>2</sup> cells and for blade-coated, fullerene-free, large-area (>1 cm<sup>2</sup>) OPVs of 9.22% for 1.04 cm<sup>2</sup> cells [84]. Two different solutions of zinc oxide nanoparticles were prepared and used in the inverted glass/ITO/ZnO(NP)/PBDB-T:IT-4F/MoO<sub>3</sub>/Al devices (see figure 10 for IT-4F structure): one in acetone (A-ZnO) and one in methanol (M-ZnO). Scanning electron microscopy images revealed inhomogeneities and voids in pristine ZnO films spin-coated from acetone, whereas the methanol processed films exhibited compactness and an increased homogeneity. Additionally, atomic force microscopy showed a higher surface roughness for A-ZnO than for M-ZnO, which was ascribed to the faster drying process of the former ink. For devices of the above structure, the M-ZnO electron-transport layers yielded slightly better device performances than the A-ZnO layers when spin-coating the PBDB-T:IT-4F active layers (champion PCEs of 12.81% and 12.40% for 0.12 cm<sup>2</sup> devices, respectively), whereas this improvement was more pronounced when blade-coating the active layers (champion PCEs of 12.88% and 11.74% for 0.12 cm<sup>2</sup> devices, respectively). The performance disparity was hypothesized to originate from a change in interface charge transport properties between the active layer and the ZnO layers induced by the different surface morphologies of these, motivating further studies of this.

Very recently, Pascual-San-José *et al* published an elaborate study on blade-coated P3HT:NFA devices with a range of non-fullerene acceptors in an inverted glass/ITO/ZnO(NP)/D:A/MoO<sub>3</sub>/Ag architecture [85].

Only the active layer deposition and the deposition of the ZnO(NP) electron-transport layer were, however, sought upscaled, and with an optimized efficiency of 5.6% for a P3HT:O-IDTBR active layer, the upscaling effort by Strohm *et al* [61] described in the above section 5.1 remains a stronger contribution on this specific system in terms of scalable fabrication. The strength of the study by E Pascual-San-José M Campoy-Quiles, and co-workers is, however, that they devise a high-throughput screening method incorporating variable speed blade-coating, enabling active layer thickness gradients, as well as a Kofler bench, enabling annealing temperature gradients. This continuous change of processing parameters allowed for the fabrication of more than a thousand devices of area 8 mm<sup>2</sup>. In addition, an exemplary stability study was performed on P3HT:O-IDTBR devices, yielding the dependence of efficiency on encapsulation and active layer thicknesses. A degradation to 80% of initial performance was linearly extrapolated to >5 years for encapsulated devices with thin (80 nm) active layers, as compared to 8300 h for encapsulated devices with thick (250 nm) active layers, substantially longer than the 700 h and 120 h, respectively, for the corresponding unencapsulated devices (all based on measurements up to 3000 h). Interestingly, light-beam induced-current measurements suggested that P3HT suffered from a lower degradation rate than O-IDTBR, meaning that further optimization of IDTBR micro-phases could lead to better stabilities.

As a last work in this section, the 2019 study by D Corzo, D. Baran, *et al* on digital inkjet printed active layers deserves mentioning [63]. Using the P3HT:O-IDTBR material system also mentioned in section 5.1, inverted devices with a glass/ITO/ZnO(NP)/P3HT:O-IDTBR/MoO<sub>3</sub>/Ag architecture were fabricated. By optimizing the rheologies of the ink formulations with respect to solvents and concentrations, a champion PCE of 6.47% for a 0.1 cm<sup>2</sup> cell was obtained for a homogeneous, inkjet printed active layer processed from a 1,2-dichlorobenzene solution. Increasing the active area to 2 cm<sup>2</sup> yielded only a small drop in device performance, sustaining a PCE of 6.00% (see figure 8(a)). In order to illustrate the possibility of full two-dimensional patterning using inkjet printing, a 2.2 cm<sup>2</sup> device in the shape of a marine turtle was fabricated with an efficiency of 4.76% (depicted in the inset of figure 8(b)), creatively demonstrating how versatile OPV custom designs can be.

The works highlighted above contribute with important observations on the path towards upscaling organic solar cell fabrication. First of all, the use of green, non-halogenated solvents are not only beneficial for the performance of fullerene-free OPVs deposited with scalable methods, but also for the device stability due to the elimination of the need for processing additives—and not least for the environmental friendliness of the fabrication itself. Secondly, and strongly linked to the first point, the volatilities of the solvents used during deposition of the active layers



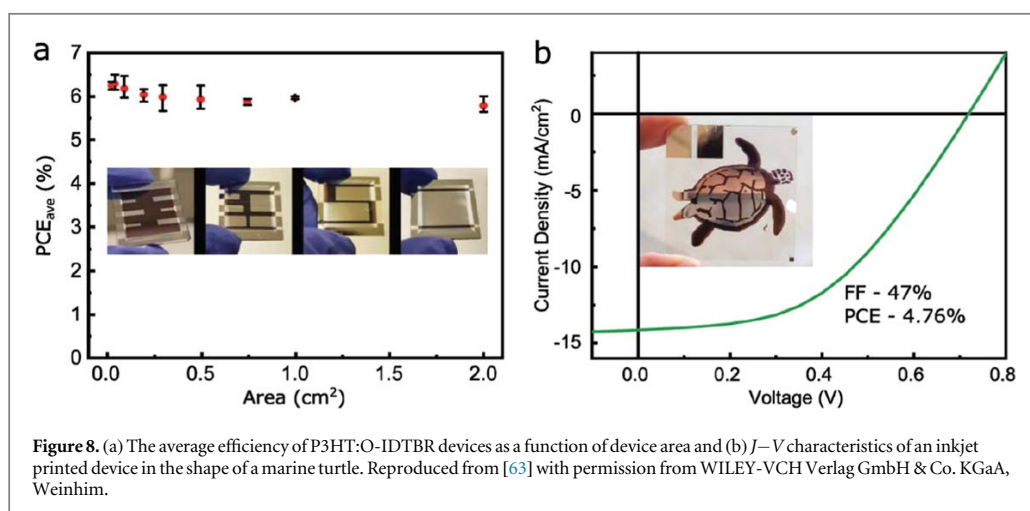


**Figure 8.** (a) The average efficiency of P3HT:O-IDTBR devices as a function of device area and (b)  $J$ - $V$  characteristics of an inkjet printed device in the shape of a marine turtle. Reproduced from [63] with permission from WILEY-VCH Verlag GmbH & Co. KGaA, Weinheim.

are crucial. Depending on the miscibility and crystallinity of the donor: acceptor couples, tuning the boiling-point of the solvent formulations is probably necessary to close the efficiency gap seen between spin-coated and scalably deposited active layers, as the slower evaporation times for techniques like blade-coating and slot-die coating could lead to unfavorable aggregation. This calls for more systematic solvent studies and preferably *in situ* morphological studies refining the, predominantly phenomenological, hypotheses based on indirect observations. Finally, we should strive to improve the smoothness of interfacial layers to promote charge transport between these and the active layers through altering the processing solvent formulations that are optimized for spin-coated fullerene devices. Surface morphology studies of slot-die coated interfacial layers processed from different solvents could hence provide essential insight into what seems to be a significant pathway for performance losses when upscaling deposition methods, especially when combined with studies of the interface between these and the active layer components.

#### 5.4. Promising material systems for upscaling

The absence in literature of ITO-, vacuum-, and fullerene-free devices on flexible substrates fabricated using solely fully scalable deposition techniques with efficiencies of more than 2% underlines the need for a concentrated effort towards this goal. Most material systems presented in sections 5.2 and 5.3 show great promise for adoption to fully scalable fabrication, and in addition to these, a number of recent record-breaking lab-scale systems fabricated solely using spin-coating and vacuum deposition deserve mentioning. In this section, we will thus review selected works with donor: acceptor pairs that have, as of now, not been used in devices with scalably deposited active layers.

Already in the first months, 2019 proved to be an extraordinary year for organic solar cells, particularly fueled by the synthesis of a novel non-fullerene acceptor by the name of BTPTT-4F (also denoted Y6; see figure 10 for structure) [8]. First, Yuan *et al* reported this synthesis

and demonstrated, at the time, record device efficiencies for single-junction OPVs of up to 15.7% (certified to 14.9%) for lab-scale cells with spin-coated PBDB-TF: BTPTT-4F active layers (PBDB-TF is also denoted PM6; see figure 9 for structure) [8]. Using both a conventional device architecture of glass/ITO/PEDOT:PSS/PBDB-TF:BTPTT-4F/PDINO/Al (see figure 11 for PDINO structure) and an inverted device architecture of glass/ITO/ZnO(NP)/PBDB-TF:BTPTT-4F/MoO<sub>3</sub>/Ag, average PCEs of 15.6% and 15.5%, respectively, both with champion PCEs of 15.7%, were reached for 0.07 cm<sup>2</sup> cells. This equally high performance in inverted architectures is crucial, because the inverted structure significantly improves the long-term stability in ambient conditions relative to conventional architectures [86], which is a prerequisite for sustainable scalability of organic solar cells. Although their following studies on conventional architectures were not carried out for inverted architectures, they showed interesting tendencies. First of all, it was found that increasing the active layer thickness did not hamper the device efficiencies significantly: going from 150 to 300 nm yielded a two percentage point drop in champion PCE from 15.7% to 13.6%. Although the open-circuit voltages and the short-circuit currents remained largely unaffected by the increased thickness, the FF went down from 74.8% to 62.3% and was thus the main reason for the efficiency drop. Most notable, however, was the impressive performance of additive-free, as-cast devices: using no annealing steps after deposition, an average PCE of 15.2% was obtained, showcasing the stability of this material system with different processing conditions.

Shortly after, Fan *et al* reported the current efficiency record for single-junction OPVs of 16.0%, also using the BTPTT-4F non-fullerene acceptor [87]. A conventional architecture of glass/ITO/PEDOT:PSS/P2F-EHp:BTPTT-4F/PFNDI-Br/Ag was employed (structures for P2F-EHp and PFNDI-Br can be found in figures 9 and 11, respectively), leading to PCEs of 11.1% for additive-free, as-cast devices and, as mentioned, the record 16.0% using devices processed with

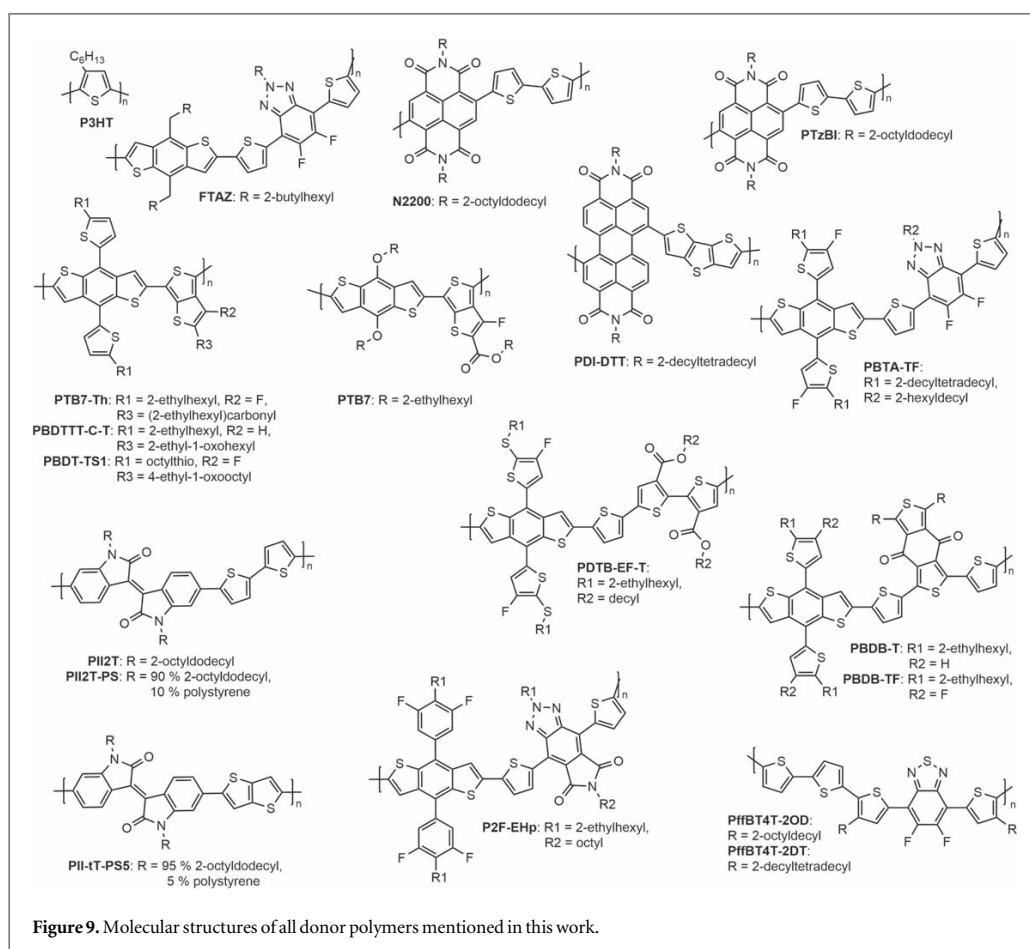


**Figure 9.** Molecular structures of all donor polymers mentioned in this work.

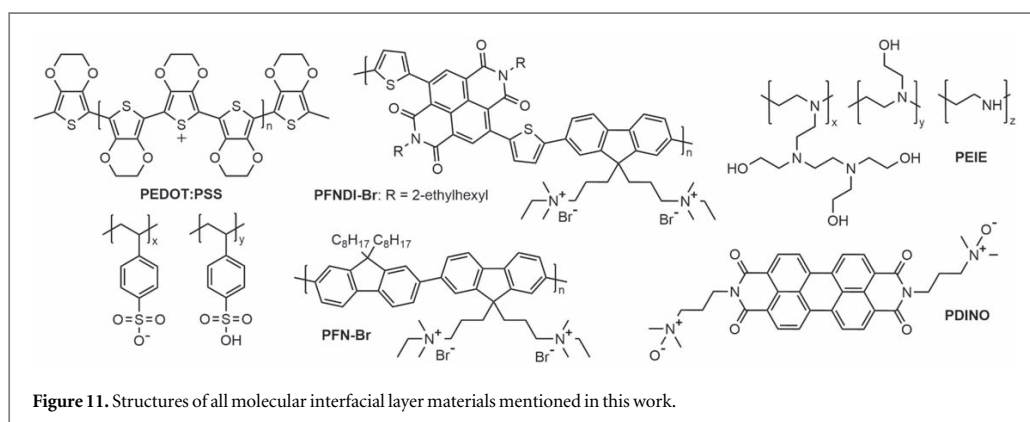
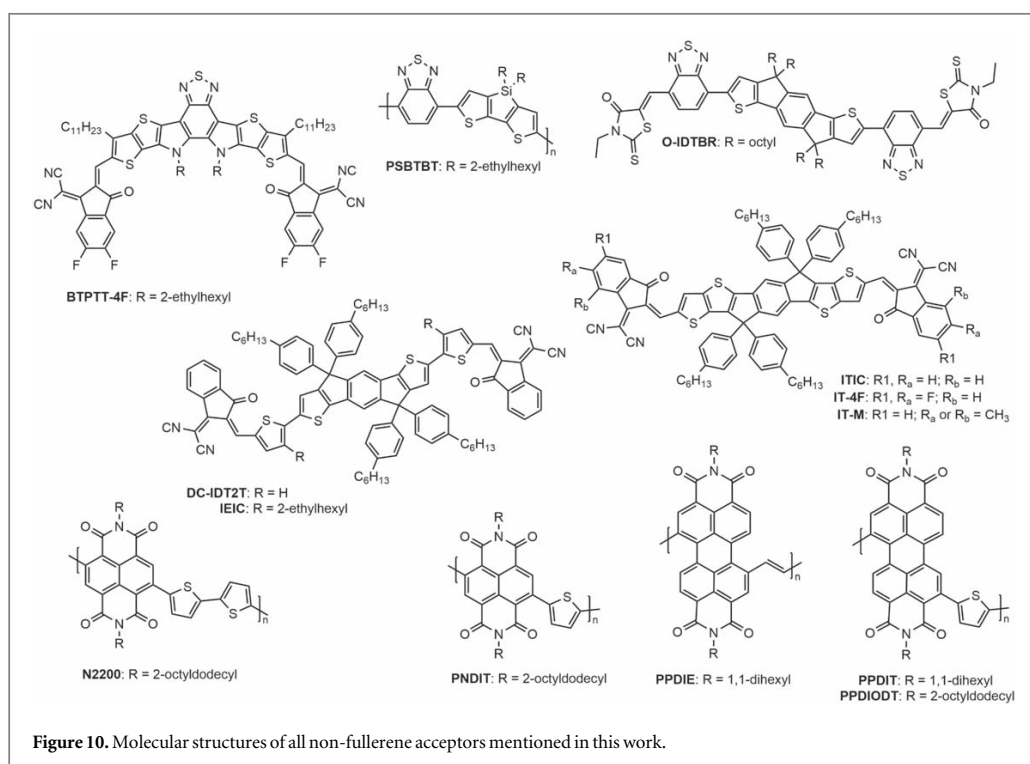
a relative amount of 1% dibenzylether solvent additive. Inverted devices were also fabricated, leading to a champion PCE of 13.1% for glass/ITO/ZnO(NP)/P2F-EHp:BTPPT-4F/MoO<sub>3</sub>/Ag cells, also processed with 1% dibenzylether. BTPPT-4F is thus indeed a promising non-fullerene acceptor that holds a great potential for application in upscaled systems.

In the previous section 5.1, the IDTBR non-fullerene acceptor was introduced, and cells and modules utilizing this in conjunction with P3HT donor polymers were reviewed. However, coupling the IDTBR acceptor with PffBT4T derivatives (see figure 9) has consistently yielded efficiencies of around 10%–11% in lab-scale devices [13, 76, 78], making this an attractive material system for testing in scalable fabrication when taking the favorable properties into account such as negligible burn-in efficiency losses [13], high open-circuit voltages above 1 V [76], and high reproducibility and lifetime when processed in green solvents (non-halogenated hydrocarbons) [78].

Finally, the ITIC family of small-molecule acceptors should be mentioned. As reviewed in section 5.2, the PBDB-T:ITIC system has already proven to be very well performing in slot-die coated layers, and coupled with the impressive results obtained for blade-coated layers as

presented in section 5.3, it is clearly indicated that variations of this material system hold great potential for scalably processed OPVs. Furthermore, in 2018, the efficiency record for single-junction organic solar cells was held by a cell incorporating an active layer based on the fluorinated IT-4F acceptor, namely PDTB-EF-T:IT-4F (see figure 9 for donor structure). In a glass/ITO/ZnO(NP)/PDTB-EF-T:IT-4F/MoO<sub>3</sub>/Ag inverted structure, average PCEs of 14.0% were obtained with a champion PCE of 14.2% (certified to 13.9%) and an impressive FF of 76% [29], further profiling ITIC derivatives as some of the best acceptor candidates for future fullerene-free OPVs.

With these high-efficiency material systems in mind, alongside the considerations regarding processing when going from spin-coating to scalable deposition described in the previous section, it seems that the active layers will not be the limiting factors for large-scale fabrication of organic solar cells with efficiencies of 10% or more. Knowing that the intrinsic charge transport and -transfer properties of the polymer donors and non-fullerene acceptors indeed facilitate high-efficiency active layers, focus can be put on optimizing the morphology of slot-die coated inks through systematic studies of processing conditions,



including dual temperature-control and solvent formulations. Furthermore, and probably equally importantly, the interfaces between the active layers and the electron- and hole-transport layers should be optimized with regards to smoothness using scalable, continuous deposition techniques.

### 5.5. Summary of the reviewed devices

In table 1, the deposition methods and characteristics of all devices reviewed in the above sections 5.1–5.4 are listed. This includes the donor and non-fullerene acceptor (D:A) materials, the deposition method of the active layer, the processing solvent formulation,

the substrate material(s), the deposition method of the top electrode, the device areas, and their corresponding champion PCEs, FF, open-circuit voltages ( $V_{oc}$ ), and short-circuit currents ( $J_{sc}$ ).

The deposition methods are classified using the smiley-model presented in section 3 by their colors green, yellow, or red to provide a quick overview. A similar classification is used for the processing solvents: halogenated solvents are marked with yellow and non-halogenated solvents with green as a representation of their environmental friendliness. Correspondingly, the substrates are marked with red for rigid glass substrates, yellow for PET substrates with

**Table 1.** Overview of the materials and deposition methods used for the reviewed devices alongside their performance characteristics.

D:A materials (see figures 9–10)	Active layer deposition	Solvent(s)	Substrate	Top electrode deposition	Device area (cm <sup>2</sup> )	PCE <sub>max</sub> (%)	FF (%)	V <sub>oc</sub> (V)	J <sub>sc</sub> (mA cm <sup>-2</sup> )	Year	References
PDI-DTT:PSBTBT	Slot-die, R2R	CB:CN	PET/ITO	Flat-bed, R2R	4.20	0.20	28.9	0.37	1.9	2013	[61]
P3HT:DPP(BT-N <sub>2</sub> ) <sub>2</sub>	Slot-die	CF	PET	Flexographic	1.00	0.07	37.6	0.53	0.3	2014	[64]
PBDTTT-C:TPPDIT	Slot-die	CB:DIO	PET	Flexographic	1.00	0.73	42.5	0.63	2.5	2014	[67]
PBDTTT-C:EDC-IDT2T	Slot-die	CB	PET	Flexographic	1.00	1.02	40.1	0.80	3.1	2015	[11]
PTB7-Th:IEIC	Slot-die	o-DCB	PET/ITO	Flexographic	0.70	2.26	36.7	0.90	5.4	2016	[68]
	Slot-die	o-DCB	PET	Flexographic	1.00	1.79	35.2	0.94	6.9		
P3HT:Ph(DPP) <sub>3</sub>	Slot-die	CF	PET	Flexographic	1.00	0.54	35.8	0.82	1.5	2016	[52]
	Doctor-blading	CB:BrA	Glass/ITO	Doctor-blading	0.10	5.25 <sup>a</sup>	66.6	0.70	11.3	2018	[76]
P3HT:O-IDTBR	Doctor-blading	CB:BrA	Glass/ITO	Doctor-blading	59.5	5.00	64.9	0.71	10.9		
	Slot-die	CB:BrA	Glass/ITO	Slot-die	59.5	4.40	64.9	0.70	9.8		
P12T-PS:PPDIT	Slot-die, R2R	CB	PET/ITO	Thermal evap.	10.0 <sup>a</sup>	4.24	45.0	0.99	9.6	2017	[3]
PTB7-Th:PPDIE	Slot-die, R2R	CB	PET/ITO	Thermal evap.	10.0 <sup>a</sup>	5.10	50.0	0.64	15.5	2017	[3]
	Slot-die	o-DCB	Glass/ITO	Thermal evap.	0.07	10.00	64.9	0.88	17.5	2019	[33]
PBDB-T:ITC	Slot-die	o-DCB	PET/ITO	Thermal evap.	0.07	8.77	58.6	0.88	17.0		
	Slot-die, R2R	o-DCB	PET/ITO	Thermal evap.	0.07	7.11	58.1	0.86	14.2		
P11-4T-PS:PPDIT	Doctor-blading	CB	Glass/ITO	Thermal evap.	0.04	3.20	46.0	1.01	7.0	2015	[47]
PBDT-TS:PDIOIT	Doctor-blading	e-MA	Glass/ITO	Thermal evap.	0.07	5.21	53.4	0.74	12.8	2016	[77]
PTzBEN2200	Doctor-blading	MeJHF	Glass/ITO	Thermal evap.	0.04	8.36	66.7	0.84	14.9	2019	[78]
	Doctor-blading	THE:IP	Glass/ITO	Thermal evap.	0.04	11.70	66.0	0.95	18.1	2017	[79]
PBTA-TE:IT-M	Doctor-blading	THE:IP	Glass/ITO	Thermal evap.	1.00	10.60	65.0	0.95	17.1		

Table 1. (Continued.)

D:A materials (see figures 9–10)	Active layer deposition	Solvent(s)	Substrate	Top electrode deposition	Device area (cm <sup>2</sup> )	PCE <sub>max</sub> (%)	FF (%)	V <sub>oc</sub> (V)	J <sub>sc</sub> (mA cm <sup>-2</sup> )	Year	References
FTAZ:IT-M	Doctor-blading	Toluene	Glass/ITO	Thermal evap.	0.07	11.00	66.1	0.95	16.8	2018	[31]
	Doctor-blading	Toluene	Glass/ITO	Thermal evap.	0.56	9.80	64.6	0.93	16.4		
PTB7-Th:ITIC	Doctor-blading	CB/DIO	Glass/ITO	Thermal evap.	0.14	9.54	71.0	0.83	16.0	2018	[80]
	Doctor-blading	CB/DIO	PET	Thermal evap.	2.03	7.60	63.0	0.81	14.7		
PBDB-T:ITIC	Doctor-blading	CB/DIO	Glass/ITO	Thermal evap.	0.04	10.00	66.1	0.89	17.1	2018	[32]
PBDB-T:IT-4F	Doctor-blading	CB/DIO	Glass/ITO	Thermal evap.	0.12	12.88	72.0	0.86	20.8	2018	[83]
	Doctor-blading	CB/DIO	Glass/ITO	Thermal evap.	1.04	9.22	N/A	N/A	N/A		
P3HT:O-IDTBR	Doctor-blading	CB:DCB	Glass/ITO	Thermal evap.	0.08	5.60	61.6	0.74	12.4	2019	[84]
P3HT:O-IDTBR	Inkjet printing	o-DCB	Glass/ITO	Thermal evap.	0.10	6.47	67.2	0.71	13.8	2019	[85]
	Inkjet printing	o-DCB	Glass/ITO	Thermal evap.	2.00	6.00	N/A	N/A	N/A		
	Inkjet printing	o-DCB	Glass/ITO	Thermal evap.	2.20	4.76	47.0	0.72	14.1		
PBDB-TE:BTPTT-4F	Spin-coating	CF:CN	Glass/ITO	Thermal evap.	0.07	15.70	76.1	0.82	25.2	2019	[8]
P2F-Ehp:BTPTT-4F	Spin-coating	CF:DBE	Glass/ITO	Thermal evap.	0.05	16.00	74.1	0.82	26.7	2019	[87]
PDTB-EF:IT-4F	Spin-coating	CB/DIO	Glass/ITO	Thermal evap.	N/A	14.20	76.0	0.90	20.7	2018	[29]

<sup>a</sup>Average value of > 10 cells; <sup>b</sup>characteristics measured over 0.12 cm<sup>2</sup> cells; CB: chlorobenzene; CN: 1-chloronaphthalene; CF: chloroform; o-DCB: 1,2-dichlorobenzene; BrA: 4-bromoanisole, o-MA: 2-methylanisole, (Me)THF: (2-methyl) tetrahydrofuran, IP: isopropanol, DBE: dibenzylether.

ITO, and green for ITO-free PET to indicate their scalability.

## 6. Conclusions and outlook

The field of organic solar cells has been moving fast in recent years, and record efficiencies are published regularly using new non-fullerene acceptor materials. In this perspective, we have sought to identify focus points for overcoming the challenge of upscaling the fabrication of organic solar cells based on these non-fullerene acceptors. By categorizing a wide range of deposition techniques in terms of their compatibility with continuous roll-to-roll setups, their material waste, and their throughput as either fully scalable, partly scalable, or non-scalable, the literature on fullerene-free OPVs was reviewed using these classifications. Although numerous studies have been published on laboratory-scale devices fabricated using non-scalable deposition techniques, only a small number have been published on devices fabricated using fully- or partly scalable deposition techniques. However, combining the knowledge gained from these few studies allows us to suggest three main priorities for meeting the lab-to-fab challenge.

- (i) First of all, implementing dual temperature control, meaning that both the ink- and substrate temperatures can be controlled simultaneously and independently, for example through the use of heated slot-die coating heads, has shown to be an impressively effective way of optimizing the active layer morphologies, leading to some of the highest efficiencies published for flexible OPVs.
- (ii) Secondly, the use of non-halogenated, i.e. 'green', solvents for active layer deposition has in several cases shown to be superior to using halogenated solvents. Some of these studies also point to the fact that processing additives, which are common in halogenated solvent formulations and which might cause device performance to deteriorate with time and illumination, can be made redundant with green solvents. Furthermore, tuning the boiling point of the active layer solvent formulation is crucial to facilitate preferential morphology evolution during evaporation when depositing active layers with scalable techniques. Systematic *in situ* studies can aid the interpretation of such studies.
- (iii) Finally, the interfacial layers should be optimized for continuous deposition techniques. The well-performing systems with roll-to-roll deposited active layers and evaporated top electrodes reviewed in section 5.2 all utilize thermally evaporated MoO<sub>3</sub> hole-transport layers. As vacuum deposition, as discussed, could very well be connected to high processing costs, solution processable formulations of molybdenum oxide hole-transport layers have

great potential as replacements of thermally evaporated MoO<sub>3</sub> layers [88], whereas also solution processable molybdenum sulfide hole-transport layers show promise with performance comparable to PEDOT:PSS-based devices [89]. Very recently, solution processed tungsten sulfide layers have also shown great promise as hole-transport layers [90]. We thus recommend that improving solution processed interfacial layers is prioritized going forward, as significant efficiency gains for scalably fabricated, flexible organic solar cells are expected if the qualities of solution processed charge transport layers can get close to the ones of the evaporated. In addition, the interface between the electron-transport layer, usually ZnO nanoparticles, and the active layer has shown to be important too as reviewed in section 5.3. Simply by changing the processing solvent, a higher smoothness and fewer voids and inhomogeneities can be achieved in spin-coated ZnO layers, in turn leading to relative efficiency increases of almost 10% for devices with blade-coated active layers [84]. Studying the surface morphology of these interfacial layers with varying processing conditions when deposited using fully scalable methods is thus important going forward, as the optimal conditions might differ significantly from the spin-coated ones.

If these three points are addressed, we are confident that the 10-10 goals of 10% efficiency and 10 years stability for scalably fabricated organic solar cells can be reached [1, 7, 24], making sustainable, large-scale fabrication viable. We urge that large-area devices (>1 cm<sup>2</sup>) fabricated using scalable deposition techniques are reported alongside the laboratory-scale champion devices, preferably accompanied by stability analyses, in order to move towards these goals and identify promising material systems for upscaling.

## Acknowledgments

We acknowledge financial support from the H2020 European Research Council through the SEEWHI Consolidator grant, ERC-2015-CoG-681881.

## Conflicts of interest

There are no conflicts of interest to report.

## ORCID iDs

Anders S Gertsen  <https://orcid.org/0000-0002-4712-0339>

Marcial Fernández Castro  <https://orcid.org/0000-0003-3294-2994>



Roar R Søndergaard  <https://orcid.org/0000-0003-3567-3400>

Jens W Andreassen  <https://orcid.org/0000-0002-3145-0229>

## References

- [1] Søndergaard R, Hösel M, Angmo D, Larsen-Olsen T T and Krebs F C 2012 Roll-to-roll fabrication of polymer solar cells *Mater. Today* **15** 36–49
- [2] Lucera L, Kubis P, Fecher F W, Bronnbauer C, Turbiez M, Forberich K, Ameri T, Egelhaaf H and Brabec C J 2015 Guidelines for closing the efficiency gap between mono-junction solar cells and roll-to-roll printed modules *Energy Technol.* **3** 373–84
- [3] Gu X *et al* 2017 Roll-to-roll printed large-area all-polymer solar cells with 5% efficiency based on a low crystallinity conjugated polymer blend *Adv. Energy Mater.* **7** 1602742
- [4] Espinosa N, Hösel M, Angmo D and Krebs F C 2012 Solar cells with one-day energy payback for the factories of the future *Energy Environ. Sci.* **5** 5117–32
- [5] Peng J, Lu L and Yang H 2013 Review on life cycle assessment of energy payback and greenhouse gas emission of solar photovoltaic systems *Renew. Sustain. Energy Rev.* **19** 255–74
- [6] Emmott C J, Urbina A and Nelson J 2012 Environmental and economic assessment of ITO-free electrodes for organic solar cells *Sol. Energy Mater. Sol. Cells* **97** 14–21
- [7] Gambhir A, Sandwell P and Nelson J 2016 The future costs of OPV—A bottom-up model of material and manufacturing costs with uncertainty analysis *Sol. Energy Mater. Sol. Cells* **156** 49–58
- [8] Yuan J *et al* 2019 Single-junction organic solar cell with over 15% efficiency using fused-ring acceptor with electron-deficient core *Joule* **3** 1140–51
- [9] Lin Y and Zhan X 2014 Non-fullerene acceptors for organic photovoltaics: an emerging horizon *Mater. Horiz.* **1** 470–88
- [10] Lin Y, Wang J, Zhang Z-G, Bai H, Li Y, Zhu D and Zhan X 2015 An electron acceptor challenging fullerenes for efficient polymer solar cells *Adv. Mater.* **27** 1170–4
- [11] Cheng P, Bai H, Zawacka N K, Andersen T R, Liu W, Bundgaard E, Jørgensen M, Chen H, Krebs F C and Zhan X 2015 Roll-coated fabrication of fullerene-free organic solar cells with improved stability *Adv. Sci.* **2** 1500096
- [12] Gasparini N *et al* 2017 Burn-in free nonfullerene-based organic solar cells *Adv. Energy Mater.* **7** 1700770
- [13] Cha H *et al* 2017 An efficient, 'burn in' free organic solar cell employing a nonfullerene electron acceptor *Adv. Mater.* **29** 1701156
- [14] Zhang G, Zhao J, Chow P C Y, Jiang K, Zhang J, Zhu Z, Zhang J, Huang F and Yan H 2018 Nonfullerene acceptor molecules for bulk heterojunction organic solar cells *Chem. Rev.* **118** 3447–507
- [15] Cheng P, Li G, Zhan X and Yang Y 2018 Next-generation organic photovoltaics based on non-fullerene acceptors *Nat. Photon.* **12** 131–42
- [16] Du X, Heumüller T, Gruber W, Classen A, Unruh T, Li N and Brabec C J 2019 Efficient polymer solar cells based on non-fullerene acceptors with potential device lifetime approaching 10 years *Joule* **3** 215–26
- [17] Fan Q *et al* 2018 High-performance as-cast nonfullerene polymer solar cells with thicker active layer and large area exceeding 11% power conversion efficiency *Adv. Mater.* **30** 1704546
- [18] Wang N, Yang W, Li S, Shi M, Lau T-K, Lu X, Shikler R, Li C-Z and Chen H 2019 A non-fullerene acceptor enables efficient P3HT-based organic solar cells with small voltage loss and thickness insensitivity *Chin. Chem. Lett.* **30** 1277–81
- [19] Krebs F C, Gevorgyan S A and Alstrup J 2009 A roll-to-roll process to flexible polymer solar cells: model studies, manufacture and operational stability studies *J. Mater. Chem.* **19** 5442–51
- [20] Li N *et al* 2013 Towards 15% energy conversion efficiency: a systematic study of the solution-processed organic tandem solar cells based on commercially available materials *Energy Environ. Sci.* **6** 3407–13
- [21] Burgués-Ceballos I, Stella M, Lacharme P and Martínez-Ferrero E 2014 Towards industrialization of polymer solar cells: material processing for upscaling *J. Mater. Chem. A* **2** 17711–22
- [22] Po R, Bernardi A, Calabrese A, Carbonera C, Corso G and Pellegrino A 2014 From lab to fab: how must the polymer solar cell materials design change? An industrial perspective *Energy Environ. Sci.* **7** 925–43
- [23] Min J, Luponosov Y N, Cui C, Kan B, Chen H, Wan X, Chen Y, Ponomarenko S A, Li Y and Brabec C J 2017 Evaluation of electron donor materials for solution-processed organic solar cells via a novel figure of merit *Adv. Energy Mater.* **7** 1700465
- [24] Azzopardi B, Emmott C J M, Urbina A, Krebs F C, Mutale J and Nelson J 2011 Economic assessment of solar electricity production from organic-based photovoltaic modules in a domestic environment *Energy Environ. Sci.* **4** 3741–53
- [25] Bin H *et al* 2016 11.4% efficiency non-fullerene polymer solar cells with trialkylsilyl substituted 2D-conjugated polymer as donor *Nat. Commun.* **7** 13651
- [26] Li S, Ye L, Zhao W, Zhang S, Mukherjee S, Ade H and Hou J 2016 Energy-level modulation of small-molecule electron acceptors to achieve over 12% efficiency in polymer solar cells *Adv. Mater.* **28** 9423–9
- [27] Zhao W, Li S, Yao H, Zhang S, Zhang Y, Yang B and Hou J 2017 Molecular optimization enables over 13% efficiency in organic solar cells *J. Am. Chem. Soc.* **139** 7148–51
- [28] Zhang S, Qin Y, Zhu J and Hou J 2018 Over 14% efficiency in polymer solar cells enabled by a chlorinated polymer donor *Adv. Mater.* **30** 1800868
- [29] Li S, Ye L, Zhao W, Yan H, Yang B, Liu D, Li W, Ade H and Hou J 2018 A wide band gap polymer with a deep highest occupied molecular orbital level enables 14.2% efficiency in polymer solar cells *J. Am. Chem. Soc.* **140** 7159–67
- [30] Zheng Z *et al* 2018 A highly efficient non-fullerene organic solar cell with a fill factor over 0.80 enabled by a fine-tuned hole-transporting layer *Adv. Mater.* **30** 1801801
- [31] Ye L, Xiong Y, Zhang Q, Li S, Wang C, Jiang Z, Hou J, You W and Ade H 2018 Surpassing 10% efficiency benchmark for nonfullerene organic solar cells by scalable coating in air from single nonhalogenated solvent *Adv. Mater.* **30** 1705485
- [32] Zhang L, Lin B, Hu B, Xu X and Ma W 2018 Blade-cast nonfullerene organic solar cells in air with excellent morphology, efficiency, and stability *Adv. Mater.* **30** 1800343
- [33] Na S-I *et al* 2019 High performance roll-to-roll produced fullerene-free organic photovoltaic devices via temperature-controlled slot die coating *Adv. Funct. Mater.* **29** 1805825
- [34] Huang Y-C, Cha H-C, Chen C-Y and Tsao C-S 2017 A universal roll-to-roll slot-die coating approach towards high-efficiency organic photovoltaics *Prog. Photovolt.* **25** 928–35
- [35] Swartwout R, Hoerantner M T and Bulovic V 2019 Scalable deposition methods for large-area production of perovskite thin films *Energy Environ. Mater.* **2** 119–43
- [36] Li N, McCulloch I and Brabec C J 2018 Analyzing the efficiency, stability and cost potential for fullerene-free organic photovoltaics in one figure of merit *Energy Environ. Sci.* **11** 1355–61
- [37] Bundgaard E *et al* 2015 Matrix organization and merit factor evaluation as a method to address the challenge of finding a polymer material for roll coated polymer solar cells *Adv. Energy Mater.* **5** 1402186
- [38] Bente H, Mori D, Ohkita H and Ito S 2016 Recent research progress of polymer donor/polymer acceptor blend solar cells *J. Mater. Chem. A* **4** 5340–65
- [39] Yan C, Barlow S, Wang Z, Yan H, Jen A K, Marder S R and Zhan X 2018 Non-fullerene acceptors for organic solar cells *Nat. Rev. Mater.* **3** 18003
- [40] Sun H, Chen F and Chen Z-K 2019 Recent progress on non-fullerene acceptors for organic photovoltaics *Mater. Today* **24** 94–118
- [41] Espinosa N, Garc-Valverde R, Urbina A and Krebs F C 2011 A life cycle analysis of polymer solar cell modules prepared using

- roll-to-roll methods under ambient conditions *Sol. Energy Mater. Sol. Cells* **95** 1293–302
- [42] Espinosa N, Garc-Valverde R, Urbina A, Lenzmann F, Manceau M, Angmo D and Krebs F C 2012 Life cycle assessment of ITO-free flexible polymer solar cells prepared by roll-to-roll coating and printing *Sol. Energy Mater. Sol. Cells* **97** 3–13
- [43] Tsang M P, Sonnemann G W and Bassani D M 2016 Life-cycle assessment of cradle-to-grave opportunities and environmental impacts of organic photovoltaic solar panels compared to conventional technologies *Sol. Energy Mater. Sol. Cells* **156** 37–48
- [44] Krebs F C 2009 Fabrication and processing of polymer solar cells: a review of printing and coating techniques *Sol. Energy Mater. Sol. Cells* **93** 394–412
- [45] Roth B, Søndergaard R and Krebs F C 2015 Roll-to-roll printing and coating techniques for manufacturing large-area flexible organic electronics *Handbook of Flexible Organic Electronics* ed S Logothetidis (Oxford: Woodhead Publishing) ch 7 pp 171–97
- [46] Diao Y *et al* 2013 Solution coating of large-area organic semiconductor thin films with aligned single-crystalline domains *Nat. Mater.* **12** 665
- [47] Diao Y *et al* 2015 Flow-enhanced solution printing of all-polymer solar cells *Nat. Commun.* **6** 7955
- [48] Gu X, Shaw L, Gu K, Toney M F and Bao Z 2018 The meniscus-guided deposition of semiconducting polymers *Nat. Commun.* **9** 534
- [49] Song S, Lee K T, Koh C W, Shin H, Gao M, Woo H Y, Vak D and Kim J Y 2018 Hot slot die coating for additive-free fabrication of high performance roll-to-roll processed polymer solar cells *Energy Environ. Sci.* **11** 3248–55
- [50] Aziz F and Ismail A 2015 Spray coating methods for polymer solar cells fabrication: a review *Mater. Sci. Semicond. Process.* **39** 416–25
- [51] Andersen T R *et al* 2014 Scalable, ambient atmosphere roll-to-roll manufacture of encapsulated large area, flexible organic tandem solar cell modules *Energy Environ. Sci.* **7** 2925–33
- [52] Brandt R G, Zhang F, Andersen T R, Angmo D, Shi M, Gurevich L, Krebs F C, Andreasen J W and Yu D 2016 Roll coated large area ITO- and vacuum-free all organic solar cells from diketopyrrolopyrrole based non-fullerene acceptors with molecular geometry effects *RSC Adv.* **6** 41542–50
- [53] Carlé J E *et al* 2017 Overcoming the scaling lag for polymer solar cells *Joule* **1** 274–89
- [54] Heliatick, 'About Heliatick.' <https://heliatick.com/en/heliatick/about-us> (Accessed: 30 April, 2019)
- [55] Destouesse E, Top M, Lamminaho J, Rubahn H, Fahlteich J and Madsen M 2019 Slot-die processing and encapsulation of non-fullerene based ito-free organic solar cells and modules *Flex. Print. Electron.* **4** 045004
- [56] He Y and Li Y 2011 Fullerene derivative acceptors for high performance polymer solar cells *Phys. Chem. Chem. Phys.* **13** 1970–83
- [57] Lin Y *et al* 2016 High-performance electron acceptor with thienyl side chains for organic photovoltaics *J. Am. Chem. Soc.* **138** 4955–61
- [58] Dai S *et al* 2017 Fused nonacyclic electron acceptors for efficient polymer solar cells *J. Am. Chem. Soc.* **139** 1336–43
- [59] Zhan X, Tan Z, Domercq B, An Z, Zhang X, Barlow S, Li Y, Zhu D, Kippelen B and Marder S R 2007 A high-mobility electron-transport polymer with broad absorption and its use in field-effect transistors and all-polymer solar cells *J. Am. Chem. Soc.* **129** 7246–7
- [60] Gené Z, Mammò W, Wang E and Andersson M R 2019 Recent advances in n-type polymers for all-polymer solar cells *Adv. Mater.* **31** 1807275
- [61] Strohm S, Machui F, Langner S, Kubis P, Gasparini N, Salvador M, McCulloch I, Egelhaaf H-J and Brabec C J 2018 P3HT: non-fullerene acceptor based large area, semi-transparent PV modules with power conversion efficiencies of 5%, processed by industrially scalable methods *Energy Environ. Sci.* **11** 2225–34
- [62] Lin Y *et al* 2018 Printed nonfullerene organic solar cells with the highest efficiency of 9.5% *Adv. Energy Mater.* **8** 1701942
- [63] Corzo D, Almasabi K, Bihar E, Macphree S, Rosas-Villalva D, Gasparini N, Inal S and Baran D 2019 Digital inkjet printing of high-efficiency large-area nonfullerene organic solar cells *Adv. Mater. Technol.* **4** 1900040
- [64] Liu Y, Larsen-Olsen T T, Zhao X, Andreasen B, Søndergaard R R, Helgesen M, Norrman K, Jørgensen M, Krebs F C and Zhan X 2013 All polymer photovoltaics: from small inverted devices to large roll-to-roll coated and printed solar cells *Sol. Energy Mater. Sol. Cells* **112** 157–62
- [65] Angmo D and Krebs F C 2013 Flexible ITO-free polymer solar cells *J. Appl. Polym. Sci.* **129** 1–14
- [66] Roth B, Benatto G A d R, Corazza M, Carlé J E, Helgesen M, Gevorgyan S A, Jørgensen M, Søndergaard R R and Krebs F C 2016 Improving the operational stability of PBDTTTz-4 polymer solar cells modules by electrode modification *Adv. Eng. Mater.* **18** 511–7
- [67] Chen M-R, Fan C-C, Andersen T R, Dam H F, Fu W-F, Lin Y-Z, Bundgaard E, Krebs F C, Zhan X-W and Chen H-Z 2014 Solvent-resistant small molecule solar cells by roll-to-roll fabrication via introduction of azide cross-linkable group *Synth. Met.* **195** 299–305
- [68] Dam H F and Krebs F C 2012 Simple roll coater with variable coating and temperature control for printed polymer solar cells *Sol. Energy Mater. Sol. Cells* **97** 191–6
- [69] Carlé J E, Andersen T R, Helgesen M, Bundgaard E, Jørgensen M and Krebs F C 2013 A laboratory scale approach to polymer solar cells using one coating/printing machine, flexible substrates, no ITO, no vacuum and no spincoating *Sol. Energy Mater. Sol. Cells* **108** 126–8
- [70] Cheng P, Lin Y, Zawacka N K, Andersen T R, Liu W, Bundgaard E, Jørgensen M, Chen H, Krebs F C and Zhan X 2014 Comparison of additive amount used in spin-coated and roll-coated organic solar cells *J. Mater. Chem. A* **2** 19542–9
- [71] Liu K, Larsen-Olsen T T, Lin Y, Beliatas M, Bundgaard E, Jørgensen M, Krebs F C and Zhan X 2016 Roll-coating fabrication of flexible organic solar cells: comparison of fullerene and fullerene-free systems *J. Mater. Chem. A* **4** 1044–51
- [72] Rossander L H, Zawacka N K, Dam H F, Krebs F C and Andreasen J W 2014 *In situ* monitoring of structure formation in the active layer of polymer solar cells during roll-to-roll coating *AIP Adv.* **4** 087105
- [73] Zawacka N K, Andersen T R, Andreasen J W, Rossander L H, Dam H F, Jørgensen M and Krebs F C 2014 The influence of additives on the morphology and stability of roll-to-roll processed polymer solar cells studied through ex situ and *in situ* X-ray scattering *J. Mater. Chem. A* **2** 18644–54
- [74] Richter L J, DeLongchamp D M and Amassian A 2017 Morphology development in solution-processed functional organic blend films: an *in situ* viewpoint *Chem. Rev.* **117** 6332–66
- [75] Rossander L H, Dam H F, Carlé J E, Helgesen M, Rajkovic I, Corazza M, Krebs F C and Andreasen J W 2017 In-line, roll-to-roll morphology analysis of organic solar cell active layers *Energy Environ. Sci.* **10** 2411–9
- [76] Baran D *et al* 2016 Reduced voltage losses yield 10% efficient fullerene free organic solar cells with >1 V open circuit voltages *Energy Environ. Sci.* **9** 3783–93
- [77] Baran D *et al* 2017 Reducing the efficiency-stability-cost gap of organic photovoltaics with highly efficient and stable small molecule acceptor ternary solar cells *Nat. Mater.* **16** 363–70
- [78] Wadsworth A *et al* 2017 Highly efficient and reproducible nonfullerene solar cells from hydrocarbon solvents *ACS Energy Lett.* **2** 1494–500
- [79] Ye L *et al* 2016 High performance organic solar cells processed by blade coating in air from a benign food additive solution *Chem. Mater.* **28** 7451–8
- [80] Lin B *et al* 2019 Molecular packing control enables excellent performance and mechanical property of blade-cast all-polymer solar cells *Nano Energy* **59** 277–84



- [81] Zhao W, Zhang S, Zhang Y, Li S, Liu X, He C, Zheng Z and Hou J 2018 Environmentally friendly solvent-processed organic solar cells that are highly efficient and adaptable for the blade-coating method *Adv. Mater.* **30** 1
- [82] Kim W, Kim J K, Kim E, Ahn T K, Wang D H and Park J H 2015 Conflicted effects of a solvent additive on ptb7:pc71bm bulk heterojunction solar cells *J. Phys. Chem. C* **119** 5954–61
- [83] Jacobs I E, Wang F, Bedolla Valdez Z I, Ayala Oviedo A N, Bilsky D J and Moulé A J 2018 Photoinduced degradation from trace 1, 8-diiodooctane in organic photovoltaics *J. Mater. Chem. C* **6** 219–25
- [84] Ji G, Zhao W, Wei J, Yan L, Han Y, Luo Q, Yang S, Hou J and Ma C-Q 2019 12.88% efficiency in doctor-blade coated organic solar cells through optimizing the surface morphology of a ZnO cathode buffer layer *J. Mater. Chem. A* **7** 212–20
- [85] Pascual-San-José E, Rodrez-Martínez X, Adel-Abdelaleim R, Stella M, Martínez-Ferrero E and Campoy-Quiles M 2019 Blade coated P3HT:non-fullerene acceptor solar cells: a high-throughput parameter study with a focus on up-scalability *J. Mater. Chem. A* **7** 20369–82
- [86] Tan M J, Zhong S, Li J, Chen Z and Chen W 2013 Air-stable efficient inverted polymer solar cells using solution-processed nanocrystalline ZnO interfacial layer *ACS Appl. Mater. Interfaces* **5** 4696–701
- [87] Fan B, Zhang D, Li M, Zhong W, Zeng Z, Ying L, Huang F and Cao Y 2019 Achieving over 16% efficiency for single-junction organic solar cells *Sci. China Chem.* **62** 746–52
- [88] Yi Q *et al* 2015 Aqueous solution-deposited molybdenum oxide films as an anode interfacial layer for organic solar cells *ACS Appl. Mater. Interfaces* **7** 18218–24
- [89] Wei J, Yin Z, Chen S-C, Cai D and Zheng Q 2016 Solution-processed MoS<sub>x</sub> thin-films as hole-transport layers for efficient polymer solar cells *RSC Adv.* **6** 39137–43
- [90] Lin Y *et al* 2019 17% efficient organic solar cells based on liquid exfoliated WS<sub>2</sub> as a replacement for PEDOT:PSS *Adv. Mater.* **31** 1902965

## Paper II

**Title:**

Nanostructure of organic semiconductor thin films: Molecular dynamics modeling with solvent evaporation

**Authors:**

Anders S. Gertsen, Michael Korning Sørensen, and Jens W. Andreasen\*

**Published in:**

Physical Review Materials, vol. 4, 075405, 2020.

**Digital object identifier:**



10.1103/PhysRevMaterials.4.075405

©2020 American Physical Society. Reprinted with permission.

---

\*Corresponding authorship

# Nanostructure of organic semiconductor thin films: Molecular dynamics modeling with solvent evaporation

Anders S. Gertsen , Michael Korning Sørensen, and Jens W. Andreasen *Department of Energy Conversion and Storage, Technical University of Denmark, Fysikvej 310, DK-2800 Kgs. Lyngby, Denmark*

(Received 12 March 2020; accepted 7 July 2020; published 29 July 2020)

We present a procedure for simulating solution deposition of organic thin-films on explicitly modeled substrates via solvent evaporation simulations in a molecular dynamics framework. Additionally, we have developed force fields for the family of IDTBR nonfullerene acceptors, which have been widely employed in the literature as *n*-type materials in several types of organic semiconductor devices, and we analyzed their structure-property relationships using a combination of grazing incidence x-ray scattering measurements, atomistic molecular dynamics simulations, and quantum chemical calculations. We find that thermal fluctuations can have a significant impact on calculated electron transfer integrals, and that the  $\pi$ -stacking interactions of the electron withdrawing benzothiadiazole building blocks are key to high electron coupling in amorphous thin films of *n*-type materials.

DOI: [10.1103/PhysRevMaterials.4.075405](https://doi.org/10.1103/PhysRevMaterials.4.075405)

## I. INTRODUCTION

Organic photovoltaics (OPVs) represent a promising technology for low-cost, lightweight, flexible solar cells with remarkably low energy payback times when deposited using scalable, roll-to-roll compatible fabrication techniques [1–3]. Traditionally, OPVs have utilized fullerene derivatives as electron acceptors, but the emergence of nonfullerene, small-molecule acceptors (NFAs) and the advances that these have carried with them in recent years are testament to their present and, not least, future importance in the field [4,5]. Record efficiencies of more than 18% have been reached when utilizing NFAs [6], surpassing those of fullerene-based devices due to, e.g., lower voltage losses and higher current generation [7]. Several accompanying and equally important advantages of NFA OPVs include the significant reduction of performance losses within the first few days or weeks under illumination (i.e., reduced burn-in) [8,9] as well as impressive thermal stabilities [10–12]. These latter two properties are influenced not only by the differences in electronic properties of NFAs and fullerenes, but also by their morphological differences [10,13–16].

Experimental morphology studies on organic thin-films can be conducted in various ways. The most commonly employed methods are grazing incidence x-ray scattering experiments in wide-angle or small-angle geometries (GIWAXS and GISAXS, respectively). These methods can provide quantitative, statistical information on structural parameters: The former of molecular order such as  $\pi$ -stacking distances and lamellar stacking distances in both neat films and blend films, and the latter of mesoscale order such as domain sizes in blend films. To interpret data from these measurements, molecular dynamics (MD) simulations can prove helpful by providing

a more qualitative insight into the short-range structural parameters, and, in combination with quantum chemical calculations, elucidating different aspects of the structure-property relationships [17,18].

In recent years, IDTBR NFAs [see Fig. 1; cf. the supplemental information (SI), Sec. S1 for full names of all compounds mentioned in this paper] [19] have gained significant attention due to the stable, burn-in free, and highly efficient OPV devices based on these [8–10,15,20,21]. Furthermore, it has very recently been shown that the structural packing of IDTBR acceptors deduced from single crystals can explain the high *n*-type mobilities in organic thin-film transistors (OTFTs) of IDTBR derivatives [22]. Common for OPVs and OTFTs is that the active layer film thicknesses are often less than 100 nm, and with air-interface and substrate effects arguably becoming increasingly important with thinner films, it calls for inclusion of these in thin-film simulations [23]. Although very thin-films are favorable in terms of computational cost, the structural relaxation of solution processed thin-films happens on time-scales that are inaccessible to atomistic MD, and *a priori* knowledge of the molecular packing is thus often necessary [24]. This reduces the predictive power of the simulations. Coarse-grained models of various resolution, i.e., describing a few atoms or up to whole monomers by effective particles or “beads,” have successfully been employed to simulate bulk, blend morphologies and their scattering signatures [25–27], but extensive fitting of the coarse-grained force fields to either atomistic simulations or experiments is needed for new materials. Additionally, a too coarse resolution can greatly limit the chemical specificity of the model, in turn hampering further property calculations. In particular, novel donors and NFAs for OPV applications are structurally complex and thus more difficult to coarse-grain than the benchmark system **P3HT:PC<sub>61</sub>BM**. The construction of reliable, atomistic models is hence often a prerequisite for reliable coarse-grained models, and with the multitude of interactions

\*jewa@dtu.dk

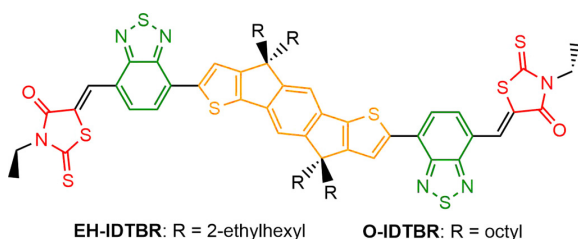


FIG. 1. Structures of **EH-IDTBR** and **O-IDTBR**; orange marks the indacenodithiophene (IDT) subunit, green marks the benzothiadiazole (BT), and red marks the rhodanine (RH).

needed for simulating solution processed thin-films due to substrate and air-interface effects, they are a necessary first step.

Different approaches to modeling deposition of organic thin-films in nonequilibrium MD simulations, including vapor deposition and solvent evaporation, have been published during the years [28]. Our work is centered around organic thin-films processed from solution using deposition techniques such as spin-coating and slot-die coating [3], and the focus herein will thus be on solvent evaporation simulations. Only a few studies on solvent evaporation MD simulations have been published: One of the more complete efforts in trying to capture as many effects as possible simultaneously was published by Peter, Meyer, and Baschnagel [29]. By omitting periodic boundary conditions (PBCs) in the direction of the surface normal and including potential walls at the top and bottom surfaces of the box instead, they tuned the Lennard-Jones parameters of the bottom potential wall to attract the oligomer and solvent in question, thus mimicking a substrate. The top potential wall was placed far from the solution and made strongly attractive for the solvent, allowing for nonequilibrium diffusion of solvent through the film that would eventually condense at the top wall due to the attractive Lennard-Jones interactions. This method was refined by Negi, Lyulin, and Bobbert [30], who simulated thin-films of coarse-grained **P3HT:PC<sub>61</sub>BM** processed from different solvents. They allowed the solvent particles to diffuse through the film into a suspended solvent vapor above and would not remove solvent molecules until a certain density was reached in the top part of the box. The evaporation schemes themselves used in these papers hence have several advantages in terms of the physical processes included, but the time-scales needed to capture effects like nonequilibrium solvent diffusion through an oligomer thin-film are only reachable for very coarse-grained models. Furthermore, the substrate effects were not explicitly considered, and with the two described studies being the only ones that, to our knowledge, include these effects in solvent evaporation simulations, there is still room for improvement.

Three studies have been published in which substrate effects were not considered, but where alignment effects of molecules in a drying film were sought by using semi-isotropic pressure coupling, i.e., only allowing the box to compress in the  $z$ -direction. Two of these relied on very coarse models [31,32], whereas a good compromise between chemical specificity and computational speed-up from coarse-

graining was achieved using the MARTINI force-field [33] to coarse-grain a **P3HT:PC<sub>61</sub>BM** system by Alessandri, Marink, and co-workers [34]. In this, the rate of solvent removal was exponential with 1.25% per step to capture the effect of slower solvent evaporation with a decreasing solvent fraction, and the resulting morphologies were very convincing, which was underlined by the simulated diffraction patterns having distinct peaks for both the  $\pi$ - and lamellar stacks close to the experimental ones, albeit hampered by implicit limitations of the coarse-grained bead types employed.

A few studies have more closely explored the structure-property relationships in systems relevant for OPVs using atomistic molecular dynamics simulations with solvent evaporation [35–37]. Common for these was that no substrate effects were included and that isotropic pressure coupling was used during the solvent removal process. Although this evaporation method can give some insight into the bulk properties of the resulting dry materials, it is not expected to be fully representative for a thin-film.

In this work, we seek to devise a model for solution deposition of organic thin-films on substrates. This encompasses substrate effects, air-interface effects, and semi-isotropic pressure coupling in nonequilibrium, atomistic MD solvent evaporation simulations with no periodic boundary conditions in the  $z$ -direction. In addition to this model, we present here MD force fields for **O-IDTBR** and **EH-IDTBR** (see Fig. 1) as well as an analysis of the IDTBR thin-film nanostructure by combining GIWAXS experiments with the nonequilibrium MD solvent evaporation simulations. Furthermore, we present calculations of the electronic couplings between IDTBR molecules extracted from the MD simulations to analyze the structural pathways for electron transport in semicrystalline IDTBR domains, shedding light on their structure-property relationships.

## II. METHODS

All molecular dynamics (MD) simulations were carried out in GROMACS 2018.3 [38] based on the OPLS-AA force field [39,40]. A robust and flexible script for solvent removal has been developed, allowing for a range of different removal schemes (from a suspended solvent vapor only, with a gradient through the system or randomly from the full extent of the system) and rates (linear and exponential) with separate control of the MD run parameters through a directory of configuration files (.mdp files). This script can be obtained from the authors upon request. This section is organized as a top-down description of the workflow, starting with the sample preparation and GIWAXS experiments in Sec. II A. Hereafter, the solvent evaporation simulations are described in Sec. II B, the substrate, air-interface, and solvent effects in Sec. II C, the force-field parametrization procedure for the IDTBR force fields in Sec. II D, and additional validation based on crystal simulations in Sec. II E.

### A. Sample preparation and GIWAXS measurements

To compare the simulations to experimental data, thin-films of **O-IDTBR** and **EH-IDTBR** (purchased from 1-Material Inc.) were prepared on silicon wafers. The Si(100)

substrates were initially cleaned for 30 min in an ultrasonic bath: 10 min in isopropanol, 10 min in acetone, and 10 min in demineralized water. The molecules, **O-IDTBR** and **EH-IDTBR**, were dissolved in chloroform at a concentration of 30 mg/mL for 1 h on a 50 °C hot-plate with magnetic stirring. The solutions were then cooled down to room temperature before being spin-cast onto the substrates at 600 rpm for 30 s and subsequently dried for ten minutes at 70 °C. We furthermore fabricated a set of thin-films using the same procedure, which were additionally subject to annealing at 130 °C for 10 min in order to probe its effects on the thin-film properties. This dataset is presented in the SI, Fig. S4 [19]. The sample preparation procedure was identical to the one in Ref. [20], and the final film thicknesses are thus expected to be similar (280–290 nm).

All GIWAXS experiments were performed with an MP-Genix.G06 microfocus x-ray source from Xenocs operated at 50 keV and 1 mA, monochromated to probe with a wavelength of 1.54 Å (8.04 keV), and collimated with a set of pinholes downstream. The sample stage and image plate were kept in vacuum to avoid diffuse air scattering. A circular beam stop was placed just in front of the image plate. Alignment of the samples were carried out by using an x-ray eye camera while translating and rotating the sample stage. The incident angle was set to 0.18° to maximize scattering from the thin-film and to avoid a signal from the silicon substrate. The distance from sample to detector was calibrated with Si powder to be 118.15 mm.

### B. Solvent evaporation simulations

The simulation box, having starting dimensions of  $10 \times 10 \times 60$  nm, was initiated with a  $\text{SiO}_2$  substrate in the bottom (cf. Sec. II C) and a solution of 448 IDTBR molecules

randomly distributed in preequilibrated chloroform on top of this (using `gmx insert-molecules` and `gmx solvate`). PBCs were only applied in the  $x$ - and  $y$ -directions, whereas potential walls were applied in the  $z$ -direction at  $z = 0$  and  $z = \text{box}_z$  as described in Sec. II C. The box was then equilibrated before initiating an exponential solvent evaporation process. For this, 2.5% of the remaining solvent was removed every step randomly throughout the extent of the box until reaching the near-linear regime (defined as removing less than 0.025% of the initial amount of solvent each step), whereafter the evaporation was continued linearly until a dry film was obtained. This amounts to a total of 133 steps. Both for the initial equilibration and for each step after solvent removal, the box was equilibrated for 0.2 ns in an  $NVT$  ensemble and 2.0 ns in an  $NPT$  ensemble using the Berendsen barostat ( $\tau = 2.0$  ps) before running a 3.0 ns production run in the  $NPT$  ensemble using the Parrinello-Rahman barostat ( $\tau = 12.0$  ps), adding up to a total drying time of 0.7  $\mu\text{s}$ . The V-rescale thermostat ( $\tau = 0.2$  ps) and a leap-frog integrator with 2 fs steps were used for all runs. Furthermore, semi-isotropic pressure coupling of 1.0 bar was used with an isothermal compressibility of  $4.5 \times 10^{-5} \text{ bar}^{-1}$  in the  $z$ -direction and  $0.0 \text{ bar}^{-1}$  in the  $x$ - and  $y$ -directions to facilitate shrinking of the box only in the  $z$ -direction to mimic the conditions in a drying thin-film. The particle mesh Ewald (PME) scheme was used to treat long-range electrostatics (a short-range cutoff of 1.2 nm), whereas a cutoff of 1.2 nm was used for van der Waals (vdW) interactions. All hydrogens were constrained with the LINCS algorithm to reduce computational time.

Having obtained dry thin-films, these were subjected to a 100 ns simulated annealing cycle in an  $NPT$  ensemble: 10 ns with a linear temperature increase from 300 to 600 K, 70 ns at 600 K, 10 ns with a linear temperature decrease from 600 to 300 K, and a final 10 ns at 300 K. The resulting annealed

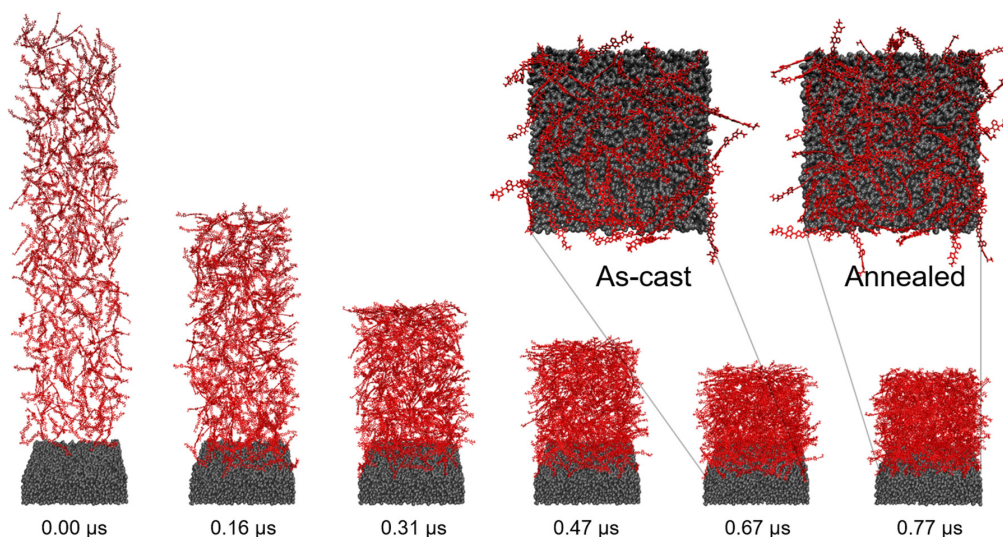


FIG. 2. Visualization of the solvent evaporation procedure for O-IDTBR (red) on an amorphous  $\text{SiO}_2$  substrate (gray). The final frames from five steps out of the total 133 steps are shown in addition to the annealed thin-film with their corresponding simulation times. Insets show the bottom layer of IDTBR molecules, i.e., molecules that are fully or partly within 4.5 Å of the substrate, for the as-cast and annealed thin-films. Side chains and solvent molecules are not shown for clarity.

075405-3



thin-films, having a thickness of approximately  $10 \text{ nm}^3$ , were then used for analysis in addition to the as-cast thin-films. The evaporation process is visualized in Fig. 2.

### C. Substrate, air-interface, and solvent interactions

As we are seeking to validate the model using GIWAXS experiments, we have modeled the substrate using an explicit  $\sim 2 \text{ nm}$  layer of amorphous silicon dioxide ( $\text{SiO}_2$ ) due to the thin-films being deposited on silicon wafers with native oxide (cf. Sec. II A). The parameters for  $\text{SiO}_2$  were based on the atomistic Clay force field [41] as adopted in Ref. [42], using exclusively nonbonded interactions between the silicon and oxygen atoms. The specific surface interactions between organic, conjugated molecules and  $\text{SiO}_2$  modeled using parameters from the Clay force field were validated by Roscioni *et al.* in a study of pentacene crystal growth [43]. We adapted the parameters to the OPLS-AA force field and initiated silicon and oxygen atoms randomly in a stoichiometric ratio 1:2 (5500 and 11 000 atoms, respectively) in a  $10 \times 10 \times 5 \text{ nm}$  box without PBC in the  $z$ -direction using a strongly attractive bottom potential wall and a top potential wall with low interaction. The system was equilibrated in an  $NVT$  ensemble with the V-rescale thermostat at 600 K and subsequently cooled down to 300 K over the course of 1 ns, resulting in a  $\sim 2 \text{ nm}$  layer of amorphous  $\text{SiO}_2$  aligned to the bottom of the box. This slab was used in the solvent evaporation simulations, held in place by an attractive interaction with a bottom potential wall of the 9-3 type in GROMACS, which is in essence a Lennard-Jones potential integrated over the volume behind the box boundary with an assigned density in atoms per  $\text{nm}^3$  of a given atom type. Here, a density of  $49.94 \text{ nm}^{-3}$ , similar to the experimental value for bulk, crystalline silicon, is used. The atom type defining the interaction strength between the bottom wall and the  $\text{SiO}_2$  was the same as the silicon atom type used for the  $\text{SiO}_2$ , but due to the potential walls in GROMACS only incorporating vdW interactions and not Coulombic interactions, the specific interaction was increased by a factor of  $10^3$  to account for this (as a rule of thumb, ionic bonds are approximately a factor of  $10^3$  times stronger than vdW forces). Any artefacts introduced by this are well shielded by the  $\sim 2 \text{ nm}$   $\text{SiO}_2$  slab that is dominated by ionic interactions, and the bottom potential wall will thus not interact with the solution deposited on the  $\text{SiO}_2$ .

The air-interface in the solvent evaporation simulations was also modeled using a potential wall of the 9-3 type with an assigned density of  $0.012 \text{ nm}^{-3}$ , corresponding to the experimental value for molecular nitrogen,  $\text{N}_2$ , in ambient conditions with the standard OPLS-AA parameters for nitrogen defining the interaction strengths with the rest of the system. For both the top and bottom walls, the potentials were

continued linearly within a distance of 1 nm from the box edges.

The solvent used for the sample preparation was chloroform, which was modeled using the OPLS-AA parameters by Caleman, van der Spoel, and co-workers [44]. To evaluate the solute-solvent interaction, the free energies of solvation (i.e., going from gas phase to solvation),  $\Delta G_{\text{solv}}$ , for **O-IDTBR** and **EH-IDTBR** in chloroform were calculated using the Bennett's acceptance ratio (BAR) method and compared to corresponding simulations in two other commonly used solvents for IDTBR-based OPVs, namely chlorobenzene and *o*-xylene (both based on toluene OPLS-AA parameters also from Ref. [44]). The detailed simulation procedures can be found in the SI, Sec. S2.2 [19]. Additionally, solvation free energies in 1-octanol (based on standard OPLS-AA parameters) have been calculated in order to compare to a bad solvent for IDTBR. The results are listed in Table I. As is seen, chloroform and chlorobenzene are almost equally good solvents for IDTBR, and these two chlorinated solvents are better than the nonchlorinated *o*-xylene, reproducing the qualitative tendencies seen in experiments [45]. Here, the room-temperature solubility of **O-IDTBR** in chlorobenzene was found to be  $45.8 \text{ mg/mL}$ , whereas it was found to be  $18.9 \text{ mg/mL}$  in *o*-xylene [45]; this corresponds to a difference in free energy of solvation of  $2.2 \text{ kJ/mol}$ , which is slightly lower than the  $6.2 \pm 1.3 \text{ kJ/mol}$  predicted from the calculations. Estimating the **O-IDTBR** solubilities for chloroform and 1-octanol using a relative measure from the solubility in chlorobenzene yields values of around  $87 \text{ mg/mL}$  for chloroform and  $10^{-2} \text{ mg/mL}$  for 1-octanol (i.e., practically insoluble, as expected). Note that the less negative  $\Delta G_{\text{solv}}$  values for **EH-IDTBR** compared to **O-IDTBR** do not necessarily equal lower solubility, as the thermodynamic equilibrium between the solid-state **EH-IDTBR** and a given solvent is different from that of solid-state **O-IDTBR** and the same solvent.

We note that the present simulations do not include mechanical shear stress effects, although these are expected to be relevant for spin-coating deposition. It has previously been found in a combined experimental and atomistic MD study that medium or high shear rates (corresponding to spin-coating speeds of several thousand rpm) can promote crystallinity in organic thin-films, but that low shear rates did not promote crystallinity significantly [46]. Another MD study employing very coarse-grained models of an OPV donor:Acceptor blend found that high shear rates could promote phase separation and increase crystallinity of the acceptor domains, but again that low shear rates did not have a significant effect compared to simulations not including shear stress [32]. Although the simulations herein are thus a truer representative of drop-casting than they are of spin-coating due to the lack of inclusion of shear stress, the very slow spin-coating speeds employed for the sample fabrication (600 rpm)

TABLE I. Calculated free energies of solvation in different solvents (300 K, 1 bar) for the presented models of **O-IDTBR** and **EH-IDTBR**.

$\Delta G_{\text{solv}}$ (kJ/mol)	Chloroform	Chlorobenzene	<i>o</i> -xylene	1-octanol
<b>O-IDTBR</b>	$-357.3 \pm 0.9$	$-355.7 \pm 0.9$	$-349.5 \pm 0.8$	$-330.0 \pm 0.9$
<b>EH-IDTBR</b>	$-326.8 \pm 0.2$	$-319.8 \pm 0.8$	$-312.5 \pm 0.6$	$-301.4 \pm 2.1$

induces only low mechanical shear stress in the thin-films and ensures better comparability than for samples spun at the usual speeds of  $\sim 2000$  rpm. Work on including these effects in future simulations is ongoing.

#### D. IDTBR force-field parametrization

The force fields for IDTBR nonfullerene acceptors developed herein were built in the framework of OPLS-AA with parameters based on density functional theory (DFT) calculations carried out in GAUSSIAN 16 [47]. For these, we employed the extensively used global hybrid functional B3LYP [48–50], which incorporates 20% exact exchange, as well as the  $\omega$ B97X-D functional [51,52], which is a highly parametrized, range-separated functional incorporating 100% exact exchange at long range. In combination with the empirical atom-atom dispersion correction (denoted by D),  $\omega$ B97X-D is highly accurate in describing thermochemistry and nonbonded interactions [52]. Throughout, we have used the Pople style basis-set 6-311++G(d,p) [53,54], a triple- $\zeta$  basis with diffuse and polarization functions on both heavy atoms (nonhydrogens) and hydrogens to capture the relevant effects of all nonbonded interactions. Using these quantum chemical calculations, we carefully parametrized the potentials involving atom types that were not present in OPLS-AA as well as all torsional potentials, the exact procedures of which are listed in the SI, Sec. S2.1, along with all resulting nonstandard OPLS-AA parameters used [19,55].

Summarizing, the atomic partial charges were assigned based on symmetrized ESP (ChelpG) charges of the minimum energy conformation of a methyl-substituted IDTBR optimized at the B3LYP/6-311++G(d,p) level of theory, and the atom types were assigned based on the existing OPLS-AA atom types and renamed copies of these (see the SI, Fig. S1 and Table S1) [19], taking great care to capture the asymmetry around the  $sp^3$ -hybridized linking carbon in the indacenodithiophene (IDT) subunit (we refer to the discussion in the SI, Sec. S2.1) [19]. Bond-type parameters were mainly adopted from OPLS-AA, and the backbone equilibrium angles were in most cases determined from the B3LYP/6-311++G(d,p) optimized minimum energy conformation, whereas the side-chain equilibrium angles and the force constants for both backbone and side-chain angles were adopted from OPLS-AA. Most of the proper dihedrals in the IDTBR backbone are modeled by the standard OPLS-AA Ryckaert-Bellemans (RB) parameters for aromatic systems, whereas for the side chains they are modeled by the standard OPLS-AA RB parameters for alkanes. However, and most importantly, dihedral parameters for the torsional potentials of the linking bonds between rhodanine (RH) and benzothiadiazole (BT), between IDT and BT, and between IDT and the side chains were determined through an iterative Boltzmann inversion (IBI) procedure, resulting in coefficients for Ryckaert-Bellemans functional forms that, when included in the remainder of the force field, reproduce the  $\omega$ B97X-D/6-311++G(d,p) torsional potentials. Using this specific DFT level of theory is consistent with the recommendations in the most recent publication on the reparametrization of OPLS-AA peptide backbone torsions [56]. Our IBI procedure was performed as follows:

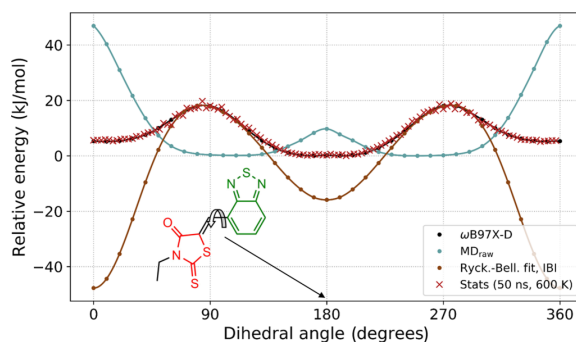


FIG. 3. Visualization of the IBI fitting procedure employed to mimic the  $\omega$ B97X-D potentials for the rhodanine-benzothiadiazole (RH-BT) torsion using Ryckaert-Bellemans functions to parametrize the force field.

(a) DFT relaxed scan at the  $\omega$ B97X-D/6-311++G(d,p) level of theory (i.e., geometry optimizations while constraining only the relevant torsional angle) of a methyl-substituted IDTBR in vacuum.

(b) MD relaxed scan (with a convergence criterion of a maximum force of  $10 \text{ kJ mol}^{-1} \text{ nm}^{-1}$ ) of the torsional angle of reduced systems (i.e., RH-BT for the RH-BT torsion, 4,4,9,9-tetramethyl-IDT-BT for the IDT-BT torsion, and 4,4-diethyl-9,9-dimethyl-IDT for the IDT-to-side-chain torsions) with IDTBR partial charges using our parametrized version of the OPLS-AA force field with the potentials of the four dihedral quadruplets in question set to zero.

(c) Nonlinear least-squares fitting of a Ryckaert-Bellemans functional form [57] [Eq. (1)] to the difference between the DFT scan and the MD scan:

$$V_{\text{RB}}(\phi_{ijkl}) = \sum_{n=0}^5 C_n \cos^n(\psi) \quad \text{with} \quad \psi = \phi - 180^\circ, \quad (1)$$

where  $\phi_{ijkl}$  is the dihedral angle of a quadruplet in degrees. This provided the initial RB parameter guesses.

(d) Long vacuum simulation (10–50 ns depending on the iteration) in an  $NVT$ -ensemble at 600 K using 1 fs steps and subsequent collection of torsion statistics (using `gmx angle`).

(e) Boltzmann inversion of the statistics and fitting of RB parameters to the difference between the resulting potential and the  $\omega$ B97X-D potential—these RB parameters are then linearly combined with the ones from the previous step.

(f) Iterations of steps (d) and (e) until convergence [which is defined by a root-mean-square deviation (RMSD) of  $< 1.0 \text{ kJ/mol}$  for the MD statistics to the DFT potential].

The resulting Boltzmann inverted statistics are visualized in Fig. 3 for the RH-BT torsion, and in the SI, Figs. S2 and S3, for the IDT-BT and the IDT-to-side-chain torsions, respectively [19], and the optimized RB parameters for these torsions are listed in the SI, Table S2 [19].

#### E. Crystal simulations and validation

Recently, crystal structures based on x-ray diffraction measurements of single crystals grown by antisolvent vapor diffusion were published for **O-IDTBR** and **EH-IDTBR** [22]. As

it has previously been shown that **O-IDTBR** has a crystallization transition at  $T_c = 115^\circ\text{C}$  [20], a high structural order can potentially be induced locally in annealed thin-films of **O-IDTBR**, whereas this is not the case for **EH-IDTBR** (cf. the SI, Sec. S3) [19]. We have thus chosen to include simulations based on these crystal structures in order to investigate the differences in both structure and properties between ordered, crystalline domains and more disordered domains in the thin-films. The crystal simulations were performed using the same force fields and run parameters as for the thin-films but with full periodic boundary conditions and anisotropic pressure coupling (i.e., with no considerations of interface effects), with isothermal compressibilities of  $4.5 \times 10^{-5} \text{ bar}^{-1}$  in all directions.

The crystal simulations additionally allowed for further validation of the force fields. First, the RMSD between the experimental crystal structures and the corresponding energy-minimized structures (to maximum interatomic forces  $< 10 \text{ kJ mol}^{-1} \text{ nm}^{-1}$ ) using the IDTBR force fields was calculated. This yielded values of only 0.17 and 0.31 Å for **O-IDTBR** and **EH-IDTBR**, respectively, demonstrating that especially the bonded parameters of the force field very accurately reproduce the experimental molecular geometries. Secondly, the crystal lattice parameters ( $a$ ,  $b$ ,  $c$ ) of 173 K NPT equilibrated boxes were compared to the experimental ones (obtained at 173 K) in order to get an impression of how well the nonbonded parameters of the force field were able to describe the intermolecular interactions and hence the crystal packing. Relative deviations of 2.9%, -1.1%, and 0.4% were found for ( $a$ ,  $b$ ,  $c$ ) of the **O-IDTBR** crystal simulation, whereas deviations of -3.6%, 5.0%, and 0.0% were found for **EH-IDTBR**. For **O-IDTBR**, the deviation of 2.9% along  $a$  corresponds to an elongation in the  $\pi$ -stacking direction, whereas the deviations of -3.6% and 5.0% along  $a$  and  $b$  for **EH-IDTBR** can collectively be seen as a slide of the  $\pi$ -stacks. All of these deviations are, however, minor, which demonstrates that the nonbonded parameters are indeed able to describe the intermolecular interactions reasonably well.

### III. RESULTS AND DISCUSSIONS

The results presented are based on **O-IDTBR** and **EH-IDTBR** thin-films cast from chloroform onto an amorphous  $\text{SiO}_2$  substrate through 0.7  $\mu\text{s}$  atomistic MD solvent evaporation simulations as well as on their 0.1  $\mu\text{s}$  annealed versions (adding up to a total simulation time of 0.8  $\mu\text{s}$ ). The detailed simulation procedures can be found in Sec. II B. These are compared to results from GIWAXS measurements of **O-IDTBR** and **EH-IDTBR** thin-films spin-cast from chloroform onto silicon wafers (cf. Fig. 4). The detailed sample preparation procedures can be found in Sec. II A. Furthermore, MD simulations based on the experimentally obtained **O-IDTBR** and **EH-IDTBR** crystal structures [22] are presented to be able to compare the results from the thin-film simulations to corresponding results from perfectly ordered systems.

To reduce computational cost, the simulations were initiated at an IDTBR concentration of approximately 200 mg/mL, which is an order of magnitude higher than the initial concentration of the solutions used in experiments. This was, however, deemed to be sufficiently dilute, having

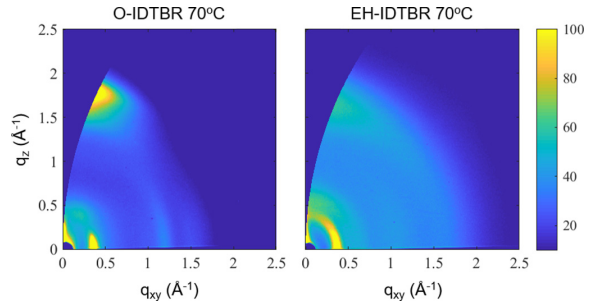


FIG. 4. 2D GIWAXS data of the **O-IDTBR** (left) and **EH-IDTBR** (right) thin-films cast on silicon substrates and dried at  $70^\circ\text{C}$ .

a low number of close interactions ( $< 8 \text{ Å}$ ) of less than 5% relative to the dry films. The dry, simulated thin-films have a thickness of  $\sim 10 \text{ nm}$ , which is an order of magnitude thinner than the experimental samples. Again, this is necessary to keep the computational cost at a feasible level. As the nanostructural characteristics such as  $\pi$ -stacking and relative alignment to the substrate occur at length-scales at least an order of magnitude lower than the extent of the system, these are expected to be statistically representative, whereas the system size is only sufficient to extract qualitative tendencies of longer-range order.

#### A. Structural properties

In Fig. 4, GIWAXS images of **O-IDTBR** and **EH-IDTBR** thin-films on silicon wafers are shown. From the sharper peak features in the **O-IDTBR** image, it can qualitatively be deduced that **O-IDTBR** has a higher degree of order than **EH-IDTBR** in thin-films. Looking at the **O-IDTBR** data, a broad out-of-plane peak can be observed at  $q_z \sim 1.8 \text{ Å}^{-1}$ , indicating  $\pi$ -stacking with a face-on orientation to the substrate. For the in-plane direction, a sharp feature at  $q_{xy} \sim 0.4 \text{ Å}^{-1}$  indicates a longer-range order being present. This feature is unlikely to be directly related to the length of the side chains as usually seen for lamellar stacks in polymeric thin-films with side chains attached to  $sp^2$ -hybridized carbons. Instead, IDTBR molecules employ  $sp^3$ -hybridized linking carbons, to each of which two side chains are bonded [cf. (1)]. These side chains thus have a preferential conformation that is normal to the plane of the backbone, i.e., pointing away from each other, which induces bulkiness around the central IDT unit. This, in turn, means that the  $\pi$ -stacking is expected to occur between the terminal RH units and/or the bridging BT units in the thin-films, and that the in-plane feature could be related to distances between “columns” of these  $\pi$ -stacks. Similar, but less defined, features are present for **EH-IDTBR** thin-films. These are analyzed in detail both qualitatively and quantitatively below.

As the basis of the structural analysis of the simulations, the center of mass (COM) of each of the conjugated ring-systems was defined as distance evaluation points: One for each of the RH units, one for each of the BT units, one for each of the thiophenes in the IDT unit, and one for the central benzene in the IDT unit, amounting to a total of seven evaluation points per molecule (cf. Fig. 1). The normal vectors



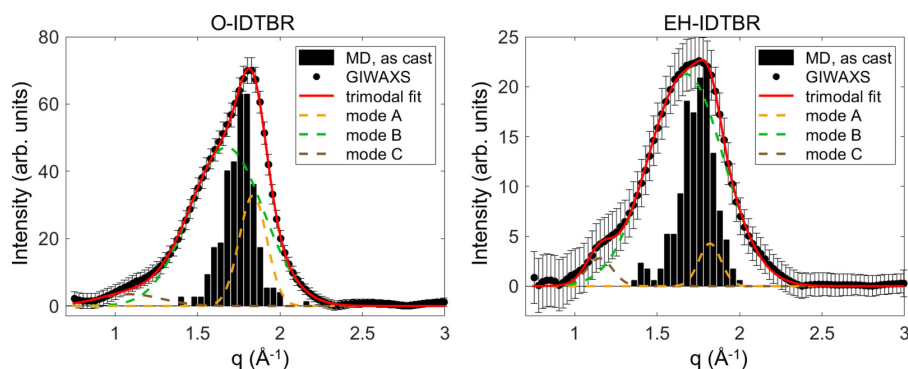


FIG. 5. Azimuthal integrations (black dots) and corresponding fits (red lines) to the (010)  $\pi$ -stack peaks of the **O-IDTBR** and **EH-IDTBR** thin-films cast at 70 °C compared to the  $\pi$ -stacking distances extracted from the as-cast simulated thin-films (gray bars).

of the individual planes spanned by these seven ring systems were also computed to be able to evaluate the relative orientation of the molecular pairs. To quantify the  $\pi$ -stacking distance in the simulations, the distance from each evaluation point in each molecule to all evaluation points in all other molecules were computed, and the shortest interaction for each molecule was extracted (see the SI, Fig. S11 for representative images of  $\pi$ -stacking molecular pairs) [19]. These were then subject to a filtering based on an evaluation of relative alignment using a cutoff of  $\arccos(0.9) \sim 25.8$  degrees from perfectly (anti)parallel alignment to define cofaciality (only a few molecular pairs were disqualified from this). For the cofacial pairs, the average of the distance from the relevant evaluation point of molecule A to the plane of the relevant ring-system of molecule B and the distance from the relevant evaluation point of molecule B to the plane of the relevant ring-system of molecule A was defined as the  $\pi$ -stacking distance to account for cases in which the  $\pi$ -stacking ring-systems were slightly offset with respect to each other (as the direct evaluation point to evaluation point distance would in this case be an overestimation of the actual  $\pi$ - $\pi$ -distance). Histograms of the resulting  $\pi$ -stacking distances for all cofacial, closely interacting molecular pairs in the as-cast thin-film simulations are plotted in Fig. 5 with the corresponding GIWAXS data for the low-temperature cast (70 °C) thin-films. The real-space  $\pi$ -stacking distances for all simulations (as-cast and annealed thin-films as well as the crystal structures) and the values extracted from the GIWAXS data for the low-temperature cast thin-films are presented in Table II.

As seen in Fig. 5, the simulated  $\pi$ -stacking distances are in excellent correspondence with the GIWAXS data for both

**O-IDTBR** and **EH-IDTBR** in terms of the maximum intensity positions for the high- $q$  peak at  $q_z$ . Further analysis of the GIWAXS results shows that trimodal GAUSSIAN functions fit the data very precisely: Two high-intensity modes in the high- $q$  range, which are associated with the  $\pi$ -stacking, and a low-intensity tail mode in the lower- $q$  range, which could be ascribed to packing of side chains. The mean values and the corresponding errors of the fits of the former two, mode A and mode B, are listed in Table II. This multimodality is not unambiguously present in the histograms of the simulation data, although some indications of shoulders toward the lower- $q$  range of the histograms can be seen. The resolution of this effect in the thin-film simulations is most probably limited by statistics as only 448 molecules are included in these, and the simulation values listed in Table II are hence only based on single GAUSSIAN fits. However, manual inspection of the molecular pairs from the simulations suggests that the bulkiness of the terminal ethyl group on the RH unit is the reason for the bimodality of the  $\pi$ -stacking observed in experiments: If the ethyl group points inward in a  $\pi$ -stack including a RH unit, the stack is slightly distorted and elongated, while a similar stack but with the ethyl group pointing outward will have a closer interaction. As seen in Fig. 6 showing two representative  $\pi$ -stacking pairs from the simulations, the distances are furthermore very close to the ones identified in the GIWAXS analysis for mode A and mode B. A future molecular design of IDTBR derivatives should hence include fully planar terminal units instead of the ethyl substituted RH unit in order to promote shorter  $\pi$ -stacking distances and thus stronger intermolecular electronic coupling (cf. Sec. III C).

Looking at the  $\pi$ -stacking distances in Table II, no significant differences between **O-IDTBR** and **EH-IDTBR** can

TABLE II. Mean and standard deviation in Å of GAUSSIANS fitted to the  $\pi$ -stacking distances from the simulations compared to the  $\pi$ -stacking distances and the corresponding errors extracted from GIWAXS measurements (modes A and B from multimodal Gaussian fits; cf. Fig. 5).

$\pi$ -stack (Å)	MD simulations			GIWAXS	
	as-cast	anneal.	crystal	mode A	mode B
O-IDTBR	$3.60 \pm 0.22$	$3.68 \pm 0.25$	$3.52 \pm 0.09$	$3.43 \pm 0.02$	$3.76 \pm 0.01$
EH-IDTBR	$3.64 \pm 0.25$	$3.68 \pm 0.26$	$3.51 \pm 0.12$	$3.45 \pm 0.03$	$3.76 \pm 0.01$

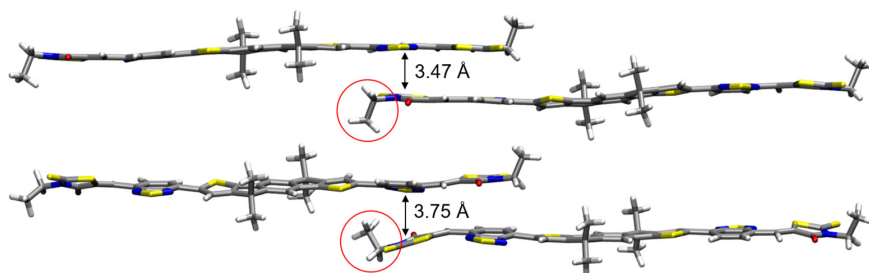


FIG. 6. Representative molecular pairs from **EH-IDTBR** crystal simulations at 300 K illustrating the bimodality of the  $\pi$ -stacks caused by the terminal ethyl group on the RH units (circled in red). The  $\pi$ -stacking distances for the two specific pairs as calculated with the method described in Sec. III A are indicated. The side chains on IDT are substituted for methyl groups for clarity (only in the visualization).

be seen. The distances increase slightly in the thin-film simulations upon annealing from  $3.60 \pm 0.22$  Å the as-cast **O-IDTBR** thin-film to  $3.68 \pm 0.25$  Å for the annealed and from  $3.64 \pm 0.25$  Å the as-cast **EH-IDTBR** thin-film to  $3.68 \pm 0.26$  Å for the annealed. These are all in good agreement with the GIWAXS data, spanning the range of both modes from the measurements. The simulations of the ordered crystals logically pack closer with lower standard deviations, namely  $3.52 \pm 0.09$  Å for **O-IDTBR** and  $3.51 \pm 0.12$  Å for **EH-IDTBR**. In conclusion, the short-range structural properties are very satisfactorily modeled using the solvent evaporation simulation procedure devised herein.

Regarding longer-range order, the GIWAXS measurements on the low-temperature cast thin-films showed intense peaks in  $q_{xy}$  with values of  $17.57 \pm 0.02$  and  $17.08 \pm 0.05$  Å based on fits using the Voigt model for **O-IDTBR** and **EH-IDTBR**, respectively, whereas the corresponding numbers for the 130 °C annealed samples were  $14.40 \pm 0.02$  and  $16.49 \pm 0.40$  Å (see the SI, Fig. S6) [19]. Regrettably, this longer-range order was not present to a quantifiable degree in the thin-film simulations (simulated scattering signals were very weak; cf. the SI, Fig. S7) [19,58]. However, it can be seen from radial distribution functions of the IDTBR COMs (note: The molecular COMs, not the residual COMs corresponding to the individual evaluation points) that some of the characteristic distances from the crystal simulations coincide with the more probable distances from the thin-film simulations (see Fig. 7). The **O-IDTBR** as-cast thin-film exhibits a broad distribution from 10 to 20 Å, which upon annealing sharpens to a bump with a maximum probability density at 14.5 Å with a weak shoulder at around 17.2 Å. The former of these is also present as a peak in the crystal simulations, corresponding to an intermolecular distance across the side-chain-filled space in the plane perpendicular to the  $\pi$ -stacking plane (cf. red arrows on the left panel of Fig. 7). This could thus have the necessary contrast to show up in scattering measurements, and it indeed corresponds very well to the strong peak at 14.40 Å found for the 130 °C annealed **O-IDTBR** thin-film.

Looking at the **EH-IDTBR** thin-film simulations, the maximum probability density moves from 12.4 to 13.0 Å upon annealing, and the shoulder at around 17.0 Å gets more pronounced. The distances are also present as intense peaks in the crystal simulation, and they both show up in the GIWAXS spectrum, the former, however, with a low intensity. An inspection of the crystal structure shows that the latter indeed

seems to have more contrast, i.e., extending across a side-chain-filled space, and it occurs in the plane perpendicular to the  $\pi$ -stacking plane (cf. red and blue arrows in the right panel of Fig. 7).

In summary, these results indicate that the simulated annealing has, although to a low degree, increased the structural order for the low- $q$  range in the thin-film simulations. It remains, however, that the reasonably accessible simulation times for atomistic MD are not sufficient to induce a high structural order in the low- $q$  range from randomly initiated simulations of solution deposited small-molecule systems.

### B. Effects of the substrate

As described in Sec. II C, the parameters used for the amorphous  $\text{SiO}_2$  substrate have previously been validated in terms of their interaction with organic molecules in vapor deposition simulations [43]. To further validate these in the context of solvent evaporation simulations, we have compared the relative orientation of the molecules and the substrate plane in the simulations to the experimental  $\pi$ -stack orientation extracted from the (010) peak from the GIWAXS measurements, and we plotted these in Fig. 8. Each of the GIWAXS data points represents the intensity of a fixed- $q$  integration over a  $2^\circ$  wedge in  $\omega$  of the spectra shown in Fig. 4 using an analysis similar to the one visualized in Fig. 5. These fits are shown in the SI, Figs. S8 and S9 [19]. The simulation data points are obtained as the angles between the normal vector of the substrate and the normal vectors of the planes spanned by each of the seven evaluation point ring-systems in the IDTBR molecules.

Although the relative orientations from the simulations show a quantitative deviation from the corresponding GIWAXS data, the qualitative behaviors are very similar: A face-on stacking is favored for both thin-films, i.e., highest intensities at low  $\omega$ -values, with a tendency for **O-IDTBR** to be more textured than **EH-IDTBR**, i.e., having a sharper orientation profile. Regarding the quantitative deviation, it is important to note that whereas the GIWAXS intensity depends strongly on the local order of several molecules and will thus not yield a signal for a disordered region, all molecules have equal weight in the analysis of the simulated thin-films regardless of the order of their surrounding molecules. This can explain the less sharp decrease of the signal from the simulated thin-films with higher angles compared to the

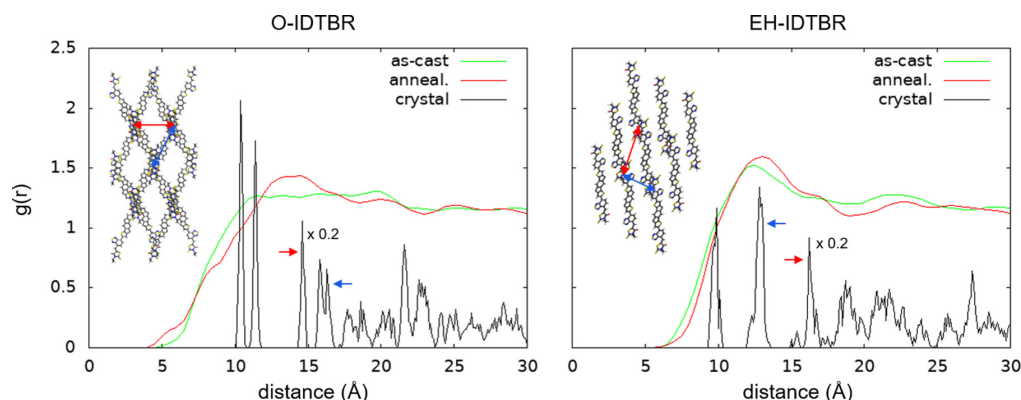


FIG. 7. Radial distribution functions of the COM positions in the simulations of **O-IDTBR** (left) and **EH-IDTBR** (right) as-cast thin-films (green; Bezier spline fit), annealed thin-films (red; Bezier spline fit), and crystals (black; scaled by a factor of 0.2). Insets are top views ( $\pi$ -stacks in the out-of-plane direction) of the ideal crystal structures without side chains to ease the view; red arrows mark the distances present as peaks in the GIWAXS spectra of the annealed thin-films, whereas blue arrows mark distances that do not show up in these GIWAXS spectra.

measurements. Summarizing, the substrate effects of amorphous  $\text{SiO}_2$  are satisfactorily modeled with the employed parameters in the context of this study. We note, however, that functional devices such as OPVs or OFETs are most often deposited directly on top of organic layers of polymers or small molecules that act as charge collection layers between the active layer and the solid-state oxide or metal electrodes. Surface properties such as the hydrophobicity of these layers can vary significantly from that of amorphous  $\text{SiO}_2$ , which affects the thin-film growth [59]. In this study, a simple setup with few components was prioritized to enable a more direct comparison between simulations and experiments, but future

studies should thus focus on implementing substrates that are more directly relevant for functional devices.

### C. Electronic properties

To determine if the structural characteristics discussed are indeed beneficial to the transport properties, we extracted the unique molecular pairs from each of the simulated **O-IDTBR** and **EH-IDTBR** as-cast and annealed thin-films to perform electronic structure calculations on them. To reduce computational costs, the side chains were substituted by methyl groups, a procedure that is justified by the insulating nature of alkyl side chains as well as the negligible impact of their length/size on the backbone electronic structure [60]. We then did single-point DFT calculations at the B3LYP/6-31G(d) level of theory on the pairs and each of the molecules that the pairs consist of, and afterward we calculated the electronic couplings from their frontier orbitals [highest occupied molecular orbital (HOMO); lowest unoccupied molecular orbital (LUMO)] using the projective method [61,62], which is valid for intermolecular coupling of identical molecules. The use of B3LYP/6-31G(d) is justified as a compromise between computational cost and accuracy in terms of the description of frontier orbital properties (see below). Note that incorporating diffuse functions in the basis set for the single-point calculations of the pairs would lead to an overcomplete basis because diffuse functions centered on one molecule would overlap with the other molecule in the pair, thus inhibiting the use of the projective method by causing the orthogonalization of the overlap matrices to break down.

To assess the description of the frontier orbitals at the chosen level of theory, B3LYP/6-31G(d), the HOMO and LUMO energies were computed for each molecule in the extracted pairs used for the coupling calculations and plotted in the left panel of Fig. 9; in the right panel, frontier orbitals of a B3LYP/6-31G optimized, methyl-substituted IDTBR are visualized. Although a direct comparison of calculated LUMO energies in vacuum to electrochemical measurements in solvent of electron affinity is not valid, the calculated HOMO

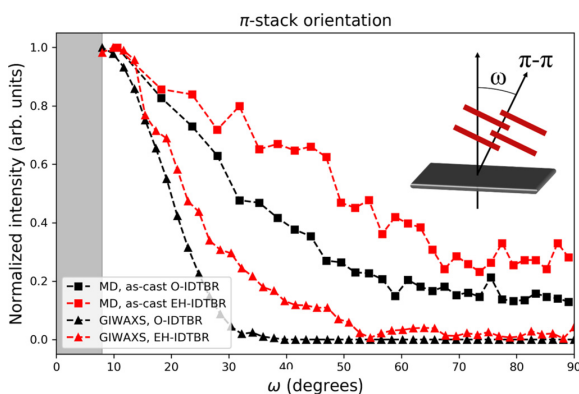


FIG. 8. Orientational distribution of the  $\pi$ -stacks relative to the substrate (cf. the inset) obtained from the (010) GIWAXS-peak for **O-IDTBR** and **EH-IDTBR** low-temperature cast thin-films (black and red squares, respectively) compared to the corresponding MD distributions computed as the angles between the normal vector of the substrate and those of each of the evaluation point ring-systems in the as-cast thin-films (black and red triangles, respectively). The gray-shaded area from  $0^\circ$  to  $8^\circ$  represents the range of angles not probed due to the fixed grazing incidence angle.

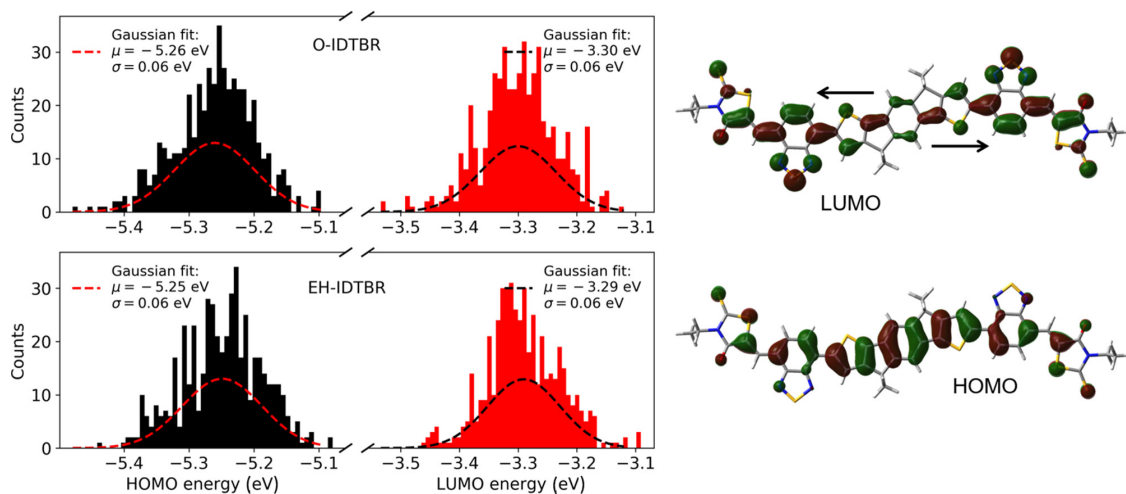


FIG. 9. Left: Frontier orbital energies of the 500 molecules from the 250 most closely stacked pairs in each of the simulated **O-IDTBR** and **EH-IDTBR** as-cast thin-films on  $\text{SiO}_2$  substrates. The arithmetic mean,  $\mu$ , and standard deviation,  $\sigma$ , of a GAUSSIAN fit to each of the data-sets are indicated. Right: Frontier orbitals of a B3LYP/6-31G(d) optimized, methyl substituted IDTBR molecule. Arrows mark the directions of the change in electron density when going from HOMO to LUMO. An isovalue (contour threshold) of 0.02 au is used in the visualization.

energies can serve as a good estimate of the ionization potential for high-throughput calculations. For both **O-IDTBR** and **EH-IDTBR**, the HOMO and LUMO energies were centered around  $-5.25$  and  $-3.29$  eV, leading to a HOMO-LUMO gap of 1.96 eV, which is close to the experimental  $\lambda_{\text{max}}$  of uv-vis thin-film absorptions of 1.80 and 1.84 eV, respectively [20]. Experimentally, the **O-IDTBR** and **EH-IDTBR** as-cast thin-film electron affinities were determined to be  $-3.88$  and  $-3.90$  eV, whereas the ionization potentials were estimated to be  $-5.51$  and  $-5.58$  eV based on optical gaps of 1.63 and 1.68 eV, respectively [20]. The correspondence of the calculated values to these are decent. To test the dependence of the basis set, the calculations were repeated for an optimized, methyl-substituted IDTBR molecule at the B3LYP/6-31G(d) and B3LYP/6-311++G(d,p) levels of theory. The significant increase in number of basis functions (from 996 to 1668) yielded HOMO and LUMO energies of  $-5.53$  and  $-3.47$  eV, respectively, which are improvements compared to the  $-5.28$  and  $-3.17$  eV of the small basis-set calculation, albeit minor ones. The B3LYP/6-31G(d) level of theory is hence deemed a reasonable compromise between cost and accuracy for these high-throughput calculations of frontier orbital properties, while the close correspondence between values for quantum mechanically optimized geometries and geometries extracted from MD simulations additionally serves as a validation of the IDTBR force fields.

The electronic couplings calculated for the as-cast and annealed thin-films of **O-IDTBR** and **EH-IDTBR** are presented in Fig. 10 as box plots for pairs with a distance of less than  $4.5 \text{ \AA}$  (dependence on distance and intermolecular orientation can be found in the SI, Figs. S12 and S13) [19]. These are compared to couplings calculated from MD runs at 300 K of their experimentally obtained crystal structures [22]. For both as-cast and annealed versions of **O-IDBTR** and **EH-IDTBR** thin-films, the median values for electron coupling, i.e., electron transfer integrals, are centered around 11 meV

with slightly higher mean values of around 15 meV. No significant differences are observed between the two materials in thin-films, but for the crystal structures, **EH-IDTBR** exhibits only half the electron coupling strength of **O-IDTBR**. This correlates nicely with the results presented in Ref. [22] for geometries of single crystals deduced from x-ray diffraction at 173 K; here, the four unique types of interactions considered in the **O-IDTBR** unit cell were calculated to have couplings of 9, 51, 58, and 59 meV, whereas the two types in the **EH-IDTBR** unit cell were calculated to be 17 and 39 meV. These results were obtained using the same level of theory as was used herein, hence making them directly comparable—here, however, we include the effects of dynamics at 300 K and sample geometries from simulations spanning a large number of unit cells, which explains the wide distribution and the lower means of calculated values seen. Looking at the hole couplings, the tendencies are similar to the ones for the electron couplings, but the absolute values are in general lower by around 5 meV. Interestingly, the high structural order in **O-IDTBR** crystals yields hole couplings that are of the same strength as the crystal electron couplings, and almost 20 meV higher than the **O-IDTBR** thin-film hole couplings,

TABLE III. Percentages of different interaction types relative to the total number of pairs with  $\pi$ - $\pi$  interactions closer than  $4.5 \text{ \AA}$ .

Amount (%)	<b>O-IDTBR</b>			<b>EH-IDTBR</b>		
	as-cast	anneal.	crystal	as-cast	anneal.	crystal
type						
RH-RH	8.6	4.3		12.0	8.8	
BT-BT	27.5	32.4	35.1	35.1	35.0	
IDT-IDT	0.9	3.2				
RH-BT	33.3	25.9	61.4	42.9	41.9	100.0
RH-IDT	13.5	20.0	3.5	4.7	6.2	
BT-IDT	16.2	14.1		5.2	8.1	

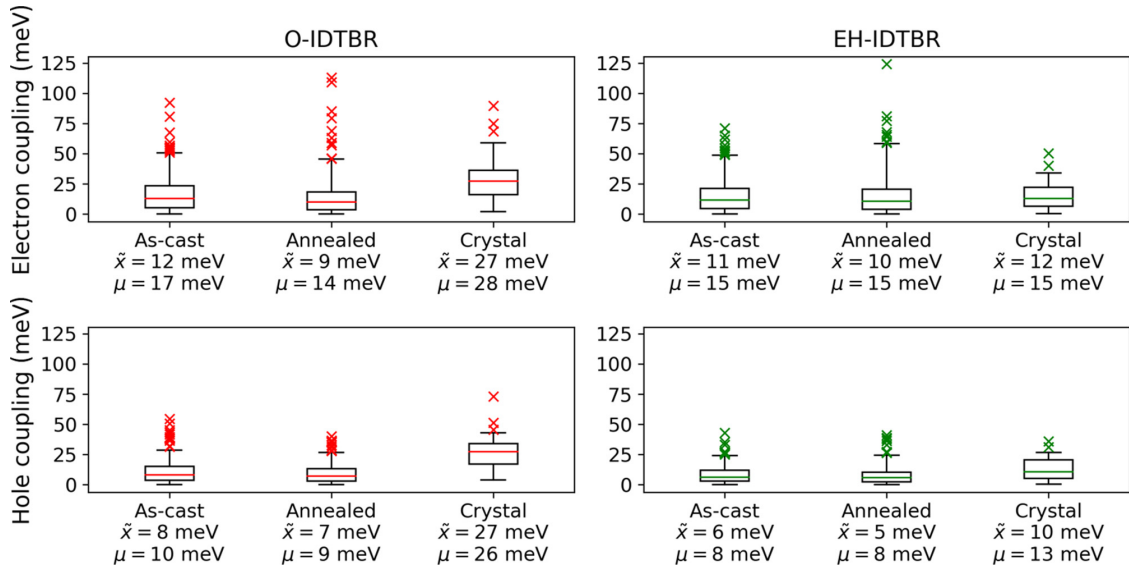


FIG. 10. Box plots of electronic couplings for electron (top row) and hole (bottom row) transfer (also referred to as effective electron/hole transfer integrals,  $J_{e/h}$ ) for pairs stacked closer than  $4.5 \text{ \AA}$  in each of the simulated **O-IDTBR** (left column) and **EH-IDTBR** (right column) as-cast and annealed thin-films on  $\text{SiO}_2$  substrates compared to the corresponding couplings in their simulated crystal structures. Phase dependency is not considered (absolute values presented). The top 5% of the values are plotted as outliers (red and green  $\times$ 's). Median,  $\bar{x}$ , and arithmetic mean,  $\mu$ , are indicated for each dataset.

whereas the hole couplings for **EH-IDTBR** crystals are only slightly larger than for the disordered thin-films.

To rationalize the above findings, the different types of close interactions (i.e.,  $\pi$ -stacks, cf. Sec. III A) were analyzed and listed in Table III as percentages relative to the total number of pairs extracted, and in Tables IV and V as the mean electron and hole coupling strengths in meV, respectively. First and foremost, it is a clear tendency in Table III that close interactions of types BT-BT and RH-BT are the most frequent, both in the thin-films and in the crystals. This is expected to be beneficial to the electron transfer properties due to the molecular design of IDTBR with an electron donating central IDT unit flanked by electron withdrawing BT and RH units. As seen in the right panel of Fig. 9, the LUMO of IDTBR is localized mainly on the BT unit, and the electron coupling data in Table IV are indeed consistent with this, showing stronger couplings for interaction types involving the BT unit with a tendency of BT-BT interactions being the strongest in

the thin-films. However, in the **O-IDTBR** crystal, the RH-BT interaction is significantly stronger than the same type in the **EH-IDTBR** crystal even though the individual geometries are very similar (parallel backbones, parallel  $\pi$ -planes; representative structures visualized in Fig. 11)—the only apparent difference is the relative orientation of the BT unit with respect to the RH and IDT units and the resulting inter-molecular stacking. When the RH oxo group of a molecule A points in the direction of the BT sulfur of a molecule B (as is the case for **EH-IDTBR** crystals), the LUMO-LUMO overlap in the  $\pi$ -stack of molecule A and B is not as favorable as when the RH thioketone points in the direction of the BT sulfur (as is the case for **O-IDTBR** crystals), which leads to, on average, electronic couplings of only half the strength for both electrons (see Table IV) and holes (see Table V). In Ref. [22], the electron couplings for exactly these types of close interactions were found to be 9 meV for **O-IDTBR** and 39 meV for **EH-IDTBR** based on the experimentally

TABLE IV. Mean electron coupling,  $\mu(J_e)$ , in meV of different interaction types of pairs with  $\pi$ - $\pi$  interactions closer than  $4.5 \text{ \AA}$ .

$\mu(J_e)$ (meV)	<b>O-IDTBR</b>			<b>EH-IDTBR</b>		
type	as-cast	anneal.	crystal	as-cast	anneal.	crystal
RH-RH	16	6		9	13	
BT-BT	23	20	25	18	20	
IDT-IDT	15	8				
RH-BT	16	17	31	15	14	15
RH-IDT	14	8		23	4	
BT-IDT	13	12		15	16	

TABLE V. Mean hole coupling,  $\mu(J_h)$ , in meV of different interaction types of pairs with  $\pi$ - $\pi$  interactions closer than  $4.5 \text{ \AA}$ .

$\mu(J_h)$ (meV)	<b>O-IDTBR</b>			<b>EH-IDTBR</b>		
type	as-cast	anneal.	crystal	as-cast	anneal.	crystal
RH-RH	8	4		7	10	
BT-BT	13	12	16	8	7	
IDT-IDT	26	1				
RH-BT	9	9	32	9	9	13
RH-IDT	14	9		8	7	
BT-IDT	9	7		11	7	



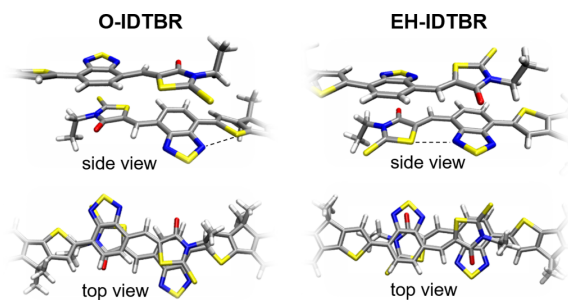


FIG. 11. Representative geometries of the RH-BT type of close interactions in **O-IDTBR** and **EH-IDTBR** crystal structures. The relative alignment of the BT unit to the RH and IDT units strongly influences the strength of the electronic coupling between the molecules.

determined crystal structures at 173 K. We were able to reproduce these results, and it thus remains that either the consideration of dynamics and sampling at 300 K and/or the force fields themselves are the causes of this qualitative change in relative coupling strength. The latter was addressed in Sec. II D, which showed a good correspondence between the experimental crystal structures and the simulated crystal structures, and the inclusion of dynamics and the sampling from larger simulations thus seem to be key to predicting the charge-transport properties of molecular ensembles, even when crystal structures are available, as the electronic transfer integrals are sensitive to the structural changes induced by temperature.

Looking at the BT-RH stacking in the thin-films, our analysis (cf. the SI, Fig. S10) [19] shows that little to no difference between **O-IDTBR** and **EH-IDTBR** can be observed, both for as-cast and annealed crystals, with both materials predominantly exhibiting the BT-RH stacking geometry seen for **O-IDTBR** crystals (left column of Fig. 11). This is expected due to this stacking geometry involving two IDTBR molecules that are both in their minimum energy configurations with respect to the torsional angle between BT and RH (cf. Figs. 3 and 11). The structural ordering seen in the **EH-IDTBR** crystal is thus not present to any significant degree in the thin-film simulations. It is important to note that although our findings for the crystal simulations are consistent with the experimental findings of higher mobilities in **O-IDTBR** OTFTs than in **EH-IDTBR** OTFTs [22], the simulation times reachable with atomistic MD are not sufficient to induce any significant crystallinity in the IDTBR thin-film simulations. It is apparent from the coupling calculations that an increased crystallinity would indeed be beneficial for the charge-transport properties of **O-IDTBR** thin-films when comparing the thin-film simulations to the crystal simulations. **O-IDTBR** has by differential scanning calorimetry been shown to have an exothermic crystallization transition with  $T_c = 115^\circ\text{C}$ , whereas **EH-IDTBR** has no such transition [20]. It can thus be concluded that the increased structural order upon annealing of **O-IDTBR** thin-films to more than  $115^\circ\text{C}$  is responsible for better charge-transport properties, but that this does not hold true for **EH-IDTBR** thin-films, whose structural order and, in turn, charge-transport properties will seemingly not benefit significantly

from annealing as seen in the SI, Fig. S4 [19], which is fully consistent with the simulation results presented herein.

#### IV. CONCLUSIONS

In summary, in the present work we have devised a molecular dynamics solvent evaporation procedure that includes substrate and air-interface effects to model solution deposition of organic thin-films. The procedure is general and can be used in combination with any given substrate and for both atomistic and coarse-grained MD simulations. Here, we used our newly developed all-atom force fields for **O-IDTBR** and **EH-IDTBR** to investigate the structure-property relationships in their thin-films. It was found that the short-range structural properties, i.e.,  $\pi$ -stacking, and the qualitative alignment effects relative to the substrate were accurately modeled, but it was evident that the time-scales feasible for atomistic MD, here on the order of 1  $\mu\text{s}$ , were not sufficient to induce significant longer-range order in small-molecule thin-films. Upon linking the structural findings to electronic properties, it was found that the  $\pi$ -stacking interactions of benzothiadiazole units were beneficial for the charge-transport properties of IDTBR thin-films, exhibiting high electronic transfer integrals even in disordered systems. This result is believed to be relevant for a range of *n*-type materials with similar molecular designs. Additionally, we saw indications of the terminal ethyl group on the rhodanine units inducing steric effects that are detrimental to the RH-BT type of stacking when the backbones are parallel, and future efforts in material development should focus on substituting this ethyl group with a methyl group or substituting the rhodanine unit altogether with planar, even stronger electron withdrawing units, which could additionally be beneficial for the long-wavelength absorption properties. We have become aware that this has recently been done in Ref. [63], where the rhodanine was substituted for a dicyano moiety, leading to small efficiency increases in organic solar cells.

Further work will focus on thin-film morphologies of organic solar cell active layer blends based on these IDTBR acceptors and relevant polymer donors. Additionally, a coarse-grained force field for IDTBR is currently being developed to investigate whether higher structural order can be obtained with bigger system sizes and longer simulation times.

#### ACKNOWLEDGMENTS

The authors acknowledge financial support from the H2020 European Research Council through the SEEWHI Consolidator grant, ERC-2015-CoG-681881. A.S.G. thanks the team responsible for the Niflheim supercomputer at the Technical University of Denmark, Department of Physics where all calculations were performed. A.S.G. thanks Jenny Nelson and Jarvist M. Frost for guidance and discussions regarding the electronic coupling calculations, Elisabeth Rice and Francesco Salerno for providing a script for the projective method, Anne A. Y. Guilbert and Drew Pearce for support on MD simulations during a half year secondment at Imperial College London, and Natalie Stingelin for facilitating it. A.S.G. acknowledges generous funding from Otto Mønstedts Fond (Grant No. 17-70-1617) in connection with this secondment.

- [1] N. Espinosa, M. Hosel, D. Angmo, and F. C. Krebs, Solar cells with one-day energy payback for the factories of the future, *Energy Environ. Sci.* **5**, 5117 (2012).
- [2] C. J. Emmott, A. Urbina, and J. Nelson, Environmental and economic assessment of ITO-free electrodes for organic solar cells, *Sol. Energy Mater. Sol. Cells* **97**, 14 (2012).
- [3] A. S. Gertsens, M. F. Castro, R. R. Søndergaard, and J. W. Andreasen, Scalable fabrication of organic solar cells based on non-fullerene acceptors, *Flex. Print. Electron.* **5**, 014004 (2020).
- [4] C. Yan, S. Barlow, Z. Wang, H. Yan, A. K. Jen, S. R. Marder, and X. Zhan, Non-fullerene acceptors for organic solar cells, *Nat. Rev. Mater.* **3**, 18003 (2018).
- [5] G. Zhang, J. Zhao, P. C. Y. Chow, K. Jiang, J. Zhang, Z. Zhu, J. Zhang, F. Huang, and H. Yan, Nonfullerene acceptor molecules for bulk heterojunction organic solar cells, *Chem. Rev.* **118**, 3447 (2018).
- [6] Q. Liu, Y. Jiang, K. Jin, J. Qin, J. Xu, W. Li, J. Xiong, J. Liu, Z. Xiao, K. Sun, S. Yang, X. Zhang, and L. Ding, 18% efficiency organic solar cells, *Sci. Bull.* **65**, 272 (2020).
- [7] J. Hou, O. Inganäs, R. H. Friend, and F. Gao, Organic solar cells based on non-fullerene acceptors, *Nat. Mater.* **17**, 119 (2018).
- [8] N. Gasparini, M. Salvador, S. Strohm, T. Heumüller, I. Levchuk, A. Wadsworth, J. H. Bannock, J. C. de Mello, H.-J. Egelhaaf, D. Baran, I. McCulloch, and C. J. Brabec, Burn-in free nonfullerene-based organic solar cells, *Adv. Energy Mater.* **7**, 1700770 (2017).
- [9] H. Cha, J. Wu, A. Wadsworth, J. Nagitta, S. Limbu, S. Pont, Z. Li, J. Searle, M. F. Wyatt, D. Baran, J.-S. Kim, I. McCulloch, and J. R. Durrant, An efficient, “burn in” free organic solar cell employing a nonfullerene electron acceptor, *Adv. Mater.* **29**, 1701156 (2017).
- [10] D. Baran, R. S. Ashraf, D. A. Hanifi, M. Abdelsamie, N. Gasparini, J. A. Röhr, S. Holliday, A. Wadsworth, S. Lockett, M. Neophytou, C. J. M. Emmott, J. Nelson, C. J. Brabec, A. Amassian, A. Salleo, T. Kirchartz, J. R. Durrant, and I. McCulloch, Reducing the efficiency-stability-cost gap of organic photovoltaics with highly efficient and stable small molecule acceptor ternary solar cells, *Nat. Mater.* **16**, 363 (2017).
- [11] W. Zhao, D. Qian, S. Zhang, S. Li, O. Inganäs, F. Gao, and J. Hou, Fullerene-free polymer solar cells with over 11% efficiency and excellent thermal stability, *Adv. Mater.* **28**, 4734 (2016).
- [12] X. Du, T. Heumüller, W. Gruber, A. Classen, T. Unruh, N. Li, and C. J. Brabec, Efficient polymer solar cells based on non-fullerene acceptors with potential device lifetime approaching 10 years, *Joule* **3**, 215 (2019).
- [13] M. Jørgensen, K. Norrman, S. A. Gevorgyan, T. Tromholt, B. Andreasen, and F. C. Krebs, Stability of polymer solar cells, *Adv. Mater.* **24**, 580 (2012).
- [14] P. Cheng, H. Bai, N. K. Zawacka, T. R. Andersen, W. Liu, E. Bundgaard, M. Jørgensen, H. Chen, F. C. Krebs, and X. Zhan, Roll-coated fabrication of fullerene-free organic solar cells with improved stability, *Adv. Sci.* **2**, 1500096 (2015).
- [15] D. Baran, T. Kirchartz, S. Wheeler, S. Dimitrov, M. Abdelsamie, J. Gorman, R. S. Ashraf, S. Holliday, A. Wadsworth, N. Gasparini, P. Kaienburg, H. Yan, A. Amassian, C. J. Brabec, J. R. Durrant, and I. McCulloch, Reduced voltage losses yield 10% efficient fullerene free organic solar cells with >1 V open circuit voltages, *Energy Environ. Sci.* **9**, 3783 (2016).
- [16] N. Li, J. D. Perea, T. Kassir, M. Richter, T. Heumüller, G. J. Matt, Y. Hou, N. S. Güldal, H. Chen, S. Chen, S. Langner, M. Berlinghof, T. Unruh, and C. J. Brabec, Abnormal strong burn-in degradation of highly efficient polymer solar cells caused by spinodal donor-acceptor demixing, *Nat. Commun.* **8**, 14541 (2017).
- [17] F. D. Angelis, R. Berardi, J. Bisquert, J.-L. Bredas, G. D’Avino, N. Greenham, C. Groves, E. Hontz, T. Kirchartz, R. Marcus, D. McMahon, L. Muccioli, J. Nelson, S. Orlandi, M. Pastore, A. Pizzirusso, M. Ricci, C. Risko, O. Roscioni, T. V. Voorhis, A. Walker, S. Yost, and C. Zannoni, Multiscale modeling of organic and hybrid photovoltaics, in *Topics in Current Chemistry*, edited by D. Beljonne and J. Cornil (Springer-Verlag, Berlin, 2014), Vol. 352, pp. 1–400.
- [18] Q.-Q. Pan, S.-B. Li, Y.-C. Duan, Y. Wu, J. Zhang, Y. Geng, L. Zhao, and Z.-M. Su, Exploring what prompts ITIC to become a superior acceptor in organic solar cell by combining molecular dynamics simulation with quantum chemistry calculation, *Phys. Chem. Chem. Phys.* **19**, 31227 (2017).
- [19] See Supplemental Material at <http://link.aps.org/supplemental/10.1103/PhysRevMaterials.4.075405> for GROMACS force field files for **O-IDTBR** and **EH-IDTBR** for use with OPLS-AA, complete compound names, detailed force-field parametrization procedures and tables of parameters, experimental details and GIWAXS data for 130°C annealed thin-films, details of the structural analysis, and dependence of electronic coupling on intermolecular distance and relative orientation.
- [20] S. Holliday, R. S. Ashraf, A. Wadsworth, D. Baran, S. A. Yousaf, C. B. Nielsen, C.-H. Tan, S. D. Dimitrov, Z. Shang, N. Gasparini, M. Alamoudi, F. Laquai, C. J. Brabec, A. Salleo, J. R. Durrant, and I. McCulloch, High-efficiency and air-stable P3HT-based polymer solar cells with a new non-fullerene acceptor, *Nat. Commun.* **7**, 11585 (2016).
- [21] A. Wadsworth, R. S. Ashraf, M. Abdelsamie, S. Pont, M. Little, M. Moser, Z. Hamid, M. Neophytou, W. Zhang, A. Amassian, J. R. Durrant, D. Baran, and I. McCulloch, Highly efficient and reproducible nonfullerene solar cells from hydrocarbon solvents, *ACS Energy Lett.* **2**, 1494 (2017).
- [22] H. Bristow, K. J. Thorley, A. J. P. White, A. Wadsworth, M. Babics, Z. Hamid, W. Zhang, A. F. Paterson, J. Kosco, J. Panidi, T. D. Anthopoulos, and I. McCulloch, Impact of non-fullerene acceptor side chain variation on transistor mobility, *Adv. Electron. Mater.* **5**, 1900344 (2019).
- [23] M. Yoneya, H. Minemawari, T. Yamada, and T. Hasegawa, Interface-mediated self-assembly in inkjet printing of single-crystal organic semiconductor films, *J. Phys. Chem. C* **121**, 8796 (2017).
- [24] T. E. Gartner and A. Jayaraman, Modeling and simulations of polymers: A roadmap, *Macromol.* **52**, 755 (2019).
- [25] E. Jankowski, H. S. Marsh, and A. Jayaraman, Computationally linking molecular features of conjugated polymers and fullerene derivatives to bulk heterojunction morphology, *Macromolecules* **46**, 5775 (2013).
- [26] M. M. Henry, M. L. Jones, S. D. Oosterhout, W. A. Braunecker, T. W. Kemper, R. E. Larsen, N. Kopidakis, M. F. Toney, D. C. Olson, and E. Jankowski, Simplified models for accelerated



- structural prediction of conjugated semiconducting polymers, *J. Phys. Chem. C* **121**, 26528 (2017).
- [27] Y.-B. Lan, P.-H. Sher, C.-K. Lee, C.-W. Pao, C.-S. Tsao, Y.-C. Huang, P.-T. Huang, C.-I. Wu, and J.-K. Wang, Revealing ordered polymer packing during freeze-drying fabrication of a bulk heterojunction poly(3-hexylthiophene-2, 5-diyl):[6, 6]-phenyl-c61-butyric acid methyl ester layer: In situ optical spectroscopy, molecular dynamics simulation, and X-ray diffraction, *J. Phys. Chem. C* **121**, 14826 (2017).
- [28] G. Han, Y. Yi, and Z. Shuai, From molecular packing structures to electronic processes: Theoretical simulations for organic solar cells, *Adv. Energy Mater.* **8**, 1702743 (2018).
- [29] S. Peter, H. Meyer, and J. Baschnagel, Molecular dynamics simulations of concentrated polymer solutions in thin film geometry. II. Solvent evaporation near the glass transition, *J. Chem. Phys.* **131**, 014903 (2009).
- [30] V. Negi, A. Lyulin, and P. Bobbert, Solvent-dependent structure formation in drying P3HT:PCBM films studied by molecular dynamics simulations, *Macromol. Theor. Simul.* **25**, 550 (2016).
- [31] C.-K. Lee and C.-W. Pao, Nanomorphology evolution of P3HT/PCBM blends during solution-processing from coarse-grained molecular simulations, *J. Phys. Chem. C* **118**, 11224 (2014).
- [32] C.-K. Lee and C.-W. Pao, Multiscale molecular simulation of solution processing of SMDPPEH:PCBM small-molecule organic solar cells, *ACS Appl. Mater. Interfaces* **8**, 20691 (2016).
- [33] S. J. Marrink, H. J. Risselada, S. Yefimov, D. P. Tieleman, and A. H. de Vries, The MARTINI force field: Coarse grained model for biomolecular simulations, *J. Phys. Chem. B* **111**, 7812 (2007).
- [34] R. Alessandri, J. J. Uusitalo, A. H. de Vries, R. W. A. Havenith, and S. J. Marrink, Bulk heterojunction morphologies with atomistic resolution from coarse-grain solvent evaporation simulations, *J. Am. Chem. Soc.* **139**, 3697 (2017).
- [35] G. Han, X. Shen, R. Duan, H. Geng, and Y. Yi, Revealing the influence of the solvent evaporation rate and thermal annealing on the molecular packing and charge transport of DPP(TBFu)2, *J. Mater. Chem. C* **4**, 4654 (2016).
- [36] G. Han, Y. Guo, X. Ma, and Y. Yi, Atomistic insight into donor/acceptor interfaces in high-efficiency nonfullerene organic solar cells, *Solar RRL* **2**, 1800190 (2018).
- [37] A. F. Marmolejo-Valencia, Z. Mata-Pinzón, L. Dominguez, and C. Amador-Bedolla, Atomistic simulations of bulk heterojunctions to evaluate the structural and packing properties of new predicted donors in OPVs, *Phys. Chem. Chem. Phys.* **21**, 20315 (2019).
- [38] M. J. Abraham, T. Murtola, R. Schulz, S. Páll, J. C. Smith, B. Hess, and E. Lindahl, GROMACS: High performance molecular simulations through multi-level parallelism from laptops to supercomputers, *Software X* **1-2**, 19 (2015).
- [39] W. L. Jorgensen, D. S. Maxwell, and J. Tirado-Rives, Development and testing of the OPLS all-atom force field on conformational energetics and properties of organic liquids, *J. Am. Chem. Soc.* **118**, 11225 (1996).
- [40] G. A. Kaminski, R. A. Friesner, J. Tirado-Rives, and W. L. Jorgensen, Evaluation and reparametrization of the OPLS-AA force field for proteins via comparison with accurate quantum chemical calculations on peptides, *J. Phys. Chem. B* **105**, 6474 (2001).
- [41] R. T. Cygan, J.-J. Liang, and A. G. Kalinichev, Molecular models of hydroxide, oxyhydroxide, and clay phases and the development of a general force field, *J. Phys. Chem. B* **108**, 1255 (2004).
- [42] S. Leroy and M. Wendland, Simulation of forces between humid amorphous silica surfaces: A comparison of empirical atomistic force fields, *J. Phys. Chem. C* **116**, 26247 (2012).
- [43] O. M. Roscioni, G. D'Avino, L. Muccioli, and C. Zannoni, Pentacene crystal growth on silica and layer-dependent step-edge barrier from atomistic simulations, *J. Phys. Chem. Lett.* **9**, 6900 (2018).
- [44] C. Coleman, P. J. van Maaren, M. Hong, J. S. Hub, L. T. Costa, and D. van der Spoel, Force field benchmark of organic liquids: Density, enthalpy of vaporization, heat capacities, surface tension, isothermal compressibility, volumetric expansion coefficient, and dielectric constant, *J. Chem. Theor. Comput.* **8**, 61 (2012).
- [45] S. Strohm, F. Machui, S. Langner, P. Kubis, N. Gasparini, M. Salvador, I. McCulloch, H.-J. Egelhaaf, and C. J. Brabec, P3HT: Non-fullerene acceptor based large area, semi-transparent PV modules with power conversion efficiencies of 5%, processed by industrially scalable methods, *Energy Environ. Sci.* **11**, 2225 (2018).
- [46] J. H. Yang, T. Ryua, Y. Lansac, Y. H. Jang, and B. H. Lee, Shear stress-induced enhancement of the piezoelectric properties of PVDF-TrFE thin films, *Org. Electron.* **28**, 67 (2016).
- [47] M. J. Frisch, G. W. Trucks, H. B. Schlegel, G. E. Scuseria, M. A. Robb, J. R. Cheeseman, G. Scalmani, V. Barone, G. A. Petersson, H. Nakatsuji *et al.*, GAUSSIAN 16 Revision A.03, 2016. GAUSSIAN Inc., Wallingford CT.
- [48] C. Lee, W. Yang, and R. G. Parr, Development of the Colle-Salvetti correlation-energy formula into a functional of the electron density, *Phys. Rev. B* **37**, 785 (1988).
- [49] A. D. Becke, Density functional thermochemistry. III. The role of exact exchange, *J. Chem. Phys.* **98**, 5648 (1993).
- [50] P. J. Stephens, F. J. Devlin, C. F. Chabalowski, and M. J. Frisch, Ab initio calculation of vibrational absorption and circular dichroism spectra using density functional force fields, *J. Phys. Chem.* **98**, 11623 (1994).
- [51] J.-D. Chai and M. Head-Gordon, Systematic optimization of long-range corrected hybrid density functionals, *J. Chem. Phys.* **128**, 084106 (2008).
- [52] J.-D. Chai and M. Head-Gordon, Long-range corrected hybrid density functionals with damped atom-atom dispersion corrections, *Phys. Chem. Chem. Phys.* **10**, 6615 (2008).
- [53] R. Krishnan, J. S. Binkley, R. Seeger, and J. A. Pople, Self-consistent molecular orbital methods. XX. A basis set for correlated wave functions, *J. Chem. Phys.* **72**, 650 (1980).
- [54] J. S. Binkley, J. A. Pople, and W. J. Hehre, Self-consistent molecular orbital methods. 21. Small split-valence basis sets for first-row elements, *J. Am. Chem. Soc.* **102**, 939 (1980).
- [55] A. A. Y. Guilbert, J. M. Frost, T. Agostinelli, E. Pires, S. Lilliu, J. E. Macdonald, and J. Nelson, Influence of bridging atom and side chains on the structure and crystallinity of cyclopentadithiophene-benzothiadiazole polymers, *Chem. Mater.* **26**, 1226 (2014).
- [56] M. J. Robertson, J. Tirado-Rives, and W. L. Jorgensen, Improved peptide and protein torsional energetics with the OPLS-AA force field, *J. Chem. Theor. Comput.* **11**, 3499 (2015).

- [57] M. J. Abraham, D. van der Spoel, E. Lindahl, B. Hess, and the GROMACS development team, GROMACS User Manual version 2016.3, 2017.
- [58] C. F. Macrae, I. J. Bruno, J. A. Chisholm, P. R. Edgington, P. McCabe, E. Pidcock, L. Rodriguez-Monge, R. Taylor, J. van de Streek, and P. A. Wood, Mercury CSD 2.0 - new features for the visualization and investigation of crystal structures, *J. Appl. Crystallogr.* **41**, 466 (2008).
- [59] B. Kang, M. Jang, Y. Chung, H. Kim, S. K. Kwak, J. H. Oh, and K. Cho, Enhancing 2D growth of organic semiconductor thin films with macroporous structures via a small-molecule heterointerface, *Nat. Commun.* **5**, 4752 (2014).
- [60] Z. Ma, H. Geng, D. Wang, and Z. Shuai, Influence of alkyl side-chain length on the carrier mobility in organic semiconductors: Herringbone vs pi-pi stacking, *J. Mater. Chem. C* **4**, 4546 (2016).
- [61] J. Kirkpatrick, Calculating intermolecular charge transport parameters in conjugated materials, Ph.D. thesis, Imperial College London, 2007.
- [62] E. Rice, Computational modelling of electronic states, charge transfer and charge transport in organic semiconductors. Ph.D. thesis, Imperial College London, 2018.
- [63] A. Wadsworth, H. Bristow, Z. Hamid, M. Babics, N. Gasparini, C. W. Boyle, W. Zhang, Y. Dong, K. J. Thorley, M. Neophytou, R. S. Ashraf, J. R. Durrant, D. Baran, and I. McCulloch, End group tuning in acceptor-donor-acceptor nonfullerene small molecules for high fill factor organic solar cells, *Adv. Funct. Mater.* **29**, 1808429 (2019).



Technical  
University of  
Denmark

Fysikvej, Building 310  
2800 Kgs. Lyngby  
Tlf. 45 25 25 25

[www.energy.dtu.dk](http://www.energy.dtu.dk)